Dissertation

Advances in the acquisition and processing of subseafloor temperature and pressure data and their interpretation in the context of convergent margin processes

zur Erlangung des Doktorgrades der Naturwissenschaften
am Fachbereich Geowissenschaften
der Universität Bremen
vorgelegt von

Martin Heesemann

Bremen, Juli 2008

7.7.2008

Martin Heesemann
Würzburger Str. 86
28215 Bremen

Erklärung

Hiermit versichere ich, dass ich

1. die Arbeit ohne unerlaubte fremde Hilfe angefertigt habe.
2. keine anderen als die von mir angegebenen Quellen und Hilfsmittel benutzt habe und
3. die den benutzten Werken wörtlich oder inhaltlich entnommenen Stellen als solche kenntlich gemacht habe.

Bremen, den 7.7.2008

Contents

Kurzfassung

Temperatur und Druckmessungen am Meeresboden liefern uns wichtige Informationen über dynamische Prozesse im Erdinneren. Um an diese wertvollen Daten zu gelangen, werden zuverlässige Sonden, die hoch auflösende Messwerte liefern, benötigt. Außerdem sind Fehlerkorrekturverfahren erforderlich, die Störungen der Messdaten, welche beim Eindringen der Sonden in den Meeresboden entstehen, korrigieren. Letztendlich müssen die Temperatur und Druckmessungen, zusammen mit Informationen aus anderen geophysikalischen Messungen und geologischen Beobachtungen, im Rahmen von konzeptionellen oder numerischen Modellen interpretiert werden, damit wir aus ihnen etwas über geologische Prozesse lernen können.

Beispiele für moderne Druck- und Temperatursonden sind das Advanced Piston Corer Temperature Tool in der 3. Version (APCT-3), der Miniaturized Temperature Logger (MTL) und die Davis-Villinger Temperature and Pressure Probe (DVTPP). Das APCT-3 setzt neue Standards in den Bereichen Genauigkeit, Auflösung und Zuverlässigkeit, was die Messung von Temperaturen während der Kernentnahme in Integrated Ocean Drilling Program (IODP) Bohrlöchern angeht. MTLs sind aufgrund ihrer hohen Langzeitstabilität und Auflösung hervorragend dafür geeignet Temperaturen in marinen Bohrlöchern über lange Zeiträume zu beobachten. Das DVTPP ist die erste Bohrlochsonde, die im Rahmen des Ocean Drilling Program (ODP) dazu verwendet wurde, um In-situ Formationsporendrücke zu messen.

TP-Fit ist ein neues Programmpaket, das es ermöglicht Temperaturdaten von Bohrlochsonden in Hinsicht auf die während des Eindringens der Sonden entstehenden Störungen zu korrigieren. Im Zuge der Entwicklung von TP-Fit wurden außerdem zum ersten Mal systematisch die Fehler, die bei der Analyse von Bohrlochtemperaturdaten auftreten können, erfasst und quantifiziert. TP-Fit basiert auf numerischen Modellen der Temperatursonden, die mit Hilfe der Finite Elemente (FE) Methode berechnet wurden. Im Vergleich zu Modellen die in älteren Programmen zur Abschätzung der ungestörten Formationstemperatur benutzt wurden, spiegeln die neuen FE Modelle die komplexen Geometrien der verschiedenen Sonden deutlich besser wider. Außerdem ist es mit TP-Fit möglich Daten aller derzeit im Rahmen von ODP/IODP im Einsatz befindlicher Sonden in einer konsistenten Art und Weise zu prozessieren. Das Programm ist modular ausgelegt, um nachträgliche Erweiterungen, z.B. in Hinblick auf neue Temperatursonden oder das Prozessieren von DVTPP Druckdaten, zu vereinfachen.

Um aus Meeresbodentemperaturmessungen etwas über Prozesse an konvergenten Plattenrändern zu lernen, wurden die Messungen mit andere geophysikalische und geologische Beobachtungen in einem neuen FE Modell kombiniert. Das Ziel der Modellierung war es die Temperaturverteilung an der Bruchfläche des Tsunami-Erdbebens, das 1992 vor der Küste Nicaraguas stattfand, abzuschätzen. Diese Temperaturverteilung ist eine wichtige Einflussgröße, die die obere Grenze der seismogenen Zone—der Bereich der Plattengrenze an einer Subduktionszone, in dem es durch bruchhafte Verformung zu Erdbeben kommen kann—bestimmt. Im Vergleich zu anderen thermischen Modellen von Subduktionszonen zeichnet sich das neue Modell durch die detaillierte Abbildung der Strukturen im graben nahen oberen Bereich der Subduktionszone aus. Dies ist der Bereich in dem sich auch die Obergrenze der seismogenen Zone befindet.

Außerdem wurden Messungen von Meeresbodentemperaturen dazu verwendet, um Massen- und Energieströme, die in Subduktionszonen ein- und austreten, zu detektieren. Z.B. wurde anhand von Temperaturmessungen das Eintreten von kaltem Meerwasser in die ozeanische Kruste am „Outerrise“ vor der Küste im Süden Chiles nachgewiesen. Zusammen mit der Beobachtung von niedrigen seismischen Krustengeschwindigkeiten in diesem Bereich wurde die These entwickelt, dass die ozeanische Kruste und der obere Mantel vor ihrer Subduktion durch zahlreiche Brüche und Hydrierung durch Meerwasser verändert werden. In einem anderen Beispiel wurden Fluidströme durch den Schlammkegel Mound Culebra, der sich am Kontinentalhang vor der Costa Ricanischen Halbinsel Nicoya befindet, u.a. durch die Interpretation von Temperaturmessungen nachgewiesen.

Abstract

Subseafloor temperature and pore fluid pressure data can provide important constraints on most dynamic earth processes. Acquiring this data using direct measurements requires reliable probes that measure accurate data with high resolution. Additionally, algorithms to correct for disturbances—created during probe insertion into the formation of interest—are needed. Finally, to expand or knowledge about earth processes, the measured data have to be combined with geologic findings and data from other geophysical surveys using conceptual or numerical models of the studied processes.

Examples for modern temperature and pressure probes are the third version of the Advanced Piston Corer Temperature probe (APCT-3), the Miniaturized Temperature Logger (MTL), and the Davis-Villinger Temperature and Pressure Probe (DVTPP). The development of the APCT-3 sets new standards in accuracy, resolution, and reliability for measuring temperatures during piston coring in Integrated Ocean Drilling Program (IODP) boreholes. MTLs provide innovative means for long-term monitoring of borehole temperatures offering high resolution and excellent long term stability. The DVTPP is the first downhole tool that is capable to measure in-situ formation pore pressures in Ocean Drilling Program (ODP) boreholes.

TP-Fit is a new software package capable to correct temperature data of downhole tools for the disturbance created during insertion into the formation. During the development of TP-Fit, the accuracy of data analysis algorithms to process downhole temperature data was studied systematically, for the first time. TP-Fit uses finite element (FE) method models of the probes' thermal responses for the data analysis that represent the probes geometry better than reference models used in prior software packages. Using TP-Fit it is possible to process data from all temperature probes currently in use in the ODP/IODP consistently within a single software. Moreover, the program structure is modular and allows future additions as the processing of DVTPP pressure measurements.

Combining subseafloor temperature measurements with other geophysical and geological data, a thermal FE model was used to estimate the temperature field at the subduction thrust fault of the 1992 Nicaragua tsunami earthquake. Fault temperature is a controlling factor of the updip limit of the seismogenic zone—the portion of the interface between the subducting and the overriding plate at convergent margins that produces earthquakes via stick-slip sliding. Compared to previous thermal models of subduction zones, the model focuses particularly on details that effect the temperature distribution close to the trench where the updip limit of the seismogenic zone is located.

Subseafloor temperature measurements can be used to detect mass and energy inputs and outputs of subduction zones. For example, cold seawater infiltrating oceanic crust was detected using temperature data at the southern Chile trench-outer rise. This supported the interpretation of reduced seismic velocities as evidence that structures of the oceanic crust and the uppermost mantle are altered by fracturing and hydration before they enter the subduction zone. In another example, active fluid venting through the mud dome Mound Culebra, located on the continental slope offshore Nicoya Peninsula, Costa Rica, was inferred from subseafloor temperature measurements along with data from other geophysical surveys and gravity coring.

Preface

When I started to work on my PhD thesis in Summer 2002, the initial plan was to continue the work I had done during my diploma thesis „Modeling and analysis of transient pressure measurements in ODP boreholes for undisturbed formation pressure estimation“ (*Heesemann*, 2002) and to carry it on to a broader level in the frame of the DFG funded Temperature Probes of the ODP (TEMPO) project. I should have participated in Ocean Drilling Program (ODP) Leg 204 (July–September 2002) to measure formation temperatures and pressures with the APCT, DVTP, and DVTPP tools. Next steps would have been to develop enhanced processing algorithms to extrapolate the measured data to undisturbed formation values, to process the data with the new algorithms, and to interpret the data in the scientific context (gas hydrates) of the Leg 204. Meanwhile, I should have supported the development of the APCT-3, an enhanced APCT tool. But right from the start things did not work out as anticipated and the following research continued on winding paths that took a while to travel.

First of all, my application for the ODP Leg, even though strongly supported by the co-chief scientist Prof. Dr. Gerhard Bohrmann, was rejected. There was still hope, that I could use the measured data as shore-based scientist and carry out the initial plan after the end of Leg 204. In order to fill the time gap, I participated in RV Meteor cruise M54-2 (August–September 2002) with funding from the Middle America Margin Subsurface Temperature (MAMAST) project. During this time I helped to measure and to process seafloor heat-flux data, off Costa Rica. However, after Leg 204 has ended, there was no data for me to work with, since my request to use the temperature data as a shore-based scientist was rejected and most of the pressure measurements did not work out properly; most of them were affected by an plumbing error inside of the DVTPP. So I decided to focus my research on the interpretation of the MAMAST heat-flux data. I developed a finite element model for the thermal state of subduction zones based on the Femlab® toolbox (now COMSOL-Multiphysics®)—which I already knew from the work in my diploma thesis—during the continuation project MAMAST II. At the same time, the development of the APCT-3, which progressed more slowly than anticipated, was continued as part of the continuation project TEMPO II.

During the same time I also had the opportunity to participate in IODP Expedition 301T (August–September 2004), a short leg on the transit between two Expeditions to recover longterm temperature and fluid sampling observatories from ODP Sites 1253 and 1255, off Costa Rica. On this expedition, I had the chance to learn at first-hand how operations on a drill ship, that I only knew in theory, work. I was also able to connect one part of my prior research interests, measuring temperatures and pressures in marine boreholes, with the other part, the thermal structure of the subduction zone, off Costa Rica and Nicaragua.

After the MAMAST project ran out, I joined the BMBF funded „from The Incoming Plate to mega-Thrust EarthQuake processes“ (TIPTEQ) project. During TIPTEQ I continued to refine the thermal model of subduciton zones using constraining heat-flux measurements that I helped to acquire during RV-Sonne cruise SO-181-1b (December 2004–January 2005). Meanwhile, the development of the APCT-3 tool has been finished. This was just in time, so that first measurements with the prototype could be made during IODP Expedition 311 (August–October 2005) and the India gas hydrate Leg (May 2006), before the JOIDES Resolution was brought to a shipyard for extensive remodeling. Propelled by the success of the APCT-3 tool, I refocused on the data analysis of the temperature data, since none of the old programs could handle the data from the new tool properly. The outcome was TP-Fit, a program to extrapolate undisturbed formation temperatures from measurements of all kinds of tools commonly used during the ODP/IODP. The feed-back on TP-Fit from the scientific community was very encouraging. Therefore, by the time the TIPTEQ project ran out in July 2007, I accepted an offer from the IODP/TAMU to implement some further enhancements in TP-Fit as contract work. This work resulted in a better integration of the software, with the shipboard work flow and the database system.

If my application for ODP Leg 204 would not have been rejected, that path to this thesis would probably have been much straighter and shorter. But the way it was, I have covered a lot more scientific ground, which is also reflected in the unusually broad subject of the thesis. Moreover, I am grateful for the opportunities I had to spend time with so many wonderful people from all over the world and from different scientific communities along the way.

1 Introduction

More than fifty years ago, *Revelle and Maxwell* (1952) carried out first subseafloor temperature measurements in order to quantify the heat flux through oceanic lithosphere (*Nagihara and Lister*, 1993). Ever since, marine temperature measurements have constantly been adding to our knowledge about submarine processes. For example, they revealed the cooling of oceanic lithosphere (e.g. *Stein and Stein*, 1992) while aging in the tectonic cycle. They also detected dewatering of accretionary prisms (e.g. *Yamano et al.*, 1984), and pinpointed inflow and advection of fluids in the upper oceanic crust (e.g. *Fisher et al.*, 2003a; *Hutnak et al.*, 2007).

Quantifying pore pressures is equally important in order to study many marine processes. Despite of the demand of accurate pore pressure data there are only few reliable probes that measure pore pressure. Therefore, direct pore pressure measurements are scarce and studies depending on pore pressures often use estimates derived from the consolidation state of sediments, determined from samples in laboratory experiments or from the analysis of seismic impedances (e.g. *Bekins and Screaton*, 2007; *Saffer*, 2007).

This thesis focuses on the direct measurement of temperatures and pressures; examples how temperatures can be derived from the depth of bottom simulating reflectors (BSRs), imaged using seismic methods, are provided in Chapter 4 (*Heesemann et al.*, submitted 2008a; *Grevemeyer et al.*, 2004). To study submarine geology using direct temperature and pressure measurements three requirements have to be met:

Data acquisition Reliable probes that measure accurate data are needed.

Data analysis Since it appears that temperature and pressure probes inevitably disturb the formation during measurement, reliable algorithms to correct for these disturbances have to be applied in order to obtain accurate results.

Data interpretation The measurements have to be combined with other geologic findings and data from geophysical surveys in conceptual or numerical models of the studied processes.

Advances in all steps listed above, to which brief introductions are given in the following sections, are the objectives of this thesis.

1.1 Temperature and pressure probes

Subseafloor temperatures and pressures vary laterally, with depth, and in time. To resolve changes in all these dimensions by direct measurements, different probes and approaches have to be combined. For example, measurements at a distinct time in the upper few meters of the sediments are relatively simple to perform and therefore they can be repeated often at different locations providing a good lateral resolution. Yet, to study variations of temperatures and pressures at greater depth, measurements in costly boreholes are required. Therefore, the gain of depth information comes at the cost of reduced lateral resolution, since establishing marine boreholes is expensive and time consuming. At last, monitoring pressures and temperatures over long periods of time add another level of complication. In order to retrieve the data, the probes have to be relocated and revisited or have to be equipped with technology to transmit the data back to the scientists. Additionally, when monitoring temperatures and pressures in boreholes, the boreholes have to be sealed in order to prevent disturbances from the open borehole.

1.1.1 Seafloor measurements

Temperature

To measure temperatures in the first few meters of the sediments, heat-flux probes of the violin bow design (cf. Figure 1.1A) are commonly used (*Hyndman et al.*, 1979; *Hartmann and Villinger*, 2002). Besides measuring thermal gradients in the seabed they provide in-situ thermal conductivities, and many measurements can be carried out in a short period of time on „pogostick“ profiles (i.e. a series of measurements carried out during a single tool deployment). Surface heat-flux values computed using data measured with these probes are the basis of the studies presented

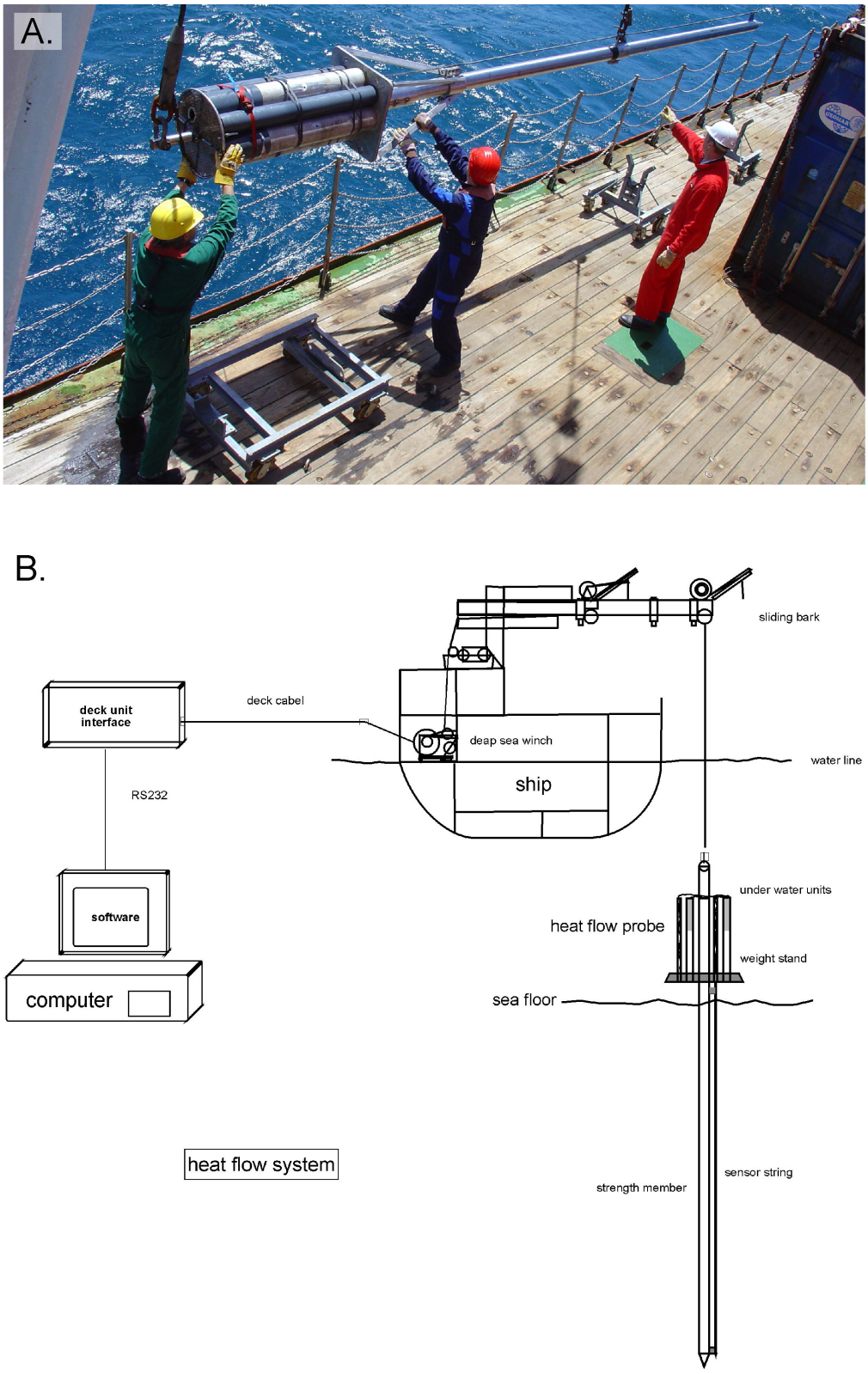

Figure 1.1: A. Modern heat-flux probe of the violin bow design about to be deployed. B. Schematic illustration of the data acquisition with a heat-flux probe (courtesy of Hans-Hermann Gennerich). Real time communication with the probe facilitates „pogostick“ deployments.

in Chapter 4. Besides heat-flux probes, miniaturized temperature loggers (MTLs) (*Pfender and Villinger*, 2002) are tools to measure temperatures in multiple ways. For measurements similar to heat-flux probe measurements, MTLs (cf. Figure 1.2) can be attached to gravity corer barrels (*Pfender and Villinger*, 2002; *Fisher et al.*, 2003b). Moreover, MTLs can also reliably monitor temperatures over long periods of time (*Heesemann et al.*, 2005, in Chapter 2).

Pressure

Several probes that measure pressures at the seafloor exist, but up to now, they are not as commonly used as heat-flux probes. To measure pore pressures in a „pogostick“ fashion the tethered probe was designed by *Davis et al.* (1991) and lately *Stegmann et al.* (2006); *Stegmann and Kopf* (2007) presented free-fall instruments for cone penetrating tests that also provide pore pressure measurements. However, there is one problem with measuring pore pressures: disturbances created during the insertion into the formation can take several hours to days to decay. Therefore, compared to heat-flux probes, only a limited number of measurements can be performed. Other probes, developed to monitor pore pressures in the seabed for a longer period of time, are the free falling Pop Up Pore Pressure Instrument (PUPPI) (*Schultheiss and McPhail*, 1986), and the Satellite-Linked Autonomous Pore Pressure Instrument (SAPPI) (*Kaul et al.*, 2004).

1.1.2 Borehole measurements

Boreholes provide the opportunity to measure temperatures and pressures during the time they are drilled and they can be used as observatories to monitor temperatures and pressures over extended periods of time. In fact, temperature was among the first downhole properties to be measured during scientific ocean drilling (*von Herzen and Maxwell*, 1964).

Downhole temperature tools

Unlike to onshore boreholes, a marine drill site can not be easily revisited after temperature disturbances due to drilling have decayed. Therefore, the simplest method to measure formation temperatures and pressures in marine boreholes is to perform the measurements while the borehole is established. In order to circumvent disturbances due to drilling, the probes have to be inserted into the undisturbed formation at the bottom of the borehole, which is only possible in unconsolidated and semi-consolidated sediments. Regarding temperature measurements, such probes were designed and improved for many years. There are two different types of borehole temperature tools. Firstly, the APCT temperature probes that are placed in the cutting shoe of the advanced piston corer (APC) and log formation temperatures while APC sediments cores are taken. Secondly, probes that are lowered to the bottom of the hole by wireline and require a dedicated tool run.

The first downhole temperature probe that was regularly used during scientific ocean drilling was the Uyeda tool that required a dedicated tool run. The Uyeda tool was first deployed in 1978 during the Deep Sea Drilling Project (DSDP) Leg 60 (*Uyeda and Horai*, 1982). Later, this tool was merged with the Barnes fluid sampler and became the water sampling temperature probe (WSTP). The dedicated temperature tool, which is mostly used today, is the Davis-Villinger temperature probe (DVTP), shown in Figure 1.3, which was introduced during ODP Leg 68 (*Davis et al.*, 1997).

The first APCT tool was deployed in 1984 during DSDP Leg 86 (*Horai and Von Herzen*, 1985), and its use almost immediately became a routine part of drilling operations. The tool, was improved and redesigned two times and since Intgerated Ocean Drilling Program (IODP) Expedition 311 the third generation of the tool (APCT-3), presented in Chapter 2 (*Heesemann et al.*, 2007), is in operation.

Downhole pressure tools

The use of standard tools for direct measurements of fluid pressures such as drill stem tests, packer tests, and repeat formation testers is difficult during (Ocean Drilling Program) ODP/IODP legs, because of the unstable nature of the boreholes and the operation complexities of working from a moving platform in deep waters (*Moore and Tobin*, 1997). Additionally, these tests are typically made many hours or days after drilling and thus follow significant changes of the pressure environment caused by the borehole (*Moore et al.*, 1995).

In order to fill that gap, two down-hole tools for measuring formation pressures are currently under development. Both tools, the Temperature-Two-Pressure Probe (T2P) which is based on the Fugro-McClelland Marine Geosciences Inc.'s piezoprobe

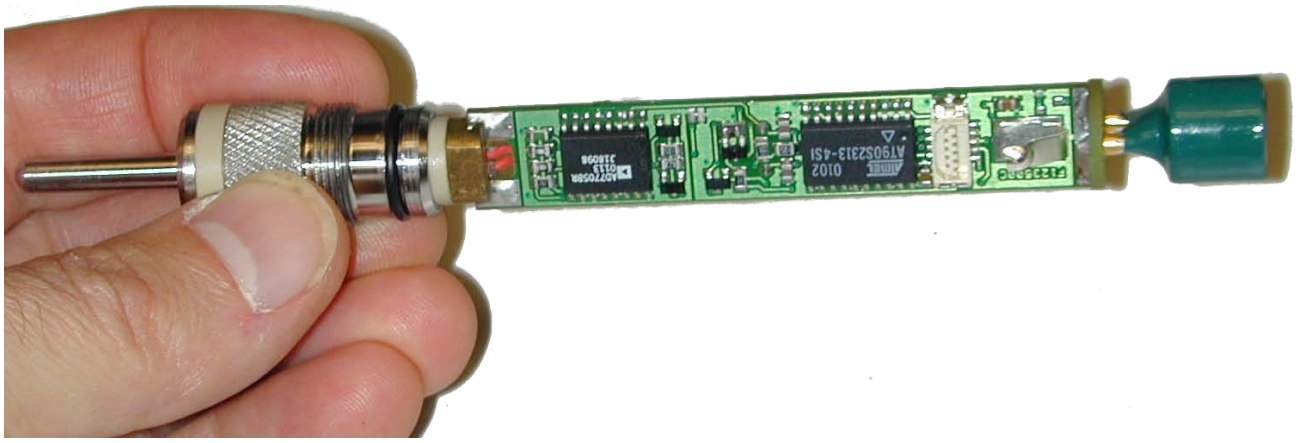

Figure 1.2: Circuit-board of a miniaturized temperature logger (MTL) unveiled after removing the pressure-housing.

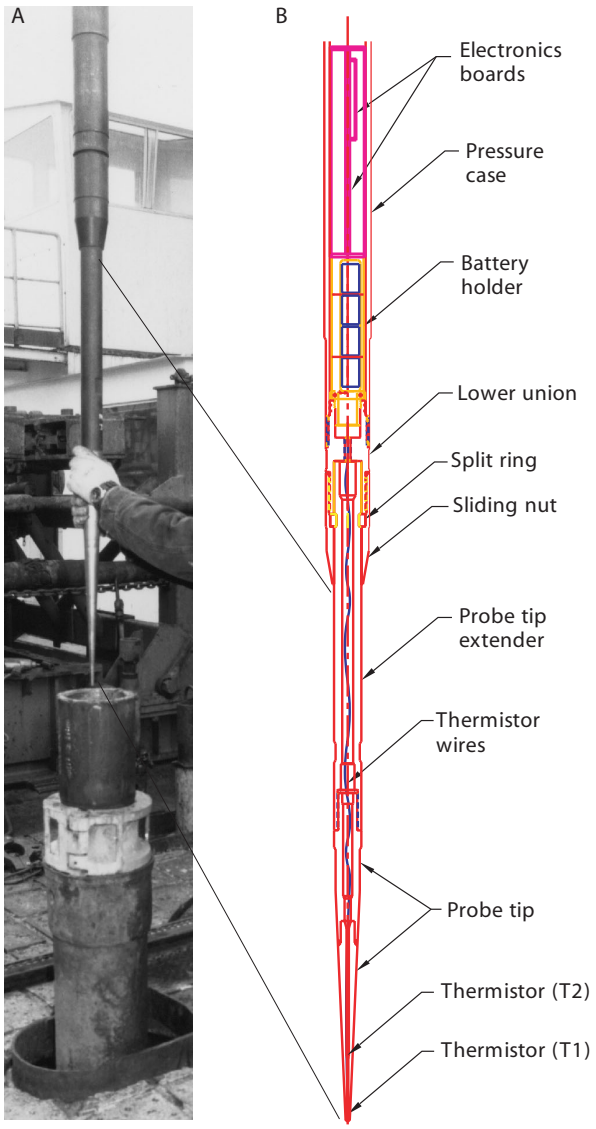

Figure 1.3: A. Davis-Villinger temperature probe (DVTP) about to be deployed. B. Techincal details of the DVTP (from *Graber et al.*, 2002).

(*Whittle et al.*, 2001; *Long et al.*, 2007; *Flemings et al.*, 2008), as well as the Davis-Villinger Temperature and Pressure Probe (DVTPP) which is described in Chapter 3, follow the concept of several tools that were designed to observe pore pressures in the upper meters of the seabed. All of these devices consist of a lance that penetrates the sediments and a pressure sensor on top of the lance that is connected to the formation's pore-space by hydraulic tubing extending from pressure ports drilled through the lance.

While the T2P is an attempt to modify a cone-penetrometer in a way that it disturbs the tested formation as little as possible, the DVTPP is an advanced version of the robuster Davis-Villinger temperature probe (DVTP). The DVTP was extended by adding a high resolution Paroscientific pressure gauge. In 2000, first measurements using a prototype of the DVTPP, have been performed during ODP Leg 190 (*Moore et al.*, 2001).

The concepts underlying the measurements of the T2P and the DVTPP are very similar. Measurements take place ahead of the drill-bit, where the formation is assumed to be undisturbed from drilling. Furthermore, both of the tools incorporate temperature sensors that allow the determination of formation temperatures along with formation pressures. The main difference of the tools is their geometry: on one hand, the DVTPP design is much more robust providing the possibility to do measurements in stiff sediments where even the advanced piston corer (APC) fails. On the other hand, the T2P causes smaller disturbances during insertion into the formation.

Borehole observatories

Boreholes also provide the possibility to install observatories that measure temperatures and pressures over long periods of times. These observatories are, however, expensive to install and to maintain. Therefore, they provide even less opportunities to monitor lateral variations. To measure formation temperatures and pressures the borehole has to be sealed to obviate interaction with the seawater. Especially for measuring pressures, the probed sections of the formation have to be packed off, since the borehole has either a hydrostatic pressure gradient, or there will be vigorous fluid flow that counteracts the non hydrostatic pressure gradient in the open hole.

The circulation obviation retrofit kit (CORK) (cf. Figure 1.4) is an instrument that overcomes these problems by sealing the cased holes and monitoring pressures and temperatures for long periods of time in order to allow the decay of drilling disturbances (*Davis et al.*, 1992). At the formation of interest, the holes are left open or the casing is perforated to allow the measurement of pore pressures right below the seal, where the sensor is situated (*Becker and Davis*, 2004).

Figure 1.4: Scientists and technical-staff of the ODP drillship JOIDES Resolution prepare a CORK borehole observatory for installation on a marine borehole (from *Becker and Davis*, 2000)).

1.2 Analysis of temperature and pressure data

All probes (including boreholes), when inserted into a formation, create temperature and pore pressure disturbances. Usually, if one waits long enough, the formation will recover from these disturbances and return to its undisturbed state (cf. Figure 1.5). The magnitude of the disturbance and the time it takes until the formation has recovered to its undisturbed state differs from measurement to measurement and also between probes. Usually, it is not practicable during a formation temperature or pore pressure measurement to wait until the disturbance has completely vanished. Therefore, algorithms to extrapolate transient pressure and temperature data to undisturbed formation values are required (cf. manuscripts in Chapter 3).

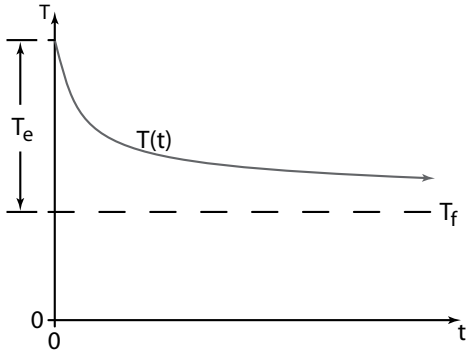

Figure 1.5: Decay of a disturbance (in this case temperature) that is caused by the insertion of a probe. The temperature is initially raised by excess temperature T_e above the undisturbed formation temperature T_f.

1.3 Interpretation of temperature and pressure data in the context of convergent margins

All advances regarding the interpretation of temperature and pressure data presented in Chapter 4 of this thesis are in the context of processes at convergent margins which, due to their social and economic importance, have long been studied by earth scientist from different disciplines.

Convergent margins are coastal regions that are, especially in the circum-Pacific „ring of fire“, among the most densely inhabited areas of the world even though they are also the regions that are threatened by some of the most devastating geohazards. The worlds largest earthquakes, most tsunamis, and explosive volcanism, all take place at convergent margins. On the other hand, converging tectonic plates give rise to essential goods as most of the worlds ore deposits and, taking into account geologic time scales, most of the worlds continental crust (*Dixon and Moore*, 2007; *MARGINS Office*, 2003).

The research results regarding coastal continental margins in general and convergent margins in particular were summarized by the scientific community during the planing phase of the MARGINS program (1988–1993). These efforts were undertaken in order to focus future interdisciplinary research on fundamental questions of earth science that, if answered, would have the greatest impact on our understanding of convergent margins and subduction zones. When the MARGINS Program officially started in 1998, research related to different marine aspects of convergent margins was focused into two initiatives: the Seismogenic Zone Experiment (SEIZE) initiative and the Subduction Factory (SF) initiative (*MARGINS Office*, 2003).

1.3.1 Seismogenic Zone Experiment

SEIZE focuses on the seismogenic zone (cf. Figure 1.6), which is the portion of the interface between the subducting and the overriding plate at convergent margins that produces earthquakes via stick-slip sliding (e.g. *Brace and Byerlee*, 1966), at two locations. The first location, off Japan, is covered by the Nankai Trough Seismogenic Zone Experiment (NanTroSEIZE) and the second site, off Costa Rica and Nicaragua, is investigated by the Costa Rica Seismogenesis Project (CRISP). The research questions, fundamental for the understanding of seismogenic zones (*MARGINS Office*, 2003), studied at these locations are:

1. What is the physical nature of asperities?
2. What are the temporal relationships among stress, strain and pore fluid composition throughout the earthquake cycle?
3. What controlls the updip and downdip limits of the seismogenic zone of subduction thrusts?
4. What is the nature of tsunamigenic earthquake zones?
5. What is the role of large thrust earthquakes in mass flux?

1.3.2 Subduction Factory

The SF initiative focuses on the flux and recycling of fluids and volatiles in subduction zones. Additionally, the overall mass balance across subduction zones is studied (cf. Figure 1.7). In this context the term Subduction Factory is used to illustrate the fact, that we have only direct access to the input materials that enter a subduction zone at the deep sea trench and the materials it returns to the surface (e.g. volcanic magmas and ore deposits). All processes within the subduction factory are hidden from our view (*MARGINS Office*, 2003).

For the SF initiative, there are also two high priority locations where research is carried out. Firstly, the same area off Nicaragua and Costa Rica as for the SEIZE initiative and, secondly, the western Pacific margins of Tonga, Izu-Bonin, and the Marianas. Two of the studies (*Grevemeyer et al.*, 2004; *Heesemann et al.*, submitted 2008a) presented in Chapter 4 were carried out as part of the Collaborative Research Center „Volatiles and Fluids in Subduction Zones: Climate Feedback and Trigger Mechanisms for Natural Disasters“ (SFB 574) which is the German counterpart of the SF initiative. The SFB 574 also focuses on the subduction zone off Nicaragua and Costa Rica, as well as, on the Chile margin. The fundamental research questions with respect to the subduction factory (*MARGINS Office*, 2003) are:

1. How do forcing functions such as convergence rate and upper plate thickness regulate production of magma and fluid from the Subduction Factory?

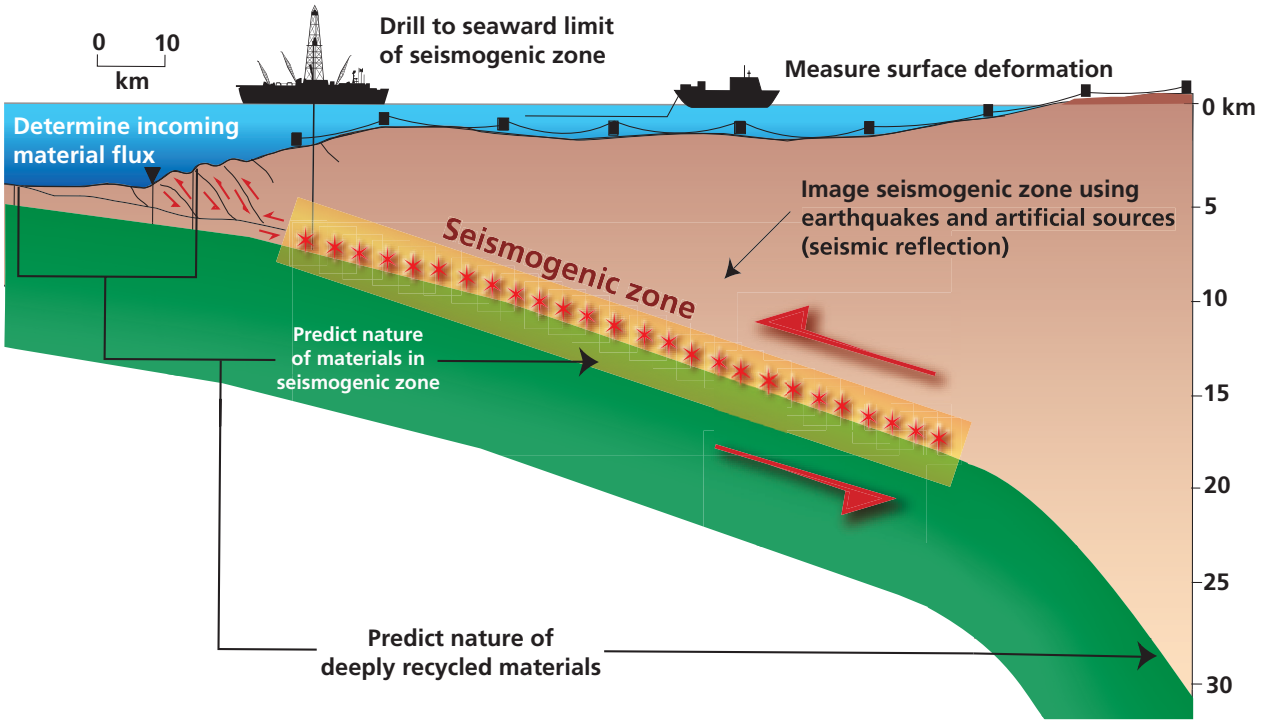

Figure 1.6: Methods used by scientists involved in the SEIZE initiative to probe, image, and model the seismogenic zone of subduction zones (from *MARGINS Office*, 2003).

2. How does the volatile cycle (H_2O and CO_2) impact biological, physical and chemical processes from trench to deep mantle?

3. What is the mass balance of chemical species and material across Subduction Factory, and how does this balance affect continental growth and evolution?

1.4 Objectives of the thesis

The objectives of the work that led to this thesis were to twofold. Firstly, to increase the quantity and accessibility of high quality subseafloor formation temperature and pore pressure data available for the scientific community in the future. Steps taken toward this goal include evaluation and improvement of the accuracy, reliability and handling of temperature and pressure probes as well as of the algorithms and software packages to estimate undisturbed formation values from transient measurements. The second objective of my work was to contribute to answering the fundamental research questions asked by the convergent margin research community. This goal was approached by acquiring subseafloor temperatures along with other geophysical data—plans for DVTPP pore pressure measurements during ODP Leg 204 had to be abandoned as pointed out in the preface—and interpreting this data toward answering the research questions. One focus during the interpretation was to integrate geophysical and geological data from different sources into coherent thermal models.

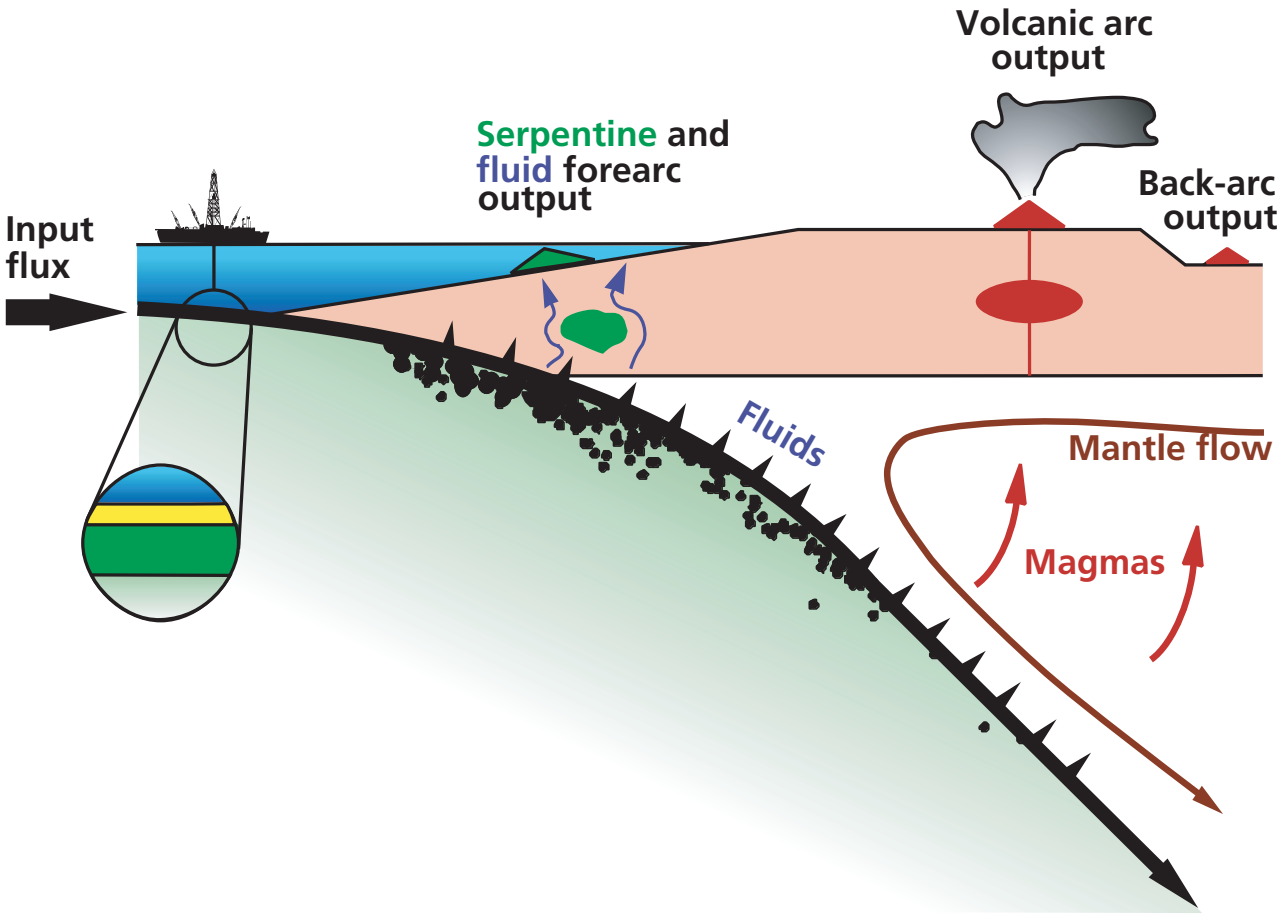

Figure 1.7: The Subduction Factory: input, processing, and output of fluids, and volatiles within a subduction zone (from *MARGINS Office*, 2003). The input of fluids and volatiles consists of the pore fluids of subducted sedimentary sections and hydrated crust and mantel material (inset).

1.5 Outline and strategy

My efforts to evaluate and enhance probes to measure subseafloor formation temperatures and pore pressures are documented in two publications in Chapter 2 and a manuscript in Chapter 3. In these chapters, each paper is preceded by a short introduction that summarizes my specific contributions. The first publication (*Heesemann et al.*, 2007, pp. 20) focuses on the development of the APCT-3 probe, which I supported during the work for this thesis, and the resulting advances in measuring downhole temperatures. In the second publication (*Heesemann et al.*, 2005, pp. 40), an innovative way for long-term monitoring of borehole temperatures using miniaturized temperature loggers (MTLs) is described. The prototype of the DVTPP, the first downhole tool capable to measure formation pore pressures in ODP boreholes, is described in the manuscript (*Heesemann et al.*, submitted 2008b, pp. 96). The main topic of the manuscript is, however, the extrapolation of the transient pressure measurements to undisturbed formation pressures, therefore it is placed in Chapter 3.

Chapter 3 focuses on the analysis of data from ODP/IODP downhole temperature and pressure tools. In the first manuscript (*Heesemann et al.*, in prep. 2008a, pp. 61), the algorithm to extrapolate undisturbed formation temperatures from transient data of downhole tool is systematically evaluated and improved, mainly by providing new reference models that more precisely reflect the geometries of the different probes. Next, TP-Fit (*Heesemann*, 2008, pp. 90), a new software capable to analyze data of all ODP/IODP temperature probes currently in use, is presented. The design and implementation of TP-Fit was part of the work leading to this thesis and is based on the research presented in the previous manuscript. Chapter 3 concludes with a manuscript (*Heesemann et al.*, submitted 2008b, pp. 96) that describes an algorithm how to estimate undisturbed formation pressures from DVTPP data.

The studies presented in Chapter 4 show how the combination of different types of temperature measurements with other geophysical and geological data sheds light on processes at convergent margins. The first manuscript (*Heesemann et al.*, submitted 2008a, pp. 109) presents a numerical finite element (FE) model which is used to estimate the temperature at the subduction thrust fault of the 1992 Nicaragua tsunami earthquake. The development of the model was a major part of the work leading to this thesis. In contrast to other thermal models of subduction zones (e.g. *Wang et al.*, 1995), the new FE model focuses particularly on details that effect the temperature distribution close to the trench where the updip limit of the seismogenic zone is located, which was e.g. suggested in the SEIZE initial science plan (*MARGINS Office*, 2003). The model combines constraints derived from numerous geophysical surveys and geological evidence to shed a little light on three points concerning the five fundamental research questions raised by the SEIZE initiative: (1) the physical nature of asperities, (2) controls of the updip limit of the seismogenic zone of subduction thrusts, and (3) the nature of tsunamigenic earthquake zones.

In the remaining two publications of Chapter 4, inputs and outputs of the subduction factory are detected using violin-bow heat-flux probe measurements. Firstly, *Contreras-Reyes et al.* (2007) (Chapter 4, pp. 124) interpret reduced seismic velocities as evidence that structures of the oceanic crust and the uppermost mantle are altered by fracturing and hydration before they enter the subduction zone. Using the heat-flux data it was possible to identify a location where cold seawater infiltrates the oceanic crust. Secondly, (*Grevemeyer et al.*, 2004) (Chapter 4, pp. 144) inferred active fluid venting through the mud dome Mound Culebra, located on the continental slope offshore Nicoya Peninsula, Costa Rica, from violin bow heat-flux probe measurements, and data from other geophysical surveys and gravity coring.

2 Measurement of temperatures and pressures

This chapter consists of two publications that document efforts to evaluate and enhance probes to measure subseafloor formation temperatures. The first publication (*Heesemann et al.*, 2007, pp. 20) focuses on the development of the APCT-3 probe, which I supported during the work for this thesis. Furthermore, it points out advances in measuring downhole temperatures that were achieved. The second publication (*Heesemann et al.*, 2005, pp. 40), describes an innovative way for long-term monitoring of borehole temperatures using miniaturized temperature loggers (MTLs). The prototype of the DVTPP, the first downhole tool capable to measure formation pore pressures in ODP boreholes, is introduced in the manuscript (*Heesemann et al.*, submitted 2008b, pp. 96). The main topic of the manuscript is, however, the extrapolation of the transient pressure measurements to undisturbed formation pressures. Therefore it is placed in Chapter 3.

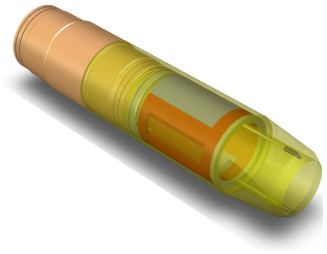

APCT-3

Publication: Testing and deployment of the new APCT-3 tool to determine in-situ temperatures while piston coring

Heesemann, M., H. Villinger, A. T. Fisher, A. M. Tréhu, and S. Witte (2007), Testing and deployment of the new APCT-3 tool to determine insitu temperatures while piston coring, in *Expedition Reports*, *Proceedings of the Integrated Ocean Drilling Program*, vol. 311, doi:10.2204/iodp.proc.311.108.2006.

Contributions

Andrew T. Fisher and Heinrich Villinger initiated the development of the APCT-3, a downhole tool to measure temperatures while piston coring, in 2002. Firstly, Martin Heesemann computed the thermal response of the mechanical parts of the tool in order to evaluate whether the probes time-constant can be decreased by optimizing the cutting shoe geometry. Subsequently, ANTARES Datensysteme GmbH was contracted to design and assemble the electronic parts of the APCT-3.
The following publication introduces the APCT-3 tool, explains required calibration procedures, and shows first temperature data. Martin Heesemann compiled the manuscript and analyzed the calibration data, Heinrich Villinger and Andrew T. Fisher supervised the research, Anne M. Tréhu deployed the tool during IODP Expedition 311 and acquired calibration data, and Steffen Witte supplied technical drawings and specifications.

Data report: testing and deployment of the new APCT-3 tool to determine in situ temperatures while piston coring[1]

Martin Heesemann,[2] Heinrich Villinger,[2] Andrew T. Fisher,[3] Anne M. Tréhu,[4] and Steffen White[5]

Chapter contents

[1]Heesemann, M., Villinger, H., Fisher, A.T., Tréhu, A.M., and White, S., 2006. Data report: testing and deployment of the new APCT-3 tool to determine in situ temperatures while piston coring. *In* Riedel, M., Collett, T.S., Malone, M.J., and the Expedition 311 Scientists. *Proc. IODP,* 311: Washington, DC (Integrated Ocean Drilling Program Management International, Inc.). doi:10.2204/iodp.proc.311.108.2006
[2]Universität Bremen, Department of Geosciences, Klagenfurter Strasse, 28359 Bremen, Germany. Correspondence author: **heesema@uni-bremen.de**
[3]Institute of Geophysics and Planetary Physics and Department of Earth Sciences, University of California, Santa Cruz, 1156 High Street, Santa Cruz CA 95064, USA.
[4]**Expedition 311 Scientists' addresses.**
[5]ANTARES Datensysteme, GmbHRudolf-Diesel-Strasse 6, 828816 Stuhr, Germany.

Abstract

During Integrated Ocean Drilling Program Expedition 311, the third-generation advanced piston corer temperature (APCT-3) tool, a new downhole tool to determine in situ formation temperatures while piston coring, was successfully tested and deployed for the first time. Its development was partly driven by the need to replace the advanced piston corer temperature tools, which were lost or damaged during many successful deployments over the last 15 y. Additionally, many important scientific problems require instruments having greater stability, accuracy, measurement frequency, and robustness than were available in the past. During all nine deployments during Expedition 311, the APCT-3 tool proved to be robust, reliable, and user-friendly regarding its mechanics, electronics, and operation software. In addition, the test deployments also provided temperature data that were important for achieving expedition objectives. Moreover, it was demonstrated that the APCT-3 tool is capable of measuring temperatures with a resolution and absolute accuracy (depending on careful calibration) of ~1 mK at a sampling interval of 1 s, an improvement of about one order of magnitude compared to earlier instrumentation.

Introduction

Geothermal measurements provide important constraints on dynamic Earth processes; therefore, temperature was among the first downhole properties to be measured during the Deep Sea Drilling Project (DSDP) (Von Herzen and Maxwell, 1964). New tools were developed and modified during DSDP (Horai, 1985; Uyeda and Horai, 1982) and throughout the Ocean Drilling Program (ODP) (Davis et al., 1997; Fisher and Becker, 1993; Shipboard Scientific Party, 1992). Temperature measurements made during marine scientific drilling have been used to investigate heat transfer from the interior of Earth, oceanic lithosphere evolution, continental margin formation and subduction, and hotspot volcanism. In addition, these data have been used to examine processes associated with fluid flow and gas hydrate formation (e.g., Erikson et al., 1975; Hyndman et al., 1987; Pribnow et al., 2000). Undoubtedly, measurements of formation and fluid temperature will remain a high priority for downhole tool operations in the Integrated Ocean Drilling Program (IODP).

During a 2004 IODP downhole tools workshop (Flemings et al., 2004), all participants agreed that precise downhole temperature measurements are essential for fulfilling the goals of the IODP Initial Science Plan (ISP) (Kappel and Adams, 2001) in all three of the primary research themes:

1. Deep biosphere and subseafloor ocean,
2. Environmental change processes and effects, and
3. Solid earth cycles and geodynamics.

With these goals in mind, researchers began developing the next generation of tools to measure subseafloor temperatures during routine piston coring operations. This data report summarizes results of the first in situ deployments of a new instrument that will help to achieve high-priority IODP goals.

Soon after development of the advanced piston corer (APC) during the late stages of DSDP, researchers developed a miniature sensor and logger package designed to fit in the APC cutting shoe to measure sediment temperatures as a core was taken (Horai and Von Herzen, 1985); the Advanced Piston Corer Temperature (APCT) tool. This tool allowed DSDP (and later, ODP) personnel to determine in situ temperatures within the undisturbed formation well ahead of the drilling bit without making a dedicated tool run. The APCT tool was first deployed during DSDP Leg 86 in 1984, and its use almost immediately became a routine part of drilling operations. Eight of these first-generation APCT tools were purchased by ODP at the start of the new program, but these tools became damaged over the years until none was left by the time of ODP Leg 117. It took several years to develop a replacement tool, but this was finally accomplished in time for ODP Leg 139 in 1991 (Shipboard Scientific Party, 1992). Ten of the second-generation APCT tools were purchased for ODP use and were deployed successfully during numerous expeditions over the next 12 y, through the end of ODP at-sea operations.

By the end of ODP operations in 2003, most of the second-generation APCT tools had been lost or damaged, and several of the remaining tools had been serviced one or more times to repair damage. In addition, evaluation and comparison of in situ temperatures determined with the APCT tool and with other downhole tools (e.g., Shipboard Scientific Party, 1997) suggested that there was a need to re-evaluate tool design, performance, calibration, and analysis procedures and to develop a third generation of APCT instrumentation. Funds for the development of a third-generation APCT system were secured by a joint German and U.S. team led by H. Villinger (University of Bremen) and A. Fisher (University of California, Santa Cruz). In order to produce instruments with greater stability, accuracy, measurement frequency, and robustness than were available in the past, and in order to minimize development time and cost, the research team worked cooperatively on design of the new instruments with Fa. Antares (Stuhr, Germany), who had recently developed a miniaturized temperature data logger (MTL), also in cooperation with the University of Bremen (Pfender and Villinger, 2002; Jannasch et al., 2003). The design team consulted extensively with personnel from the U.S. operator for IODP to evaluate the design of the existing APCT coring shoe and related hardware in order to retain compatibility of system components with conventional coring operations. Work on the new system progressed during 2004–2005, and a prototype was made available in time for testing at sea during IODP Expedition 311. This third-generation APCT system is herein referred to as the APCT-3 tool.

The prototype APCT-3 tool was calibrated immediately before Expedition 311, as described below, and deployed nine times during the expedition. The calibrated APCT-3 prototype was also used to cross-check calibration of previous generation APCT tools that were also used during the expedition. The primary scientific objective of Expedition 311 was to understand processes that control the distribution and amount of gas hydrate in the shallow sediments of the accretionary margin offshore Vancouver Island, northeastern Pacific Ocean (see the **"Expedition 311 summary"** chapter). Determination of subseafloor temperature is particularly important for achieving this objective because thermal conditions fundamentally control gas hydrate stability. Comparison of in situ temperatures, gas hydrate stability, and the depth of bottom-simulating reflectors (BSRs) determined with seismic reflection surveys will help to determine whether the gas hydrates found in the Expedition 311 region are in thermodynamic equilibrium. Thermal data collected during Expedition 311 are reported in individual site chapters along with preliminary determinations of in situ temperatures, thermal gradients, and heat flow derived from the data.

Tool description

Like the earlier generation APCT tools, the APCT-3 tool fits in an annular cavity in the APC cutting shoe (Fig. **F1A**). Tool electronics are arranged on a cylindrical frame; sensor and registration prongs extend close to the end and outside edge of the cutting shoe. During

standard deployment, the APC inner core barrel is run to bottom on the coring wireline at the bottom of the borehole. Pump pressure is then applied to the drill pipe, which acts as a hydraulic accumulator. When pressure is great enough, it severs shear pins and strokes the inner core barrel 9.5 m into the sediment, well beyond the thermal influence of drilling operations. Following penetration, the core barrel is decoupled from the drill string and the APCT-3 is left stationary for 7–10 min. This allows part of the thermal disturbance associated with frictional heating of the penetration to decay. Finally, the coring shoe and core barrel are extracted from the formation and returned to the deck, where communication with the APCT-3 tool can be established and data are extracted for analysis.

The APCT-3 temperature logger consists of a temperature sensor and two circuit boards mounted on a cylindrical supporting frame (Fig. **F1B**). There is sufficient space on the electronics frame to hold a second electronics set, although this space is currently not used. It is anticipated that scientists may wish to develop additional measurement capabilities in the future using this space. At the base of the frame are two prongs that fit into index holes at the bottom of the annular cavity in the cutting shoe. These prongs help keep the electronics in place during deployment, and one of them houses the temperature sensor.

The sensor element for the APCT-3 tools is an aged, glass-encapsulated thermistor (Model YSI 55032). This thermistor has a high temperature coefficient (~4% per degree change in temperature) across a wide usable temperature range from –80° to +100°C (Fig. **F2B**) and can withstand temperatures as high as 200°C for brief periods. The lead wires of the sensor are soldered to the circuit board that holds the logger electronics. This board contains a microprocessor, a 16-bit analog to digital (A/D) converter, a real-time clock, and nonvolatile memory for as many as 65,000 readings.

Electrical power is supplied by two standard lithium batteries mounted on a second circuit board, which is easily serviceable and replaceable. The battery capacity allows at least 600,000 readings equaling continuous operation for ~1 week at a sampling rate of 1 s. Even if there is a total loss of battery voltage, the recorded data are preserved in nonvolatile memory. The APCT-3 electronics can safely be operated at ambient temperatures from –10° to 60°C. Nominal temperature resolution of the complete instrument is ≤2.5 mK over a range from –6° to +55°C, and ≤1.0 mK at temperatures ≤25°C (Fig. **F2**). This range should be adequate for the vast majority of shallow environments in which APC coring is likely to be attempted during IODP.

Communication with the APCT-3 temperature logger is accomplished using custom software (WinTemp) and an interface box that connects to the contact pins of the logger on one side (Fig. **F1B**) and to the RS-232 port (or universal serial bus [USB] port by adapter) of a personal computer (PC) running Microsoft Windows 2000/XP. WinTemp was originally developed for use with MTLs and provides a graphic interface for programming and data recovery. Using a logger setup dialog, it is possible to set the logger's real-time clock or synchronize it with the clock of the PC. The operator sets logging start date and time, logging duration, and a constant sample interval during deployment ranging from 1 s to 255 min. The software also provides functionality to retrieve temperature data from the logger, clear the tool's memory, check battery voltage, and display real-time readings of digital counts, resistance, and apparent temperature.

After recovering data from a tool, WinTemp displays calculated temperatures in text format, and data can be saved in a binary file (*.wtf), a WinTemp-specific format, or exported to an ASCII-format file (*.dat). The latter file consists of a multiline header, which includes the logger identification number and columns of measurement dates, times, A/D converter readings, computed thermistor resistances, and computed temperatures. Computations of resistance and temperature are based on the information contained in a calibration file (*.wtc), which is assigned to an individual logger. Tool-specific calibration information is stored in the binary data files along with the logger readings.

Antares supplies calibration files with every delivered logger. The contents of these files are based on the specifications of the electronic components comprising the APCT-3 data logger and the resistance-temperature curves supplied by the manufacturer of the thermistors. These calibration files offer an absolute accuracy on the order of ±0.1°C, but considerably greater accuracy on the order of ±0.001°–0.002°C can be achieved through careful calibration and processing, as discussed below.

Once data are converted to temperatures using the calibration coefficients, additional processing is required to estimate undisturbed formation temperature. As with all penetrating subseafloor temperature measurement tools, a tool response function must be used to extrapolate observations (e.g., Bullard, 1954; Davis et al., 1997; Horai, 1985). This function depends on tool geometry, distribution of frictional heat generated during tool penetration, and thermal

properties of the sediments and the tool. For conventional oceanic heat flux measurements the analytical F(a,t) function is used as a reference for comparison with observations (Bullard, 1954; Carslaw and Jaeger, 1959). Use of the F(a,t) function presumes, however, that the geometry of the probe is well described by a semi-infinite solid cylinder, which is not the case for the more complex geometry of the APCT-3 tool.

An analytical solution for a one-dimensional radial geometry was developed for the first-generation APCT tool (Horai, 1985), with a central cylinder of sediment, a ring of metal, and an infinite surrounding region of sediment. This approach, like that for a thin cylindrical probe, is based on the assumption that the tool behaves as if it extends vertically well away from the sensor and that heat transport following tool insertion is purely radial within a homogeneous medium. This approach was adapted for use in software having a graphical interface (TFit) that was developed as part of the second-generation APCT tool.

Decay curves are calculated for different sediment thermal conductivity values, and a curve is usually selected on the basis of independent observations of thermal conductivity from needle probe measurements on recovered core. It is common practice during processing to allow an arbitrary shift in time between modeled and measured decay curves so as to minimize the misfit between measured and modeled decay curves. This time shift is intended to correct for a series of nonideal behaviors, including incomplete knowledge of tool insertion time, finite time for insertion (possibly involving multiple frictional pulses), finite tool response time, incomplete thermal coupling between the sensor and the shoe, modification to sediment properties both inside and outside the tool, short-term advection immediately adjacent to the coring shoe, and nonhorizontal heat conduction.

As a practical matter, there is often considerable uncertainty in sediment thermal properties, including heterogeneity, immediately adjacent to the APC coring shoe, so the user must process data using a range of assumed sediment thermal conductivities in order to evaluate uncertainties. Even in the case of ideal tool response (i.e., no motion of shoe during temperature decay following the initial friction spike), it is not possible to use statistical-fit criteria to determine the effective thermal conductivity; essentially all decay curves can be made to fit the data, albeit on the basis of different time shifts. In cases where the decay curve is not ideal, it may be necessary to use only part of the record and different record segments may indicate different equilibrium temperatures. As a result of these uncertainties, a range of extrapolated temperatures will be generated, and it is often not possible to determine the equilibrium temperature with uncertainties <0.1°–0.2°C.

In addition, the geometry of the APC coring shoe is not one-dimensional and radial. The shoe is tapered at its front end, and the probe tip is located close to the front of the shoe (Fig. **F1A**). As a result, the measured temperature in the shoe may decay according to a function that differs from that derived for a one-dimensional, radial analytical model. Additional deviations from the one-dimensional model may result from heterogeneities in sediment properties (natural or induced by tool penetration) and associated frictional heating or conduction of heat vertically along the coring shoe.

The complete APCT-3 project includes considerable modeling and analysis, much of which is still underway, to evaluate uncertainties in extrapolated temperatures and improve standard procedures. For the purposes of prototype testing during Expedition 311 and the results presented in this volume, we have used TFit software developed for the second-generation APCT tool. This allowed rapid analysis of available data and comparison with data collected using earlier tools. We will reanalyze Expedition 311 data later when the rest of APCT-3 modeling and software development is complete.

Tool performance

Calibration

The prototype APCT-3 tool was made available for use only a few days prior to the start of Expedition 311. Fortunately, there was time for calibration across a limited range of 1.5°–9.5°C. During calibration, the APCT-3 and a calibrated reference thermistor were submerged in a continuously stirred, cylindrical water bath ~60 cm in diameter and ~75 cm high. Calibration bath temperatures were maintained by competing cooling and heating systems controlled using the reference sensor. Temperatures measured with the reference sensor have absolute accuracy of better than 2 mK and were recorded when the temperature in the tank was within a small window around each of five temperature values used for calibration. The limited temperature range of pre-Expedition 311 calibration resulted mainly from limitations in available time. A wider temperature range will be used for calibration of the production APCT-3 tools and prototype during the coming year.

There are two general ways to apply calibrations to APCT-3 temperature data. One way is to apply an ex-

perimentally determined calibration to the exported ASCII data. Alternatively, one could also create new calibration files (*.wtc) that are used by the WinTemp software. To do the latter, one must supply two pairs of A/D converter readings, x (digital counts), and corresponding resistances R (Ohm) and three pairs of resistances and corresponding reference temperatures T (°C). The x-R pairs are used to identify the scale m and the offset b in the equation

$$R = m(x + b)/(13{,}1071 - [x + b]), \quad (1)$$

which is used to compute resistances R from logger readings x. Subsequently, the R-T pairs are used to compute the coefficients A_i in a standard (Steinhart and Hart, 1968; Bennett, 1972) equation:

$$1/T = A_1 + A_2\ln(R) + A_3\ln^3(R). \quad (2)$$

Note that although WinTemp requires entering reference temperatures in Celsius, computations in Equation E2 are done in Kelvin and R is dimensionless (resistance divided by 1 Ω). This empirical equation is known to provide a good match to thermistor characteristics with a minimum number of free parameters. Figure **F3** illustrates the ability of the Steinhart and Hart equation to reproduce the resistance-temperature characteristics of the selected thermistor (YSI 55032) across the APCT-3 measurement range with three reference temperatures (–5°, 25°, and 55°C). Temperatures predicted by the equation provide an accuracy of about ±10 mK with respect to the reference temperatures specified by the thermistor manufacturer. This accuracy is maintained during moderate extrapolation of a few degrees beyond the range of the reference points. It is, however, possible to improve the accuracy gained with the Steinhart and Hart equation by increasing the number of coefficients (A_i) or by reducing the calibration temperature range.

Figure **F4A** shows the calibration reference temperatures and respective APCT-3 temperatures, which were computed with the standard WinTemp calibration file. The differences between reference temperature and APCT-3 temperature range from about –37 mK at 1.5°C to –29 mK at 9.5°C (Fig. **F4B, F4C**). Linearly extrapolated over the whole measurement range from –5° to 55°C, these differences range from –44 to 18 mK, respectively. Using an ad hoc approach, all APCT-3 temperature data shown in the site chapters of the Expedition 311 *Proceedings of the Integrated Ocean Drilling Program* were corrected by adding a constant offset of 30 mK. This approach is justified because the accuracy of undisturbed formation temperatures extrapolated by the TFit software is on the order of ±0.1°C. To take advantage of the APCT-3's enhanced resolution and accuracy in a new temperature extrapolation algorithm, however, a more sophisticated calibration approach will be developed for future use with the production APCT-3 tools.

Reference temperatures and resistances, computed using Equation E1 and the constants b and m provided by Antares, were used to determine optimized coefficients A_i in Equation E2 (see Fig. **F4D;** Table **T1**). The resulting standard deviation of the differences between reference temperatures and APCT-3 temperatures of 0.6 mK (Fig. **F4E, F4F**) is similar to the APCT-3's temperature resolution in the given temperature interval (Fig. **F2**). Numerous temperature data measured with MTLs testify (e.g., Heesemann et al., 2005) that this excellent signal to noise ratio is typically achieved by the Antares temperature logger electronics. As shown in Figure **F5,** small temperature undulations in the order of a few mK that occur while a temperature plateau is held in the calibration bath are resolved by the reference thermistor as well as the calibrated APCT-3 temperatures.

During rapid temperature changes, there is, however, a small apparent time lag between the APCT-3 temperature and the reference temperature resulting in increased temperature differences. For instance, this behavior causes the increased temperature differences during oscillations at the beginning of the temperature plateaus (cf. Figs. **F4B, F5B**). The time lag is caused by a somewhat greater response time for the APCT-3 electronics than for the reference sensor. This is not surprising since the APCT-3 tool is placed inside a coring shoe having a large thermal mass, and there is an imperfect contact between the sensor and shoe, with heat sink compound used to fill the gap between the sensor prong and the index hole in the coring shoe.

The thermal time constant of the APCT-3 tool in the coring shoe characterizes the response time of the temperature measurement system to an abrupt change in temperature. It is defined as the time that is required until the difference between the sensor temperature and the new ambient temperature is reduced to 1/e (~36.8%) of the initial temperature difference. Typical time constants of glass-encapsulated thermistors in a well-stirred bath are ~1.5 s. During Expedition 311, experiments to estimate the time constant of the APCT-3 cutting shoe were performed. The tool was alternately submerged in containers with cold and warm water (cf. Fig. **F6A**). As shown in Figure **F6B,** the three resulting rapid transients were normalized so that the beginning of all transients equals one and all transients approach zero. Because of temperature variations in the containers, the steady-state temperature that is set to zero is not well defined. Nevertheless, it is possible to demonstrate that the APCT-3's time constant is on the order of 10 s.

Results from Expedition 311

During Expedition 311, nine APCT-3 deployments were performed in depths ranging from ~30 to ~114 meters below seafloor (mbsf). The overall data quality was excellent, and the standard TFit program was applied to all data measured at Sites U1325, U1326, and U1329. The three measurements at Site U1328 could not be processed because the deployments were disturbed by heave resulting from high seas. A complete temperature data set of a typical APCT-3 deployment (Core 311-U1325B-8H; 71.5 mbsf) is shown in Figure **F7.** Plots of all temperature data obtained during Expedition 311 are provided in their respective site chapters.

All important stages of an APCT-3 deployment cause a specific temperature signal, as recorded by the tool. These stages are as follows (numbers refer to parts of the example record in Fig. **F7**):

1. The APCT-3 is powered on in the laboratory.
2. The tool is lowered down the water column inside the drill string.
3. The tool stops at the mudline to establish a reference temperature for comparison with other downhole temperature. Since temperature variations during this stop are on the order of 0.1°C (Fig. **F7B**), this comparison does not replace a proper calibration of all tools but can help to reveal major intertool calibration problems.
4. The tool is lowered down the hole and briefly stopped at the bit near the bottom of the hole.
5. The coring shoe penetrates the formation in ~5 s (Fig. **F7C**).
6. While the cutting shoe is held in the formation, the temperature peak, caused by frictional heating, decays slowly, and measured temperatures approach the undisturbed formation temperature. After 6–10 min, when sufficient data to allow extrapolation to undisturbed formation temperature is recorded, the decay with a remaining rate of ~1 mK/s (Fig. **F7D**) is interrupted.
7. The tool is extracted from the formation, which also causes frictional heating (Fig. **F7E**).
8. The tool is once again stopped at the mudline.
9. The tool is carried up through the water column.
10. The tool is recovered on deck.

Figure **F8A** compares second-generation APCT data (Core 311-U1329C-11H; 95.6 mbsf) with APCT-3 data (Core 311-U1329C-13H; 114.6 mbsf). The APCT data exhibit a higher temperature peak caused by frictional heating in this example, probably as a result of penetrating sandier sediments, and there is a slower decay toward undisturbed formation temperature. Even though the temperature resolution as well as the time resolution of the APCT-3 surpasses the values of the older APCT by about one order of magnitude, both recorded decay curves appear to be well resolved. The derivative with respect to time of the APCT-3 data (Fig. **F8B**), however, reveals that temperature changes at the end of the decay curve are on the order of 1 mK/s, matching the resolution of the APCT-3 tool.

As shown in Figure **F9** a time resolution of 10 s is not sufficient to resolve the temperature changes of the heat pulse generated during the penetration of the probe. Figure **F9A–F9C** shows one temperature peak measured at a sampling interval of 1 s and three hypothetical measurements of the same data recorded using a sampling interval of 10 s. Whereas time and magnitude of the temperature peak are well resolved in the APCT-3 measurement, the errors in estimated peak time and magnitude of the theoretical APCT measurements (e.g., Fig. **F9B**) are as much as ~5 s and ~20%, respectively. It should be noted that early-time data (the first 20–60 s) following APCT insertion are typically omitted when estimating equilibrium formation temperatures; therefore, it is not clear whether the lack of temporal resolution common during many earlier deployments resulted in a systematic bias in calculated formation temperatures. Additional analysis of APCT-3 response will be completed as part of the ongoing project, but initial tests with the APCT-3 tool give confidence as to the performance of the new electronics.

In order to cross-check the APCT-3 data with other downhole temperature data, we attempted to colocate measurements with the Davis Villinger Temperature Probe (DVTP). Unfortunately, these attempts failed because of bad weather conditions. Nevertheless, APCT-3 data are consistent with temperatures measured with other tools. For instance, the linear vertical temperature profile at Site U1329 (Fig. **F10**) provides additional qualitative verification of the data quality. Considering a mean thermal conductivity of 1.05 W/(m·K) (Fig. **F10B**), all estimated undisturbed formation temperatures are consistent with a conductive heat flux of ~72 mW/m^2. Furthermore, the extrapolated seafloor temperature of 3.5° ± 0.5°C matches seawater temperatures of 3.5° ± 0.2°C (see the **"Site U1329"** chapter) at the water depth at Site U1329 (950 m). The seawater temperatures off Vancouver Island were measured within the World Ocean Circulation Experiment (WOCE) in September 1985 (WOCE Section P01) and in February 1994 (WOCE Section PR06).

Conclusions and future plans

A third-generation temperature tool, the APCT-3, has been developed for use during scientific ocean drill-

ing when piston coring. The design of this new tool builds on the prior experience with previous temperature tools, most recently the APCT and the MTL. Consequently, the prototype described here proved to be very mature and only minor modifications are anticipated for the final production version, which should be available in the summer or fall of 2006. Field tests during Expedition 311 and calibration tests prior to the expedition demonstrate that the APCT-3 is a robust and reliable tool, with high and predictable accuracy. Even with only routine calibration, the absolute accuracy of the APCT-3 is better than ±0.05°C, surpassing the accuracy of data measured with the previous APCT tool. Because of the excellent signal to noise ratio of the APCT-3 tool, it will be possible to achieve an absolute accuracy that is on the order of its temperature resolution, which is in the range of 0.5–2.5 mK, depending on the temperature. In addition to improved accuracy, the tool provides an order of magnitude increase in the possible sampling rate. Whereas the increased temperature resolution is necessary to resolve the small temperature changes at the end of the decay of frictional heat, the APCT-3's short sampling interval of 1 s is needed to capture the rapid temperature changes that occur while the coring shoe is driven into the formation.

Unfortunately, the order of magnitude increase in resolution and accuracy of the temperature data does not necessarily lead to significant improvement in estimates of undisturbed formation temperature. These estimates depend, in large part, on the algorithm that is used to extrapolate the observed transient temperature decay to steady state. The most important deficiency of the currently used TFit algorithm is the simplified nature of the one-dimensional analytical model used to calculate the reference curves to which the measured data are compared. Considerable modeling and analysis of the tool's thermal response is under way. This information will be used to evaluate uncertainties in extrapolated temperatures and to improve standard processing procedures. Since all tools used to measure formation temperature or pore pressure generate a similar transient disturbance, we hope that the processing procedures of other tools will benefit from the analysis of the APCT-3 data. This will be a valuable contribution because the extrapolation of the decay in temperature or pressure to undisturbed formation state needs standardization to allow comparison of data sets (Flemings et al., 2004).

Acknowledgments

This research was supported by German Science Foundation (DFG) Grants Vi 133/9-1 and Vi 133/9-2, U.S. National Science Foundation (NSF) Grant OCE-0326699 to University of California, Santa Cruz (A.T.F.), and Joint Oceanographic Institutions/IODP (A.M.T.). The authors benefited enormously from the guidance provided by engineering, operations, and technical support personnel of the IODP–United States Implementing Organization (USIO) Science Operator at Texas A&M University. In particular, Peter Kannberg, Mike Meiring, and Randy Gjesvold went out of their way to accommodate this new addition to the pool of downhole tools for Expedition 311. We also thank the captain and the crew of the *JOIDES Resolution*, without whom this research would not have been possible. Robert Collier helped with the calibration tests in the temperature controlled tank at Oregon State University.

References

Bennett, A.S., 1972. The calibration of thermistors over the temperature range 0–30°C. *Deep-Sea Res.,* 19:157–163.

Bullard, E.C., 1954. The flow of heat through the floor of the Atlantic Ocean. *Proc. R. Soc. London, Ser. A,* 222:408–429.

Carslaw, H.S., and Jaeger, J.C., 1959. *Conduction of Heat in Solids* (2nd ed.)*:* Oxford (Clarendon Press).

Davis, E.E., Villinger, H., MacDonald, R.D., Meldrum, R.D., and Grigel, J., 1997. A robust rapid-response probe for measuring bottom-hole temperatures in deep-ocean boreholes. *Mar. Geophys. Res.,* 19:267–281. **doi:10.1023/A:1004292930361**

Erikson, A., von Herzen, R., Sclater, J., Girdler, R., Marshall, B., and Hyndman, R., 1975. Geothermal measurements in deep-sea drill holes. *J. Geophys. Res.,* 80:2515–2528.

Fisher, A.T., and Becker, K., 1993. A guide to ODP tools for downhole measurements. *ODP Tech. Note,* 10.

Flemings, P., Murray, R., and Fisher, A., 2004. Workshop report: downhole tools in the IODP: achieving critical goals of scientific ocean drilling. Available from the World Wide Web: **http://www.usssp-iodp.org/PDFs/DHT_Workshop_Final.pdf.**

Heesemann, M., Villinger, H., Jannasch, H.W., Kastner, M., and the Expedition 301T Scientists, 2006. Data report: Long-term temperature measurements in Holes 1253A and 1255A off Costa Rica, ODP Leg 205. *In* Morris, J.M., Villinger, H.W., and Klaus, A. (Eds.), *Proc. ODP, Sci. Results,* 205 [Online]. Available from World Wide Web: **http://www-odp. tamu.edu/publications/205_SR/209/209.htm.**

Horai, K., 1985. A theory of processing down-hole temperature data taken by the hydraulic piston corer (HPC) of the DSDP. *Tech. rep.*, Lamont-Doherty Geological Observatory, Palisades, NY.

Horai, K., and Von Herzen, R.P., 1985. Measurement of heat flow on Leg 86 of the Deep Sea Drilling Project. *In* Heath, G.R., Burckle, L.H., et al., *Init. Repts. DSDP,* 86: Washington (U.S. Govt. Printing Office), 759–777.

Hyndman, R.D., Langseth, M.G., and Von Herzen, R.P., 1987. Deep Sea Drilling Project geothermal measurements: a review. *Rev. Geophys.,* 25:1563–1582.

Jannasch, H., Davis, E., Kastner, M., Morris, J., Pettigrew, T., Plant, J.N., Solomon, E., Villinger, H., and Wheat, C.G., 2003. CORK-II: long-term monitoring of fluid chemistry, fluxes, and hydrology in instrumented boreholes at the Costa Rica subduction zone. *In* Morris, J.D., Villinger, H.W., Klaus, A., *Proc. ODP, Init. Repts.,* 205 [Online]. Available from World Wide Web: **http://www-odp.tamu.edu/publications/205_IR/chap_02/chap_02.htm.**

Kappel, E., and Adams, J. (Eds.), 2001. *Earth, Oceans and Life: Scientific Investigation of the Earth System Using Multiple Drilling Platforms and New Technologies—Integrated Ocean Drilling Program Initial Science Plan, 2003–2013:* Washington, D.C. (International Working Group Support Office).

Pfender, M., and Villinger, H., 2002. Miniaturized data loggers for deep sea sediment temperature gradient measurements. *Mar. Geol.,* 186:557–570. **doi:10.1016/S0025-3227(02)00213-X**

Pribnow, D.F.C., Kinoshita, M., and Stein, C.A., 2000. Thermal data collection and heat flow recalculations for ODP Legs 101–180. Institute for Joint Geoscientific Research, GGA, Hanover, Germany, 0120432. Available from World Wide Web: **http://www-odp.tamu.edu/publications/heatflow/ODPReprt.pdf.**

Shipboard Scientific Party, 1992. Explanatory notes. *In* Davis, E.E., Mottl, M.J., Fisher, A.T., et al., *Proc. ODP, Init. Repts.,* 139: College Station, TX (Ocean Drilling Program), 55–97.

Shipboard Scientific Party, 1997. Rough basement transect (Sites 1026 and 1027). *In* Davis, E.E., Fisher, A.T., Firth, J.V., et al., *Proc. ODP, Init. Repts.,* 168: College Station, TX (Ocean Drilling Program), 101–160. [**PDF**]

Steinhart, J.S., and Hart, S.R., 1968. Calibration curves for thermistors. *Deep-Sea Res.,* 15:497–503.

Uyeda, S., and Horai, K., 1982. Heat flow measurements on Deep Sea Drilling Project Leg 60. *In* Hussong, D.M., Uyeda, S., et al., *Init. Repts. DSDP,* 60: Washington (U.S. Govt. Printing Office), 789–800.

Von Herzen, R.P., and Maxwell, A.E., 1964. Measurement of heat flow at the preliminary Mohole site off Mexico. *J. Geophys. Res.,* 69:741–748.

Publication: 28 October 2006
MS 311-108

Appendix

Temperature data of the preliminary APCT-3 calibration (Fig. **F4**) and the response to sudden temperature change (Fig. **F6**) will be submitted to the IODP–USIO database. The APCT-3 data (CALIBRAT.DAT and RESPONSE.DAT in **"Supplementary Material"**) are provided in the WinTemp ASCII format described in **"Tool description."** Calibration reference temperatures (APC3CALB.LOG in **"Supplementary Material"**) are only given at times when the bath temperature was close to one of the five temperature holding points. Holding times are given in separate header lines before and after the temperature data of a holding point.

Figure F1. A. Mechanical design of the APC cutting shoe. **B.** APCT-3 electronics mounted on a cylindrical frame that fits the annular cavity of the cutting shoe.

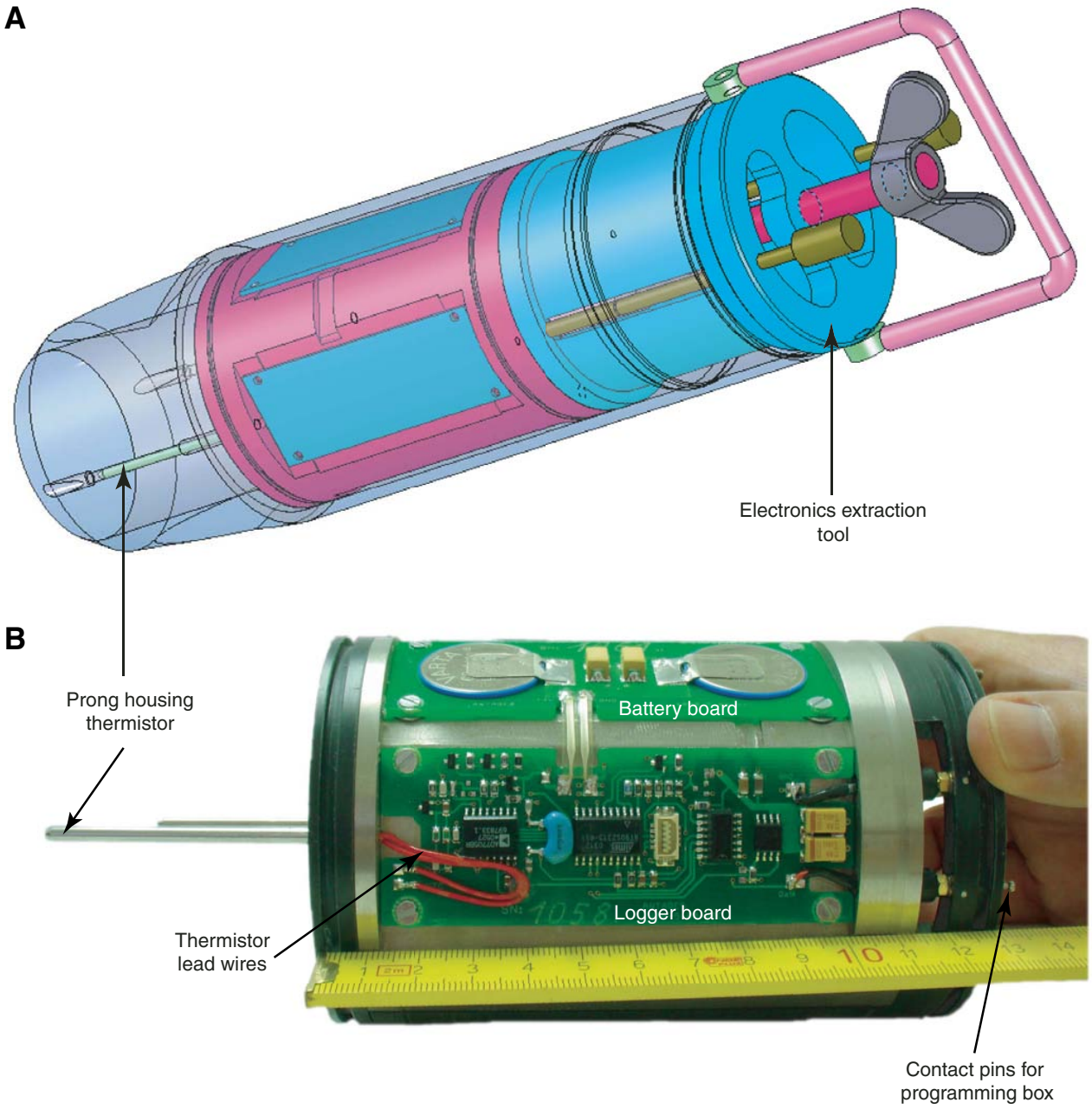

Figure F2. (**A**) Logger readings, (**B**) thermistor resistances, and (**C**) temperature resolution over the whole temperature measurement range of the APCT-3 prototype used during Expedition 311.

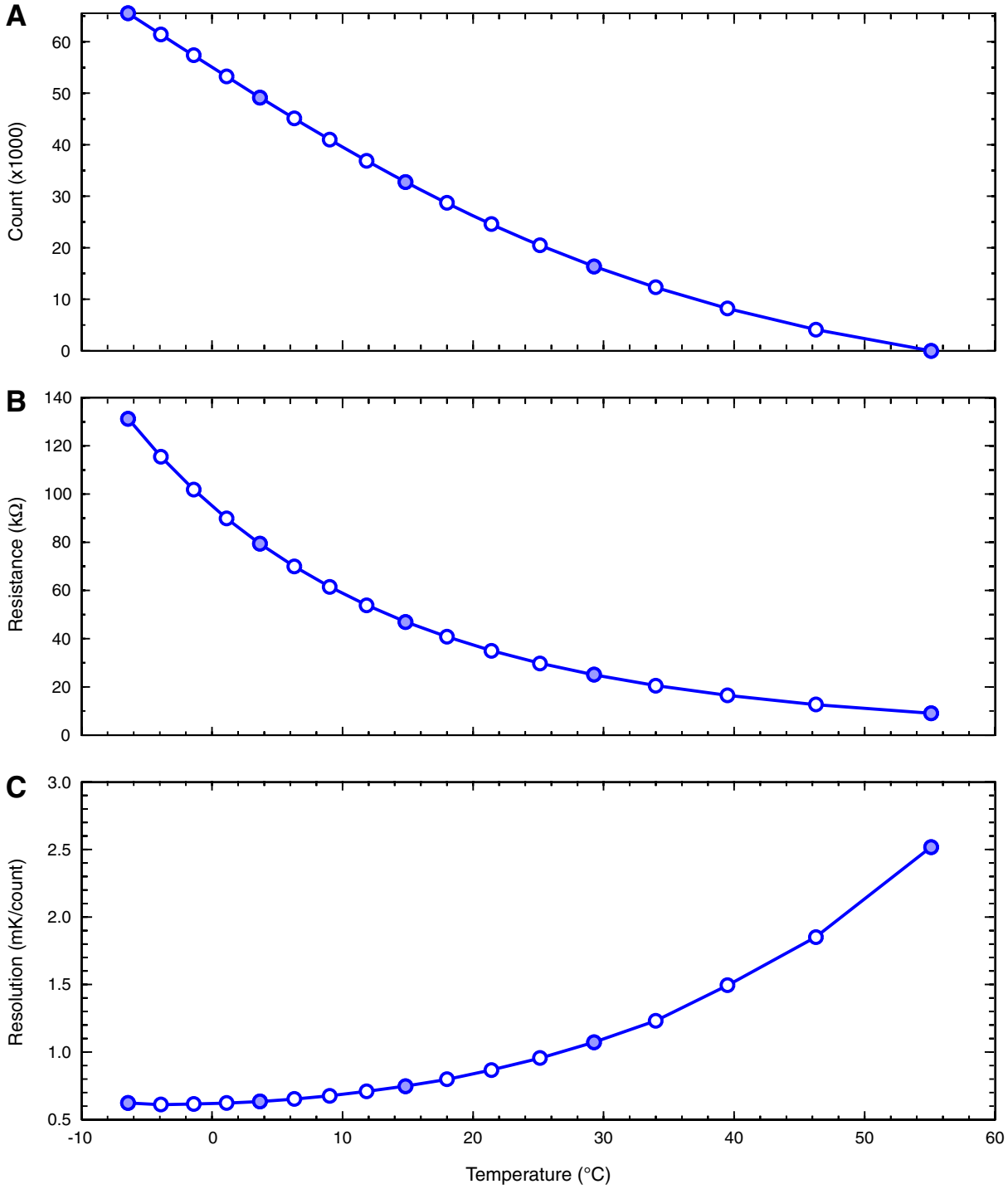

Figure F3. Expected quality of a three-point Steinhart-Hart calibration over the complete temperature measurement range of the APCT-3. **A.** Nominal thermistor characteristics provided by the manufacturer and Steinhart-Hart prediction based on three calibration points. **B.** Difference between nominal characteristics and prediction.

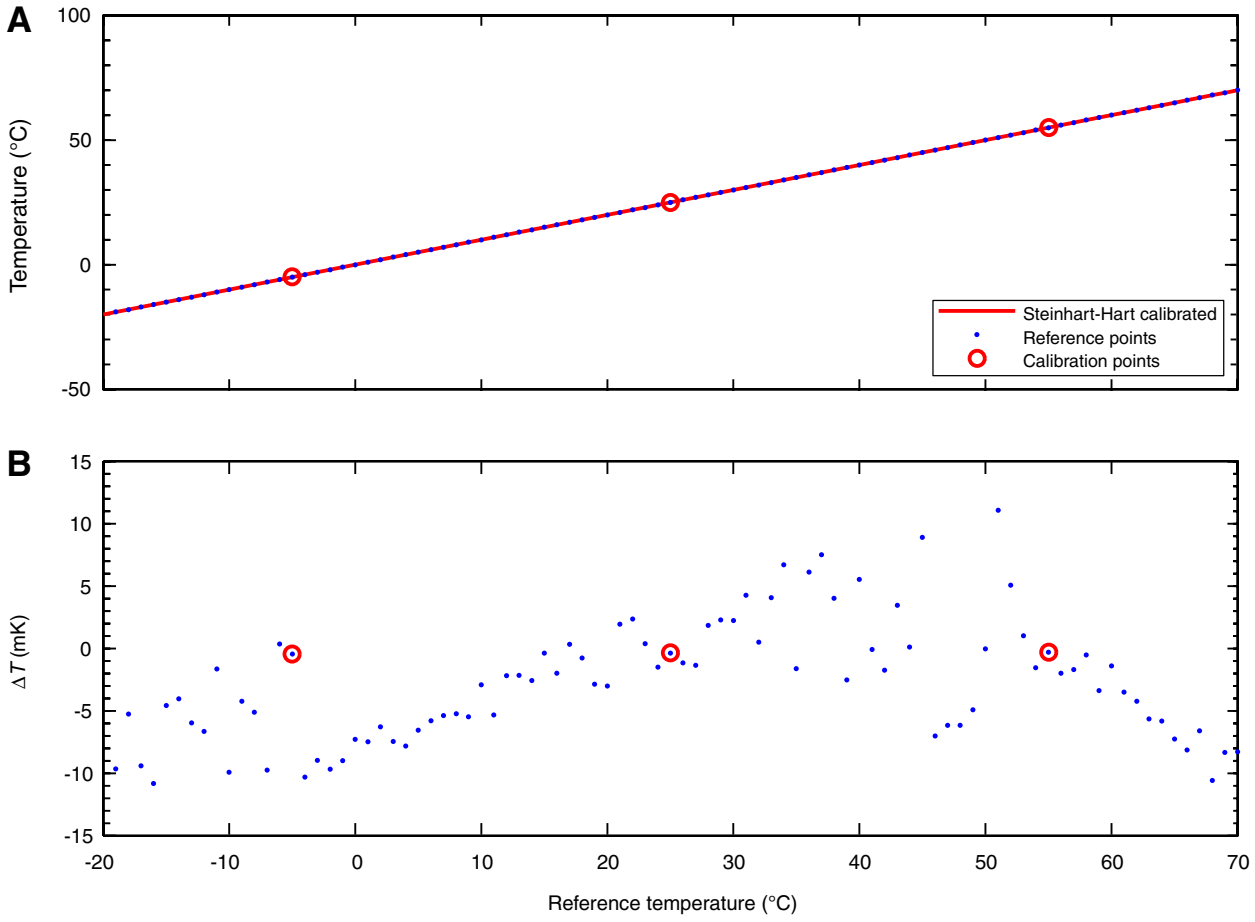

Figure F4. Preliminary APCT-3 calibration. **A.** Uncalibrated third-generation advanced piston corer temperature (APCT-3; APC3 in figure) tool temperatures and reference temperatures during calibration in well-stirred bath. **B.** Differences between reference and APCT-3 temperatures. **C.** Linear regression of temperature differences and reference temperatures. **D**. Reference temperatures as a function of thermistor resistivity (blue dots) and best fitting Steinhart-Hart parametrization. **E, F.** Differences between reference temperatures and APCT-3 temperatures computed with best fitting Steinhart-Hart approximation (cf. D).

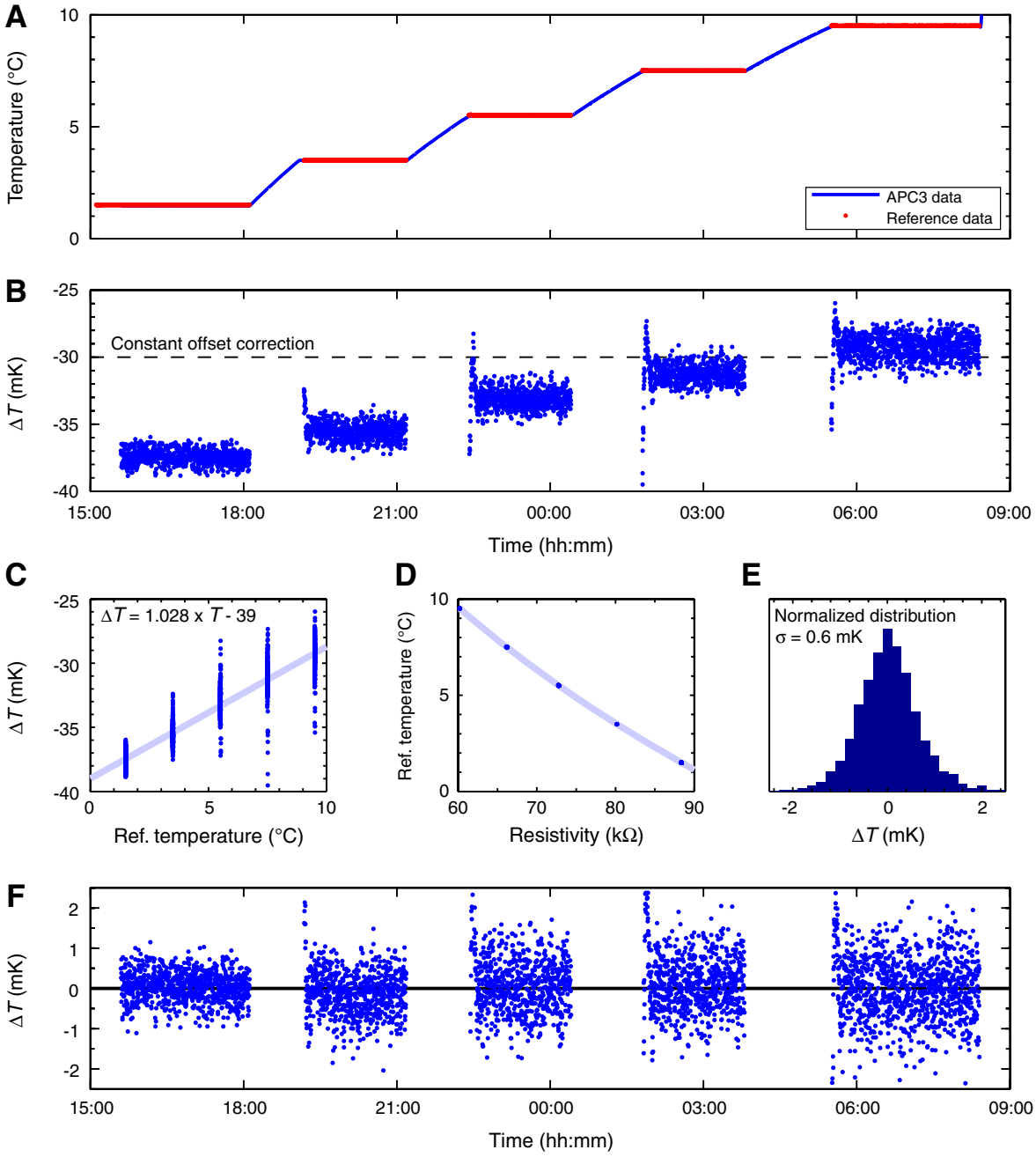

Figure F5. (**A**) Steinhart-Hart calibrated third-generation advanced piston corer temperature (APCT-3; APC3 in figure) tool temperature data and calibration bath reference temperatures demonstrates that (**B**) temperature differences remain on the order of ±1 mK even during minor temperature excursions.

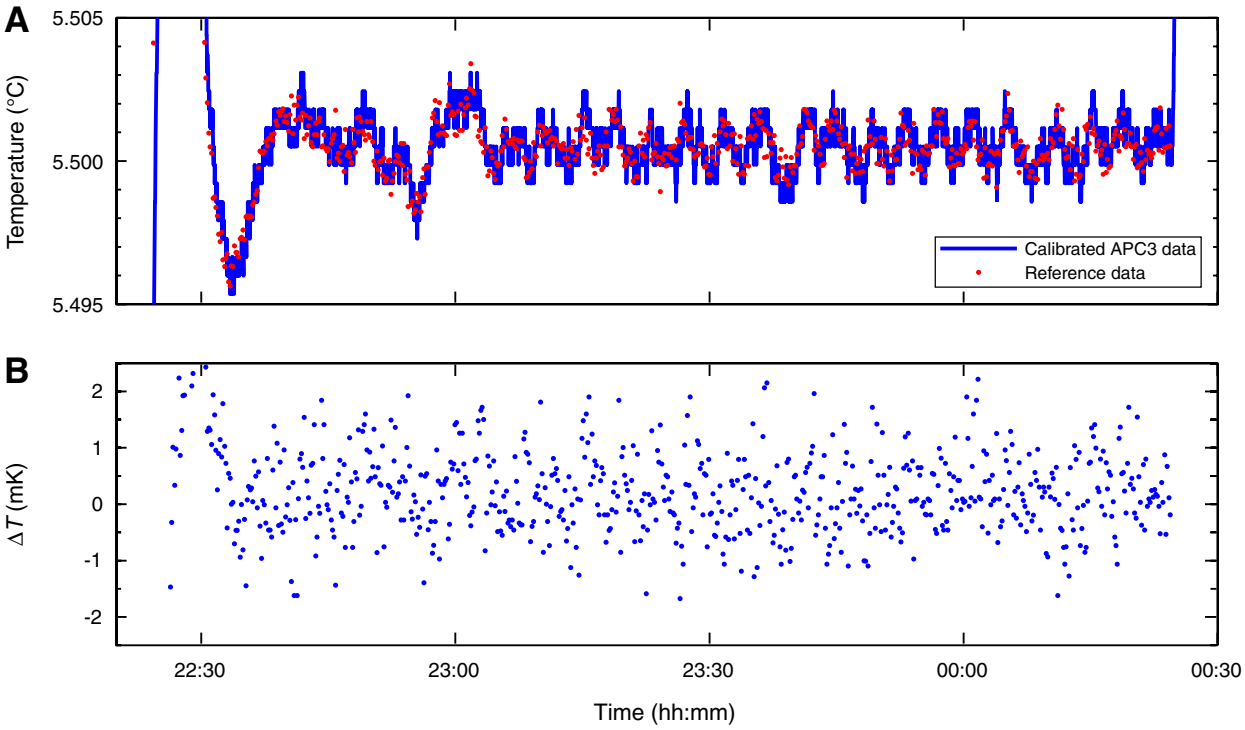

Figure F6. A. To determine the APCT-3 response to sudden temperature change, the tool was alternately submerged in cold and warm water. **B.** Comparison of three normalized temperature transients with an exponential decay function) indicates that the APCT-3 thermal time constant is ~10 s.

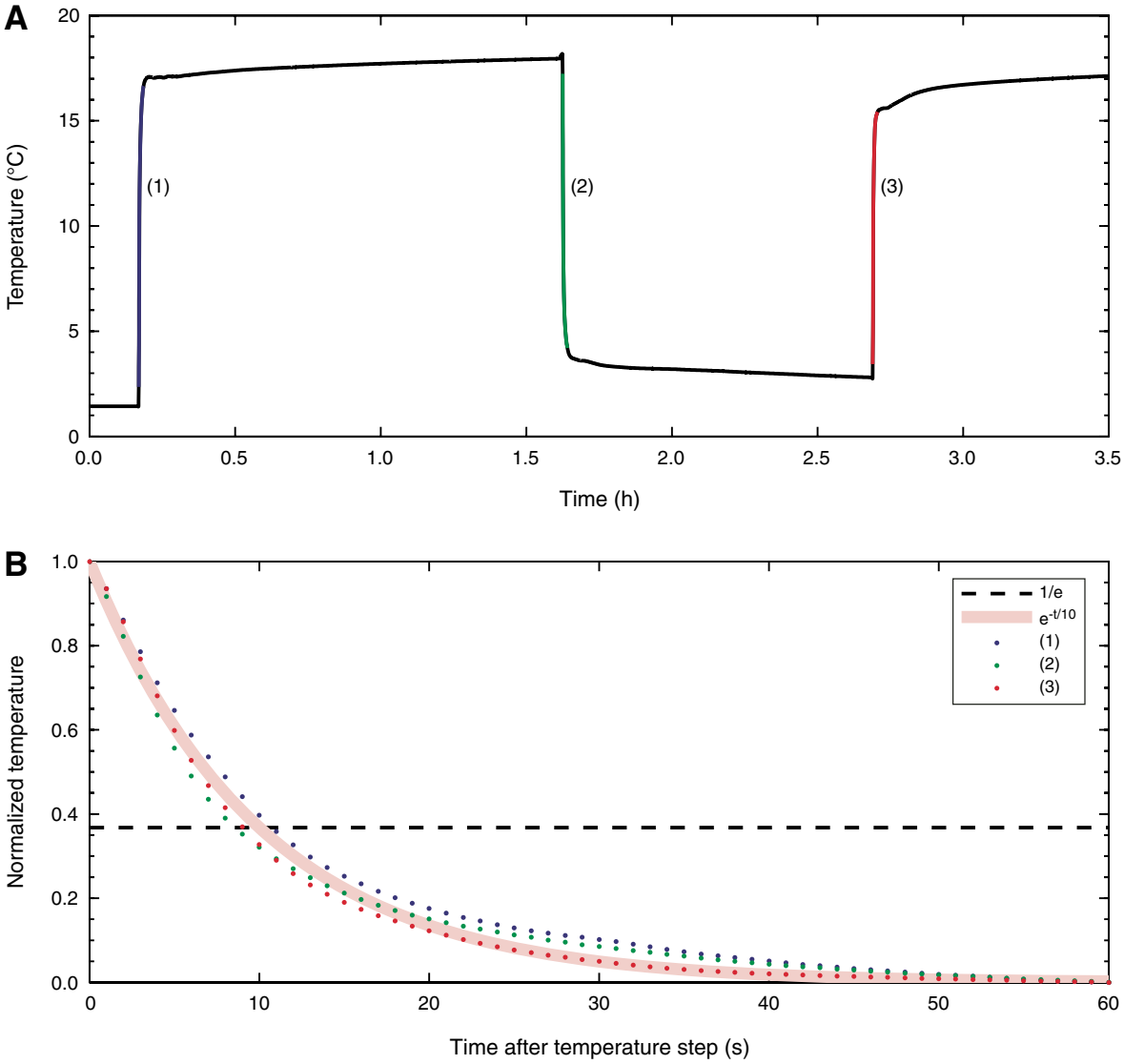

Figure F7. A. Complete temperature record of a typical APCT-3 deployment. **B–E.** Details of some important stages of deployment at differing time and temperature scales.

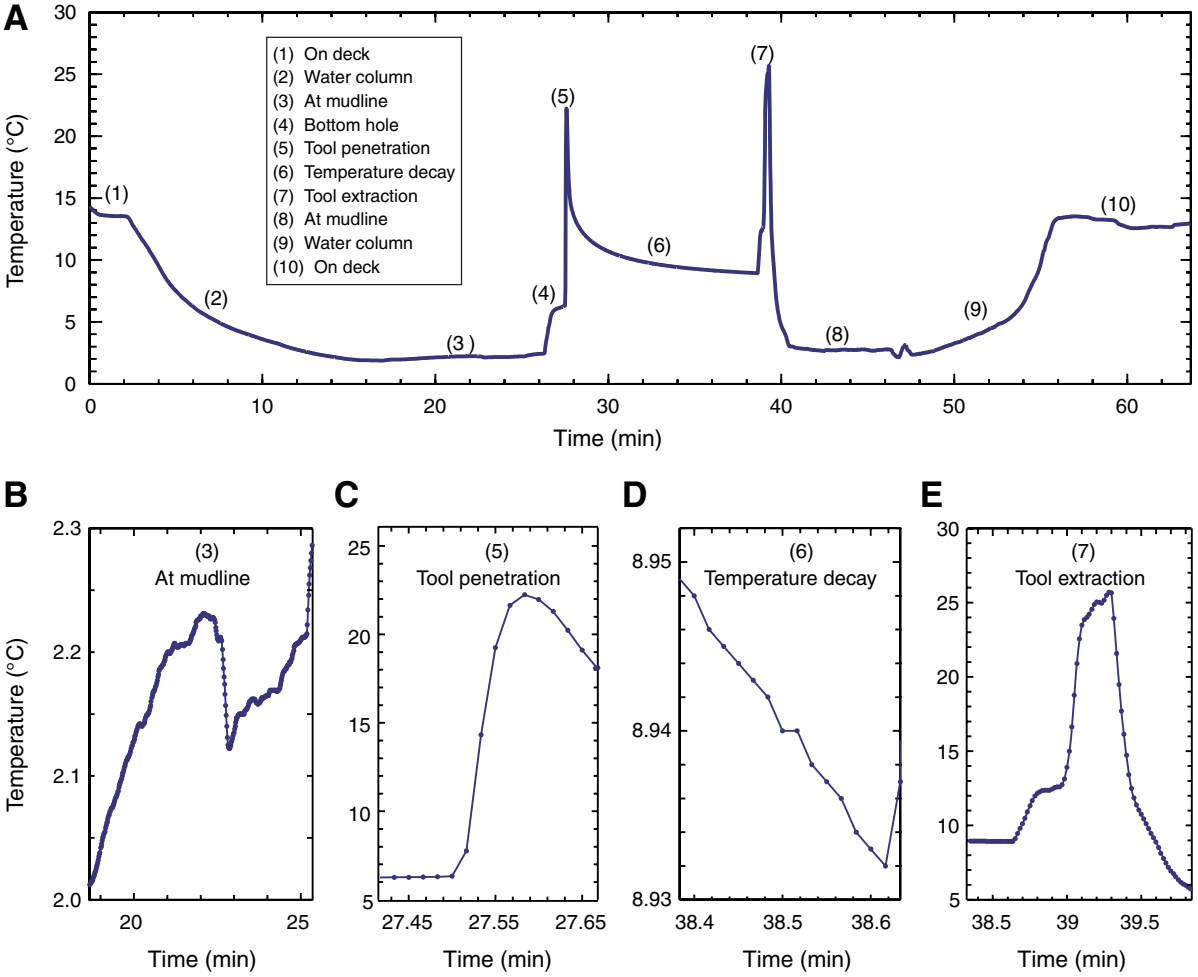

Figure F8. A. Comparison of temperature data measured at Site U1329 using the APCT (Core 311-U1329C-11H; red) and the APCT-3 (Core 311-U1329C-13H; blue). The dashed lines show the extrapolated undisturbed formation temperatures at 95.6 and 114.6 mbsf, respectively, using TFit. **B.** Derivative with respect to time of APCT-3 data showing the temperature resolution that is required to resolve a typical decay curve.

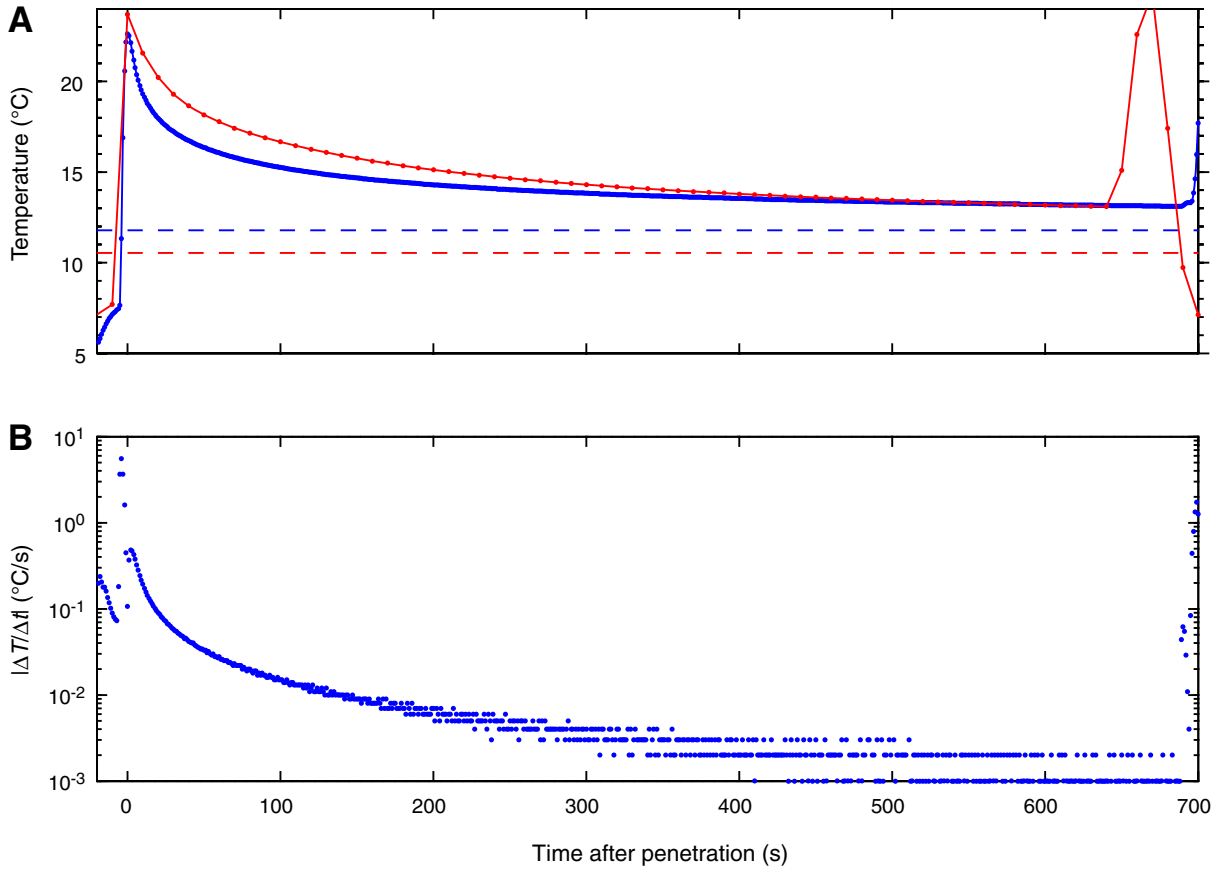

Figure F9. A–C. APCT-3 data (Core 311-U1329C-13H; white dots on blue line) compared to hypothetical data measured using a reduced sampling interval of 10 s. **D.** APCT data (Core 311-U1329C-11H).

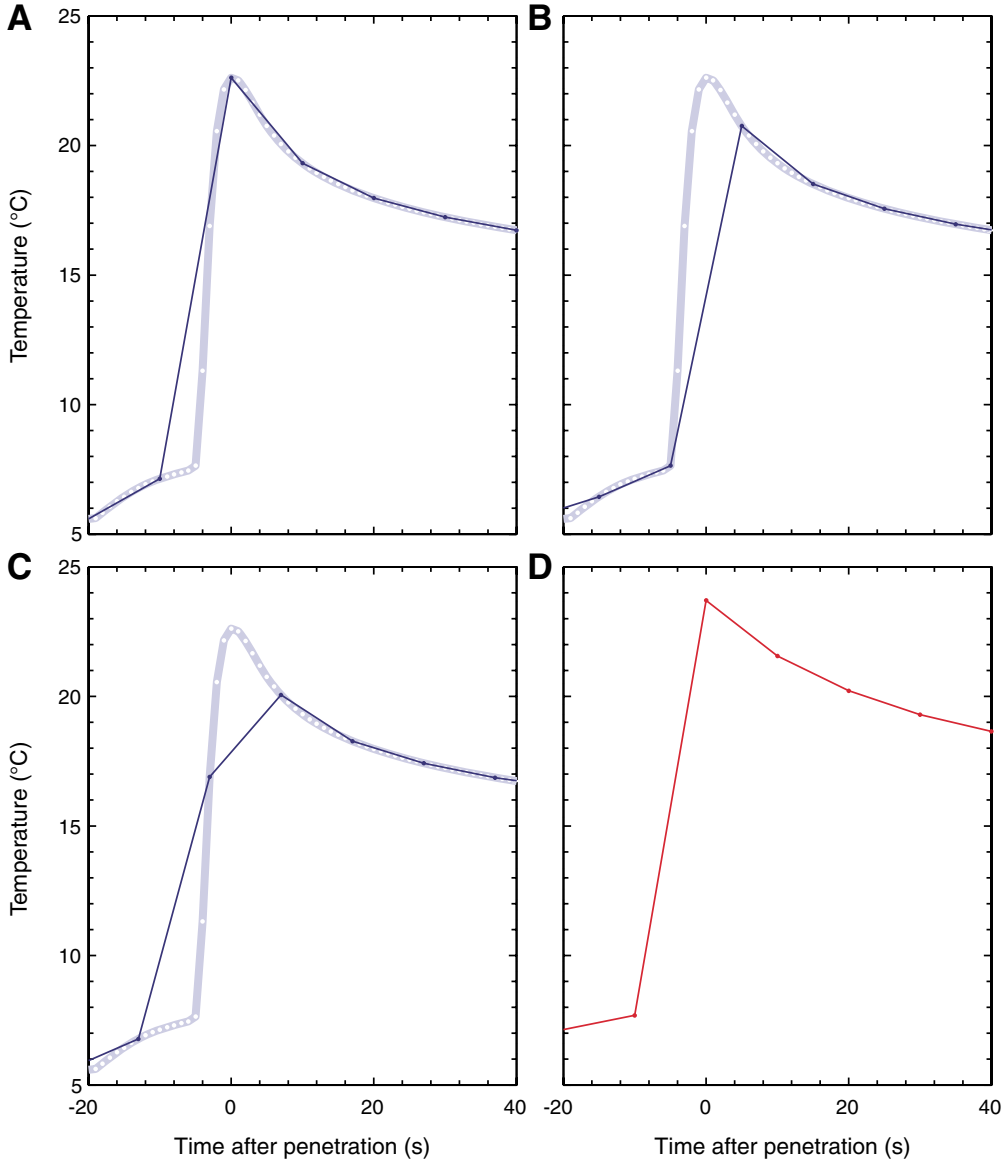

Figure F10. A. Estimated undisturbed formation temperatures measured at Site U1329. The advanced piston corer temperature (APCT) tool measurement at 33.5 mbsf, disturbed by heave, is neglected in the computation of the linear regression and the confidence interval area. APCT-3 = third-generation advanced piston corer temperature tool, DVTP = Davis-Villinger Temperature Probe. **B.** Thermal conductivity measurements of Site U1329 core material.

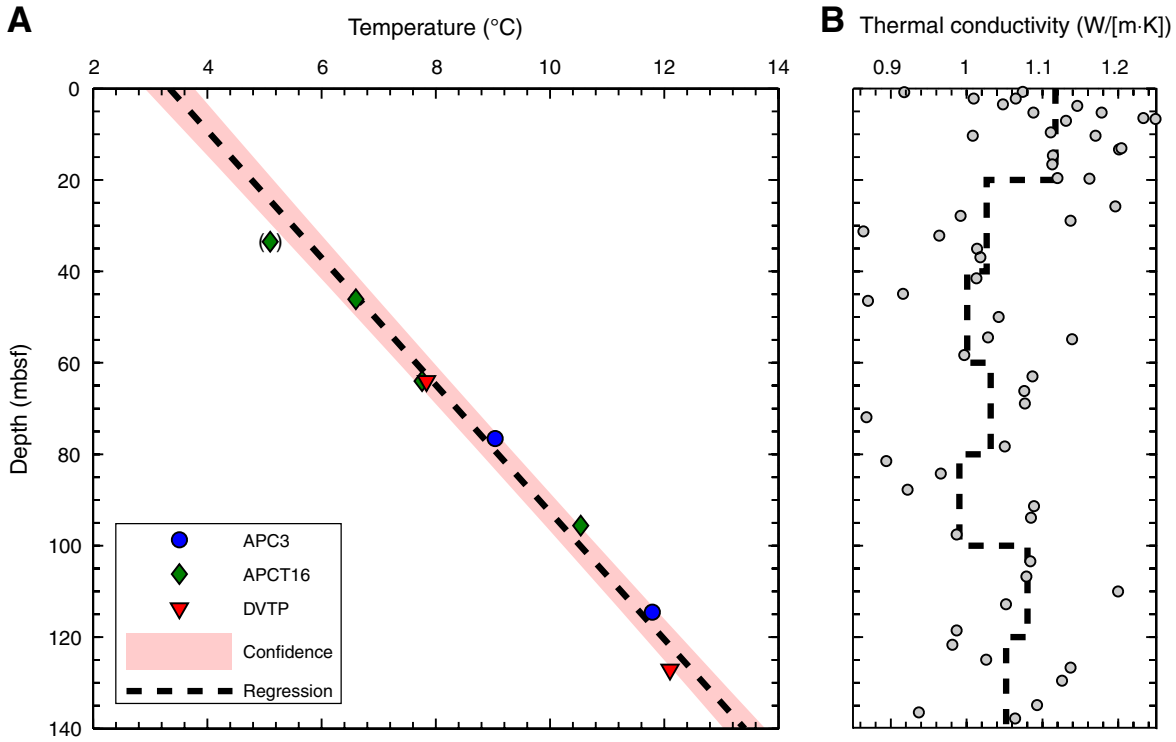

Table T1. Calibration constants.

Constant	Value	Unit
b	11899.26821	None (digital counts)
m	90961.56387	Ohm
A_1	0.000936864596	1/Kelvin
A_2	0.000221013193	1/Kelvin
A_3	0.000000126511	1/Kelvin

Note: For Equations **E1** and **E2** based on preliminary APCT-3 calibration.

Publication: Long-term temperature measurements in Holes 1253A and 1255A off Costa Rica, ODP Leg 205

Heesemann, M., H. Villinger, H. W. Jannasch, M. Kastner, and the Expedition 301T Scientists (2005), Long-term temperature measurements in Holes 1253A and 1255A off Costa Rica, ODP Leg 205, in *Proc. ODP, Sci. Results*, vol. 205, edited by J. Morris, H. Villinger, and A. Klaus.

Contributions

During ODP Leg 205, Heinrich Villinger and Marion Pfender integrated miniaturized temperature loggers (MTLs) in two borehole installations across the Middle America Trench off Nicoya Peninsula, Costa Rica (*Morris et al.*, 2003). After the MTLs recorded temperature data for $\sim$2 years, they were recovered and replaced by Martin Heesemann during IODP Expedition 301T.
The following publication presents the downhole setup at both ODP sites and explains the calibration of the recovered MTLs. Additionally, first interpretations of the data regarding heat flux, events during the deployment, and analogies to concurrently measured pressure data are discussed. The initial interpretation of the data was extended by *Davis and Villinger* (2006), later on. Martin Heesemann compiled the manuscript and analyzed the data. Heinrich Villinger and Miriam Kastner supervised the research, and Hans W. Jannasch supplied technical drawings and specifications of the downhole setup.

Morris, J.M., Villinger, H.W., and Klaus, A. (Eds.)
Proceedings of the Ocean Drilling Program, Scientific Results Volume 205

Data Report: Long-Term Temperature Measurements in Holes 1253A and 1255A off Costa Rica, ODP Leg 205[1]

Martin Heesemann,[2] Heinrich Villinger,[2] Hans W. Jannasch,[3] Miriam Kastner,[4] and the Expedition 301T Scientists

ABSTRACT

Long-term temperature measurements using miniaturized temperature loggers (MTLs) were performed in Ocean Drilling Program Holes 1253A and 1255A across the Middle America Trench off the Nicoya Peninsula, Costa Rica. All three recovered loggers, which were retrieved fully functional, provided high-resolution temperature records. These records cover a time span of ~2 yr and were sampled at an interval of 17 min. There are a number of signals in the temperature data that are most likely caused by hydrologic events. These events are also present in the pressure data recorded by Circulation Obviation Retrofit Kit (CORK)-IIs that are installed in these boreholes. Moreover, the temperature data are important input parameters for calculating pumping rates of the OsmoSamplers, within which the MTLs were integrated. Therefore, the MTL temperature records combined with the CORK-II pressure measurements and the data from the OsmoSampler fluid samples allow the investigation of subduction zone hydrologic processes.

INTRODUCTION

During Ocean Drilling Program (ODP) Leg 205 in September and October 2002, Circulation Obviation Retrofit Kit (CORK)-II observatories were installed in Holes 1253A and 1255A across the Middle America

[1]Heesemann, M., Villinger, H., Jannasch, H.W., Kastner, M., and the Expedition 301T Scientists, 2006. Data report: Long-term temperature measurements in Holes 1253A and 1255A off Costa Rica, ODP Leg 205. *In* Morris, J.M., Villinger, H.W., and Klaus, A. (Eds.), *Proc. ODP, Sci. Results,* 205, 1–20 [Online]. Available from World Wide Web: <http://www-odp.tamu.edu/publications/205_SR/VOLUME/CHAPTER/209.PDF>. [Cited YYYY-MM-DD]
[2]Universität Bremen, Department of Geoscience, Klagenfurter Strasse, 28359 Bremen, Germany.
heesema@uni-bremen.de
[3]Monterey Bay Aquarium Research Institute, 7700 Sandholdt Road, Moss Landing CA 95039, USA.
[4]Scripps Institution of Oceanography, University of California, San Diego, Geoscience Research Division, 8615 Discovery Way, La Jolla CA 92093-0212, USA.

Initial receipt: 21 March 2005
Acceptance: 9 August 2005
Web publication: 31 March 2006
Ms 205SR-209

Trench off the Nicoya Peninsula, Costa Rica, in order to study fluid flow across the margin and its implication for the seismogenic zone and the subduction factory. Hole 1253A is located on the incoming plate 0.2 km seaward from the deformation front, whereas Hole 1255, which penetrates the décollement, is located 0.4 km arcward of the deformation front (Fig. F1) (Morris, Villinger, Klaus, et al., 2003).

The CORK-II observatories include instruments that were designed to sample fluids and measure flow rates, temperatures, and pressures. Fluid sampling is performed by OsmoSamplers that were configured to operate continuously for up to 2 yr and incorporate autonomous high-precision miniaturized temperature loggers (MTLs) (Jannasch et al., 2003).

Sixteen months following the CORK-II installation, eight *Alvin* submersible dives were conducted to recover and replace the OsmoSamplers containing the MTLs. During these dives, the pressure data were successfully downloaded from the CORK heads, whereas recovering and replacing the OsmoSamplers failed. Fortunately, the *JOIDES Resolution* returned during Integrated Ocean Drilling Program (IODP) Expedition 301T in August–September 2004 and succeeded in recovering most of the OsmoSamplers and replacing them with new ones before valuable data and water samples were lost (Shipboard Scientific Party, 2004). This paper presents the complete MTL data sets and points out a number of interesting features contained in the data.

F1. Borehole locations and heat flux measurements, p. 9.

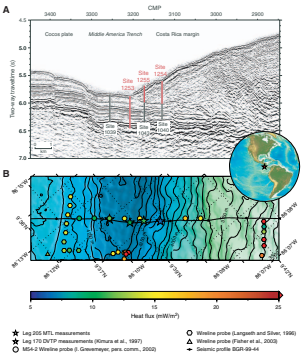

F2. Recovered MTL and construction details, p. 10.

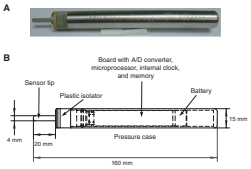

METHODS

Miniaturized Temperature Loggers

The MTLs consist of a 140 mm long × 15 mm outer diameter cylindrical data logger housing with a thin-walled tip (20 mm long with an outer diameter of 4 mm) containing the temperature sensor (Fig. F2). The pressure housing consists of high-strength corrosion-resistant steel and withstands pressure equivalent to 6000 m water depth. Programming the logger and downloading the data are performed using a readout unit without opening the pressure case. The readout unit contacts the MTL's tip and end cap with voltage delivered by the RS-232 interface connected to a PC-compatible computer. A high-strength plastic washer isolates the tip and main body to allow a two-point connection for data transfer.

The electronics of the logger consist of a microprocessor, a 16-bit analog-to-digital converter, a real-time clock, nonvolatile memory for up to 64,800 measurements, and a standard 3-V lithium battery. Logging is automatically stopped when monitoring of an internal constant reference resistor indicates that a reduction of battery voltage causes erroneous temperature readings. Even during a total loss of voltage, the recorded data are preserved in nonvolatile memory. Sample intervals can be varied from 1 s to 255 min, and a thermistor is used as a sensing element. The sensor provides a temperature range from –5° to +60°C and a resolution of ~0.5 mK at typical deep-sea temperature of 2°C (Pfender and Villinger, 2002; Jannasch et al., 2003).

MTL Calibration

Because of the interchangeability of the thermistors, the standard absolute accuracy of the MTLs is ~0.1 mK. By means of calibration it is, however, possible to enhance the absolute accuracy to approximately

±1 mK. The loggers were calibrated by placing them into a well-stirred calibration bath along with a certified reference thermometer. While the reference temperatures and readings measured by the loggers were recorded, the bath was heated stepwise throughout the temperature range in which the loggers were to be calibrated (Fig. **F3A**). The thermal time constant of the reference thermometer was lower than that of the loggers. Therefore, during times of relatively high temperature changes, the reference temperatures exceeded the logger temperatures by as much as 0.01°C (Fig. **F3B;** white areas). Hence, only data collected during times when all loggers and the reference thermometer were in thermal equilibrium with the calibration bath could be used for a sound calibration (Fig. **F3A, F3B;** shaded areas).

The utilized calibration procedure involved two steps. First, logger readings were converted to thermistor resistances. This conversion, which was provided by the WinTemp software accompanying the MTLs, was based on reference measurements with a set of high-precision resistors carried out by the manufacturer, ANTARES Datensysteme GmbH. Second, measured pairs of reference temperatures T (K) and thermistor resistances R (Ω) were used to compute the calibration coefficients A_i in the equation proposed by Steinhart and Hart (1968) and Bennett (1972) as follows:

$$1/T = A_1 \times [\ln(R)]^3 + A_2 \times [\ln(R)]^2 + A_3 \times \ln(R) + A_4.$$

Even though there is no evidence of instrument drift, the long-term stability of the utilized MTL must still be confirmed by a second calibration of the loggers. Until this is carried out, an absolute temperature accuracy of ±5 mK should be used rather than the ±1 mK implied by the presented calibration (Fig. **F3C**). This very conservative estimate is, however, still adequate for interpretation of the recovered temperature data.

F3. MTL calibration, p. 11.

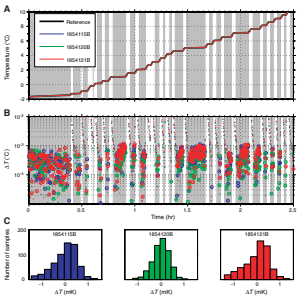

Downhole Setup

Hole 1253A is equipped with two OsmoSamplers located in the upper oceanic basement. As illustrated in Figure **F4A,** each OsmoSampler contains an MTL installed in the upper endcap of its housing. When the upper OsmoSampler was recovered it was discovered that it had been accidentally installed upside down so that the upper end cap became the lower endcap. Unfortunately, the Spectra line connecting the OsmoSamplers failed during the recovery operations, and the lower OsmoSampler in Hole 1253A was dropped to the seafloor. Hopefully, it will be retrieved on the next visit to the site.

The OsmoSampler in Hole 1255A also contains one MTL in the upper endcap, which is situated in the overthrust section of the borehole. An additional MTL is seated inside the probe that penetrates into the sealed décollement section of the borehole (Fig. **F4B**). For reference, a summary of the logger positions is provided in Table **T1.** Furthermore, Jannasch et al. (2003) give a detailed description of the OsmoSampler configuration as well as the borehole installation.

To obtain optimized usage of logger memory for a total logging duration of ~2 yr, the loggers were set to a sampling interval of 17 min resulting in a sampling frequency of ~85 per day, or ~0.001 Hz. The MTLs were set up to monitor the temperatures of the osmotic pumps starting with the assembly of the OsmoSamplers during Leg 205. A continuous

F4. OsmoSampler construction sketches, p. 12.

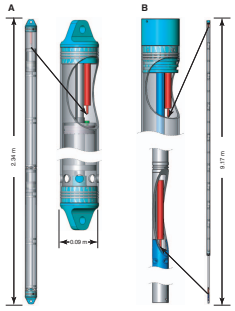

T1. MTL positions, logging times, and instrument drift, p. 20.

temperature record of the osmotic pumps is important for the correct computation of osmotic pumping rates.

RESULTS

All MTLs recovered during Expedition 301T were still fully functional, and it was not necessary to change the batteries to retrieve the data. The MTLs did not show any signs of corrosion, even though the logger recovered from Hole 1253A was covered with mud and, presumably, bacteria (Fig. F5). Therefore, we anticipate that the temperature data from the lower OsmoSampler in Hole 1253A will also be available in case the OsmoSampler can be recovered on a future visit to the site.

Complete Temperature Records

After temperature data retrieval, the internal clocks of the MTLs, which were set to Universal Time Coordinated (UTC) time before the start of logging, were compared to the actual UTC time. The observed time drifts of only a few minutes are summarized in Table T1. These offsets are small compared to the time covered by the entire data sets, so no time drift corrections were applied.

Figure F6 shows the complete temperature data sets recorded by the recovered MTLs in Holes 1253A and 1255A. At the beginning of each record there is a sudden temperature drop from room temperature to bottom water temperature. These drops occurred when the instruments were installed on 10 October 2002 in Hole 1253A and on 1 November 2002 in Hole 1255A. After installation, the measured borehole temperatures slowly approach formation temperatures until a sudden temperature drop to bottom water temperature followed by an increase to room temperature marking the recovery of the OsmoSamplers from Hole 1253A on 5 September 2004 and from Hole 1255A on 6 September 2004.

A temperature of 7.944°C, which was reached in the shallow basement of Hole 1253A, is higher than the formation temperatures measured in Hole 1255A, which are 3.578°C in the overthrust section and 3.638°C in the décollement zone (Fig. F7). Taking into account conductive heat flux estimates, this temperature difference can be explained by the greater depth below seafloor of the OsmoSampler in Hole 1253A. Considering a seafloor temperature of 1.975° ± 0.05°C, a mean temperature gradient in the formations between the OsmoSamplers and the seafloor of ~0.012 K/m is present at both sites. Assuming average thermal conductivities of 0.85 ± 0.05 W/(m·K) for the sediments on the incoming plate and 0.95 ± 0.05 W/(m·K) for sediments in the overthrust section as measured by Kimura, Silver, Blum, et al. (1997), the average heat flux estimates at Sites 1253 and 1255 are 10 ± 0.6 and 11 ± 0.7 mW/m², respectively.

Conductive lithospheric cooling models predict a heat flux of ~100 mW/m² for ~24-Ma oceanic crust underlying the sites (Stein and Stein, 1994). Heat flux measurements reported by Langseth and Silver (1996) and Fisher et al. (2003) show, however, that heat flux through seafloor created at the East Pacific Rise is generally suppressed by ~70% relative to estimates obtained by these models. This anomalously low heat flux is attributed to effective hydrothermal cooling of the upper oceanic crust, which is facilitated by seamounts and basaltic outcrops (Silver et al., 2000; Hutnak et al., 2004). With an average of 16.4 mW/

F5. Recovered MTL after 2-yr deployment, p. 13.

F6. Logger temperature data, p. 14.

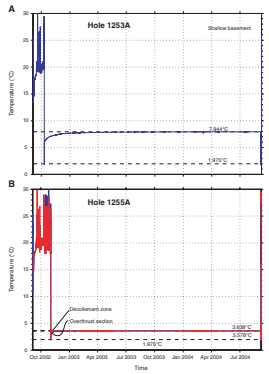

F7. Temperature equilibration comparison, p. 15.

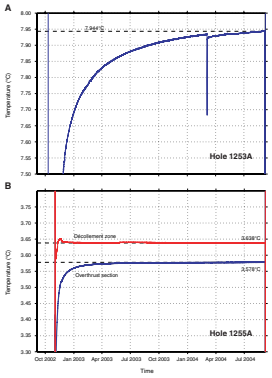

m² and a standard deviation of 7.4 mW/m², the heat flux in the working area, as shown in Figure **F1B,** is suppressed by ~85% relative to the predicted values. Moreover, the heat flux estimates derived from the borehole measurements are slightly lower than the nearby heat flux values from shallow-penetration probes used during *Meteor* cruise M54-2 (I. Grevemeyer, pers. comm., 2002). This is consistent with the observations of Ruppel and Kinoshita (2000) and is attributed to a perturbation of the thermal regime by advective flux.

The temperature equilibration in Hole 1253A took place much slower than in Hole 1255A. This is presumably due to a much higher and longer inflow of cold seawater during drilling caused by the slight subhydrostatic pressure of ~7 kPa encountered in the permeable basement in Hole 1253A. In contrast, drilling operations in Hole 1255A were much shorter and the CORK-II measured superhydrostatic pressures (Fig. **F8C**) in the sedimentary formation (Shipboard Scientific Party, 2004).

Temperature Events

Besides the long-term equilibration trends, several smaller events are documented in the temperature data. The most prominent event seen in Figure **F7A** is the sudden temperature drop on 4 March 2004 caused by the OsmoSampler recovery attempt during *Alvin* dive 3982. A zoom into this event, provided in Figure **F9A,** shows the temperature response of lifting the OsmoSamplers and thereby breaking the pressure seal at 1726 hr UTC. Also, the winch failure at 1855 hr UTC, after which the OsmoSamplers dropped back to their initial positions, is clearly seen in the temperature record. The timing of these events exactly matches the notes in the *Alvin* dive log.

Figure **F9B** shows the temperature data and a moving average over 10 samples (2 hr 50 min) of small-scale temperature variations before and after the *Alvin* recovery attempt. Amplitudes of these variations after the *Alvin* dive are smaller than before the dive. This suggests that the OsmoSamplers fell back in place properly and their seal was even better than before the dive. Moreover, some strong temperature undulations well after the *Alvin* dive are present in the data. These events have to be interpreted along with the results of the fluid sample analysis and the corresponding CORK pressure data when they become available.

The first attempt to recover the Hole 1253A OsmoSamplers during IODP Expedition 301T on 5 September 2004 failed and the OsmoSamplers dropped to the seafloor ~20 m southeast of the borehole. While the OsmoSamplers remained at this location for 2 days, an exact bottom water temperature of 1.975°C at Site 1253 was measured (Fig. **F10**). Measurements taken during ODP Leg 205, (Morris, Villinger, Klaus, et al., 2003) estimated a similar bottom water temperature of 1.989°C with an MTL mounted on the video system while reentering Hole 1253A. Measurements also indicated that the minimum temperature in the water column is located ~1500 m above the seafloor. The minimum water temperature of 1.77°C measured during Expedition 301T recovery operation is, however, significantly lower than the minimum temperature of ~1.83°C recorded during Leg 205. This information may help to constrain extreme bottom water variations with amplitudes of 0.01°C that were observed with MTLs mounted to the CORK-heads of Holes 1253A and 1255A during November 2002–March 2004 (H. Villinger, pers. comm., 2004).

F8. Small-scale temperature variations and pressure events, p. 16.

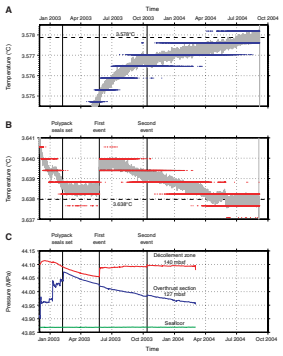

F9. Temperature signal and variations, p. 17.

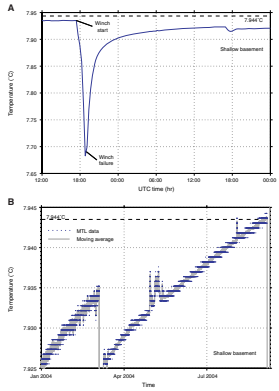

F10. Unsuccessful MTL recovery temperatures, p. 18.

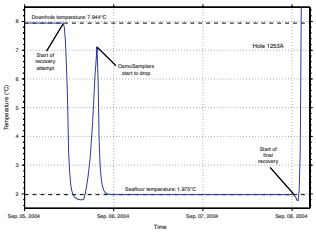

There are also some events that caused small-scale temperature variations in the data measured in Hole 1255A (Fig. **F8**). Most of these events can be correlated to variations that are also present in the CORK-II pressure data (Fig. **F8C**) These variations are (1) the setting of the polypack seals, which caused an increase of pressure in the overthrust section and a stabilization of décollement temperatures; (2) the "first event," characterized by a sudden increase of pressure as well as temperature in the décollement zone; and (3) the much smaller pressure changes of the "second event" that are hardly seen in either temperature record). At the present time, no pressure data have been downloaded from the CORK-IIs for April–July 2004 when temperatures in the décollement zone started to stabilize after an interim increase during May 2004.

Stable temperatures measured over periods of several months around April 2003 and August 2004 (Fig. **F8B**) demonstrate the high quality of temperature data recorded by the MTLs. No significant instrument drift can be seen, and the noise level does not exceed the loggers' resolution.

Fast Fourier Transform (FFT) amplitude spectra of the MTL temperature data and the CORK-II pressure records measured in Hole 1253A and Hole 1255A are dominated by frequencies slightly below 2 per day. These signals are most likely caused by tidal effects. As an example, Figure **F11** shows the FFT amplitude spectra of MTL temperatures and CORK-II seafloor pressure data recorded during November 2003–March 2004 in Hole 1255A. This time interval was chosen because there is no interference with obvious events in any of the data. Before performing the spectral analysis, linear trends were removed from the otherwise unfiltered data. The sampling rates result in Nyquist frequencies of ~42.5 and ~72 per day for temperature and pressure data, respectively. Signals exceeding the Nyquist frequencies cannot be resolved and appear possibly in lower frequencies of the spectra due to aliasing. Problems with aliasing effects are, however, unlikely since the data measured independently at different sampling rates result in similar amplitude spectra.

F11. FFT amplitude spectra, p. 19.

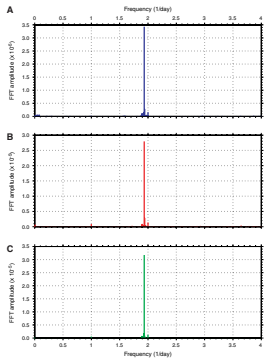

CONCLUSIONS

The presented data show that the MTLs are practicable, reliable, and, at the same time, affordable instruments to measure high-resolution downhole temperatures, even over long periods of time. There are a number of signals in the temperature data that are caused by hydrologic events. These events are also present in the pressure data recorded by the CORK-IIs installed in these boreholes. Therefore, the MTL temperature records can supplement the CORK-II pressure measurements and the data gained from the OsmoSampler fluid samples in order to understand hydrologic processes of the studied subduction zone. All of the presented temperature data will be submitted to the IODP United States Implementing Organization (USIO) database. The files are in ASCII format and include calibrated temperatures as well as uncorrected UTC times.

ACKNOWLEDGMENTS

This research was supported by the German Science Foundation (DFG) grants Vi133/4-1, Vi133/4-2, and Vi133/4-3, and by the U.S. National Science Foundation (NSF) grant OCE 0118478. This research used

samples and/or data provided by the Ocean Drilling Program (ODP). ODP is sponsored by the U.S. National Science Foundation (NSF) and participating countries under management of Joint Oceanographic Institutions (JOI), Inc. We thank the captain and the crew of the *JOIDES Resolution*, without whom this research would not have been possible. We thank Earl Davis for his helpful comments, and Michael Hutnak, Adam Klaus, and Lorri Peters for their constructive reviews.

REFERENCES

Bennett, A.S., 1972. The calibration of thermistors over the temperature range 0–30°C. *Deep-Sea Res.,* 19:157–163.

Fisher, A.T., Stein, C.A., Harris, R.N., Wang, K., Silver, E.A., Pfender, M., Hutnak, M., Cherkaoui, A., Bodzin, R., and Villinger, H., 2003. Abrupt thermal transition reveals hydrothermal boundary and role of seamounts within the Cocos Plate. *Geophys. Res. Lett.,* 30(11). **doi:10.1029/2002GL016766**

Hutnak, M., Fisher, A.T., Stein, C.A., Harris, R., Wang, K., Silver, E., Spinelli, G., Pfender, M., Villinger, H., Pisani, P.C., Deshon, H., and MacKnight, B., in press. The thermal state of 18–24 Ma upper lithosphere subducting below the Nicoya Peninsula, northern Costa Rica margin. *In* Dixon, T., and Moore, J.C. (Eds.), *Seismogenic Zone Earthquakes on the Subduction Thrust:* New York (Columbia Univ. Press).

Jannasch, H., Davis, E., Kastner, M., Morris, J., Pettigrew, T., Plant, J.N., Solomon, E., Villinger, H., and Wheat, C.G., 2003. CORK-II: long-term monitoring of fluid chemistry, fluxes, and hydrology in instrumented boreholes at the Costa Rica subduction zone. *In* Morris, J.D., Villinger, H.W., Klaus, A., *Proc. ODP, Init. Repts.,* 205, 1–36 [CD-ROM]. Available from: Ocean Drilling Program, Texas A&M University, College Station TX 77845-9547, USA. [**HTML**]

Kimura, G., Silver, E.A., Blum, P., et al., 1997. *Proc. ODP, Init. Repts.,* 170: College Station, TX (Ocean Drilling Program).

Langseth, M.G., and Silver, E.A., 1996. The Nicoya convergent margin: a region of exceptionally low heat flow. *Geophys. Res. Lett.,* 23:891–894.

Morris, J.D., Villinger, H.W., Klaus, A., et al., 2003. *Proc. ODP, Init. Repts.,* 205 [CD-ROM]. Available from: Ocean Drilling Program, Texas A&M University, College Station TX 77845-9547, USA. [**HTML**]

Pfender, M., and Villinger, H., 2002. Miniaturized data loggers for deep sea sediment temperature gradient measurements. *Mar. Geol.,* 186:557–570.

Ranero, C.R., and von Huene, R., 2000. Subduction erosion along the Middle America convergent margin. *Nature (London, U. K.),* 404:748–752.

Ruppel, C., and Kinoshita, M., 2000. Fluid, methane, and energy flux in an active margin gas hydrate province, offshore Costa Rica. *Earth Planet. Sci. Lett.,* 179:153–165.

Shipboard Scientific Party, 2004. Costa Rica hydrogeology. *IODP Prel. Rept.,* 301T. **http://iodp.tamu.edu/publications/PR/301TPR/301TPR.PDF**

Silver, E., Kastner, M., Fisher, A., Morris, J., McIntosh, K., and Saffer, D., 2000. Fluid flow paths in the Middle America Trench and Costa Rica margin. *Geology,* 28(8):679–682.

Stein, C.A., and Stein, S., 1994. Constraints on hydrothermal heat flux through the oceanic lithosphere from global heat flow. *J. Geophys. Res.,* 99:3081–3095.

Steinhart, J.S., and Hart, S.R., 1968. Calibration curves for thermistors. *Deep-Sea Res.,* 15:497–503.

Figure F1. Overview of borehole locations and heat flux measurements. **A.** Locations of Leg 205 sites (red) and Leg 170 sites (black) on migrated seismic profile BGR-99-44 (Morris, Villinger, Klaus, et al., 2003). CMP = common midpoint. **B.** Bathymetric map based on data compiled by Ranero and von Huene (2000) with compilation of heat flux measurements in the study area. MTL = miniaturized temperature logger, DVTP = Davis-Villinger Temperature Probe.

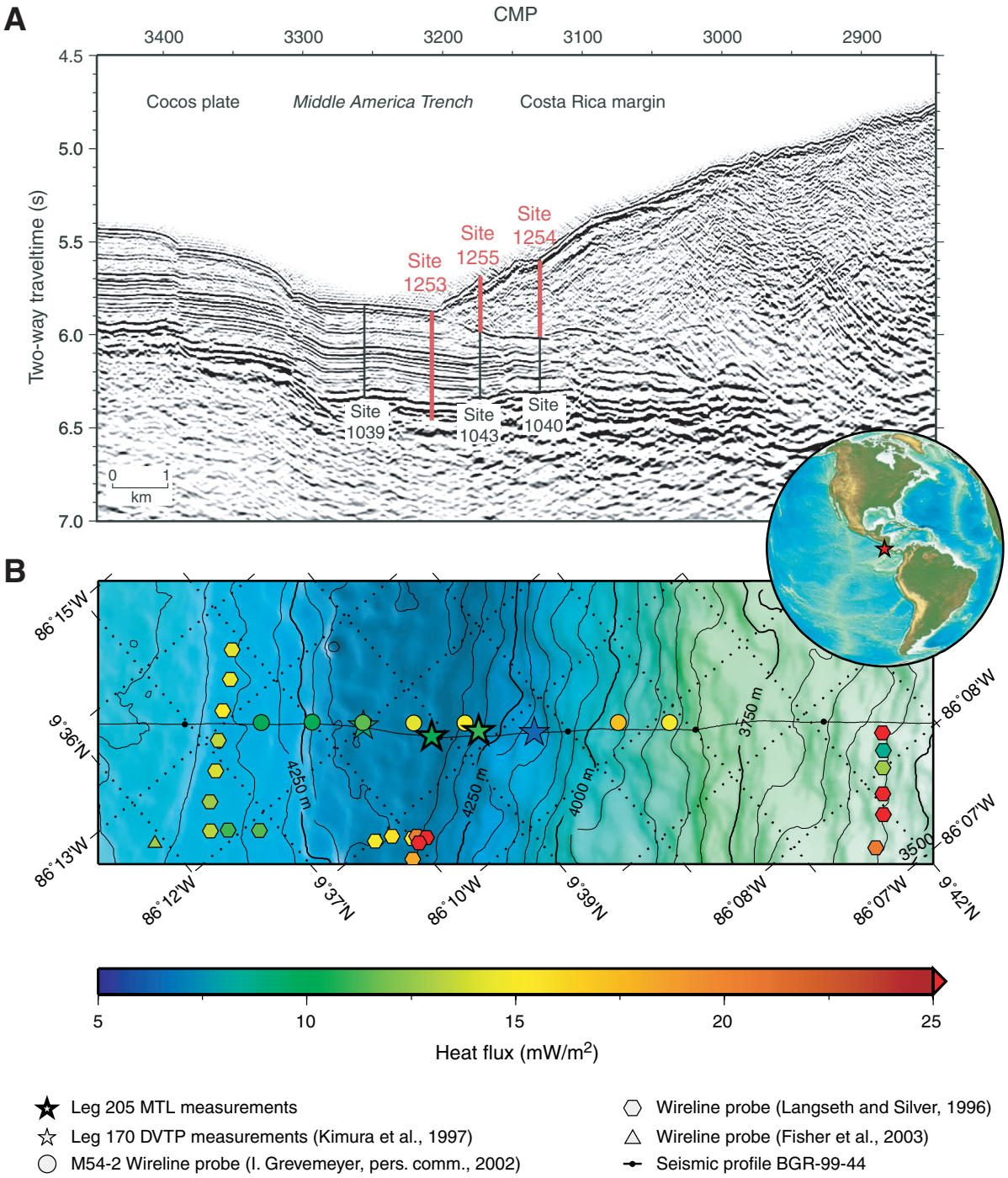

Figure F2. A. MTL after recovery during Expedition 301T. **B.** Construction details of an MTL (Pfender and Villinger, 2002). A/D = analog-to-digital.

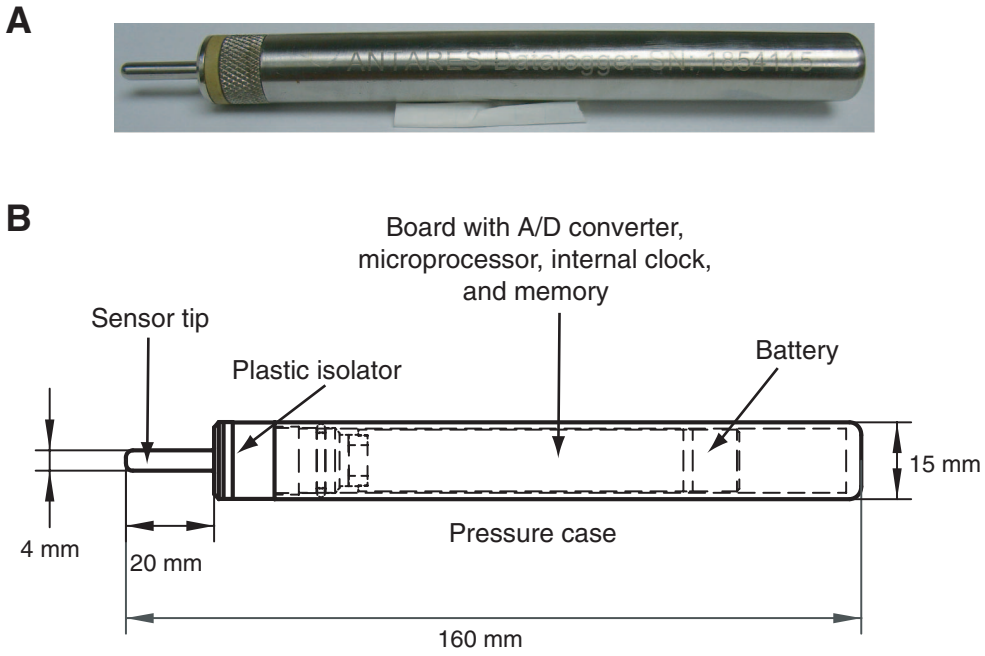

Figure F3. Calibration of MTLs with a certified reference thermometer in a well-stirred bath. **A.** Temperatures of the reference thermometer and the calibrated loggers show a stepwise increase of bath temperature. Temperatures in shaded areas are chosen for computing the calibration coefficients. **B.** Differences between the reference temperature and calibrated logger temperatures. Dots = reference temperatures that are higher than temperatures measured by the loggers, circled dots = reference temperatures slightly below the calibrated logger temperatures. **C.** Deviations of calibrated logger temperatures from reference temperatures in the shaded areas.

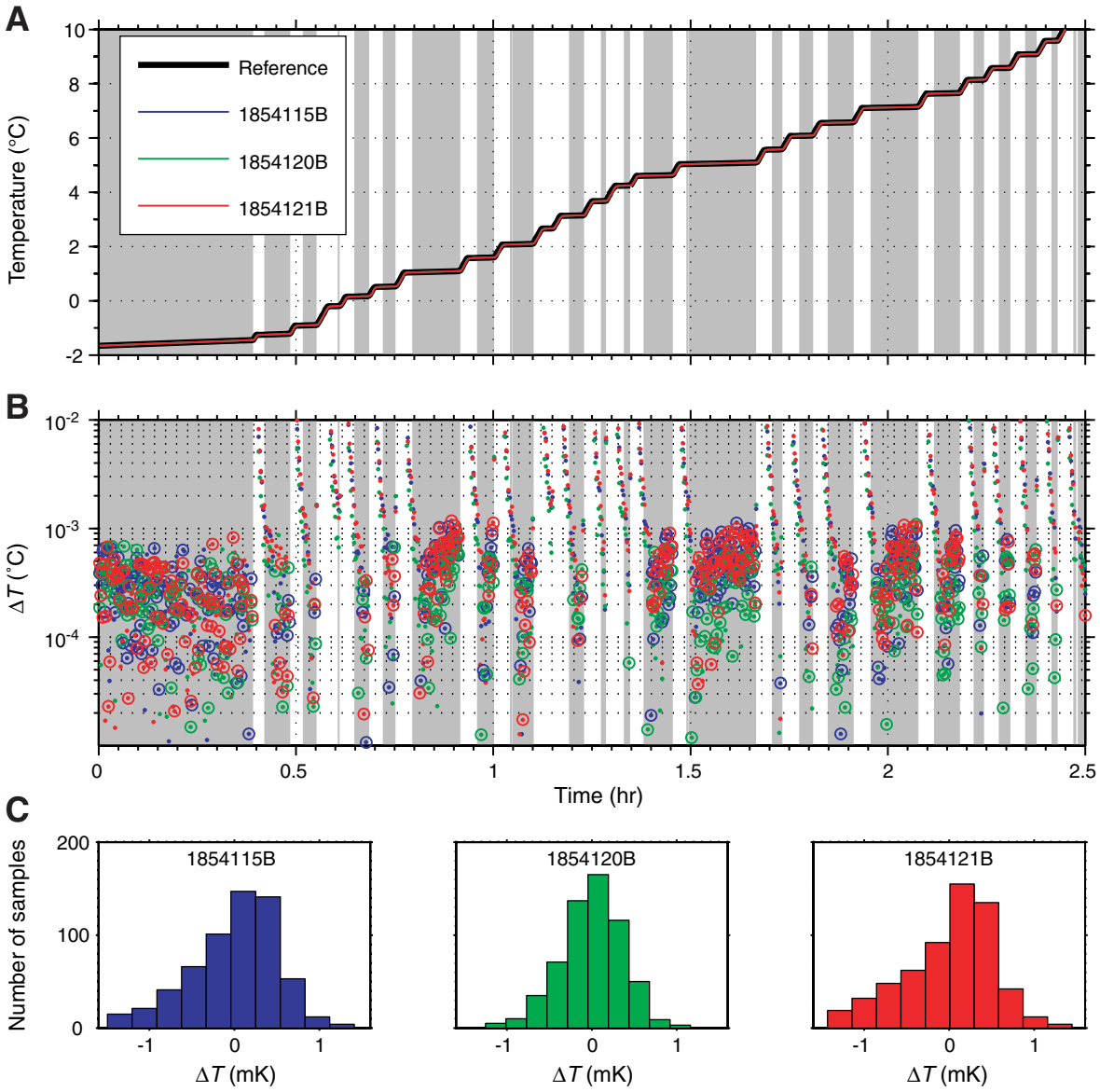

Figure F4. Construction sketches of the OsmoSamplers installed in (**A**) Hole 1253A and (**B**) Hole 1255A. Hole 1253A contains two identical OsmoSamplers with MTLs placed in the upper endcaps (cf. Fig. **F5**, p. 13.) The OsmoSampler installed in Hole 1255A contains an MTL in the upper endcap and in the probe that samples the décollement zone.

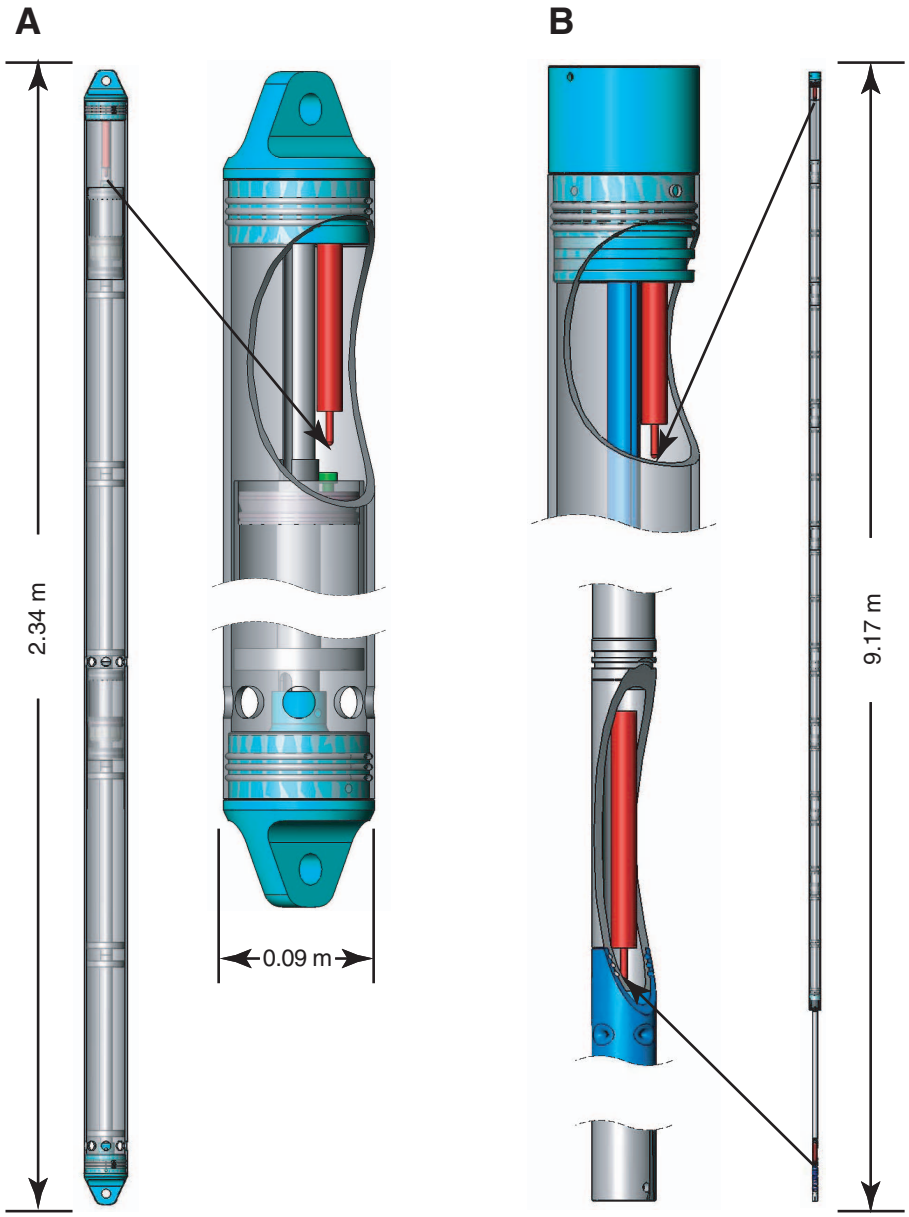

Figure F5. MTL in Hole 1253A after recovery from 2-yr deployment.

Figure F6. Complete temperature data measured by the recovered loggers. **A.** Hole 1253A. **B.** Hole 1255A.

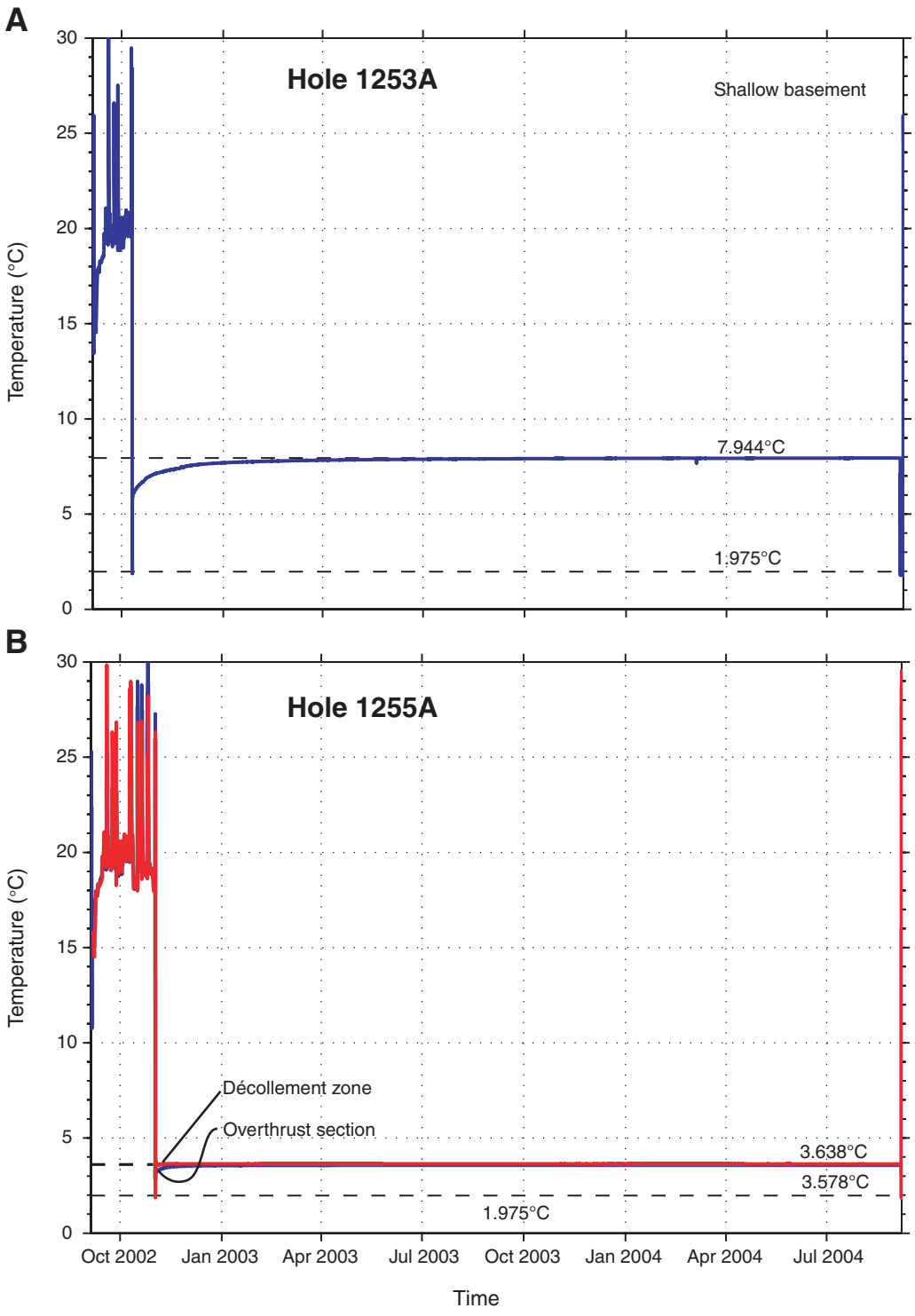

Figure F7. Comparison of the temperature equilibration following installation in (**A**) Hole 1253A and (**B**) Hole 1255A.

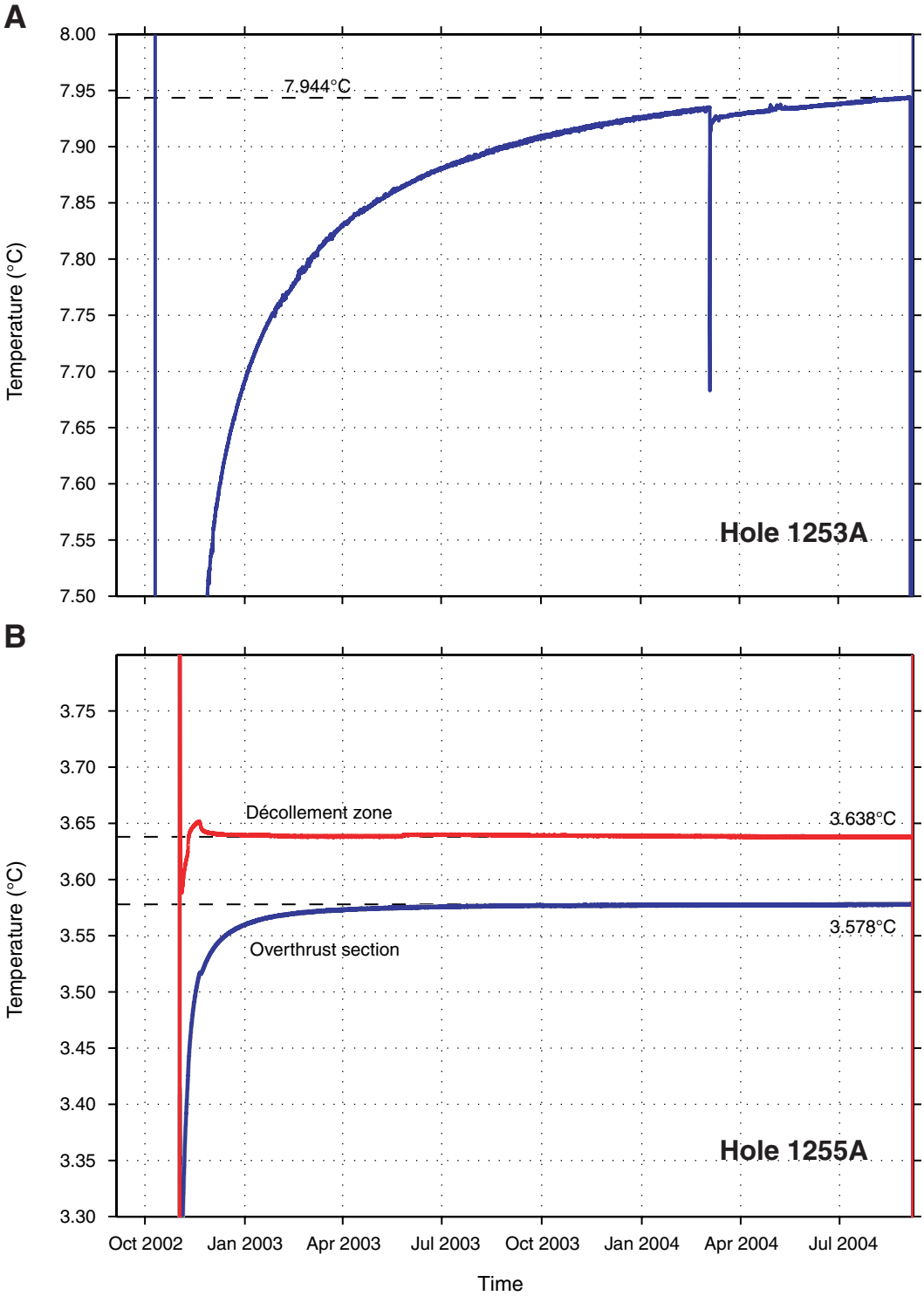

Figure F8. Small-scale temperature variations and pressure events in Hole 1255A. **A.** Overthrust section. **B.** Décollement zone. **C.** CORK-II pressure data at Site 1255.

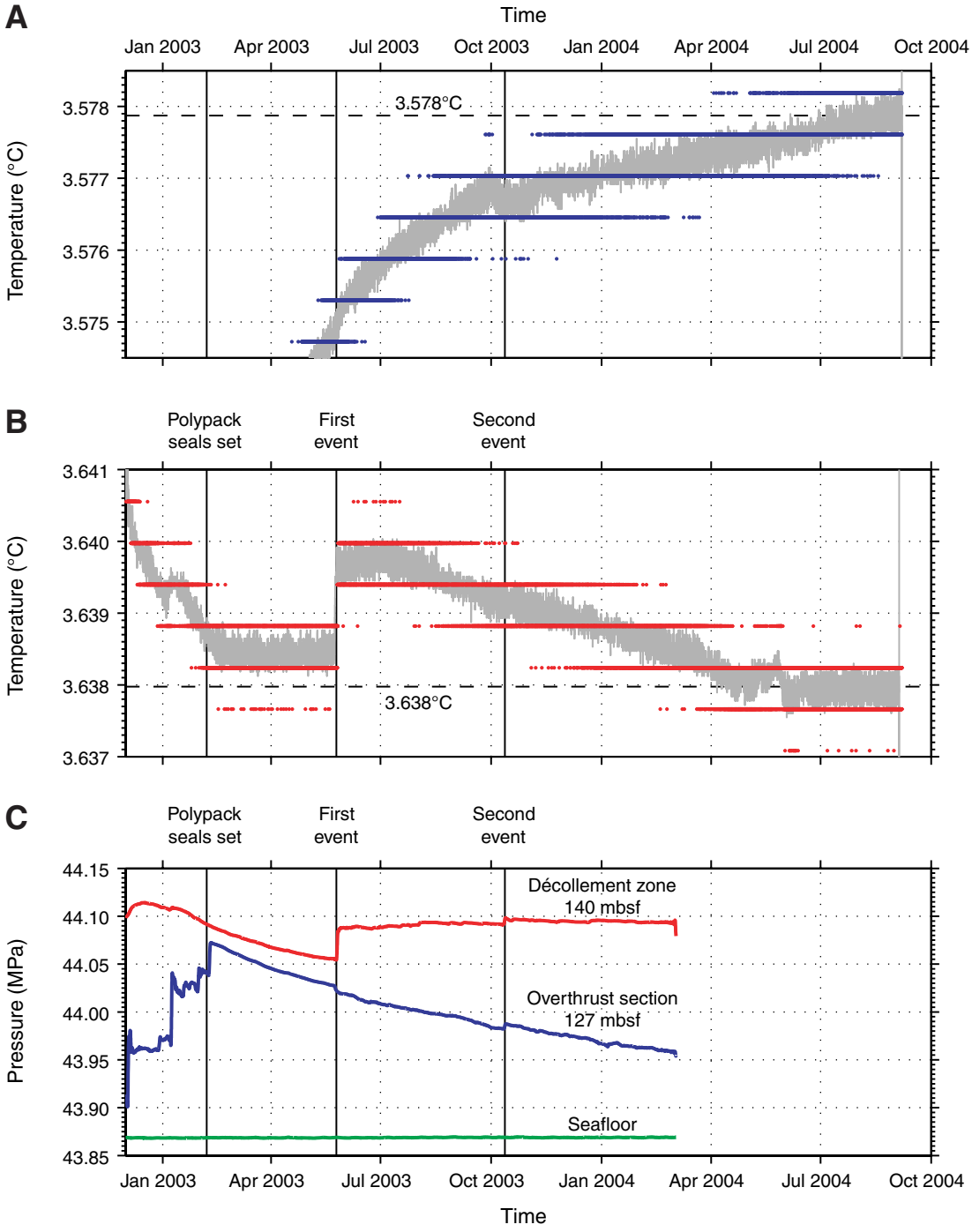

Figure F9. A. Temperature signal created by OsmoSampler recovery attempt during *Alvin* dive 3982 on 4 March 2004. **B.** Small-scale temperature variations in Hole 1253A. UTC = Universal Time Coordinated, MTL = miniaturized temperature logger.

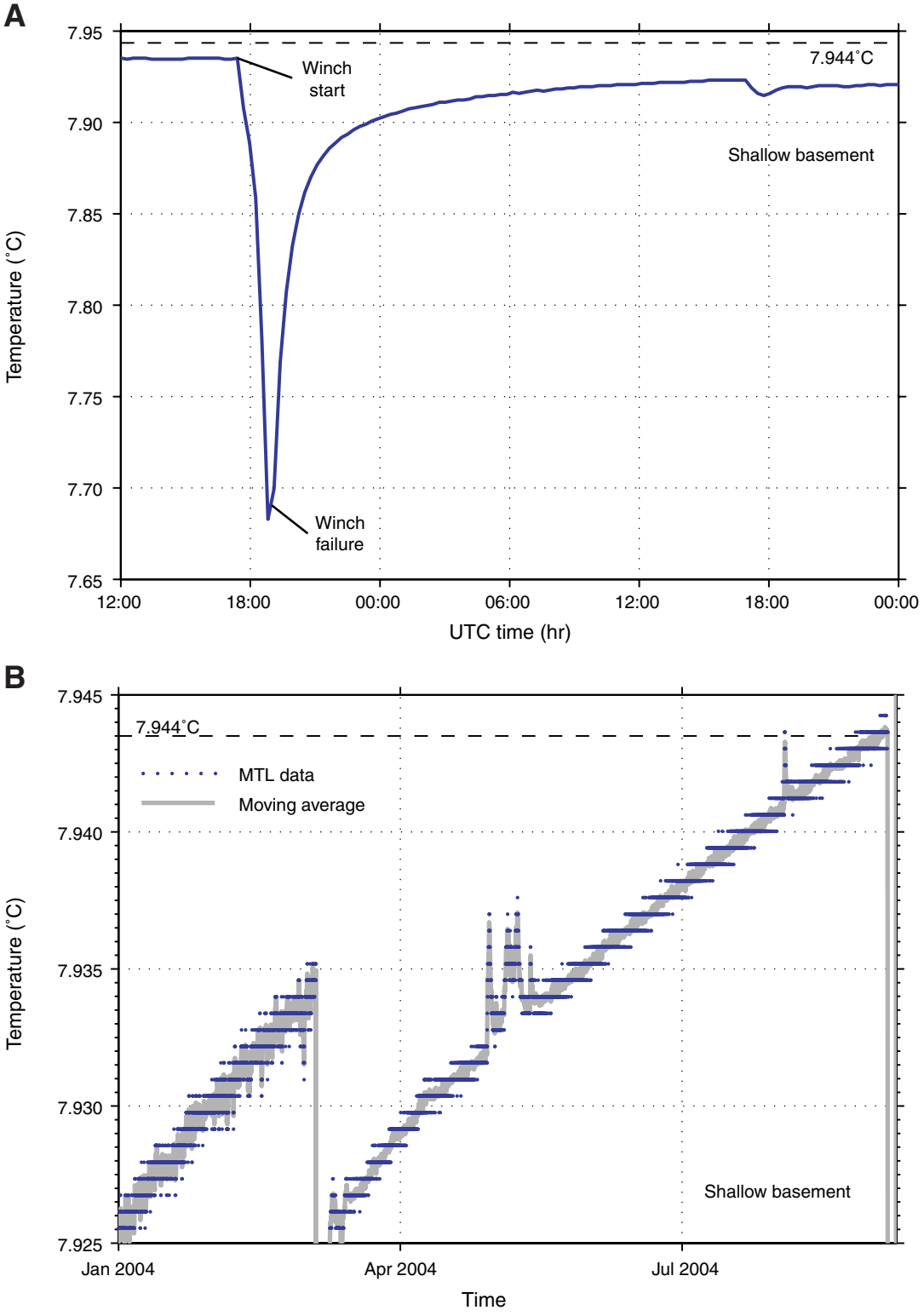

Figure F10. Temperatures measured during first unsuccessful recovery attempt during Expedition 301T when the OsmoSampler in Hole 1253A was dropped to the seafloor for ~2 days. The upper OsmoSampler with an MTL was subsequently recovered, whereas the lower OsmoSampler with an MTL could not be recovered and remains on the seafloor.

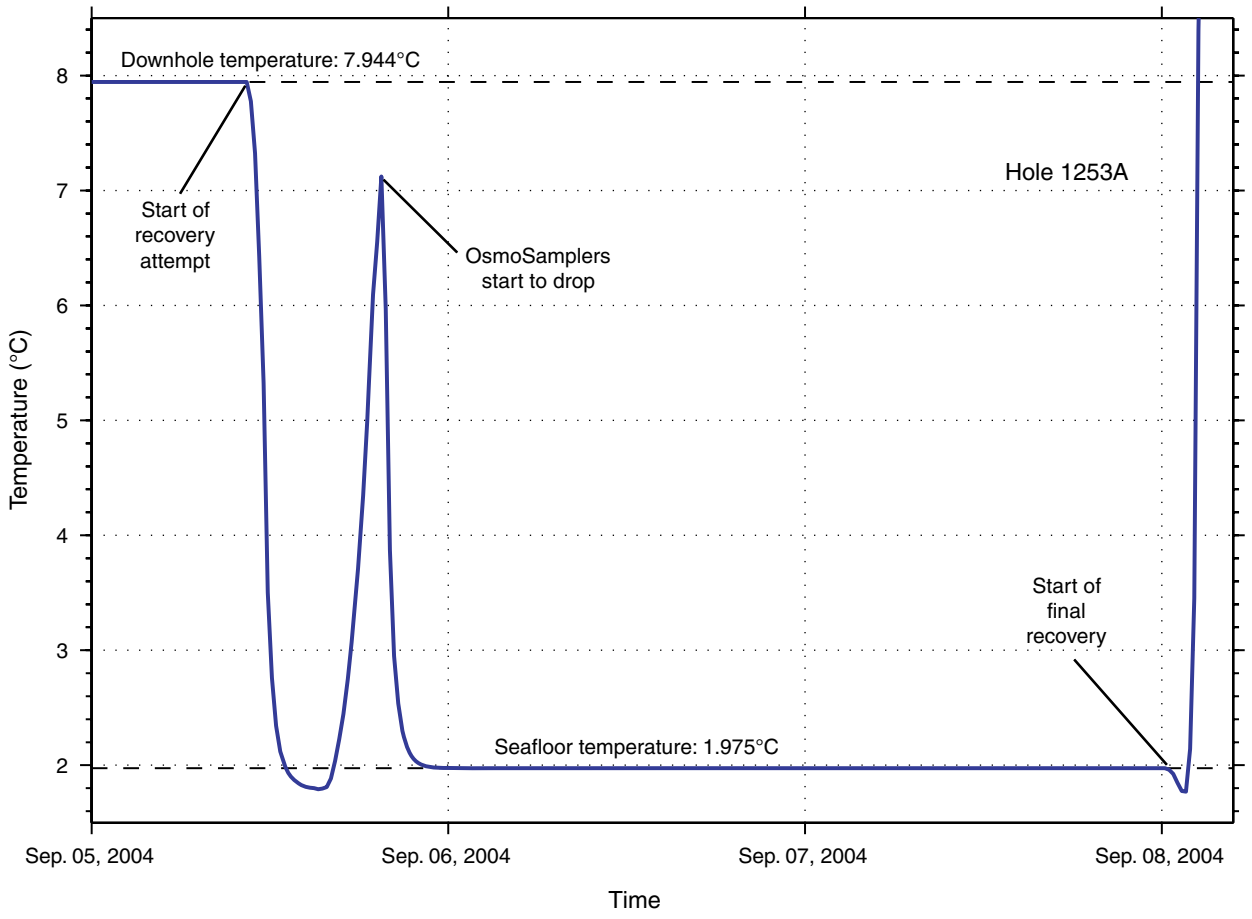

Figure F11. Fast Fourier Transform (FFT) amplitude spectra of (**A**) temperatures in the overthrust section, (**B**) temperatures in the décollement zone, and (**C**) CORK-II seafloor pressures measured during November 2003–March 2004 at Site 1255.

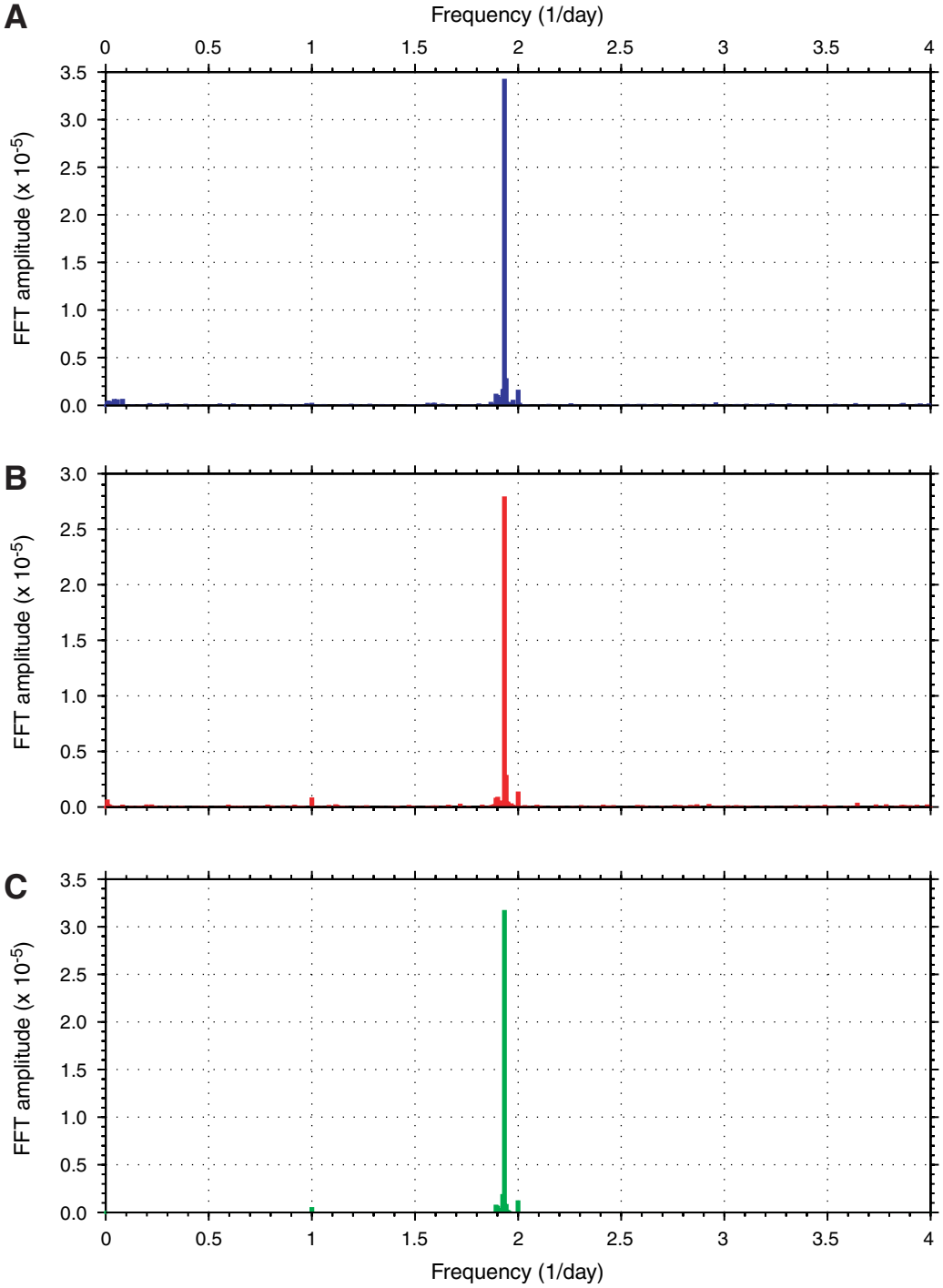

Table T1. Overview of MTL positions, logging times, and instrument drift.

MTL number	Hole	Position	Depth (mbsf)	Logging time (UTC)		Time offset (hr)
				Start	Stop	
1854115B	1255A	Overthrust section	135.1	4 Sept 2002, 1800 hr	6 Sept 2004, 1827 hr	–00:07:25
1854120B	1255A	Décollement zone	140.4	7 Sept 2002, 0000 hr	7 Sept 2004, 2132 hr	–00:06:40
1854121B	1253A	Shallow basement	501.4	4 Sept 2002, 1800 hr	8 Sept 2004, 0535 hr	00:01:52
1854131B*	1253A	Deeper basement	514.8	4 Sept 2002, 1800 hr	3 Oct 2004, 2154 hr	NA

Notes: MTL = miniaturized temperature logger, UTC = Universal Time Coordinated. * = lost on seafloor and hopefully recovered at next visit, NA = not available.

3 Analysis of temperature and pressure data

This chapter focuses on the analysis of data from ODP/IODP downhole temperature and pressure tools. In the first manuscript (*Heesemann et al.*, in prep. 2008a, pp. 61), the algorithm to extrapolate undisturbed formation temperatures from transient data of downhole tool is systematically evaluated and improved, mainly by providing new reference models that are based on more accurate geometries of the different probes. It follows the presentation of TP-Fit (*Heesemann*, 2008, pp. 90), a new software that is capable to analyze data of all ODP/IODP temperature probes currently in use. The design and implementation of TP-Fit was part of the work leading to this thesis and is based on the research presented in *Heesemann et al.* (in prep. 2008a). The chapter concludes with a manuscript (*Heesemann et al.*, submitted 2008b, pp. 96) that describes an algorithm how to estimate undisturbed formation pressures from DVTPP data.

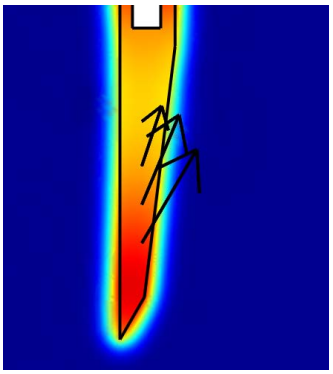

FE model of APCT

Manuscript: Estimation of in-situ formation temperatures from transient tool response in unconsolidated sediments during piston coring

Heesemann, M., A. T. Fisher, and H. Villinger (in prep. 2008a), Estimation of in-situ formation temperatures from transient tool response in unconsolidated sediments during piston coring, *Geochem. Geophys. Geosyst.*, in prep.

Contributions

As part of the APCT-3 development (*Heesemann et al.*, 2007), existing algorithms to extrapolate undisturbed formation temperatures from transient downhole measurements were inspected in order to evaluate and increase the accuracy of their results. In the following manuscript, the basic steps that are necessary to analyze downhole temperature data are introduced and possible sources of errors are identified. Subsequently, the effects of possible error sources on the accuracy of the formation temperature estimate are systematically quantified using synthetic and measured temperature data. Martin Heesemann compiled the manuscript, designed the experiments, and analyzed the data. Andrew T. Fisher and Heinrich Villinger supervised the research.

Estimation of in-situ formation temperatures from transient tool response in unconsolidated sediments during piston coring

Martin Heesemann[1,*] Andrew T. Fisher[2] Heinrich Villinger[1]

[1]Department of Geosciences, University of Bremen, Bremen, Germany.
[2]Earth Sciences Department, University of California, Santa Cruz, USA.

Since 1978, downhole tools were regularly deployed to measures temperatures in formations at the bottom of scientific drill holes. The data contributed to the resolution of many fundamental research questions in earth sciences. The algorithm that is required to estimate undisturbed formation temperatures from the transient measurements, however, did not receive much attention. Firstly, the algorithm has never been thoroughly documented and evaluated even though it basically remained unchanged over the years. Secondly, the accuracy of the formation temperature estimates has never been studied systematically. Focusing on the third version of the Advanced Piston Corer Temperature (APCT-3) probe and a new software package (TP-Fit) to analyze the temperature data, we address both issues mentioned above. Firstly, we documented the assumptions about the measured data which are inherent in the algorithm. The awareness about these assumptions will hopefully help users to judge if a measurement should not be analyzed with TP-Fit because it is subject to disturbances that violate these assumptions. Moreover, the analysis of the algorithm revealed that the estimated formation temperatures may be systematically biased. Therefore we examined the accuracy of the estimated formation temperatures using synthetic data and measurements acquired during Integrated Ocean Drilling Program (IODP) Expedition 316. Synthetic data have the advantage that the true results are known, but it is uncertain how realistic the data are. We found that the extrapolated results are by an order in magnitude closer to the true formation temperature than the last reading of a regular temperature transient measured with a downhole temperature tool. For synthetic data we found extrapolation errors up to $\pm 0.3\,^{\circ}\mathrm{C}$ for a typical APCT-3 deployment. The accuracy of the estimations of the measured data could not be accurately determined, since the true formation temperature is not known and the measurements might have been influenced by gashydrate bearing formations. However, estimation errors of up to $\pm 1\,^{\circ}\mathrm{C}$ seem to be possible with APCT-3 data.

*Corresponding author: Martin Heesemann (heesema@uni-bremen.de)

1 Introduction

Geothermal measurements provide important constraints on dynamic earth processes, and therefore temperature was among the first downhole properties to be measured during the Deep Sea Drilling Project (DSDP) (*von Herzen and Maxwell*, 1964). Those measurements have been used to investigate heat transfer from the interior of earth, the evolution of the oceanic lithosphere, the formation of continental margins, and subduction zones and hotspot volcanism. In addition results were used to examine processes associated with fluid flow and gas hydrate formation (e.g. *Erikson et al.*, 1975; *Hyndman et al.*, 1987; *Pribnow et al.*, 2000). Undoubtedly, precise measurements of formation and fluid temperature will remain a high priority for downhole tool operations in the Integrated Ocean Drilling Program (IODP), since they are essential for fulfilling the goals of the IODP Initial Science Plan (ISP) (*Kappel and Adams*, 2001) in all three of the primary research topics: (1) deep biosphere and subseafloor ocean, (2) environmental change processes and effects, and (3) solid earth cycles and geodynamics.

1.1 Overview of downhole temperature tools

Downhole temperature tools have to be inserted into the formation at the bottom of the borehole in order to measure temperatures that are not disturbed by drilling operations. Regarding their mode of operation, there are two different types of borehole temperature tools. In unconsolidated sediments, (1) measurements can be carried out using APCT temperature probes that are placed in the cutting shoe of the advanced piston corer (APC) and log formation temperatures while coring. When sediments are to stiff for piston coring, (2) specialized probes that require a dedicated tool run have to be deployed.

The first down-hole temperature probe that was regularly used during scientific ocean drilling was the Uyeda tool, which needed a dedicated deployment. It was first deployed in 1978 during Deep Sea Drilling Project (DSDP) Leg 60 (*Uyeda and Horai*, 1982). Later, the Uyeda tool was merged with the Barnes fluid sampler and became the water sampling temperature probe (WSTP). The probe specialized on temperature measurements that is mostly used today, is the Davis-Villinger temperature probe (DVTP) which was introduced during ODP Leg 68 (Figure 1B). During its deployment, the DVTP is lowered by wire-line, latched in at the bottom of the drill string, and pushed $\sim$1.1 m into the formation at the bottom of the borehole (*Davis et al.*, 1997). Following insertion, the DVTP is decoupled from the drill string and left stationary for 7-10 min to allow a partial decay of the temperature disturbance caused by the probe. Finally, the tool is extracted from the formation and retrieved on board, where the measured data is downloaded from the tool.

The first APCT tool was deployed in 1984 during DSDP Leg 86 (*Horai and Von Herzen*, 1985) and its use almost immediately became a routine part of ocean drilling operations. The tool was improved and redesigned two times and since the Integrated Ocean Drilling Program (IODP) Expedition 311 in 2005, the third generation of the tool, the APCT-3 (Figure 1), is in use. The deployment procedure for APCT tools is similar to the deployment of the DVTP, described above. However, the APCT is pushed 9.5 m into to the formation, and besides the temperature data, sediment cores are recovered (*Heesemann et al.*, 2007).

1.2 Extrapolation of transient temperature data

All probes create temperature disturbances when they are inserted into the formation. These disturbances are mainly caused by the difference between the initial temperature of the probe and the undisturbed formation temperature. Assuming that the probe is very small compared to the extent of the formation, probe and formation temperature will equilibrate and approach the undisturbed formation temperature. Unfortunately, there is often not enough time during measurements to wait until the disturbance decays to a negligible level. Firstly, drill string rotation and mud circulation have to be stopped in order to not disturb the temperature measurements, but doing so for an extended amount of time in unstable formation may results in the collapse and subsequent loss of the borehole. Secondly, concerning APCT measurements, the formation tends to settle in around the tool. Therefore, the tool extraction becomes more difficult the longer the tool stays in the formation. In order to estimate true formation temperatures from measurements of incomplete decays of the temperature disturbances, algorithms to extrapolate this transient data to infinite times were developed.

Data analysis algorithms performing this extrapolation are similar for all downhole temperature tools (*Taylor et al.*, 1999). First of all, synthetic decay

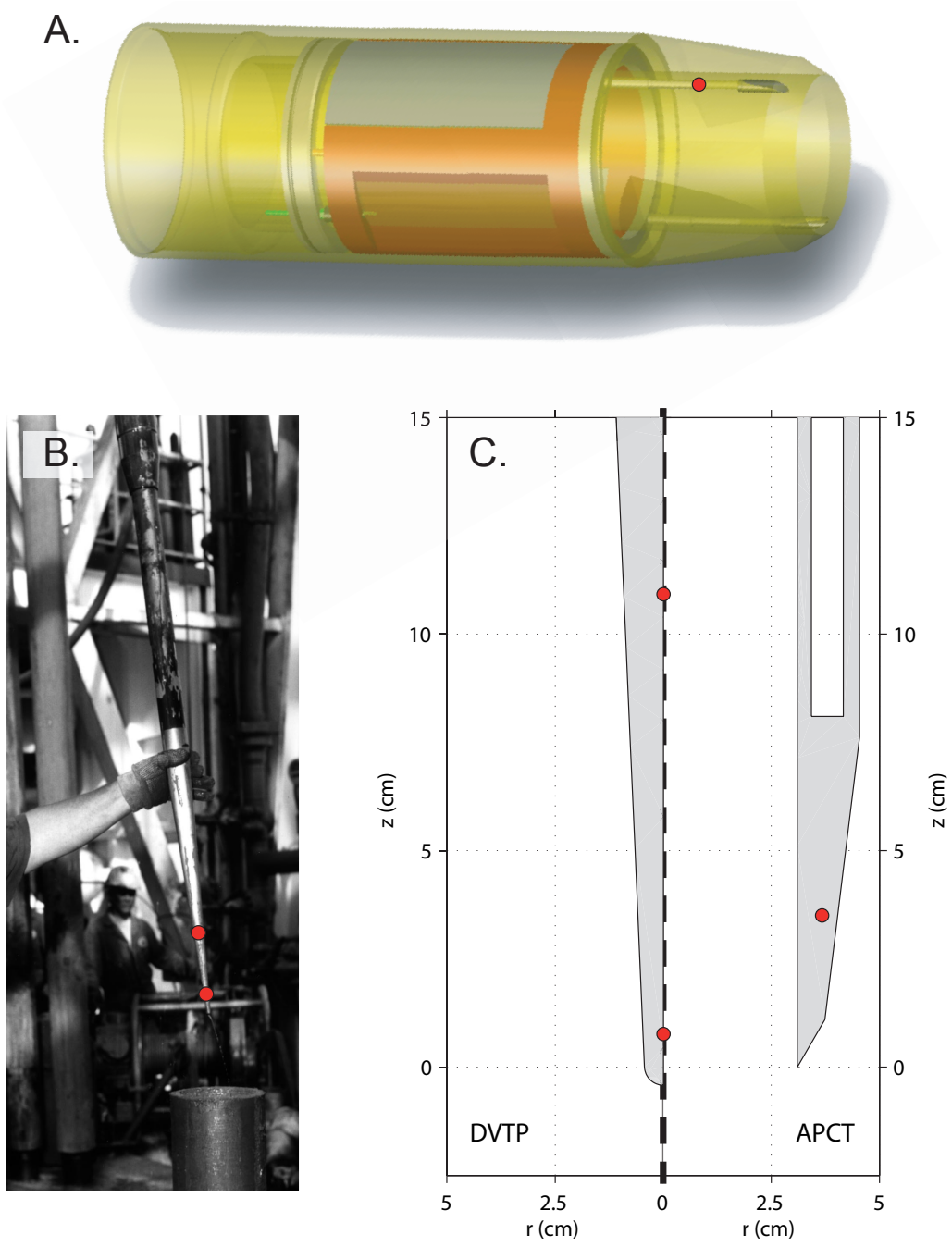

Figure 1: A. APCT-3 electronics placed in the cutting shoe of the advanced piston corer (APC). B. Tip of the DVTP that after successful deployment (photo by Roy Davis). C. Axisymmetric geometries of the DVTP and APCT temperature probes used for finite element models. Red circles (A.–C.) show locations of the temperature sensors and the bold dashed line (C.) is the axis of symmetry.

curves computed using analytic or numeric models of the thermal response of the specific tool are computed. Then, these forward models—known to be functions of probe geometry and thermal properties of the probe and the sediments (*Bullard*, 1954; *Horai*, 1985)—are compared to the measured temperature data. However, it turned out that direct comparison does not lead to a good match between the forward model and measured data. In order to reduce the misfit and, supposedly, the error of the formation temperature estimate, empirical parameters (e.g. a time-shift between the model and the data) were incorporated into the data analysis algorithms. The rationale for these parameters, adopted from the analysis of seafloor heat-flux data (*Hyndman et al.*, 1979; *Villinger and Davis*, 1987; *Hartmann and Villinger*, 2002), is to compensate aspects of the tool response that are not taken into account by the simplified forward models. These effects include possible contact resistivities between the sensor and the probe or the probe and the formation that could affect the thermal response of the tool.

The algorithms outlined above, were implemented in several software programs each customized for a specific downhole tool. For example, the CONEFIT program was specifically designed for DVTP data, while the TFit software is only capable to process APCT data (*Horai and Von Herzen*, 1985; *Davis et al.*, 1997, respectively). Due to this specialization, there was no software program that was capable to analyze the data with the new APCT-3 tool, when it was first deployed during IODP Expedition 311 (*Heesemann et al.*, 2007). To fill this gap, TP-Fit, a new software tool to estimate undisturbed formation temperatures from transient tool responses was implemented in Matlab® (*Heesemann*, 2008). TP-Fit is not only capable to process APCT-3 data; it is also possible to analyze data from of all previous generations of APCT and DVTP tools. In addition to its modular design, simplifying future extensions for new temperature or even pressure probes, TP-Fit provides new reference models for the APCT and DVTP tools. These improved forward models reflect the geometry of the temperature probes better than the forward models used by TFit and CONEFIT. Moreover, the new software contains a graphical user interface that greatly simplifies the data analysis, compared to previous software packages.

1.3 Objectives

During the last decades, downhole temperature measurements undoubtedly contributed to the resolution of many fundamental research questions in earth sciences. However, the algorithm for data analysis did not receive much attention during that time. Firstly, the algorithm has never been thoroughly documented even though it basically remained unchanged over the years. Secondly, the accuracy of the formation temperature estimates has never been studied in a systematic way. In this study, we address both issues focusing on TP-Fit and the APCT-3 tool for conciseness. However, most of our results relate to downhole temperature measurements and their analysis in general, and—where it seems appropriate—we point out differences between temperature tools and software packages.

2 Evaluation of the data analysis algorithm

In this first part of this study, we document and analyze the algorithm to estimate undisturbed formation temperatures from transient tools responses, as implemented in TP-Fit. This part starts out with providing details on how downhole tool temperature measurements are represented by the new forward models that are part of TP-Fit, on what parameters the models depend, and what assumptions about the measurements are implicitly made when analyzing data using the models. Following, all steps that are necessary in estimating undisturbed formation temperatures using the reference models, as performed using TP-Fit, are explained. The analysis of the algorithm concludes with the finding that the estimated formation temperatures may be systematically biased, because the parameters that determine the forward model cannot be determined, precisely.

2.1 The forward model

All software packages that have been used to estimate undisturbed formation temperatures from transient tool responses rely on forward models for the analysis. Supposedly, the accuracy of the formation temperature estimates depends on the degree of accuracy with which the forward models describe the thermal response of the probe during an actual measurement.

To increase the accuracy of the data analysis, we developed improved forward models for the APCT

and the DVTP probes which are included in TP-Fit. The new models are based on the finite element (FE) method and were implemented using Matlab® and the Comsol Multiphysics® FE toolbox. One advantage of FE models is that they are very well suited to capture the complex geometries of downhole temperature probes. Our new models are based on a realistic 2D radial symmetric probe geometry while the previous analytic approach was restricted to a simple 1D geometry.

Before creating a FE model, one has to select a governing equation which imposes some assumptions about the temperature measurements and leads to the parameters of the model. Then these parameters—related to the model geometry, boundary conditions, physical properties, and initial conditions—have to be adjusted in order to describe the processes occurring during a temperature probe deployment.

2.1.1 Equation of heat conduction

The forward models used in TP-Fit are based on finite element solutions of the time dependent equation of heat conduction

$$\rho C \frac{\partial T}{\partial t} = \nabla \cdot (k \nabla T), \qquad (1)$$

where ρC is the volumetric heat capacity and k is the thermal conductivity. Using this equation we assume, that there is no heat production in the model domain after the initial time t_0, and that heat transport is purely conductive. Using the data examples of APCT-3 measurements shown in Figure 2, we will discuss significance of these assumptions with respect to downhole temperature measurements.

The APCT-3 data shown in Figure 2 can be interpreted using only the assumptions stated above. Before the modeled temperature decay starts ($t < t_0$), the measured temperature rises in the 5 s from the open borehole temperature T_b ($\sim$5°C) to the initial temperature $T(t_0)$ ($\sim$17 °C). After the insertion is completed ($t \geq t_0$), the probe remains stable in the formation and equilibrates steadily—supposedly, by purely conductive heat transport—toward the undisturbed formation temperature T_f. Finally, the measurement of the transient tool response in the formation ends when the probe heats up again ($t = 530$ s) while it is extracted from the formation.

However, measurements often provide evidence for disturbances caused by movements of the temperature probe with respect to the formation. As shown in Figure 2B, tool movement during the first seconds of the equilibration can lead to difficulties in defining the time t_0 when the insertion process is finished, because it takes some time for the probe to settle. Other measurements, especially in surface sediments with low rigidity, show disturbances due to longer periods of continuous tool movement (0–100 s in Figure 2C) or sudden tool movements at discrete times (e.g. $\sim$820 s in Figure 2C) are observable. These tool movements violate the governing equation (1) in two ways. Firstly, the movement of the probe with respect to the sediments implies advective heat transport and, secondly, heat is generated due to friction between the probe and the sediments.

Besides that all assumptions of (1) have to be fulfilled, exact forward models depend on the correct choice of the FE model parameters. These parameter are related to the model geometry, the boundary conditions at the outer edges of the model domain, the physical properties k and ρC in the model domain, and the initial temperature distribution $T(t_0)$.

2.1.2 Model geometry

The downhole tool geometries in our FE models (cf. Figure 1C) are based on the technical drawings of the DVTP and the APCT cutting shoe (pers. comm. Derryl Schroeder, IODP-USIO). We took advantage of the radial symmetry of the probe using cylindrical coordinates and solving a 2-D problem. Regarding the APCT model, the 2-D geometry is a simplification, since the cutting shoe is not perfectly cylinder symmetric (cf. Figure 1A); the cutting shoe has wrench flats on two opposing sides and small drills in which the sensor can be inserted on the other two sides (*Heesemann et al.*, 2007). However, tests with a more complex 3-D FE model confirmed that this simplification does not cause significant differences in modeled temperatures at the sensor location.

Regarding the sediments surrounding the probe, we chose the extent of our model so that the distance from the temperature sensor location to the outer model boundaries is at least 15 cm in every direction. Numerical experiments showed that extending the sediment domain has no effects on the model results at the the temperature sensor location for model times shorter than one day.

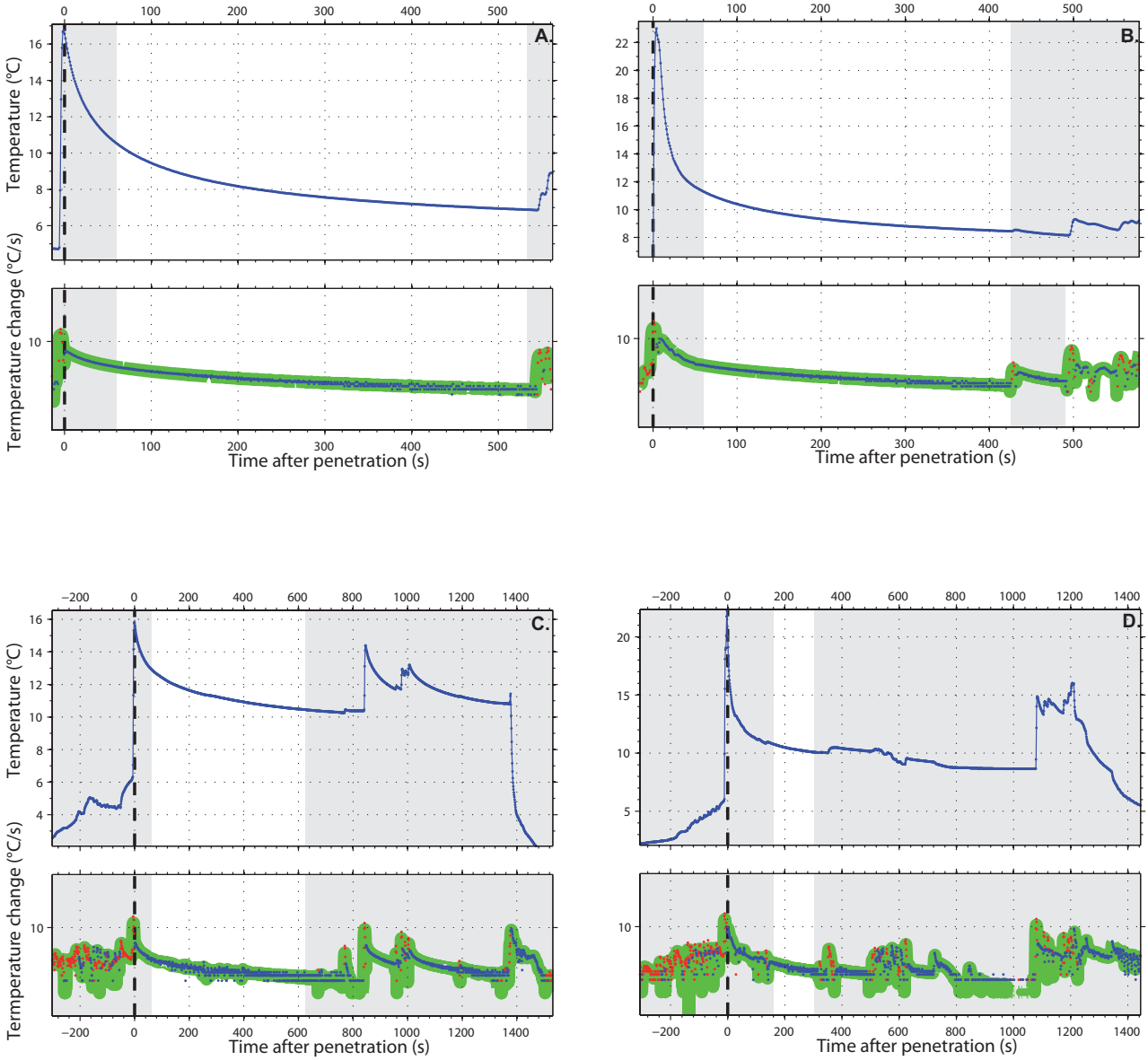

Figure 2: Examples of APCT-3 data with different qualities. A. Excellent data quality. B. Good data quality. The probe settles slowly after insertion (cf. temperature change plot) and the decay is disturbed again by tool movement at ∼420 s, starting a short new decay. C. Lightly disturbed data. The gradient plot reveals small disturbances during a extended periods of time. Influence on undisturbed formation temperature estimates are probable. D. Heavily disturbed data. Periods of continuous and discrete tool movement during the whole time of the decay.

2.1.3 Boundary conditions

One boundary of the model domain is the axis of symmetry (cf. Figure 1C), trough which no heat flux can occur. The lower and the outer boundaries (sediments far away from the probe) are fixed to the undisturbed formation temperature T_f. We assume that there is no heat flux through the upper boundary, since the heat flux should be mostly in radial direction at some distance upward from the tools tip. The cavity that holds the APCT electronics was modeled by perfectly insulating boundaries, since numerical experiments did not show significant differences to test models where the cavity was part of the model domain and assigned thermal properties of air.

2.1.4 Thermal properties

The TP-Fit reference decay curves are based on a FE model that is divided into a probe and a sediment domain. We used isotropic and homogeneous thermal properties in each domain. As a consequence, effects as contact resistivities at the sensor/probe and probe/sediment contacts as well as horizontal and vertical layering of sediment thermal properties due to sediment stratification and compaction during probe insertion, respectively, are neglected. For the APCT, the cutting shoe domain, representing "Maraging 250" steel, is assigned a thermal conductivity of 20 W/(m K) and a volumetric heat capacity of 3.7 MJ/(m^3 K) (cf. *Braccini et al.*, 2000). The DVTP probe is made from a different steel, which has a thermal conductivity of 15 W/(m K) and a volumetric heat capacity of 3.95 MJ/(m^3 K). In respect to sediment thermal properties, TP-Fit contains reference models with thermal conductivities ranging from 0.5–2.5 W/(m K) and volumetric heat capacities ranging form 2.3–4.3 MJ/(m^3 K). Note that the wide parameters ranges are supplied for completeness. Actual sediment thermal properties sediments can be determined from core samples and, for example, in-situ thermal conductivities <0.7 W/(m K) are not likely to be encountered unless there is free gas in the pore space. Thermal conductivity of 1 W/(m K) and a volumetric heat capacity of 3.4 MJ/(m^3 K) are typical for sediments cored with the APCT (cf. Figure 11 in the Appendix).

2.1.5 Initial conditions

For the temperature distribution at the initial time t_0, we assume that the probe has a homogeneous temperature ($T_0 = T(t_0)$) and that the sediment temperature (T_f) is still undisturbed around the probe. With only one temperature sensor built into the APCT tools it is impossible to prove how well the assumption of a homogeneous initial temperature distribution in the probe is met. The DVTP, however, has temperature sensors at two locations (cf. Figure 1) and it appears that the temperature readings at both locations often differ considerably (cf. Figure 3).

The assumption that the sediment is undisturbed may be wrong if one decides to extrapolate the temperature data of a secondary decay (Figure 2C). The secondary equilibration curve may have been initiated, because the probe was suddenly pushed deeper into the sediments. In this case, it might be valid to (re)set t_0 to the time, when the push is completed, and treat the data as independent decay. But this can only be done, if the probe has advanced far enough too be out of the influence of the sediments heated by the primary decay. More important, one has to make sure, that the temperature increase is not caused by an uplift of the probe due to ship heave. If the probe is uplifted, then secondary decay is definitively effected by the heat dissipated into the sediments from the primary equilibration process.

2.2 TP-Fit algorithm

As shown in the previous section, there are some data sets that should not be analyzed with the FE forward model, because they obviously violate the model assumptions. Moreover, the undisturbed formation temperature T_f, we try to estimate, is a parameter of the forward model. Therefore, a inversion scheme that uses the forward model to estimated the most probable T_f in respect to measured data is needed. The inversion scheme of all software tools used to extrapolate undisturbed formation temperatures from transient downhole tool data is based on reference models $\Theta(t)$ which are normalized so that $\Theta(t_0) = 1$ and $\Theta(t_\infty) = 0$. The usage of the reference models is analog to procedures applied by *Bullard* (1954) to analyze marine heat-flux data. *Bullard* (1954) used $F(\alpha, \tau)$, a analytic solution of the equation of conductive heat transfer (1) which describes the thermal response of a cylindrical probe with infinite length, as normalized reference model. $\Theta(t, \ldots)$, is an abstraction of $F(\alpha, \tau)$; Θ can be any normalized reference model, depending on arbitrary parameters, that describes the thermal response of a temperature probe and conforms to the assumptions of the gov-

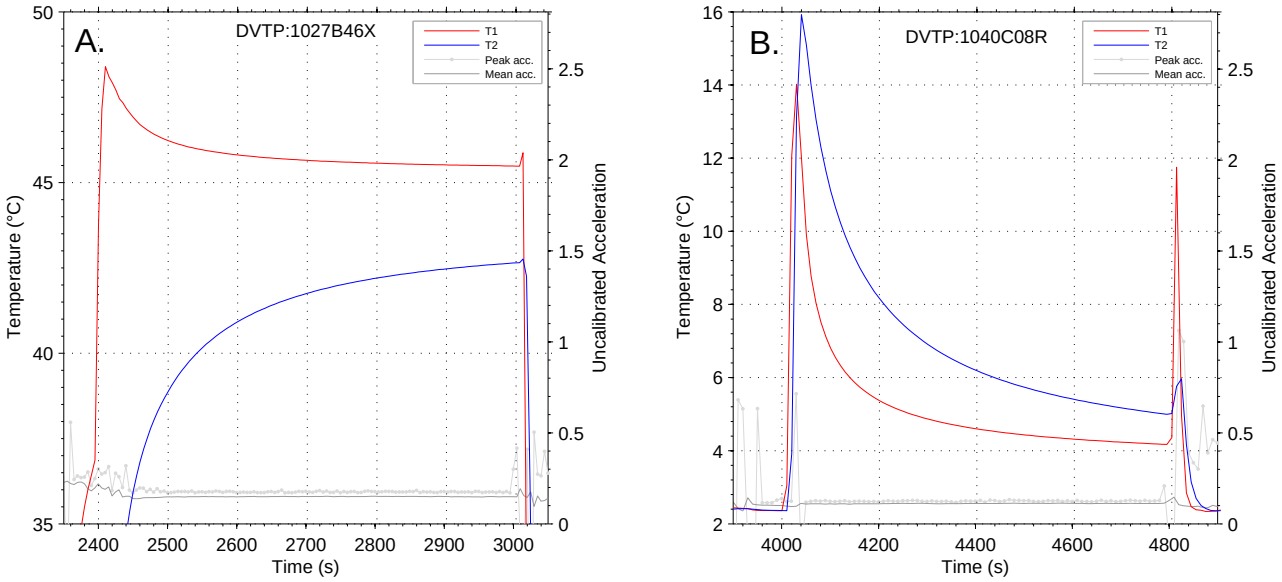

Figure 3: DVTP data with two simultaneous temperature time series, where T1 (red line) is measured closer to the tip than T2 (blue line) (c.f. Figure 1). In most cases, the temperature rise due to frictional heating during insertion is higher at the tip. This is illustrated in the first example (A.), where the temperature at the tip (T1) is raised above the formation temperature (T_f) and T2 (blue line) remains below it. There are, however, some measurements (B.) where the tip (T1) is heated less than the upper part of the probe at T2.

erning equation (1). Hence, Θ includes for example $F(\alpha, \tau)$ (as a first order analytic approximation), the FE models of the downhole tools presented above, or any other analytical, numerical, or analog model that is based on purely conductive heat transfer.

Taking advantage of the linearity of the governing equation (1) in respect to the temperature T—i.e. all valid models for a thermal tool response arbitrarily scaled and translated with respect to T lead to new valid models—measured temperature data $T(t)$ can be expressed using Θ as follows (cf. notation summary before references):

$$T(t) = T_e\,\Theta(t) + T_f + \varepsilon(t) \qquad (2)$$

Here, $T_e = T_0 - T_f$ is the initial excess temperature, T_f is the undisturbed formation temperature, and $\varepsilon(t)$ is the deviation of the measured data from the forward model (cf. Figure 4A, B). According to equation (2), linear regression of $\Theta(t)$ and $T(t)$ provides a inversion scheme to estimate T_e and T_f by minimizing the residual (ε) between forward model and data. Graphically speaking, the estimated undisturbed formation temperature T_f is the extrapolated T-axis intercept of a $\Theta(t)$ vs $T(t)$ plot (cf. Figure 4C).

As mentioned before, straight linear regression does usually not lead to a good match between forward model and measured data. In order to reduce the misfit two empirical parameters were incorporated into the data analysis algorithm. Firstly, the linear regression is not applied to the complete decay data, but only to data in a time window that omits the first part of the decay (e.g. in Figure 4 only data in the time window t_a–t_b is used for analysis). The early data is omitted, because deviations of the data from idealized forward model assumptions are considered to be more severe, early on. For example, an inhomogeneous initial temperature distribution in the probe will be less distinct at later times, since the relatively high thermal conductivity of the probe causes unevenly distributed heat in the probe to even out, quickly. Note, it is also important that the temperature data within the time-window are not subject to any disturbances (e.g. tool movement after t_0) that deviate from the reference model assumptions. Secondly, the time-shift parameter t_{Sft}, adopted from the analysis of seafloor heat-flux data (*Hyndman et al.*, 1979; *Villinger and Davis*, 1987; *Hartmann and Villinger*, 2002), was included in the algorithm. By applying a time-shift new reference models $\Theta_{Sft}(t) = \Theta(t - t_{Sft})$ are created from a basis model Θ by shifting it with respect to time. The

time-shift approach is completely empirical and was introduced to compensate for aspects of the tool response that are not taken into account by the forward models. These effects include possible contact resistivities between the sensor and the probe or the probe and the formation that could affect the thermal response of the tool.

The algorithm to extrapolate undisturbed formation temperatures from transient tool responses, as implemented in TP-Fit, combines the linear regression with the time-window and time-shift parameters and consists of the following steps:

1. Selection of the time t_0 (dashed line in Figure 4A, B), when the tool insertion process is completed. This step is necessary, since a typical time series of measured temperature data includes the complete tool deployment (see *Heesemann et al.* (2007) for a description of the deployment).

2. Determination of realistic parameters for the reference model $\Theta(t)$. Here, TP-Fit allows to adjust the sediment thermal conductivity and volumetric heat capacity.

3. Selection of the time-window (white area in Figure 4A, B, which is bounded by the window start t_a, marked by an upward pointing triangle, and the window end t_b, marked by a downward pointing triangle), which encloses a subset of the complete decay curve measured while the probe is in the formation. Note, TP-Fit automatically creates a secondary time window (diamond–downward pointing triangle in Figure 4) consisting of the last third of primary time window. Comparing the results of both time window provides information about how sensitive the results is to the somewhat subjective choice of the time window.

4. Determination of the time-shift t_{Sft} (Figure 4D), for which the linear regression between the reference model shifted in respect to time $\Theta(t - t_{Sft})$ and the measured data (Figure 4C) results in the smallest misfit.

5. Report of the T_f resulting from the model with the smallest misfit. In the graphical report provided by TP-Fit, T_f is shown as red circles and dashed red lines (Figure 4A, C) and the best fitting forward model $T_e\,\Theta(t - t_{Sft}) + T_f$ is shown as bold red line (Figure 4A).

6. Optionally, repeat steps 2.–5. with different reference model parameters and time windows.

Note, the way estimated formation temperatures are reported was not standardized, in the past. Some researchers ran the algorithm once until step 5 and reported the final results, assuming that minimizing the misfit by applying a time-shift leads to the best formation temperature estimate. Others would may go on with step 6, "play" with the model parameters, and report a range of possible formation temperatures.

2.3 Model errors

As explicated above, the linear regression of $\Theta(t)$ and $T(t)$ is the heart of the data analysis algorithm. Using the linear regression, one assumes (1) that the mean of $\varepsilon(t)$ is zero and (2) that the $\varepsilon(t)$ are uncorrelated, as expected for usual (e.g. *Gaussian* distributed) measurement errors. However, strongly correlated residuals between data and forward model (cf. Figure 4B), despite the introduction of the empirical time-shift and a time-window that omits the first part of the measured decay, show that at least the second assumption is violated.

To study the effects of these correlated errors on the formation temperature estimates, we assume that the errors are due to the choice of our reference models. So, either the reference models are oversimplified (e.g. the real initial temperature distribution is inhomogeneous), or the model parameters are not determined properly (e.g. erroneous thermal conductivity), or, most likely, a combination of both. If now, we think of $\Theta(t)$ as the abstract normalized reference model that perfectly represents the tool response, and denote the approximated reference model we actually use for the data analysis with $\tilde{\Theta}(t)$, equation (2) becomes

$$T(t) = T_e\,\tilde{\Theta}(t) + T_f + \varepsilon_T(t) + T_e\,\Delta\Theta(t). \qquad (3)$$

Here, $\Delta\Theta(t) = \Theta(t) - \tilde{\Theta}(t)$ is the deviation from the approximated reference model from the ideal reference model and ε_T is the error of the temperature measurement. Hence the deviation of the deviation of the reference model from the measured data ε (cf. equation (2)) is the sum of ε_T and the forward model error $T_e\,\Delta\Theta(t)$.

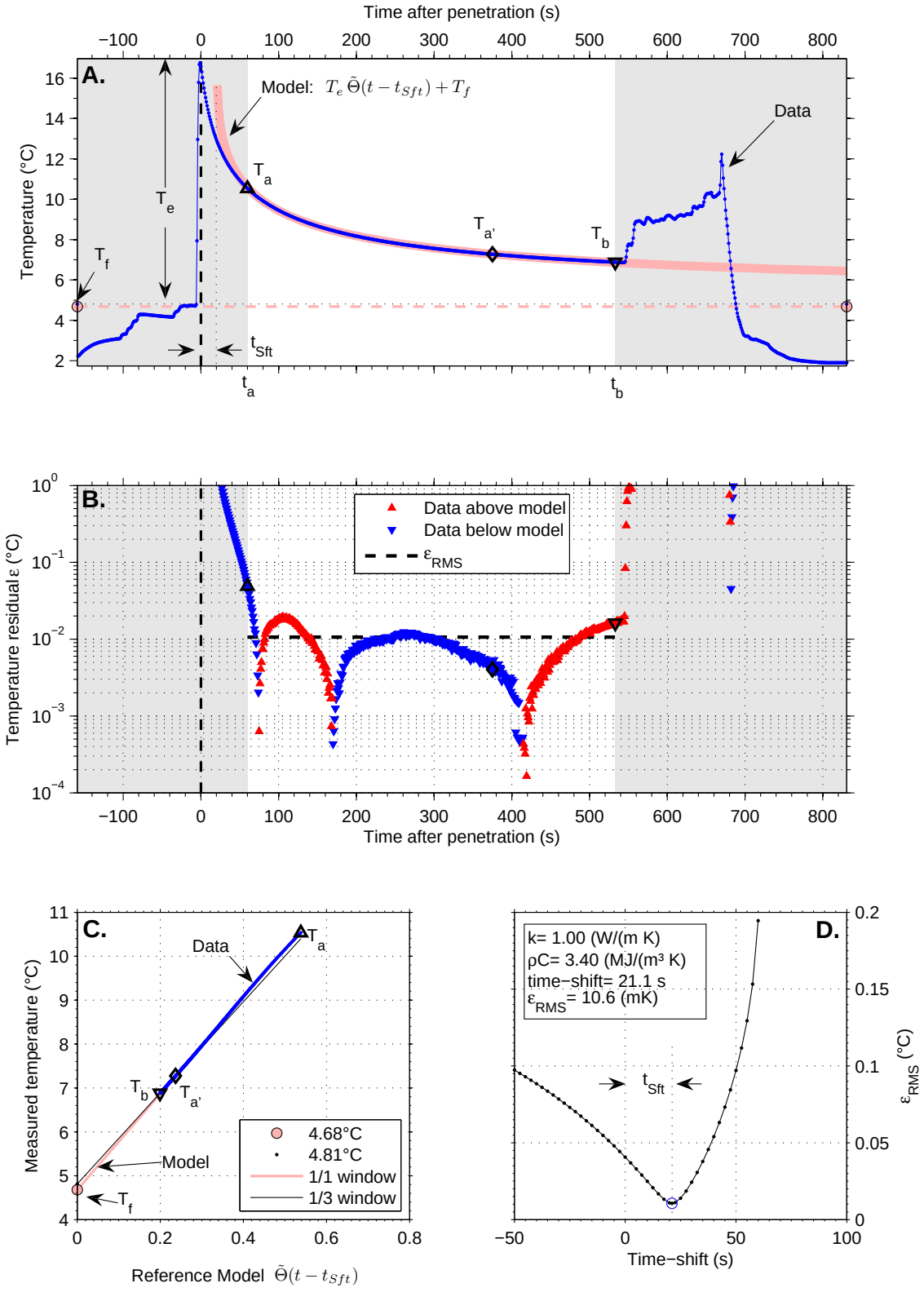

Figure 4: Graphical report of a data analysis created using TP-Fit (*described in text*).

2.3.1 Potential reference models

To estimate the significance of the forward model error $T_e \Delta\Theta(t)$ with respect to the measurement error ε_T, we computed several potentially true reference models (Figure 5A) and quantified their differences $\Delta\Theta$ to a standard reference model (Figure 5B). We chose a standard reference model that is based on the APCT geometry, a sediment thermal conductivity of 1.0 W/(m K), a volumetric heat capacity of 3.4 MJ/(m^3 K), and the assumption that the initial temperature distribution in the probe is homogeneous. Based on this model, other potentially true reference models were computed that are identical with the standard, except for one varied model parameter.

The first variation of the standard model, simulates a inhomogeneously initial temperature distribution that could be caused by frictional heating during the probe's insertion. The initial temperature distribution was modeled using a time dependent FE model of only the probe. This model was initialized with a homogeneous initial temperature of 0 °C and a constant inward directed heat flux through all boundaries (sediment/probe) was applying for 1 s. The resulting probe temperature distribution—normalized by the temperature at the sensor location—was then used as initial probe temperature distribution, simulating 1 s of frictional heating. In Figure 6 the resulting temperature distribution and its development during the decay is compared to the standard reference model. Additional variations of the standard reference model include models the simulation of 5 s of frictional heating, of a shift of the temperature sensor's location, of incorrectly estimated probe and sediment thermal properties, and of a time-shift. All model and their varied parameters are listed in Table 1 and a selection, as indicated in the table, is presented in Figure 5. For reference, Figure 5 also contains the reference model for the DVTP geometry and for the old 1-D APCT geometry which was used by the old TFit software.

2.3.2 Dependence of tool response from model parameters

Of the models shown in Figure 5 the old 1-D reference model used by TFit and the model for the DVTP deviate most from the standard APCT reference model. As expected, the temperature decay of the 1-D model is slower than of the 2-D model. In 1-D heat can only be transported in radial direction, whereas in the 2-D axisymmetric model, a major fraction of the heat additionally dissipates in z-direction (cf. Figure 6). The decay of the DVTP reference model, on the other hand, is faster than the decay of any of the APCT models. The favorable thermal response of the DVTP is due to its smaller diameter and the tapered tip.

Considering only the 2-D APCT models, most notable differences in respect to the standard reference model occur, when the initial temperature distribution is not homogeneous, but prescribed by simulated frictional heating of the probe. The average initial temperature of the heated probe models is greater than the initial temperature at the sensors location which is 1 by definition. Consequently, more excess heat is stored initially in the heated probes which takes longer to dissipate into the sediments.

Besides the influence of inhomogeneously distributed initial excess temperature, also the location of the sensor has a considerable influence on the decay curves. As expected, the temperature decays is faster when the sensor is shifted downward to the tip of the probe where a greater amount of heat can dissipate in z-direction (cf. Figure 6). On one hand, this result suggest that the response of the APCT probe can be slightly improved by shifting down the sensor as far to the tip as possible. On the other hand, extreme care has to be taken during probe construction and assembly that the temperature sensor is positioned at the same predetermined location for all tools to allow consistent measurements.

Comparing the effects of the sediment properties, the change in decay rate due to an change of the thermal conductivity k is four times as much as an equivalent (*von Herzen and Maxwell*, 1959) change in volumetric heat capacity ρC. Changing the thermal conductivity of the probe has almost no effect on the resulting decay. However, a change of the the probe's volumetric heat capacity changes the resulting decay curve, because a higher heat capacity results in a higher amount of excess heat in the probe at the same temperature difference between probe and formation. Introducing moderate shifting of the reference model with respect to results in large differences during early times of the decay. Later on, the shifted models behave very much as the reference curve.

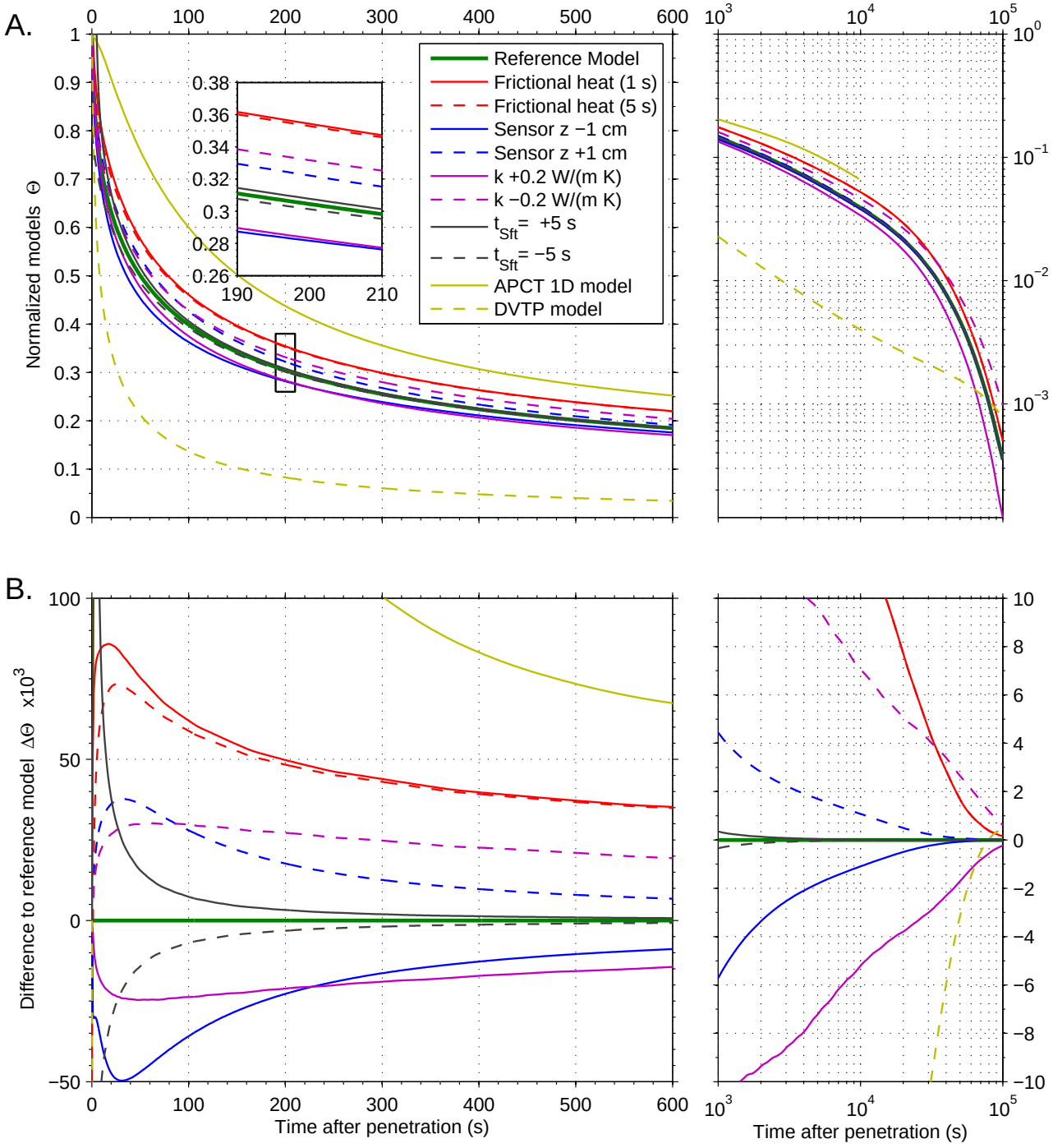

Figure 5: Comparison of normalized decay curves that simulate deviations from reference model assumptions with the reference model (bold green line). A. Black box marks the region of the decay curves that is enlarged in inset. B. Difference between the individual decay curves and the reference curve.

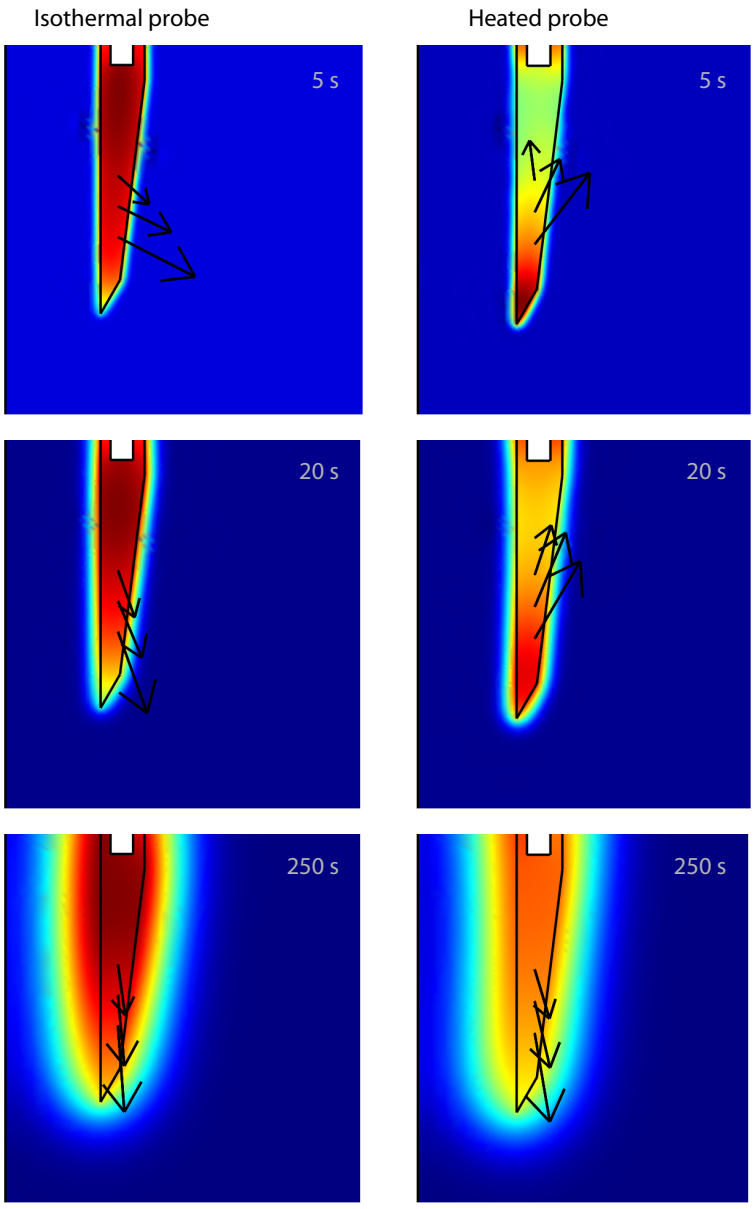

Figure 6: Different time steps of the reference model (left; green bold line in Fig. 5) and the model simulating frictional heating (right; red solid line in Fig. 5). Only part of the model domain is shown and the axes of symmetry are represented by the black lines at the right side of the models. Blue colors represent colder areas in the model domain and red colors warmer areas. Every solution does, however, use its own color map so that same colors in different solutions do not show the same temperatures. The arrows show the magnitude an the direction of the conductive heat flux at the location of the probes thermistor and 1 cm below (blue solid line in Fig. 5) and above (blue dashed line in Fig. 5) it. Again, the lengths of the arrows are scaled per solution an cannot be compared across different solutions.

2.3.3 Magnitude of model errors

It is known from tool calibrations that the accuracy of APCT-3 temperature measurements (ε_T) is in the order of 0.001 °C (*Heesemann et al.*, 2007) and from the history of APCT measurements that typical initial excess temperatures are in the order of 10 °C. Regarding the model errors, we found that $\Delta\Theta$ is in the order of 0.01–0.1 on the time scale of a typical APCT measurement (0 – 600 s). Consequently, the forward model error $T_e\,\Delta\Theta(t)$ is likely 2–3 orders in magnitude higher than the measurement error ε_T. Furthermore, $\Delta\Theta(t)$ is highly correlated and biased for all tested deviations from the standard reference model. Therefore we conclude, that using reference models $\tilde{\Theta}$ that deviate from the true reference model Θ to estimate undisturbed formation temperatures likely leads to systematically biased results.

3 Determination of the estimation error

Analyzing the algorithm to estimate undisturbed formation temperatures from transient downhole data, we found that the used forward models might differ substantially from the theoretically true model. Therefore, we examine the accuracy of the estimated formation temperatures in the second part of this study. Firstly, we quantify how errors in different reference model parameters and in assumptions affect the formation temperature estimate. In a second step, we study concurrent errors of several model parameters and their effect on the formation temperatures estimated with TP-Fit. For this purpose, we created synthetic data sets that combine the errors in several model parameters in a way that temperature measurements at different depths of a borehole are simulated. Synthetic data has the advantage that the true formation temperature is exactly known. On the other hand, it is uncertain how realistic synthetic data is. Therefore, at last, we analyze temperature data measured during IODP Expedition 316.

3.1 Estimation errors due to model uncertainty

To quantify the estimation error ΔT_f that is caused by reference model errors $\Delta\Theta$, we split $\Delta\Theta$ into a linear component and a remainder $\varepsilon_\Theta(t)$:

$$\Delta\Theta(t) = B_e\,\tilde{\Theta}(t) + B_f + \varepsilon_\Theta(t) \tag{4}$$

Here, as shown below, B_e and B_f are bias coefficients that represent the overestimation of T_e and T_f in fractions of T_e, respectively. Inserting the representation of $\Delta\Theta$ (4) into equation (3) it turns out that

$$\begin{aligned} T(t) \;=\; & (T_e + T_e\,B_e)\,\tilde{\Theta}(t) + \\ & (T_f + T_e\,B_f) + \\ & \varepsilon_T(t) + T_e\,\varepsilon_\Theta(t). \end{aligned} \tag{5}$$

Consequently, the linear regression of an estimated reference model $\tilde{\Theta}(t)$ and and the measured data $T(t)$, as performed in the data analysis, does not yield the true parameters T_e and T_f but the biased quantities

$$\tilde{T}_e = \; T_e + \Delta T_e = \; T_e + T_e B_e, \text{ and} \tag{6}$$

$$\tilde{T}_f = \; T_f + \Delta T_f = \; T_f + T_e B_f. \tag{7}$$

Here, ΔT_e and ΔT_f are the estimation errors of the initial excess temperature $\tilde{T}_e$ and the undisturbed formation temperature $\tilde{T}_f$ estimated using the regression, respectively. Accordingly, the estimation errors, which are caused by the reference model error, are proportional to the initial excess temperature T_e and the bias coefficients.

To study the systematic errors of the formation temperature estimates, which depend on $\Delta\Theta$, we compared several models Θ that differ only in one parameter from our estimated reference model $\tilde{\Theta}$ with the reference model and computed the factors B_f that determine the estimation error. Some of these models are shown in Figure 5 and the values B_f are listed in Table 1.

Having computed alternative basis model, the corresponding factors B_f that determine the error of the T_f estimate if data based on a alternative model would be analyzed with our reference model. Equation (4) suggests, that a linear regression of $\tilde{\Theta}$ and $\Delta\Theta$ yields B_f as axis intercept. This is illustrated for some models in Figure 7, where, for clarity, the linear regression is computed using only the end points of the time window ($\tilde{\Theta}(t_a)$ and $\tilde{\Theta}(t_b)$ that are marked by crosses. The graphical representation makes clear that the resulting B_f depends on the selected time window. In order to study, whether there is a optimal time-window, that reduces the magnitude of the B_f values for the most probable true reference models, B_f are computed for different window start locations (see Table 1). For all considered cases it appears that the formation temperature is either over- or underestimated, regardless of the choice of the start of the time window. However, estimation errors are systematically smaller for later window staring times.

Moreover, Figure 7 shows that the magnitude of the residual between data and model ε_Θ is not related to the uncertainty of the formation temperature estimate. The residuals for the models simulating frictional heat are the smallest of all shown models and the extrapolated formation temperatures are consistent over a large range of different time windows. Nevertheless, analysis of data based on these models with our standard reference model would result in a overestimation of T_f by $\sim 1.4\%$ of T_e.

3.2 Synthetic data

To estimate the errors of temperature measurements in a borehole, we setup synthetic measurements that simulate temperature data measured at different depth in a borehole (cf. Figure 8 and Table 2). The synthetic data is based on the assumption that the seafloor temperature and the borehole temperature T_b are 2°C and that the vertical temperature gradient within the formation is 0.05°C/m. These assumptions lead to the true formation temperatures T_f. Furthermore, we assume that the insertion process takes 4 s (-5 s to -1 s) during which frictional heating raises the temperature of the probe, due to the thermal constant of the probe, the maximum temperature is reached at t_0. We assumed that the minimum temperature increase due to frictional heating T_h is 5°C and that T_h increases by 0.07°C/m down the hole. An additional process that takes place during the probe insertion, is that the probe which we assume has a constant borehole temperature before the insertion process starts to equilibrate from the downhole temperature T_e to the formation temperature. Therefore our synthetic temperature data is calculated by

$$T(z,t) = T_h \Theta_2 + (T_b - T_f)\,\Theta_{14} + T_f, \qquad (8)$$

where $T_h = 0.07°\text{C/m}\,z + 5°\text{C}$ is the temperature increase due to frictional heating, $T_f = 0.05°\text{C/m}\,z + 7°\text{C}$ is the true undisturbed formation temperature and Θ_2 and Θ_{14} are the models that simulate the corresponding tool responses (cf. to Table 1 for numbers). Processing the synthetic data with our reference model the expected estimation error is

$$\Delta T_f = T_h B_{f,2} + (T_b - T_f)\,B_{f,14}, \qquad (9)$$

where $B_{f,2}$ and , $B_{f,14}$ are the B_f values for the model with 5 s of frictional heating and the model with a time-shift of -5 s, respectively. The asterisks in Figure 9 show, that the error estimation using the B_f values returns similar results as the actual analysis of the synthetic data with TP-Fit, using the standard model parameters and and $t_{Sft} = 0$ s. The errors calculated using the B_f values for early starts t_a of the time window are slightly increased, compared to the TP-Fit results, because the B_f values have been calculated using only two points in the linear regression (Figure 7). TP-Fit on the other hand uses all temperature data, sampled at a constant rate, for the linear regression. Therefore, a regression of Θ and T leads automatically to a stronger weight of the later part of the time window, since the decay Θ slows down and smaller values of Θ are consequently supported by more $T(t)$ data.

Furthermore, it appears, that for the simulated data, there are no simple guidelines, for selecting a time-window or the right analysis parameter combination. In average, all estimated formation temperatures are higher than the true formation temperature, regardless of the sediment thermal conductivity, time-shift, or time-window used for the data analysis. Smallest errors were achieved with a reduced sediment thermal conductivity of the reference models compared to the true sediment property, $t_{Sft} = 0$ s, and a large time-window. Notably, choosing a reference models with a underestimated sediment thermal conductivity, the estimates with $t_{Sft} = 0$ s are much closer to the truth than estimates with the time-shift the minimizes the residual ε between model and data.

3.3 Measured data

Ultimately, the data analysis has to be tested using measured data. However, the problem with measured data is, that the true T_f is generally unknown and that model parameters, e.g. as the sediment thermal properties and the initial temperature distribution of the probe, can only be estimated. During IODP Expedition 316, there were a few measurements at Hole C0008A that did not suffer so much from these general problems with measured data. At this site, several fortunate circumstances came together. Firstly, even tough there were only three measurements with excellent data quality (*Kimura et al.*, 2008), the temperature data included many constraints, that defined the temperature gradient at the Site very precisely.

Furthermore, one of the measurements with excellent data quality, contains a undisturbed decay which is almost 2 h long, i.e. it is $\sim$12 times as long as the decay of a regular temperature measurement. This measurement gives the opportunity to only use the

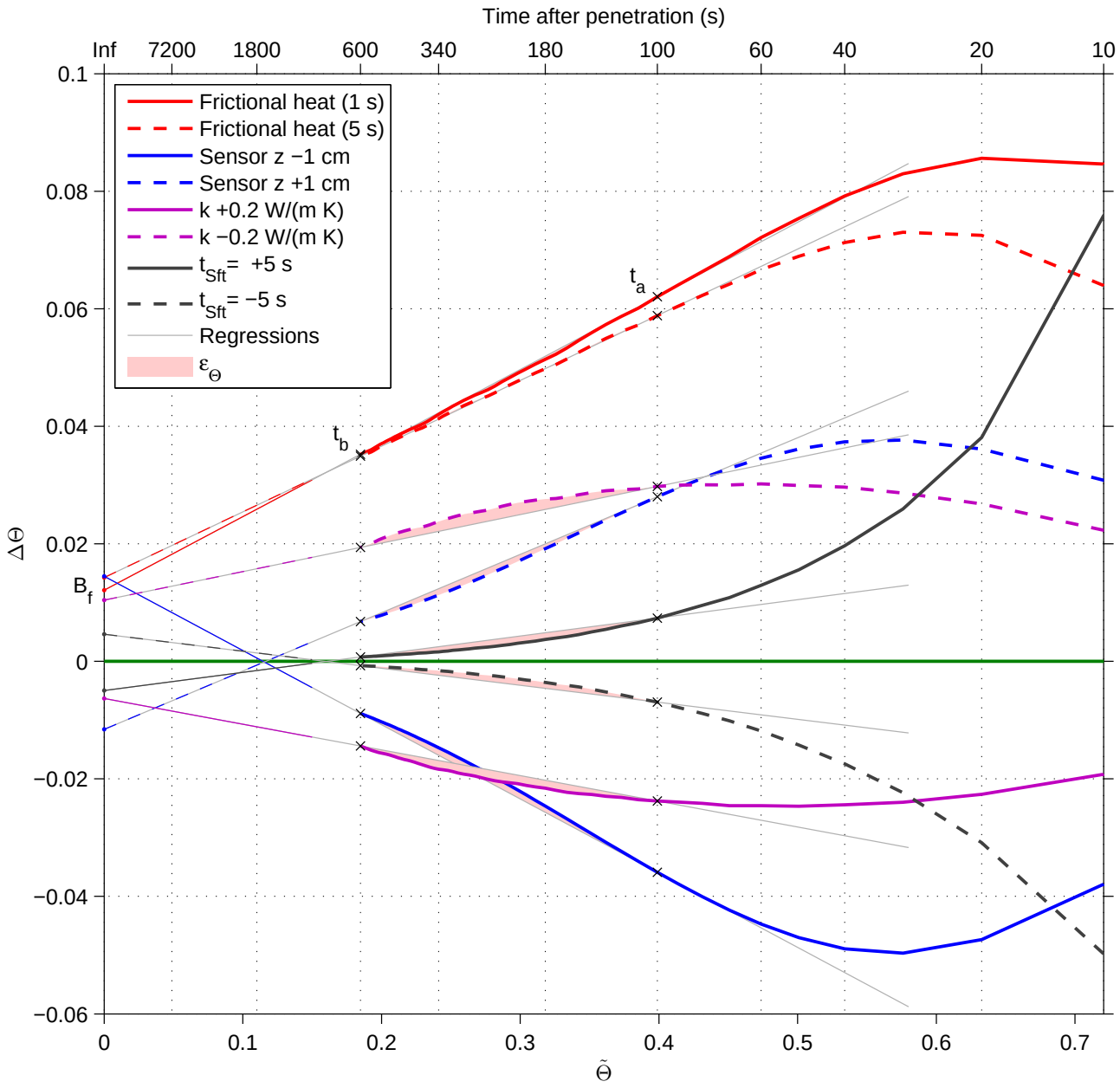

Figure 7: Linear regressions of the estimated reference model $\tilde{\Theta}$ and differences of other potential base models $\Delta\Theta$ yield B_f factors that determine the estimation errors ΔT_f that would occur when analyzing data based on one of the other base models.

Table 1: $B_f \times 10^2$ (i.e. estimate error in $\%(T_e)$) for different start points (t_a) of the time window. The time window ends always at 600 s. Bold and italic values show time windows with minimal and maximal estimation errors, respectively.

		$B_f \times 10^2$ for t_a (s)				
#	Model variation	40	60	100	180	340
1	Frictional heating 1 s*	1.20	**1.17**	1.21	1.29	*1.30*
2	Frictional heating 5 s*	*1.57*	1.46	1.43	1.43	**1.40**
3	Sensor z location -1 cm*	1.23	1.41	*1.45*	1.30	**1.02**
4	Sensor z location $+1$ cm*	-0.94	-1.10	*-1.16*	-1.04	**-0.80**
5	Sediment k $+0.2$ W/(m K)*	*-0.91*	-0.79	-0.63	-0.45	**-0.15**
6	Sediment k -0.2 W/(m K)*	*1.39*	1.25	1.04	0.80	**0.50**
7	Sediment ρC $+0.2$ MJ/(m^3 K)	*-0.30*	-0.27	-0.23	-0.18	**-0.15**
8	Sediment ρC -0.2 MJ/(m^3 K)	*0.34*	0.30	0.26	0.21	**0.18**
9	Probe k $+2$ W/(m K)	0.03	*0.04*	0.04	**0.03**	0.03
10	Probe k -2 W/(m K)	0.02	*0.03*	0.02	0.01	**0.00**
11	Probe ρC $+0.2$ MJ/(m^3 K)	*0.61*	0.56	0.47	0.37	**0.26**
12	Probe ρC -0.2 MJ/(m^3 K)	*-0.55*	-0.47	-0.39	-0.29	**-0.19**
13	$t_{Sft} = +5$ s*	*-0.93*	-0.71	-0.50	-0.34	**-0.21**
14	$t_{Sft} = -5$ s*	*0.81*	0.64	0.46	0.32	**0.21**

*Shown in Figure 5 and 7

Table 2: Analysis of synthetic and measured data using different analysis parameters.

							ΔT_f (t_a=60 s, t_b=600 s)				
z	T_f	T_b	T_0	T_e	T_h	T_b-T_f	[1]B_f	[2]Ref	[3]t_{Sft}	[4]ρC	[5]1-D
m bsf	°C	°C	°C	°C	°C	°C	°C	°C	°C	°C	°C
Synthetic data											
50.0	4.50	2.00	10.69	6.19	8.50	-2.50	0.11	0.10	0.11	0.05	0.19
100.0	7.00	2.00	14.57	7.57	12.00	-5.00	0.14	0.14	0.16	0.08	0.26
150.0	9.50	2.00	18.45	8.95	15.50	-7.50	0.18	0.17	0.21	0.11	0.33
200.0	12.00	2.00	22.33	10.33	19.00	-10.00	0.21	0.20	0.25	0.15	0.40
250.0	14.50	2.00	26.21	11.71	22.50	-12.50	0.25	0.24	0.30	0.18	0.47
300.0	17.00	2.00	30.09	13.09	26.00	-15.00	0.28	0.27	0.34	0.21	0.54
Measured data											
†53.50	4.74	4.79	16.76	12.02	11.98	0.05	0.18	-0.43	-0.06	0.00	0.35
†152.70	9.86	8.50	20.94	11.08	12.16	-1.36	0.17	-0.89	-0.78	-0.65	-0.10
200.90	12.29	16.10	28.71	16.42	13.39	3.81	0.22	0.14	0.48	0.53	0.84

[1]Estimated using B_f values and equation (9)

[2]Analysis with reference model (no time-shift, correct sediment properties)

[3]Analysis with model using time-shift and correct sediment properties

[4]Analysis with model using time-shift, and variable sediment properties

[5]Analysis with old 1-D model (using time-shift, and correct sediment properties)

†t_b reduced due to missing data.

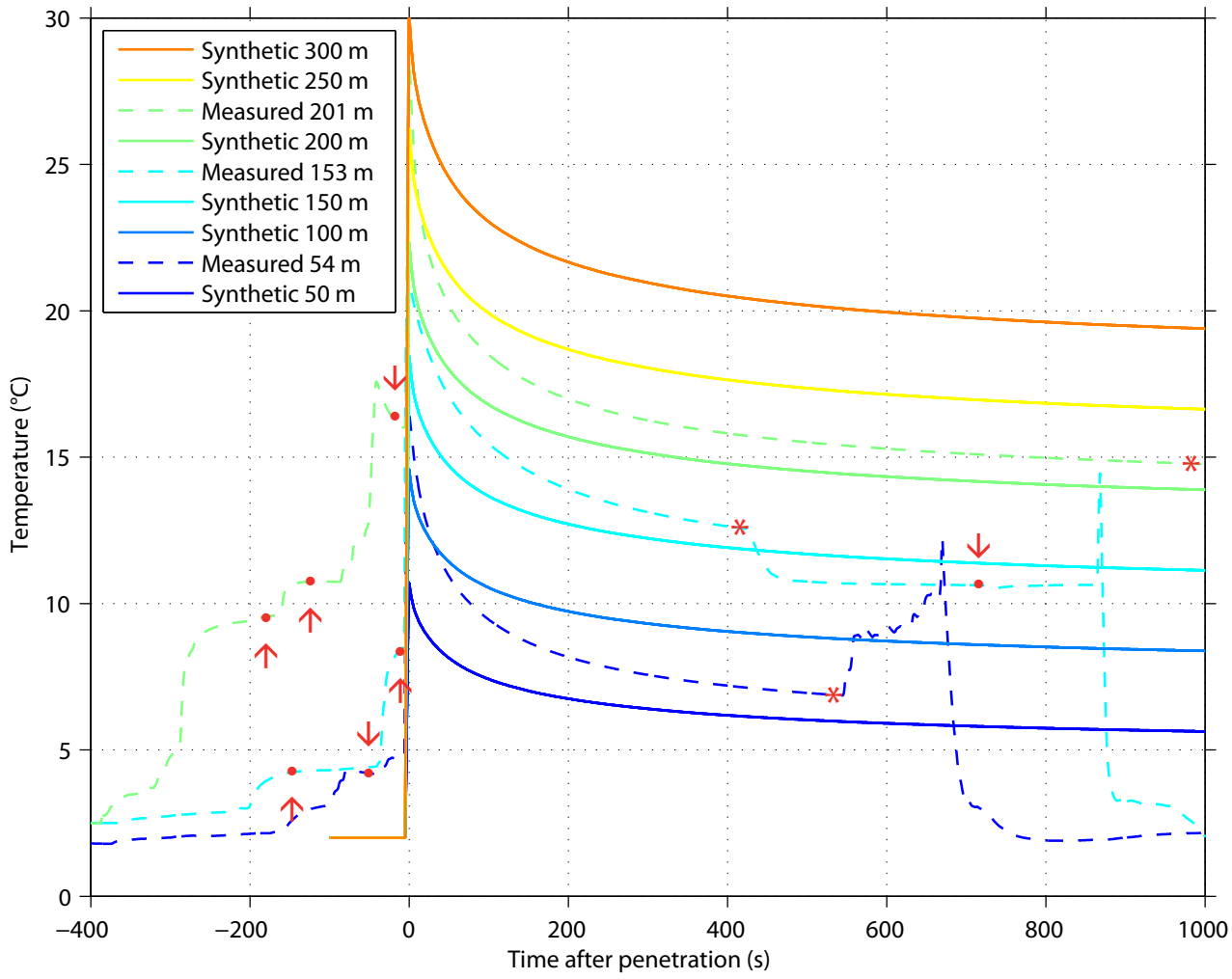

Figure 8: Data synthetic data (solid lines) simulating several measurements in one borehole and data measured during IODP Expedition 316 (dashed lines). Temperatures at the end of the temperature transients are marked by asterisks. Additional constraints data (dots) provide upper (downward pointing arrow) and lower (upward pointing arrow) limits for possible undisturbed formation temperatures.

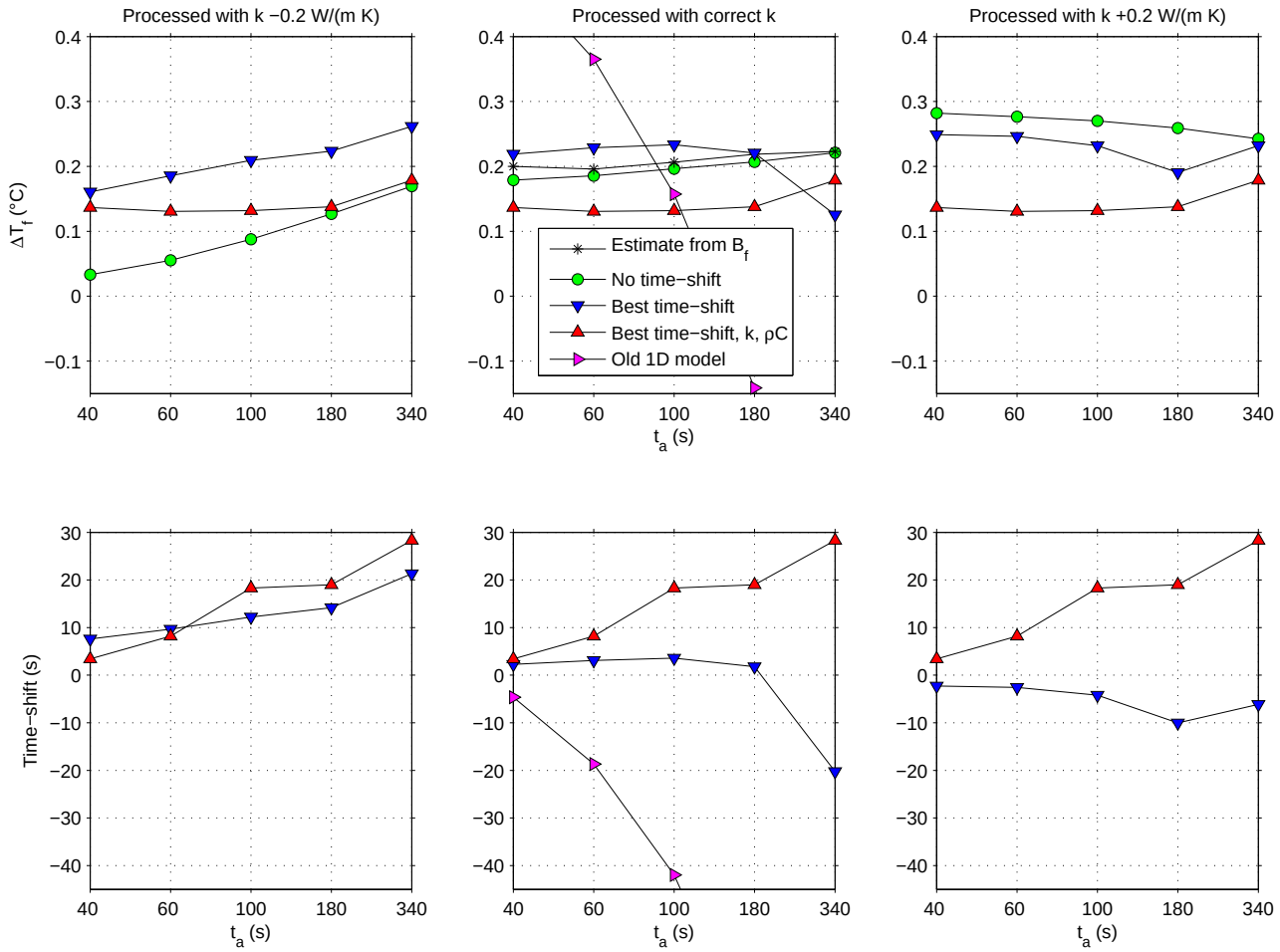

Figure 9: Analysis of synthetic borehole data with different parameters. Symbols show mean values of estimation error ΔT_f and the time-shift over all measurements. The data was analyzed with time windows starting at different t_a end always ending at $t_b = 600$ s. Circles show analysis with different thermal conductivities (k =0.8, 1.0, and 1.2 W/(m K)) and no time-shift, stars mark the estimation error computed using (9). Downward pointing triangles show the analysis with the same thermal properties, but with the time-shift that leads to the smallest misfit between model and data. Upward pointing triangles show the results for the reference curves with the sediment thermal parameters (in the ranges k =0.5–2.5 W/(m K) and ρC =2.3–4.3 MJ/(m^3 K)) and time-shifts that lead to the smallest misfit between model and data. Consequently, the upward pointing triangles are the same in all three columns and the residuals are smaller than the residual related to the analysis marked by the downward pointing triangles, which again are smaller than the residuals of the analysis without time-shift.

first part of the decay for the analysis and compare the rest of the data with the modeled results.

3.3.1 Constraints

Sometimes the temperature time series contain not only the primary equilibration, but also secondary equilibration curves. These secondary signals can often not be compared to the reference models, but they can provide upper or lower bounds of the actual formation temperature (cf. Figure 8). A the last temperature reading of a regular decay for example provides a upper limit for the formation temperature, because we can assume that if the probe is situated in the formation and does not move for several tenths of seconds, a steady temperature decrease can only be cause by a formation that is colder as the probe itself, and vice versa. As shown in Figure 8, situations that cause temperature data useful for deriving these constraints may occur before the probe is actually fired into the formation or during disturbances, during the main decay. If these constraints are measured just below the bottom of the hole, before the APCT is pushed completely into the formation, one has to consider that the constraints refer to the depth at the top of the core and not to the bottom of the core as the main decay. Assuming, a monotonic increase of sediment thermal conductivity with depth, purely conductive steady state heat transport, and only thermal conductivity values in the range of 0.7 to 1.2 W/(m K) these constraints allow to determine formation temperatures within an uncertainty of $\pm 0.25\,^{\circ}$C in Hole C0008A.

3.3.2 Results

The formation temperatures estimated from the three data sets with excellent data quality estimated using TP-Fit and different parameters are shown in Figure 10 along with the formation temperature depth profile estimated from independent constraints. Differences between these values are listed in to lower part of Table 2.

As with the synthetic borehole data, formation temperatures estimated with the reference model have smaller values than estimates that use the same model but include a time-shift, which still have smaller values that the estimates using the old 1-D model with time-shift. With the measured data, it is however not so so clear, which approach provides more accurate results. Every approach performs different at each of the three measurements. It also appears that the true measurements are not a simple superposition of the two reference models used in equation (8), since computed error estimates based on B_f values (9), as for the synthetic data, by estimating the temperature increase due to frictional heating

$$T_h = T_0 - (T_b - T_f)\,\Theta_{14}(t_0) - T_f, \qquad (10)$$

where $T_0 = T(t_0)$, does not provide good estimates for the error of the results with the standard model for the measurements at 54 and 153 mbsf.

4 Conclusions

After decades of measuring transient temperature data using downhole tools and extrapolating this data to undisturbed formation temperatures, we studied for the first time the reliability of the extrapolated results in a systematic manner. On one hand, we found that the extrapolated results are by an order in magnitude closer to the true formation temperature than the last reading of a regular decay measurement. On the other hand, it turned out that one of the basic assumptions made by the data analysis algorithm, that a good fit between the reference model and measured data leads to a good formation temperature estimates, is not true. Admittedly, the true reference model, which is unknown, leads to the right formation temperature estimate and minimizes the data misfit at the same time. However, there are reference models—indistinguishable from the true reference model—that lead to wrong formation temperature estimates and have the same small data misfit as the true reference model. This is due to correlated errors between the estimated forward model and the data caused by choosing an incorrect reference model, as we could show in theory.

Our numeric studies showed that choosing wrong model parameters for the reference model, leads in most cases to wrong formation temperature estimates and to correlated residuals between the forward model an the measured data. However, choosing a homogeneous initial temperature distribution in the probe for the reference model, and analyzing data from a probe having a inhomogeneous initial temperature distribution, which could be caused by frictional heating, leads to very small and almost uncorrelated residuals, while the undisturbed formation temperature is systematically overestimated (cf. Figures 5 and 7).

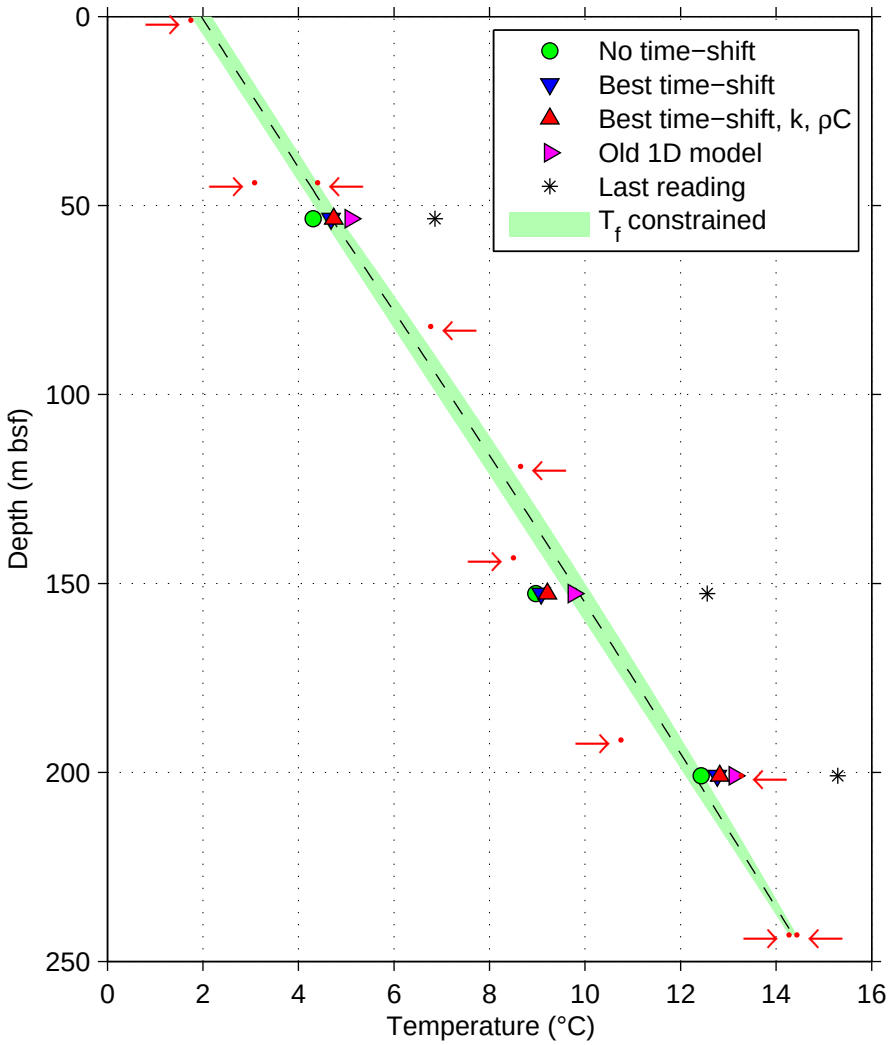

Figure 10: Measured data processed with TP-Fit using different parameters. All extrapolated values are closer to the formation temperature (green region) estimated by constraints (red dots and arrows) than the last temperature readings of the main decays (asterisks). Measurements at ∼150 m are made in gas hydrate bearing sediments.

Also analyzing real measurements, we found that minimizing the residuals between model and data, by introducing a time-shift or changing the other model parameters, does not necessarily lead to better formation temperature estimates. Therefore, the selection of the parameters for the reference model should only depend on independent information as measurements of sediment thermal properties and not on the residuals between forward model and data. Specifically, for the time-shift parameter this means that it should only be used if physically motivated or if empirical studies using actual measurements show, that a certain time shift generally results in more accurate formation temperature results. In these cases, the time shift should be fixed to these findings and not variated in order to reduce the misfit between the model and the data.

Similar considerations as for choosing the right parameters for the reference model are also true for choosing the right time window for the data analysis. The estimated formation temperature often changes with the selected time window. This shows that the reference model does not fit the data well. If the estimate is independent of the chosen time window, does however not guarantee that the estimate is right. As shown in Figure 7, it is also not guaranteed the true formation temperature is in the range of estimates that is possible with any time window. Generally, it is a good choice to select the end of the time window as late as possible, since the measured temperature has approached T_f as closely as possible. On the other hand, doubling the standard measurement time of 10 min, would not increase the accuracy of the results substantially, since the temperature decay slows down with time. The window should start some time after t_0 since deviations of the used reference model $\Theta(t)$ from the true reference model get most likely smaller with increasing time. The linear regression between the reference decay and the data weights later times of the decay automatically, since the equidistant sampling of data in time leads to increasing sampling rates for lower parts of the decay on the decay scale. Since we found that it is impossible to define a optimum start of a time window for all measurements, our (somewhat arbitrary) recommendation is to use a fixed window starting time of 60 s after the probe penetration is completed.

Regarding the accuracy of the estimated formation temperatures, our numerical experiments showed, that one should expect at least uncertainties of $\sim$1.5% of the initial excess temperature if one parameter of the reference model is not chosen right. This means an uncertainty of $\pm 0.15\,^{\circ}$C for a measurement in a formation with 10 °C and a probe temperature of 20 °C immedeately after insertion. Simulated borehole data showed that these uncertainties can add up if different model parameters are not estimated right and that also the difference between the formation temperature and the borehole temperature can play an important role of the scaling of the extrapolation uncertainty. For the simulated data, we found extrapolation errors up to $\pm 0.3\,^{\circ}$C. All formation temperatures were overestimated and the error increased systematically with increasing depth below seafloor. This means that a geothermal gradient based on the synthetic measurements would have been systematically biased. But the error of less than 1 mK/m would have been relatively small compared to a common geothermal gradient.

The shallower two of the three temperature measurements at IODP Hole C0008A we analyzed showed unexpectedly high estimation errors up to $-0.9\,^{\circ}$C with our reference model. And against the theoretical considerations, the formation temperatures were underestimated. Therefore it is possible that estimation error of $\pm 1\,^{\circ}$C are common with APCT data. On the other hand, the errors may be due to the presence of gas hydrates that have been found at Site C0008. In Hole C0008A, *Kimura et al.* (2008) found evidence for gas hydrate close to the measurement with the highest estimation error at 153 mbsf by detecting Cl minima at $\sim$120 and 136 mbsf and a maximum in methane concentrations at $\sim$140 mbsf.

With the current APCT tools and todays analysis methods it is possible to obtain important and useful information about the formation temperature by sacrificing only a minimal amount of extra ship time. The accuracy of the results is high enough to answer many scientific questions, e.g. about the local heatflux our gas hydrate stability field, especially if individual measurements can be combined by the assumption of steady state conductive heat transport in the formation and measurements of sediment thermal conductivities, as we were able to show for the data measured in Hole C0008A. We found, however, that the absolute accuracy of the undisturbed formation temperature estimates is most likely considerably worse than $\pm 0.1\,^{\circ}$C, which it was prior to this often considered to be. If the accuracy provided by APCT measurements is not sufficient, e.g. one wants to quantify the disturbance of the geothermal gradient by fluid advection, additional measurements with

probes, as the DVTP, specifically designed to measure temperatures are necessary. As seen in Figure 5, the DVTP, due to its optimized geometry, responds much faster and the DVTP approaches the true formation temperature as close in about 2 minutes as the APCT does in 2 hours.

As seen in Hole C0008A, additional constraints that are contained in the temperature records can add to the information about the true formation temperature as much as the main decays can, if the temperature information is combined in a suitable way. These additional constraints have mostly been neglected and were not recorded in a systematical manner.

We found that much of the uncertainty in extrapolation transient downhole temperature data is due to the unknown initial temperature distribution in the probe. One way to reduce this errors, future temperature probes should be equipped with with several temperature sensors at different locations. An enhanced analysis algorithm that takes all temperature measurements into account for the inversion, would have the potential to increase the accuracy of the temperature estimates considerably. Furthermore, the use of additional temperature constraints could be facilitated by adding for example acceleration sensors to the probe. Using these sensor it would be possible to distinguish whether a temperature increase, before firing the probe completely into the formation, is caused by steady sliding of the probe into the formation or by a formation temperature that is higher than the temperature of the probe.

Using the data from Hole C0008A it was not possible to decide whether an uncertainty of $\sim$0.3 °C or $\sim$1 °C is typical for extrapolated temperatures of APCT-3 data. It is clear that the higher uncertainties should be expected at the presence of gas hydrates. Further evaluations of the estimation errors could be conducted by comparing APCT-3 measurements with properly calibrated DVTP measurements at nearly the same locations in the formation.

Notation

Times (s)

t	Time after insertion ($t_0 = 0$ s) of the probe
t_0	Time when probe insertion is completed (0 s)
t_a, t_b	Start and end of the time window that is used for the data analysis
t_{Sft}	Amount of time by which a reference model is shifted when compared to measured data ($\Theta_{Sft} = \Theta(t - t_{Sft})$

Temperatures (°C)

T	Temperature at the location of the temperature sensor
T_0	$T(t_0)$
T_b	Temperature of the open borehole and the tool before it is inserted
T_e	Initial excess temperature ($T(t_0) - T_f$)
$\tilde{T}_e$	Estimated initial excess temperature ($T_e + \Delta T_e$)
ΔT_e	Estimation error of initial excess temperature
T_f	Undisturbed formation temperature
$\tilde{T}_f$	Estimated undisturbed formation temperature ($T_f + \Delta T_f$)
ΔT_f	Estimation error of undisturbed formation temperature
T_h	Probe temperature increase during insertion due to frictional heating

Physical properties

k	Thermal conductivity (W/(m K))
ρC	Volumetric heat capacity (J/(m^3 K))

Normalized reference models

Θ	True normalized forward model (i.e. equation (2) is valid)
$\tilde{\Theta}$	Estimated normalized forward model that is used in the actual data analysis
$\Delta\Theta$	Reference model error $\Theta - \tilde{\Theta}$
Θ_{Sft}	New model derived from a basis Θ by shifting in respect to time ($\Theta_{Sft}(t) = \Theta(t - t_{Sft})$)
$\Theta_{\#}$	A specific reference model where # refers to the model number in Table 1

Residuals

ε	Residual (°C) of data and forward model which is minimized during inversion
ε_T	Residual (°C) due to errors in measured temperature data ($\approx \varepsilon$ if $\tilde{\Theta} = \Theta$)
ε_Θ	Residual (dimensionless fraction of T_e) due to estimation error of reference model ($\approx \varepsilon$ for real analyses)

Bias coefficients (Dimensionless fraction of T_e)

B_e	Overestimation of T_e due to estimation error of the reference model
B_f	Overestimation of T_f due to estimation error of the reference model
$B_f, \#$	B_f with respect to model # in Table 1

Acknowledgments

Many thanks to Robert Harris and the IODP Expedition 316 scientific party for generously providing the APCT-3 raw data.

References

Braccini, S., C. Casciano, F. Cordero, F. Corvace, M. de Sanctis, R. Franco, F. Frasconi, E. Majorana, R. Passaquieti, G. Paparo, P. Rapagnani, F. Ricci, A. Solina, and R. Valentini (2000), The Maraging Steel Blades of the Virgo Superattenuator, *Meas. Sci. Tech.*, *523*, 467–476, doi: 10.1063/1.1291904.

Bullard, E. (1954), The flow of heat through the floor of the Atlantic Ocean, in *Proc. Royal Soc. Lond*, *A*, vol. 222, pp. 408–429.

Davis, E. E., H. Villinger, R. D. MacDonald, R. D. Meldrum, and J. Grigel (1997), A robust rapid-response probe for measuring bottom-hole temperatures in deep-ocean boreholes, *Marine Geophys. Res.*, *19*, 267–281, doi: 10.1023/A:1004292930361.

Erikson, A., R. von Herzen, J. Sclater, R. Girdler, B. Marshall, and R. Hyndman (1975), Geothermal measurements in deep-sea drill holes, *J. Geophys. Res.*, *80*, 2515–2528.

Fisher, A. T., and M. W. Hounslow (1990), Heat flow through the toe of the Barbados accretionary complex, in *Proceedings of the Ocean Drilling Program; Barbados Ridge; covering Leg 110 of the cruises of the drilling vessel JOIDES Resolution,Bridgetown, Barbados to Bridgetown, Barbados, sites 671-676, 19 June1986-16 August 1986*, vol. 110, edited by A. Mascle, J. C. Moore, E. Taylor, F. Alvarez, P. Andreieff, R. Barnes, C. Beck, J. H. Behrmann, G. Blanc, K. M. Brown, M. W. Clark, J. F. Dolan, A. T. Fisher, J. M. Gieskes, M. W. Hounslow, P. McLellan, K. Moran, Y. Ogawa, T. Sakai, J. Schoonmaker, P. J. Vrolijk, R. Wilkens, C. Williams, and W. R. Winkler, pp. 345–363, Texas A & M University, Ocean Drilling Program, College Station, TX, doi: 10.2973/odp.proc.sr.110.154.1990.

Hartmann, A., and H. Villinger (2002), Inversion of marine heat flow measurements by expansion of the temperature decay function, *Geophysical Journal International*, *148*(3), 628–636.

Heesemann, M. (2008), TP-Fit Version 1.0, a free software package to estimate undisturbed formation temperatures from downhole tool measurements, http://tp-fit.sourceforge.net/.

Heesemann, M., H. Villinger, A. T. Fisher, A. M. Tréhu, and S. Witte (2007), Testing and deployment of the new APCT-3 tool to determine insitu temperatures while piston coring, in *Expedition Reports*, *Proceedings of the Integrated Ocean Drilling Program*, vol. 311, doi: 10.2204/iodp.proc.311.108.2006.

Horai, K. (1985), A theory of processing down-hole temperature data taken by the Hydraulic Piston Corer (HPC) of the DSDP, *Tech. rep.*, Lamont-Doherty Geological Observatory, Palisades, NY.

Horai, K., and R. P. Von Herzen (1985), Measurement of heat flow on Leg 86 of the Deep Sea Drilling Project, *Initial reports of the Deep Sea Drilling Project covering Leg 86 of the cruises of the Drilling Vessel Glomar Challenger, Honolulu, Hawaii, to Yokohama, Japan, May-June 1982*, *86*, 759–777, geoRef ID: 1986-018136.

Hyndman, R., M. Langseth, and R. von Herzen (1987), Deep sea drilling project geothermal measurements: a review, *Rev. Geophys*, *25*, 1563–1582,, i do not have this one.

Hyndman, R. D., E. E. Davis, and J. A. Wright (1979), The measurement of marine geothermal heat flow by a multipenetration probe with digital acoustic telemetry and insitu thermal conductivity, *Marine Geophysical Researches*, *4*(2), 181–205.

Kappel, E., and J. Adams (2001), *Earth, oceans and life; IODP Initial Science Plan*, International Working Group Support Office.

Kimura, G., E. J. Screaton, D. Curewitz, , and the Expedition 316 Scientists (2008), Expedition 316 preliminary report nantroseize stage 1a: Nantroseize shallow megasplay and frontal thrusts, *Tech. rep.*, Integrated Ocean Drilling Program Management International, Inc., doi: 10.2204/iodp.pr.316.2008.

Pribnow, D., M. Kinoshita, and C. Stein (2000), Thermal data collection and heat flow recalcu-

lations for ODP Legs 101-180, *Tech. rep.*, Institute for Joint Geoscientific Research, Institute for Joint Geoscientific Research, GGA, Hannover, Germany, 0120432.

Stein, C. A., and S. Stein (1992), A model for the global variation in oceanic depth and heat flow with lithospheric age, *Nature*, *359*(6391), 123–129.

Taylor, B., P. Huchon, A. Klaus, and Shipboard Scientific Party (1999), Explanatory notes, in *Proc. ODP, Init. Repts.*, vol. 180, edited by B. Taylor, P. Huchon, A. Klaus, and et al., pp. 1–75, College Station, TX (Ocean Drilling Program), doi: 10.2973/odp.proc.ir.180.104.2000.

Uyeda, S., and K. Horai (1982), Heat flow measurements on Deep Sea Drilling Project Leg 60, in *DSDP Initial Reports*, vol. LX, doi: 10.2973/dsdp.proc.60.146.1982.

Villinger, H., and E. E. Davis (1987), A new reduction algorithm for marine heat flow measurements, *J. Geophys. Res.*, *92*, 12,846–12,856.

von Herzen, R., and M. E. Maxwell (1959), The measurement of thermal conductivity of deep sea sediments by a needle probe method, *J. Geophys. Res.*, *64*, 1557–1563.

von Herzen, R. P., and A. E. Maxwell (1964), Measurement of heat flow at the preliminary Mohole Site off Mexico, *J. Geophys. Res.*, *69*, 741–748.

A Thermal properties of marine sediments

A.

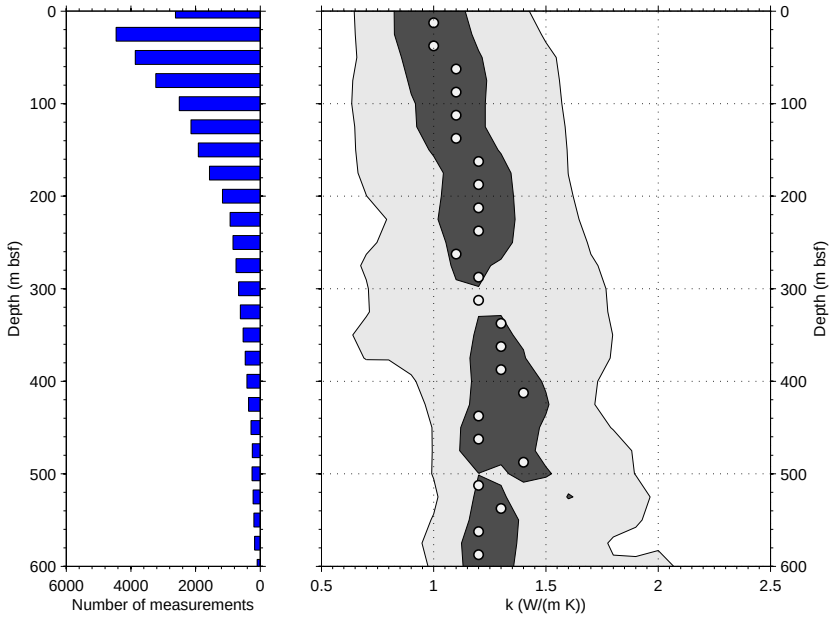

B.

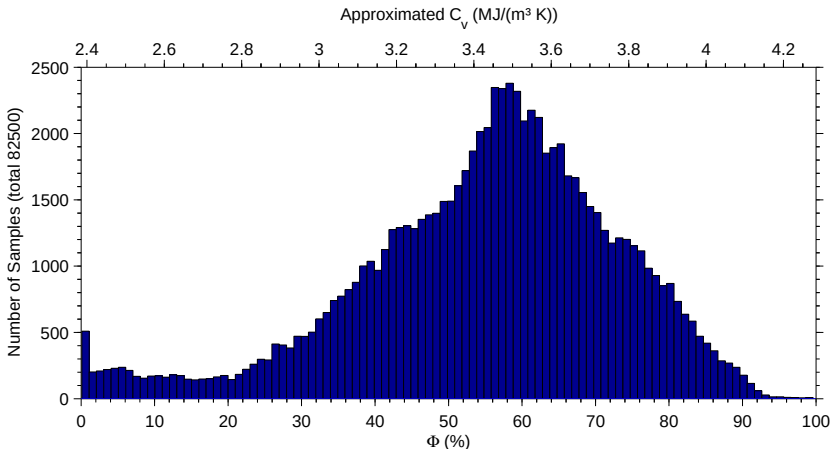

Figure 11: A. Thermal conductivities based on data from *Pribnow et al.* (2000). B. Heat capacities based on ODP moisture density data.

B Thermal response of formation to open hole

Half-space cooling model e.g. *Stein and Stein* (1992).

$$\Delta T = (T_f - T_b)\,\mathrm{erfc}(z/\sqrt{4\kappa t}) \tag{11}$$

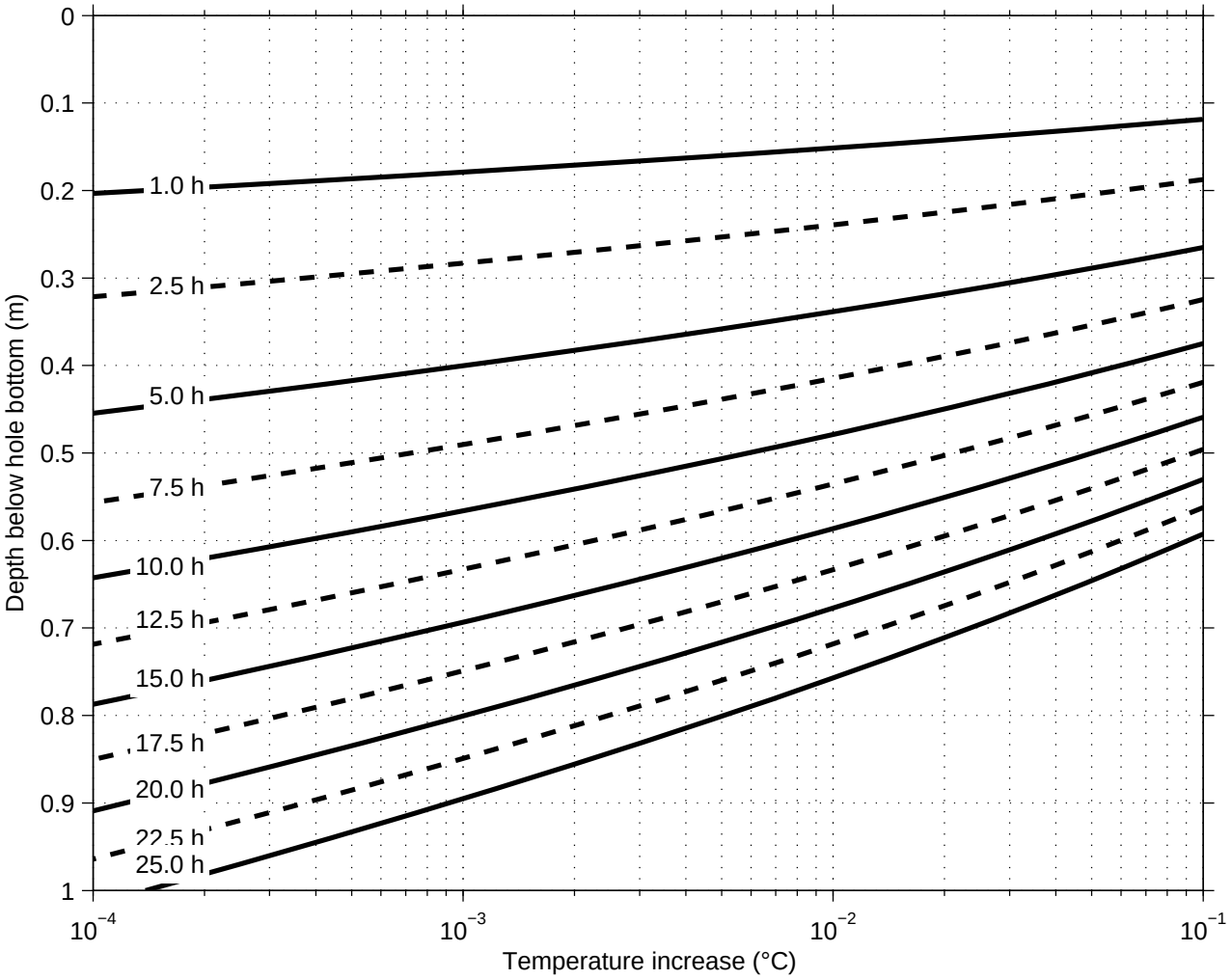

Figure 12: Response of formation ($T_f = 10\,^{\circ}\mathrm{C}$) to open borehole ($T_b = 0\,^{\circ}\mathrm{C}$). Similar plot in *Fisher and Hounslow* (1990)

Software: TP-Fit Version 1.0, a free software package to estimate undisturbed formation temperatures from downhole tool measurements

Heesemann, M. (2008), TP-Fit Version 1.0, a free software package to estimate undisturbed formation temperatures from downhole tool measurements, http://tp-fit.sourceforge.net/.

Contributions

Existing software packages to extrapolate undisturbed formation temperatures from transient downhole measurements were not capable to process data recorded by the APCT-3 tool, because of is increased sampling rate and the new data format. In the following section, a new software application, implemented in Matlab®, is described which is capable to process the data of all versions of the APCT tool (cf. *Heesemann et al.*, 2007, for a history of APCT tools) and the DVTP tool. It includes reference models (cf. *Heesemann et al.*, in prep. 2008a) for the APCT and DVTP, that reflect the geometry of the probes better than reference models used by prior software packages. Moreover, the new software contains a graphical user interface that simplifies the data analysis compared to previous software packages.

Martin Heesemann designed, implemented, and tested TP-Fit. The Integrated Ocean Drilling Program US Implementing Organization (IODP-USIO) funded the development of additional features of TP-Fit that improve the integration in shipboard work and data flow. The design of TP-Fit benefited from many constructive comments of users—e.g. Andrew T. Fisher, Heinrich Villinger, Anne M. Tréhu, Friederike Schmidt-Schierhorn, and Peter Blum and Paul Foster from the IODP-USIO—testing early versions of TP-Fit. TP-Fit is free software and can be redistributed under the conditions of the GNU General Public License Version 3.

TP-Fit Version 1.0

A free software package to estimate undisturbed formation temperatures from downhole tool measurements

Martin Heesemann

Department of Geosciences, University of Bremen, Bremen, Germany.

TP-Fit is a software package with a graphical interface that guides its users through the required steps to extrapolate undisturbed formation temperatures from transient downhole tool responses. The individual steps of the data analysis algorithm, as described by *Heesemann et al.* (in prep. 2008), are carried out by sequentially clicking the buttons of main menu bar (cf. Figure 1 (left)):

1. Determination of realistic parameters for the reference model $\Theta(t)$.
   - The correct reference model is determined automatically, depending on the format of the imported data file.
   - Measured or estimated sediment thermal conductivity k and volumetric heat capacity ρC can be supplied along with various metadata (Figure 1 (right)).
2. Selection of the time t_0, when the tool insertion process is completed.
   - t_0 can be selected in the pick-window where it is marked by a dashed line (Figure 2).
3. Selection of the time-window (white area in Figure 2 and 3) which is bounded by the window start t_a, marked by an upward pointing triangle, and the window end t_b, marked by a downward pointing triangle in Figure 3.
   - t_a and t_b can be selected in the pick-window (Figure 2).
   - The plot of the temperature variation with time helps to detect disturbances.
4. Determination of the time-shift t_{Sft}, for which the linear regression between the reference model shifted in respect to time $\Theta(t - t_{Sft})$ and the measured data results in the smallest misfit (Figure 3).
   - The time-shift that leads to the smallest misfit is automatically computed when the results are viewed with „Show Fit“.

5. Report of the T_f resulting from the model with the smallest misfit (Figure 3).
    - Results can be exported graphically, in ASCII format, and as session file that stores all information for quality control and refinements of the results, later on.
6. Optionally, repeat steps with different reference model parameters.
    - Model parameters k and ρC may conveniently modified by clicking into one of the plots in the „Contours“ window (Figure 4).
    - The „Results“ window will update automatically when parameters are changed.
    - The „Contours“ window displays the dependency of the results (e.g. undisturbed temperature estimate in the second plot) from the model parameters k and ρC.

References

Heesemann, M., A. T. Fisher, and H. Villinger (2008), Estimation of in-situ formation temperatures from transient tool response in unconsolidated sediments during piston coring, *Geochem. Geophys. Geosyst.*, in prep.

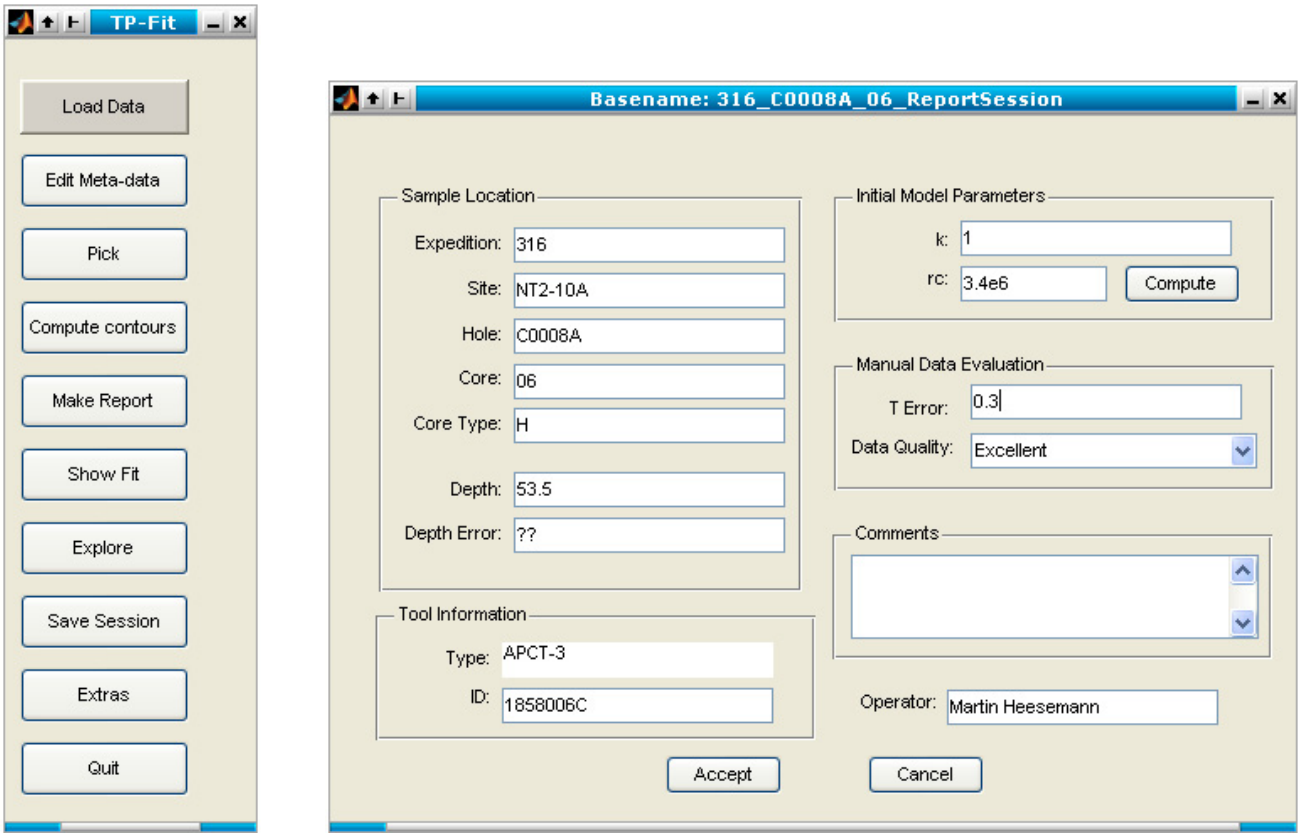

Figure 1: Main menu (left) and dialog to edit metadata and physical properties (right).

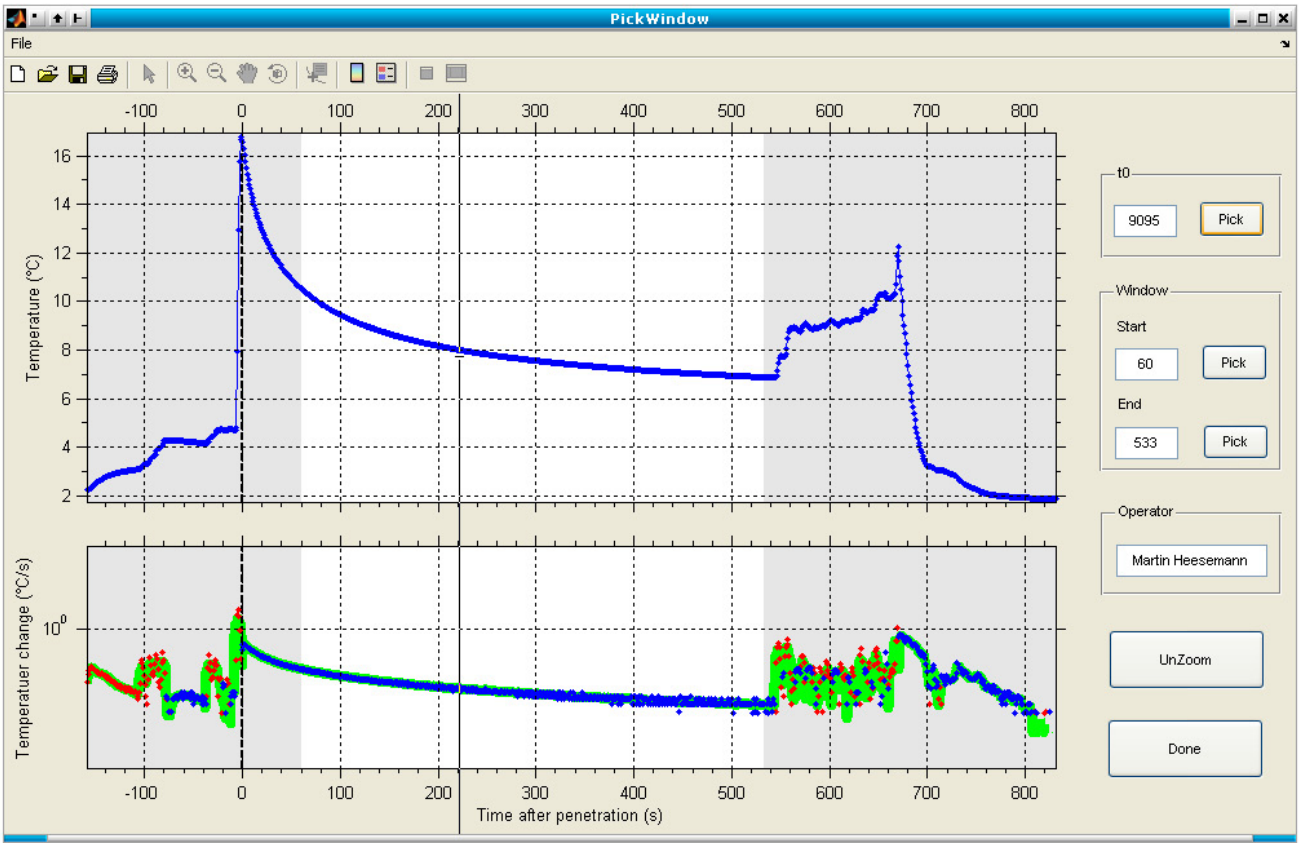

Figure 2: Pick window allows first inspection of the data and the determination of the tool penetration time t_0 and the time-window (white area).

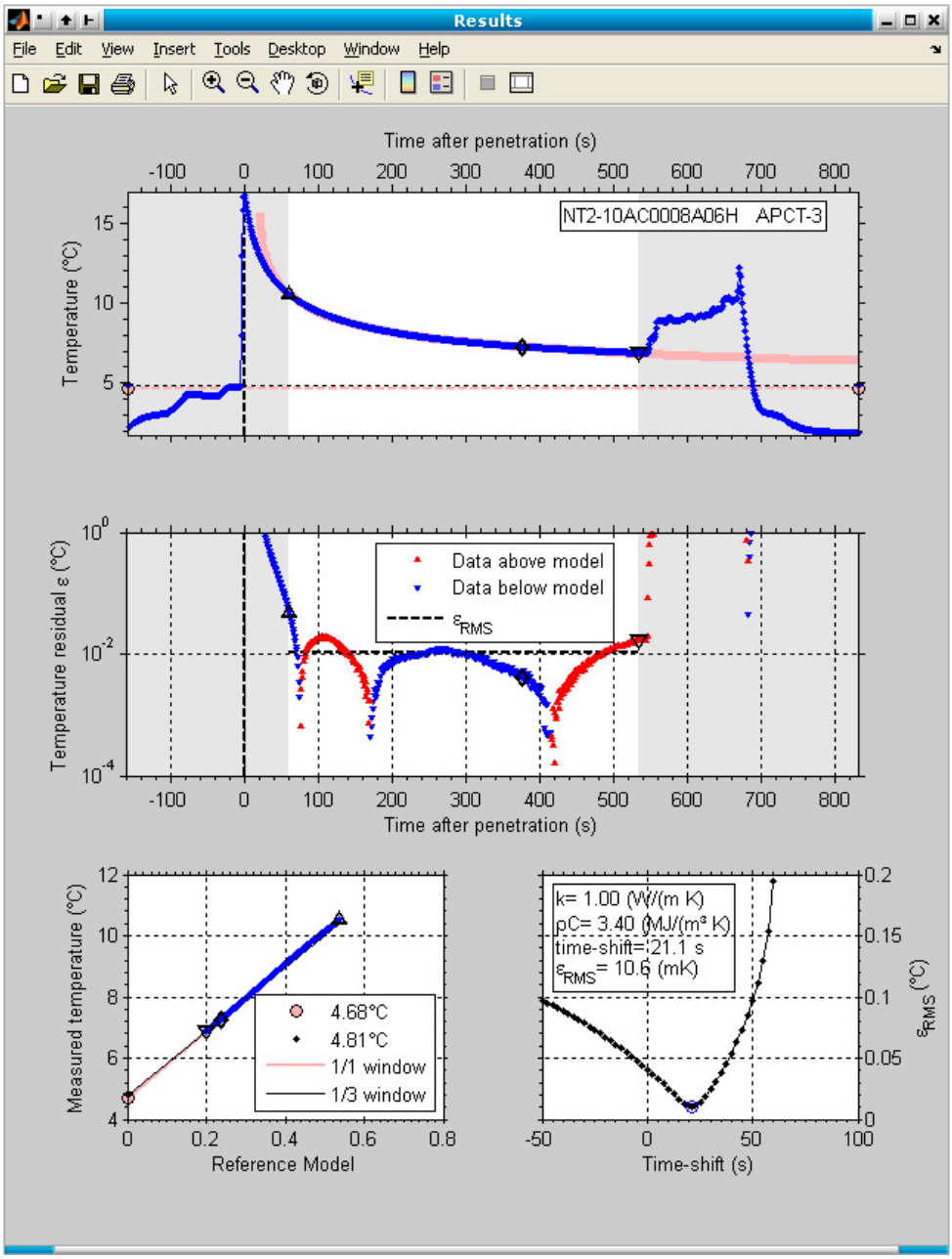

Figure 3: Graphical report of data analysis. The upper plot shows the measured data (blue dots) and the data selected for processing (white area). The reference model corresponding to the physical properties is represented by a bold red line and the temperature estimate is shown as thin red line. The plot in the middle shows the difference between data and model and reveals systematic deviations that cannot be recognized in the first plot. The lower left panel shows the measurements plotted over the normalized reference model; the undisturbed temperature (red circle on T-axis) is extrapolated by linear regression. The lower right panel shows the standard deviation between data and model over the time-shift by which the model is shifted versus the measured data. The optimal time-shift which is used in the previous plots is marked by a blue open circle.

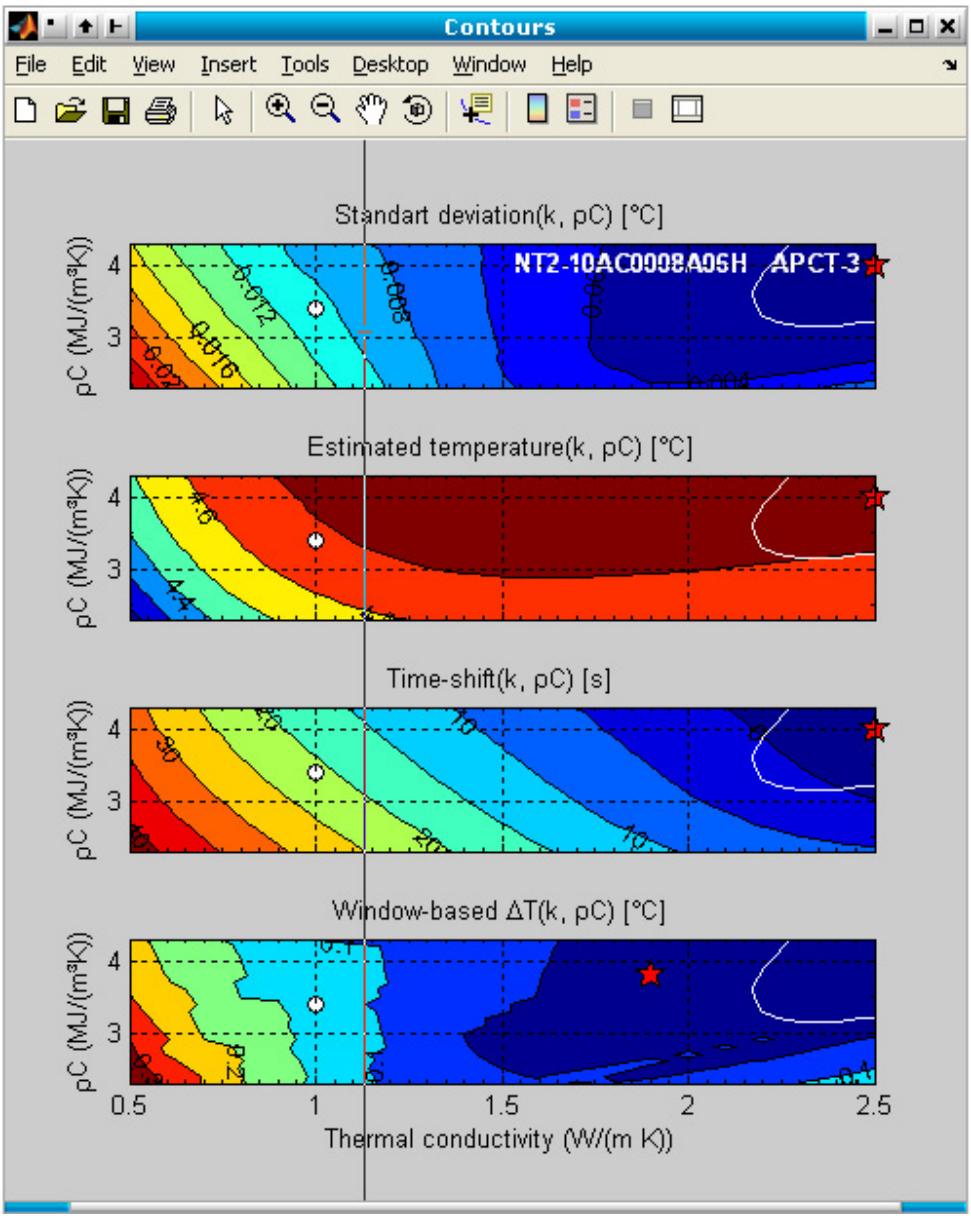

Figure 4: Contour plots of standard deviation, estimated temperature, time-shift, and difference between the estimated temperature of the whole time window and the last third of the time window as function of the model parameters k and ρC. A mouse click into one of the contour plots will move the white dots and the result with respect to the selected physical properties will be displayed in the results plot window. The red star represents the smallest standard deviation.

Manuscript: Estimating in-situ formation pressures from penetration transients of a borehole probe

Heesemann, M., H. Villinger, and E. E. Davis (submitted 2008b), Estimating in-situ formation pressures from penetration transients of a borehole probe, *Marine Geophys. Res.*.

Contributions

The DVTPP was the first tool used to measure in-situ formation pore fluid pressures in ODP boreholes. It was developed by Earl Davis, Robert Macdonald, and Robert Meldrum at the Geological Survey of Canada and the electronics were built by Richard Brancker Research, Ltd. First measurements using the a prototype tool were made during ODP Leg 190.
In the following manuscript the DVTPP, its deployment, and measured data is presented. Moreover, the estimation of undisturbed formation pressures from transient pressure data is described and expected errors of the results are discussed. Martin Heesemann compiled the manuscript, designed and implemented the data analysis software, and analyzed the data. Heinrich Villinger and Earl E. Davis supervised the research.

Estimating in-situ formation pressures from penetration transients of a borehole probe

Martin Heesemann[1] · **Heinrich Villinger**[1] · **Earl E. Davis**[2] ·
[1]**Department of Geosciences, University of Bremen, Bremen, Germany.**
[2]**Pacific Geoscience Centre, Geological Survey of Canada, Sidney, BC, Canada.**

Abstract An existing probe for measuring temperature 1.1 m below the bottom of sedimentary boreholes has been modified to allow measurement of formation fluid pressure between coring operations. The tool was designed as a compromise between being sufficiently robust to survive the high loading forces necessary for pushing the tool into consolidated material, yet small enough ($\sim$1.5 cm diameter at the measuring port near the tip of the probe) to allow partial dissipation of the thermal and pressure perturbations associated with frictional heating and volumetric strain generated during insertion. In this article we provide a technical description of the tool, a summary of data collected during preliminary tests and two legs of the Ocean Drilling Program, and an outline of a numerical model that provides a basis estimating static formation pressures from the tool insertion transients. Typical peak excess pressures generated by penetration are large, typically several times lithostatic pressure (the maximum amplitude of anticipated formation signals of interest), and characteristic decay times for perturbation dissipation are seen to be of the order of hours to days. Typical shipboard operations limit measurement times to roughly 30 minutes, giving great importance to extrapolation of early-time transient decays to estimate equilibrium formation pressure. This task is accomplished by matching observed decays to type-curves generated by a diffusional model of the probe in a permeable medium. Initial conditions for the model were estimated using two standard soil engineering formulations representing likely end-member conditions for penetration. Subsequent decay curves were generated with a finite-element-method numerical model. Tests of the algorithm using measurements and synthetic data show that typical uncertainty of extrapolation is of the order of 15% of the maximum expected signal level (lithostatic conditions). Thus, while the penetration transients are large and problematic, the tool can provide valuable information for many objectives (e.g., related to accretionary prisms). It is anticipated that some of this uncertainty can be reduced through long-term decay testing under controlled laboratory conditions, reduction of the size of the tool, and refinement of its drill-string delivery system.

Keywords Downhole tool · In-situ pore pressure · IODP · ODP · Finite elements

Corresponding author: Martin Heesemann (heesema@uni-bremen.de)

M. Heesemann
Department of Geosciences
University of Bremen
Bremen, Germany.
E-mail: heesema@uni-bremen.de

H. Villinger
Department of Geosciences
University of Bremen
Bremen, Germany.

E. E. Davis
Pacific Geoscience Centre
Geological Survey of Canada
Sidney, BC, Canada.

1 Introduction

Formation pressures provide critical information for the successful exploration and production of hydrocarbons (e.g. Law et al, 1998; Dutta, 1987) and are among the most important physical quantities that must be measured in order to accomplish the current objectives of scientific ocean drilling as stated in the Integrated Ocean Drilling Program (IODP) Initial Science Plan (Kappel and Adams, 2001). One topic of particular scientific interest is convergent margins, because they produce high formation pressures by compaction of the accreted sediments (Screaton et al, 1997) which, in turn, play a major role in the deformational and geochemical processes occurring at subduction zone plate boundaries (Becker et al, 1997; Fisher et al, 1996). Furthermore, the knowledge of fluid pressures is an important observational

constraint for models of hydrothermal circulation occurring at mid-ocean ridge flanks (Davis and Becker, 1994; Davis et al, 1992a).

Despite the demand for accurate pore pressure data there are only few reliable probes that measure pore pressure. Therefore, direct pore pressure measurements are scarce and studies depending on pore pressures often use estimates derived from the consolidation state of sediments, determined from samples in laboratory experiments, or from the analysis of seismic impedances (e.g. Bekins and Screaton, 2007; Saffer, 2007). Attempts to measure formation pressures in scientific boreholes using industry downhole tools, e.g. the Schlumberger Repeat Formation Tester (RFT) (Fisher and Becker, 1993), have largely failed (Moore et al, 1995; Moore and Tobin, 1997). Moreover, some industry tools, e.g. the Schlumberger Modular Formation Dynamic Tester (MDT), require a greater hole diameter than provided in non-riser IODP boreholes. Consequently, long-term observations in "CORKed "boreholes have been the only instruments that provide reliable formation pressure measurements (Davis et al, 1992b; Becker and Davis, 2004). However, the deployment of a Circulation Obviation Retrofit Kit (CORK) is expensive and time consuming. Moreover, the site has to be revisited in order to retrieve the data that is usually measured over a time-period of several years.

In order to fill that gap, two downhole tools for measuring formation pressures are currently under development. Both tools, the Temperature-Two-Pressure Probe (T2P) which is based on the Fugro-McClelland Marine Geosciences Inc.'s piezoprobe (Whittle et al, 2001; Long et al, 2007; Flemings et al, 2008), as well as the Davis-Villinger Temperature and Pressure Probe (DVTPP) which is described here, follow the concept of several tools that were designed to observe pore pressures in the upper meters of the seabed. Besides several cone penetrometers (e.g. Strout and Tjelta, 2005; Stegmann et al, 2006; Stegmann and Kopf, 2007), the tethered pore pressure probe (Davis et al, 1991), the free falling Pop Up Pore Pressure Instrument (PUPPI) (Schultheiss and McPhail, 1986), and the succeeding Satellite-Linked Autonomous Pore Pressure Instrument (SAPPI) (Kaul et al, 2004) provide seafloor pore pressure measurements. Each of these devices consist of a lance that penetrates the sediments and one or more pressure sensors on top of the lance that are connected to the formation's pore-space by hydraulic tubing extending from pressure ports drilled trough the lance.

The T2P is a modification of a cone-penetrometer, designed to disturb the tested formation as little as possible (Long et al, 2007; Flemings et al, 2008). The DVTPP is a modified version of the robust Davis-Villinger temperature probe (DVTP). The former has a smaller tip diameter and produces much smaller penetration pertubations than the latter (Long et al, 2007), but is more fragile and unsuitable for use in semi-consolidated sediments. In 1997, the DVTP, a down hole tool lowered by wire-line and pressed into the undisturbed formation at the bottom of the hole, was introduced to the Ocean Drilling Program (ODP) as described by Davis et al (1997). Since then, it has been successfully deployed in order to measure in-situ formation temperature profiles in many ODP boreholes. Later on, the DVTP was extended by adding a high resolution Paroscientific pressure gauge. In 2000, first measurements using a prototype of the new tool, called DVTPP, were performed during ODP Leg 190 (Moore et al, 2001).

The concepts underlying the measurements of the T2P and the DVTPP are very similar. As shown in Figure 1, measurements take place ahead of the drill-bit, where the formation is assumed to be undisturbed from drilling. Furthermore, both of the tools incorporate temperature sensors that allow the determination of formation temperatures along with formation pressures. The main difference of the tools is their geometry: on one hand, the DVTPP design is much more robust allowing measurements to be done in stiff sediments where even the advanced piston corer (APC) fails. On the other hand, the T2P causes smaller disturbances during insertion into the formation.

Pore-pressure disturbances are inevitably caused by all probes inserted into a formation. If no additional disturbances are present and one waits long enough, the formation will recover and return to its undisturbed state. Using downhole tools, however, it is usually not practical to wait until the disturbance has completely vanished, since this may take days to weeks due to the low permeability of marine sediments. Therefore, algorithms to estimate undisturbed formation pressures from transient pressure data, as presented in this paper, are required.

2 Tool description

The prototype of the DVTPP described here was assembled at the Pacific Geoscience Centre using parts of one of the DVTP temperature probes made available by the ODP. The original tool is capable of measuring bottom-hole temperatures in semi-consolidated sediment as well as open-hole temperatures. The probe was designed to be mechanically robust, but to minimize 1) the time required for sensors to approach formation temperatures, and 2) the mechanical disturbance caused by probe penetration, and thus the possibility of fracturing and invasion of drill-water (Davis et al, 1997). Because the capability for later addition of a pressure sensor had already been incorporated in the DVTP design, only minor changes to the probe tip of the DVTPP were necessary.

The new tip, shown in Figure 2, incorporates a miniature thermistor that is housed in an oil-filled needle with a diameter of 2 mm. This needle nearly fills the oil-filled interior of the main probe itself. Small ports drilled through a sleeve

near the end of the probe tip allow hydraulic communication between the pore fluid outside the probe and the annulus between the thermistor needle and the probe tip interior wall via filters beneath the sleeve set into slots cut through the tip. Dual connectors at the top of the probe's tip, one hydraulic and one electrical, pass hydraulic and temperature signals to the pressure gauge, and to the data recorder situated inside the pressure case.

2.1 Specifications of the prototype

The prototype used to carry out the measurements described here measures fluid pressure and temperature at the probe tip, as well as the internal temperature of the housing. Inside the logger there are two fixed reference resistors used to control the measurement's quality: their values should remain constant within a very small range determined by their temperature coefficients.

In order to avoid changes of the electronics used in the standard DVTP, a slightly modified CORK data logger was employed for expedience. The electronic incorporated in the logger remains operational at temperatures up to 40°C and will survive temperatures up to 80°C. This setup allows pressure to be recorded with full precision at a sampling frequency of 0.1 Hz. After completing a measurement the data are downloaded in a binary format from the logger, and then converted to an ASCII file.

The pressure gauge employed is a Paroscientific Digiquartz 8B 7000-2 with a modified pressure case where stainless steel is replaced by high strength steel in order to allow a smaller diameter. The gauge is designed to measure and withstand external pressures of 70 MPa (≈7000 m) and it has a limited tolerance of overpressure: it will be damaged or fail if the measured pressure exceeds 105 MPa. Pressures are provided at a resolution of 7 Pa and an absolute accuracy of 7 kPa of the full scale (Paroscientific, Inc., 2001).

The Digiquartz 8B is equipped with integral intelligent electronics which determine the frequency of the pressure sensitive quartz strain gauge over a user-supplied time interval. Temperature variations affecting the pressure measurements are compensated for with the output of a second quartz oscillator. Bi-directional communication via an RS-232 interface allows configuration and control of all the gauge's operating parameters as well as the retrieval of the pressure data from the data logger.

For the temperature measurements at the probe's tip, a Thermometrics GC32 glass-encapsulated chip thermistor was chosen for its tiny size. Unfortunately, this thermistor is not well matched to the CORK logger electronics resulting in a limited temperature resolution between 8 mK at 20°C and 50 mK at 100°C. Further restrictions of the prototype are the inability to acquire acceleration data and the fact that the internal thermistor is off scale at housing temperatures below

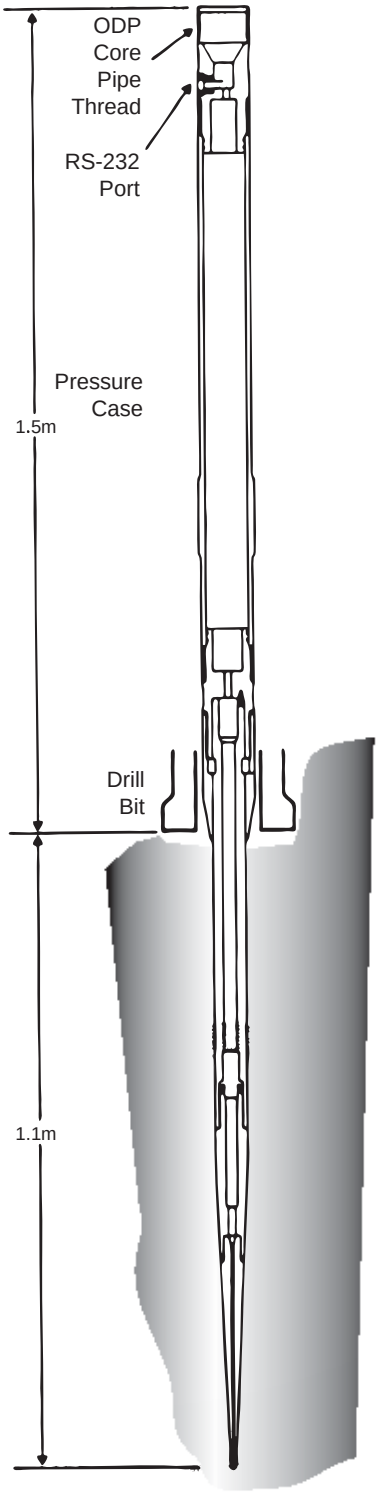

Fig. 1 Full assembly of the DVTPP during a measurement with tapered tip inserted into the formation (modified after Davis et al (1997)).

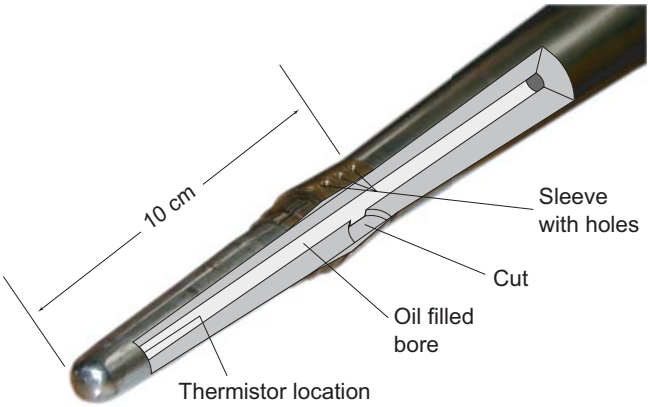

Fig. 2 Details of the tapered tip. Showing the thermistor location and the cut and the holes in the sleeve trough which the tool is hydraulically connected to the formation.

15°C. The compromises in this prototype tool can be easily dealt with in a proper design.

2.2 Deployment

The mechanical assembly is compatible with the colleted delivery system used to deploy core barrels and other bottom-hole tools. After lowering by wire-line, the probe is latched in at the bottom of the drill string with the tip of the tool extending 1.1 m below the drill bit (cf. Figure 1). The extended probe is pushed into the sediment below the bottom of the hole with a load up to 4500 kg supplied by the weight of the drill-string bottom-hole assembly. At greater loads, a release collet allows the tool to retract back into the bit. After penetration the probe is typically left stationary for a period of 10 min for temperature-only measurements and 30 min or longer for temperature and pressure measurements, to allow temperature and pressure at the probe's tip to approach undisturbed formation formation values. Typical data of a complete deployment recorded on ODP Leg 190 is presented in Figure 3. The time required for one measurement depends on water depth, and takes typically about 2 hours.

3 Data

Figure 3 shows the typical features of a DVTPP measurement. At the time of insertion an excess pore pressure peak of initial magnitude P_e is created. Then pressure decays slowly towards the undisturbed formation pressure P_0. Similar behavior is present in the temperature data.

These features are also present in the data recorded at a first test at sea. During this test on an RV-Atlantis cruise in September 1999, the DVTPP was lowered by wire-line until it penetrated the sea-floor. All three penetrations carried out during the cruise caused relatively small initial excess pore pressure peaks of about 20 kPa. Besides the smooth pressure decays that were recorded, there is also a strong tidal signal with an amplitude of about 30 kPa.

This is in agreement with data measured in similarly unconsolidated sediments using the tethered pore pressure probe or a PUPPIs, which create excess pore pressures of around 15 kPa and 30 kPa, respectively (Davis et al, 1991; Fang et al, 1993). The tidal signal measured by these tools is, however, several orders of magnitude smaller since they record differential pressures relative to the seafloor hydrostatic pressure at the seafloor, while the DVTPP supplies absolute pressure readings.

3.1 Available measurements

During ODP Leg 190, in 2000, the DVTPP was tested in a borehole for the first time. The tool was used six times in total at four different holes (Moore et al, 2001). Most measurements show relatively smooth decays, indicating successful deliveries. Unfortunately, the pressure gauge was programmed with incorrect coefficients for temperature compensation which precluded quantitative analysis of the data. Subsequently, the tool was deployed eleven times during ODP Leg 201 in early 2002 (D'Hondt et al, 2003). None of those measurements returned any useful pressure data due to a plumbing problem in the interior of the probe. The smooth decays present in the temperature data, however, suggest successful delivery of the tool. Later in 2002, further deployments were undertaken during ODP Legs 204 and 205 (Tréhu et al, 2003; Morris et al, 2003). Most of these data suffer from technical problems caused by electrical noise and tool motion after the penetration (see Figure 4). Nevertheless, there are some measurements with smooth decay curves and pressure readings at seafloor level and at the bottom of the hole returned reasonable hydrostatic pressures. Finally, the DVTPP and T2P prototypes were deployed during IODP Expedition 308 and several successful measurements were made (Flemings et al, 2006, 2008).

Figure 4 shows a selection of four DVTPP data sets. Most other penetration records gathered to date, fit well into one of the categories represented by these measurements. Except for Type I, which represents a nearly ideal deployment, all other categories are plagued by common tool delivery problems: either the insertion is unsteady (Type II), or the tool is disturbed during the measurement by being forced further into the formation (Type III), or the tool is slightly lifted during decoupling from the drill string which is characterized by a sudden pressure drop (Type IV). Note, that the categories only describe the most prominent disturbances of the measurement. Actually, rapid pressure drops, caused by the cohesion of the sediments during raising or decoupling of the probe (Long et al, 2007), can be seen in

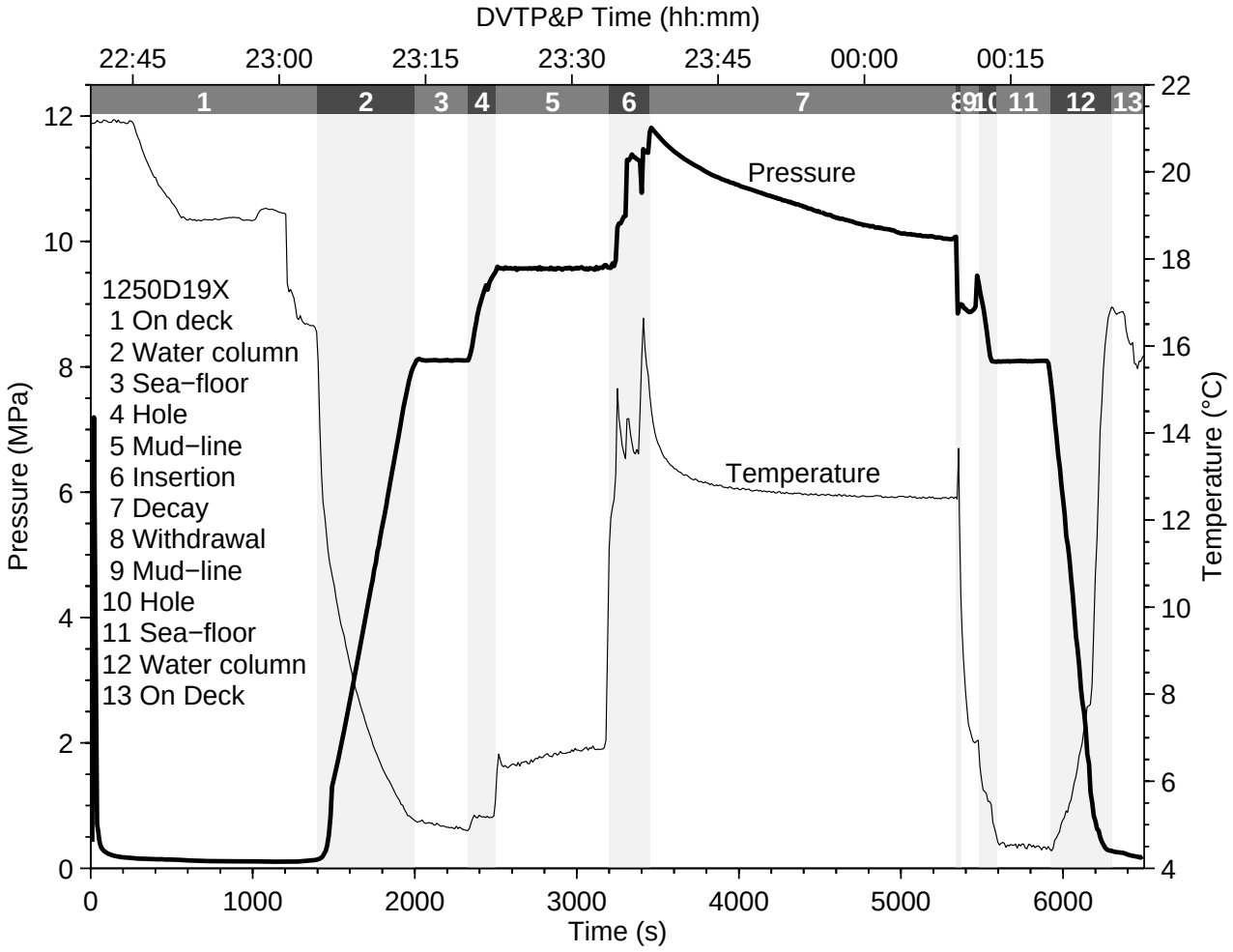

Fig. 3 Typical DVTPP data measured at ODP-Site 1250 during Leg 204: alternating shadings represent different stages of the measurement. The first stage represents the time when (1) the probe is still on deck, before it is (2) lowered to the sea-floor causing a rise in pressure and a decay in temperature. At sea-floor level (3) the probe is stopped for several minutes to carry out a function test where the bottom water temperature as well as the hydrostatic pressure are measured. After passing through the drilled hole (4) the probe is stopped again at the bottom of the hole (5), before it is inserted into the formation and a sudden increase in pressure as well as in temperature occurs (6). Before steady decays are observed in the pressure as well as in the temperature data (7) the presents of spikes indicates delivery problems during this deployment. Because of time restrictions the probe has to be withdrawn from the formation (8) before the penetration induced disturbances vanish completely. The raising of the probe (10, 12) is again interrupted by stops at the mud-line (9) as well as at the sea-floor level (11). Finally the probe is on deck again (12), where the measured data can be recovered.

all four data sets. During the Type IV measurement, however, the decoupling even affects the temperature data which is not commonly observed in the long history of standard DVTP measurements. For example in the Type III measurement the sudden pressure drop does not correspond to a distinct event in the temperature data. This suggests that the DVTPP movement during the decoupling of the Type IV measurement allowed cold water from the borehole to permeate along the probes' surface into the formation.

The outcome of all reasonable DVTPP data measured during the ODP is summarized in Figure 5, where the estimated magnitudes of the initial excess pore pressure peaks P_e are plotted versus depth below seafloor. Generally P_e increases with depth below seafloor as expected, since overburden pressure and consolidation of the formation penetrated by the tool increase with depth. Additionally, the left diagram shows that the linear increase of P_e with depth measured during Leg 204 at the Hydrate Ridge is higher than the increase found during Leg 190 in the vicinity of the Nankai Trough. This could either be caused by differing sediment properties, e.g. compressibility and permeability, or possibly an increased insertion velocity at Leg 204 deployments. In the right diagram the distribution of data in the categories defined in Figure 4 is shown. It can be seen that the quality of the deployment does not depend on the magnitude of P_e, nor on the depth below seafloor. By comparing both diagrams it is obvious that the deployments during Leg 190 generally

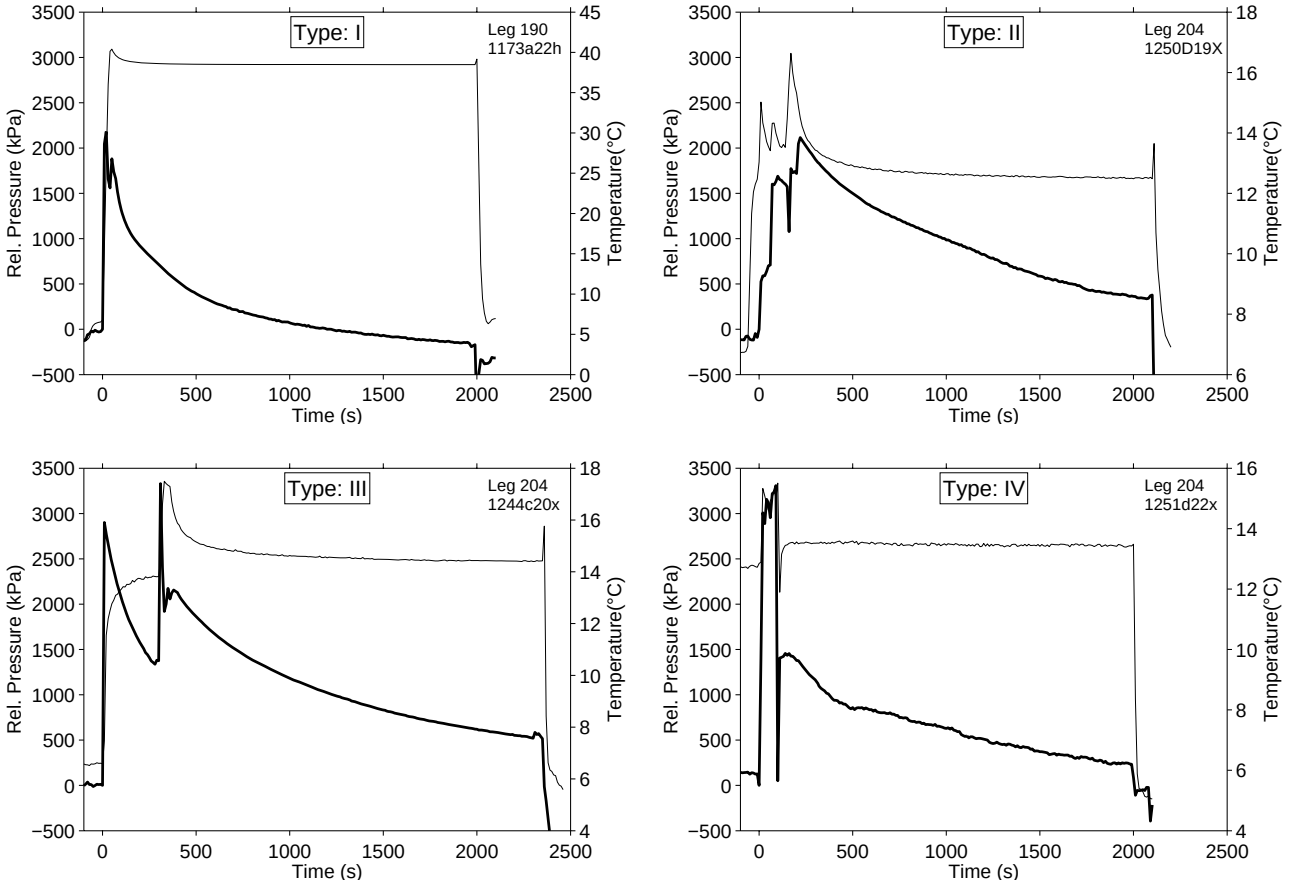

Fig. 4 Typical data sets obtained using the DVTPP. Bold lines represent the measured pressures relative to the hydrostatic pressure at the bottom of the hole and light lines show the temperatures measured at the tip of the tool. Type I: Good delivery resulting in smooth pressure decay. Increased decay of pressure readings due to incorrect temperature correction coefficients and high formation temperatures at Leg 190 sites. Type II: Steady decay after unsteady behavior during the time of insertion. Type III: Probe is forced further into the formation after a first phase of equilibration. Otherwise, distinct and undisturbed decay curves. Type IV: Abrupt pressure and temperature drop when the tool is decouple from the drill string after insertion. Moreover, pressure and temperature data suffer from small disturbances during the whole measurement.

worked out better than during Leg 204 which could also be caused by different sediment properties.

4 Data Analysis

As can be seen from Figures 3 and 4, the penetration-induced initial excess pore pressure disturbances P_e have usually not completely decayed after a feasible measuring period in the order of thirty minutes. Therefore, an algorithm providing the capability to extrapolate undisturbed formation pressures P_0 from transient measurements is needed.

Fang et al (1993) and Davis et al (1991) applied a technique that was commonly used with thermal transients (e.g. Hyndman et al, 1979) to estimate equilibrium temperatures of transient data measured with cylindrical temperature probes to analyze PUPPI and tethered probe pressure data, respectively. They plotted the last part of the pressure record versus the reciprocal time $1/t$, according to the behavior of a line source, and extrapolated to $1/t = 0$ by linear regression to infinite excess pressure decay times. The authors were, however, aware of the fact that this ad hoc approach is problematic, because some implied assumptions are violated: first of all, the geometry of the probes is not well described by a line source or a cylinder of infinite length. Moreover, unlike a thermal disturbance created by a probe, the initial pressure disturbance is not instantly formed in the probe's center, but distributed in the volume of sediment surrounding the probe. Flemings et al (2008) found that the $1/t$ extrapolation systematically results in overestimated undisturbed formation pressures and that using $1/\sqrt{t}$ usually gives more accurate results. This approach, however, is purely empirical and does not relate to any specific model of the decay and completely neglects the known probe geometry. The algorithm described here works by comparing the measured pressure data to normalized forward models—computed using the finite element method—of which the undisturbed formation pressure P_0 is known.

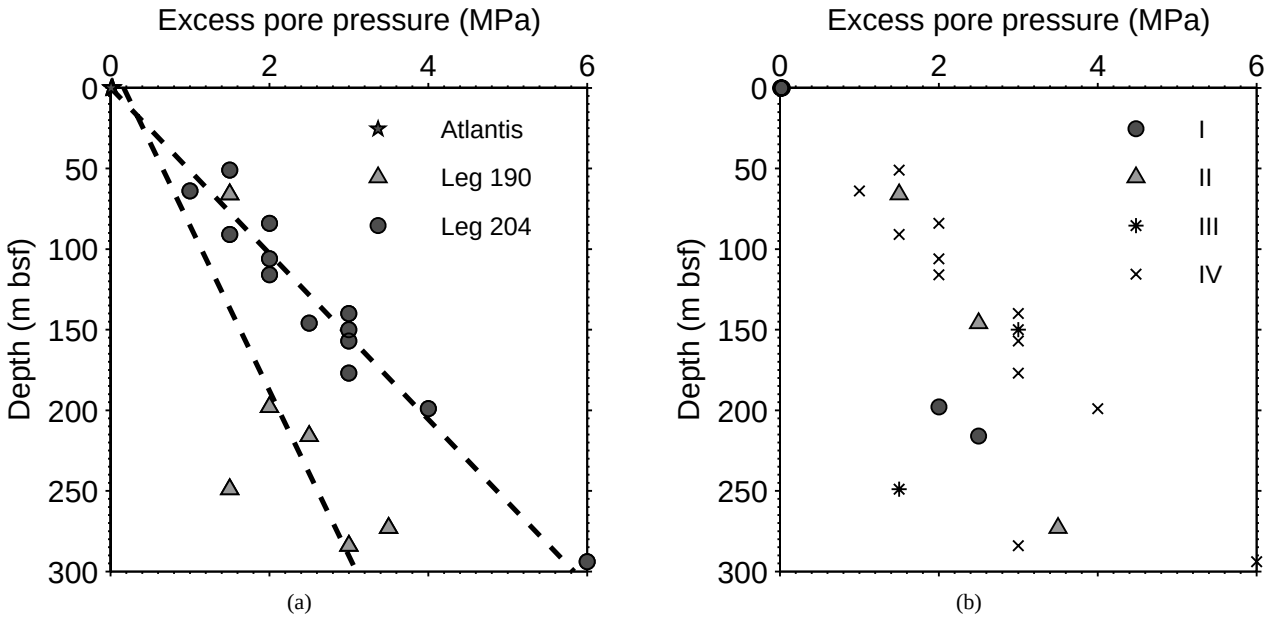

Fig. 5 Plots of initial excess pore pressures P_e versus depth below seafloor summarizing all reasonable DVTPP measurements: a) The general increase of P_e differs between legs, i.e. locations. b) The individual category, a measurement falls into (defined in Figure 4), is not bound to P_e or depth below seafloor. However, differences between legs are obvious.

4.1 Physics of excess pore pressure dissipation

In our models, the dissipation of the pore pressure disturbance is assumed to be a diffusive process that takes place in a isotropic homogeneous formation and can be described by the following governing equation (Raghavan and Ozkan, 1994):

$$\frac{\partial}{\partial t}P(\mathbf{r},t) = \eta\,\nabla^2 P, \tag{1}$$

where P is the pore fluid pressure as a function of space and time, and η is the hydraulic diffusivity. Taking into account the axial symmetry of the geometry, the problem can be reduced to 2-D in cylindrical-coordinates, where equation (1) becomes

$$\frac{\partial}{\partial t}P(\mathbf{r},t) = \frac{\eta}{r}\left[\frac{\partial}{\partial r}\left(r\frac{\partial}{\partial r}P\right) + \frac{\partial}{\partial z}\left(r\frac{\partial}{\partial z}P\right)\right]. \tag{2}$$

Solutions of this equation depend on the formation's hydraulic diffusivity η, which is a function of permeability, frame compressibility and fluid viscosity. Furthermore, solutions depend on the initial distribution and magnitude of the induced pressure disturbance, and likewise on the probe's geometry. Expressed in terms of normalized quantities for

$$\text{pressure: } \Psi = \frac{P-P_0}{P_e}, \tag{3}$$

$$\text{space coordinates: } r_n = \frac{1}{r_1}r \;\Rightarrow\; \frac{\partial}{\partial r} = \frac{1}{r_1}\frac{\partial}{\partial r_n}, \tag{4}$$

$$z_n = \frac{1}{r_1}z \;\Rightarrow\; \frac{\partial}{\partial z} = \frac{1}{r_1}\frac{\partial}{\partial z_n},$$

$$\text{and time: } \tau = \frac{\eta}{r_1^2}t \;\Rightarrow\; \frac{\partial}{\partial t} = \frac{\eta}{r_1^2}\frac{\partial}{\partial \tau} \tag{5}$$

equation (2) becomes

$$\frac{\partial}{\partial \tau}\Psi(\mathbf{r}_n,\tau) = \frac{1}{r_n}\left[\frac{\partial}{\partial r_n}\left(r_n\frac{\partial}{\partial r_n}\Psi\right) + \frac{\partial}{\partial z_n}\left(r_n\frac{\partial}{\partial z_n}\Psi\right)\right]. \tag{6}$$

Using this normalization, the time scaling factor r_1^2/η depends on the hydraulic diffusivity η and the characteristic length r_1 as is shown in equation (5). This has two implications: firstly, decay data resulting from a certain geometry and initial pressure distribution at any hydraulic diffusivity can be matched with data at any other hydraulic diffusivity by simply adjusting the time scale. Secondly, two sets of decay curves resulting from the same geometry and initial pressure distribution on different length scales, given by the initial extent of the pressure disturbance, can also be matched by adjusting the time scale. The latter implication is important, keeping in mind that the conical geometry of the DVTPP with the pressure port close to its tip is very similar viewed on a range of length scales. The combination of

these facts make it impossible to deduce the hydraulic diffusivity from decay data measured by the DVTPP without any knowledge about the length scale inherent to the penetration induced pressure disturbance.

4.2 Extrapolation algorithm

Given a reference curve that is normalized as described in the previous section, the undisturbed formation pressure P_0 of a measured data set can be estimated as follows: at first, a time-scale that has to be applied to the reference curve is chosen. Then a test whether a plot of the measurements versus the reference curve results in a linear relation is performed. If this test fails, the time-scale is iteratively changed until the test is passed. Finally, a linear regression of the measurements versus the reference curve results in P_e as linear factor and the undisturbed formation pressure P_0 represented by the intercept value.

4.3 FEM-Model

Since there are no DVTPP measurements with very long and undisturbed decay curves available, the needed reference curves were computed by using a numerical model. This model is based on the solution of equation (2) using the finite element method (FEM) toolbox Femlab® (now COMSOL-Multiphysics®). Concerning this model, the geometry of the initial pressure disturbance is critical, as mentioned before.

Unfortunately, direct measurements of the initial pressure disturbance are not available and exact numerical predictions of the disturbance are not possible, as the necessary computations would depend on many unknown soil model parameters and the exact penetration speed. Moreover, the measured data suggests that the initial pressure distribution is often modified when the probe is decoupled from the drill string. Furthermore, the solutions of several studies that treated similar problems differ significantly depending on the algorithms and soil models used. For example, the work about undrained pile installation of Baligh (1986) and the models of Long et al (2007) suggest an excess pore pressure disturbance of mainly cylindrical shape all around the probe, whereas a model of a miniature piezocone penetrometer by Abu-Farsakh et al (1998) results in a spherical disturbance that is concentrated close to the probe's tip. Finally, Lee and Elsworth (2004) and Elsworth and Lee (2005) found that the shape of the pressure disturbance that free-falling penetrometers generate depends on their dimensionless penetration rate, their geometry and the hydraulic diffusivity of the sediments. High penetration rates result in more cylindrical pressure disturbances, while high hydraulic diffusivities result in spherical disturbances. Therefore, sets of reference curves resulting from cylindrical as well as spherical initial conditions were computed and tested using the presented extrapolation algorithm.

4.4 Example of an analysis

In Figure 6 the fits between one measured transient and the FEM solutions of a spherical shaped and a cylindrical shaped initial excess pore pressure disturbance are compared. In both cases there is a good agreement between the numerical model and the measured pressure data. The time-scales r_1^2/η of both solutions are in the order of 10^4 s. Assuming the length-scales r_1, given by the extent of the initial penetration induced pressure disturbances, are in the order of 10^{-2} m realistic magnitudes of hydraulic diffusivity ($O(\eta) = 10^{-8}\,\mathrm{m^2/s}$ are obtained. The estimated undisturbed formation pressures P_0, however, differ by 66 kPa. If the spherical and the cylindrical geometries are considered to be the end-members of all realistic initial pressure distributions and the reality is more closely described by a superposition of both types, the true undisturbed formation pressure should fall somewhere in-between these extreme cases. Therefore, without knowing which geometry describes the measurement better, one would choose the mean of the two results ($P_0 = 55828 \pm 33$ kPa) as the estimated undisturbed pore pressure of the presented data. Keeping the extrapolation algorithm in mind, it is obvious that the uncertainty of the estimate scales with the magnitude of the initial excess pore pressure disturbance. In the presented case, the uncertainty of 66 kPa is about 3% of the mean initial excess pore pressure estimate P_e of about 2270 kPa.

4.5 Expected uncertainty of formation pressure estimates

Extensive testing of the algorithm with data generated by the FEM-model confirmed that the uncertainty of the results is about 5% of P_e. Theoretically, it should be possible to reduce this uncertainty below 1% if the exact geometry of the penetration induced disturbance were known. Currently, there are only a few data sets measured with the DVTPP that do not suffer from problems with the delivery system or with the prototype's logging electronics. Therefore, the extrapolation algorithm was also tested on data collected with the tethered probe by Davis et al (1991). Again, the uncertainty of the results was found to be in the order of 5% in respect to P_e.

In typical applications of DVTPP pressure measurements, the magnitude of the formation pressure P_0 relative to hydrostatic pressure P_{hydr} and lithostatic pressure P_{lith} is of greater interest than the magnitude of P_e. The uncertainties of most P_0 estimates are in the order of 15% of $P_{\mathrm{lith}} - P_{\mathrm{hydr}}$, as can be seen in Figure 7. For the computation of P_{hydr} and P_{lith}, we

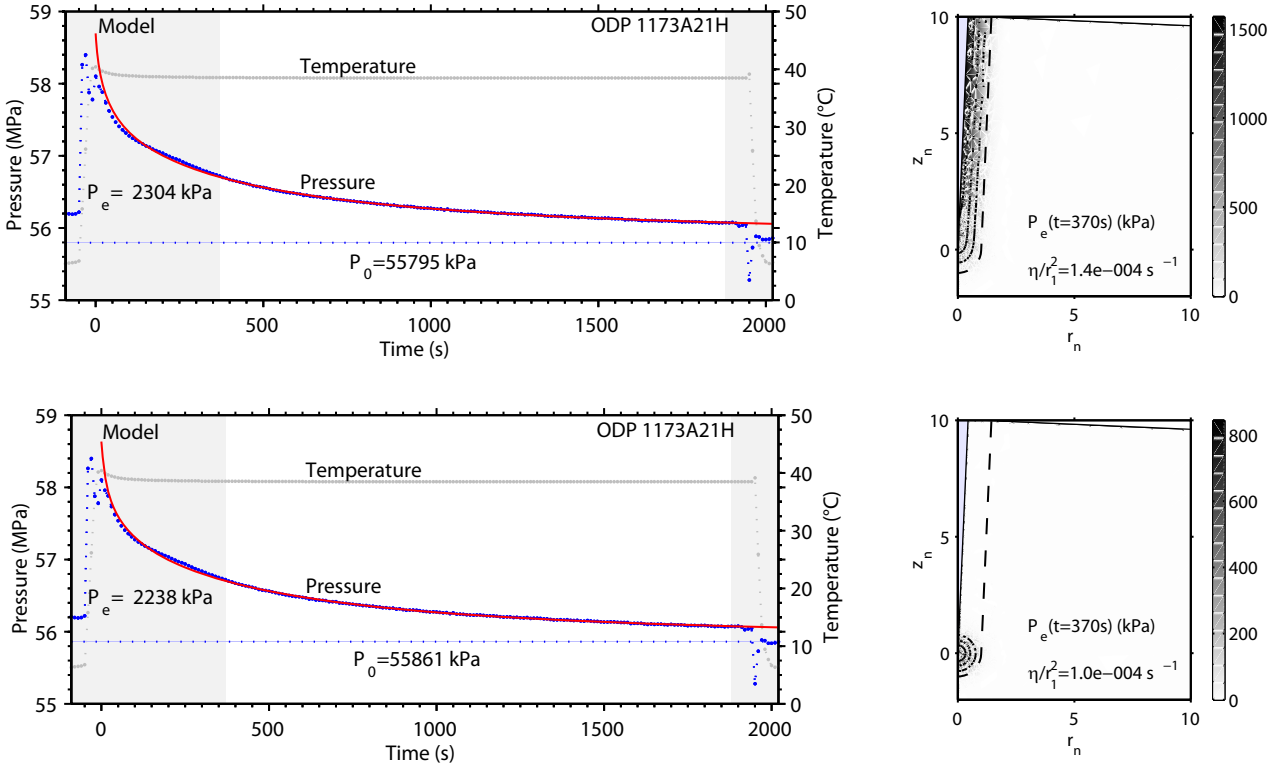

Fig. 6 Example analysis of a DVTPP measurement with two different numerical model curves which are characterized by their initial excess pore pressure distribution shown to the right. Both models, plotted as solid lines, closely resemble the measured pressure data that is represented by small dots.

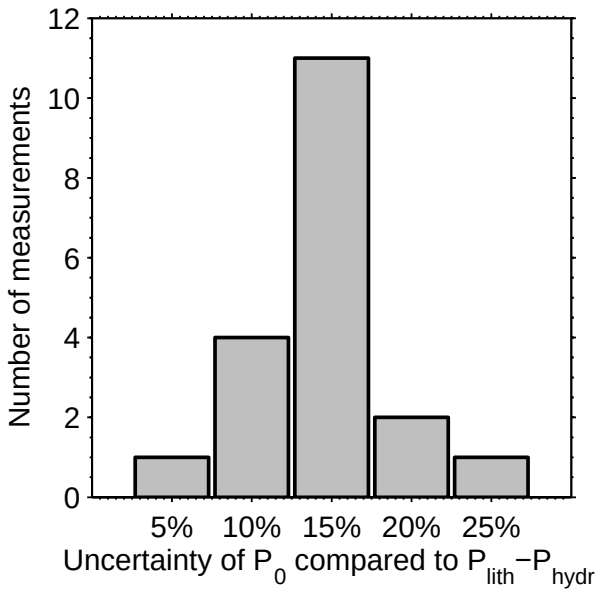

Fig. 7 Histogram comparing the uncertainty of the undisturbed formation pressure estimates (5% of P_e) of the DVTPP data presented in Figure 5 to the differences between lithostatic pressure P_{lith} and hydrostatic pressure P_{hydr}.

assumed a constant density of 1025 kg/m^3 for seawater and used bulk density data acquired during ODP Legs 190 and 204 (Moore et al, 2001; Tréhu et al, 2003), respectively.

5 Conclusions and outlook

In its current version the DVTPP has proven to be a working prototype for measuring formation pressures along with formation temperatures in ODP boreholes. The experiences with initial measurements, however, show that a number of enhancements, planned for a new version of the tool, have to be made to ensure that high data quality is gained even on routine deployments: Firstly, the probe's tip will be modified in order to reduce its diameter. This will reduce the amplitude of the penetration-induced pressure disturbance and therefore increase the accuracy of the undisturbed formation pressure estimate. Secondly, the tool delivery procedure will be reviewed with the goal of achieving a steady but low insertion velocity, reducing the pressure disturbances in the formation. Also the mechanical disturbances that sometimes occurred while the probe is located in the formation have to be eliminated. The anticipated use of new data acquisition electronics will aid this review, since its higher sampling rate and the ability to record the data of the acceleration sensor, present in the original DVTP, will provide valuable data of the delivery and decoupling system as well as on the insertion velocity. Furthermore, new electronics will provide an increased resolution and consume less electrical power. It is also planned to improve the temperature sensitivity of the tool and calibrate the tool for temperatures up to 100°C. Moreover, long-term penetration tests in a mud tank are anticipated. These tests will provide complete data sets with complete decays of pressure disturbances that can be used to calibrate and enhance the extrapolation for undisturbed formation pressures. Tests in a mud tank will not waste valuable drill-ship time, and many perturbations caused by the ship's heave and tidal pressure changes will be absent.

Considering the high demand for reliable downhole formation pressure and temperature measurements and at the same time the lack of suitable devices, the planned efforts to enhance the tool are a good investment, even if attempts to reduce the absolute accuracy of the formation pressure estimate below 15% of the quantity of interest fail.

Acknowledgements This research used samples and data provided by the Ocean Drilling Program (ODP). The ODP is sponsored by the U.S. National Science Foundation (NSF) and participating countries under management of Joint Oceanographic Institutions (JOI). The Deutsche Forschungsgemeinschaft supported this research with the grants Vi 133/9-1 and Vi 133/9-2. Funding for tool development was provided by the Geological Survey of Canada and the ODP. Engineering assistance was provided by Robert Macdonald and Robert Meldrum (Geological Survey of Canada). Electronics were built by Richard Brancker Research, Ltd. We thank the ODP/IODP technical staff for their expertise and dedication.

References

Abu-Farsakh MY, Voyiadjis GZ, Tumay MT (1998) Numerical analysis of the miniature piezocone penetration tests (PCPT) in cohesive soils. Int J Numer Anal Meth Geomech 22:791–818

Baligh MM (1986) Undrained deep penetration, II: pore pressures. Geotechnique 36(4):487–501

Becker K, Davis EE (2004) In situ determinations of the permeability of the igneous oceanic crust. In: Hydrogeology of the Oceanic Lithosphere, Cambridge University Press, pp 189–224

Becker K, Fisher AT, Davis EE (1997) The CORK experiment in Hole 949C: long-term observations of pressure and temperature in the Barbados accretionary prism. In: Proc. ODP, Sci. Results, Ocean Drilling Program, Collage Station, TX, vol 156, pp 247–252

Bekins BA, Screaton EJ (2007) Pore pressure and fluid flow in the northern Barbados accretionary complex. In: Dixon T, Moore C (eds) The seismogenic zone of subduction thrust faults, Columbia University Press, New York

Davis EE, Becker K (1994) Formation temperatures and pressures in a sedimented rift hydrothermal system: 10 month of CORK observations, holes 857D and 858G. In: Proc. ODP, Sci. Results, Ocean Drilling Program, Collage Station, TX, vol 139, pp 649–666

Davis EE, Horel G, MacDonald RD, Villinger H, Bennett RH, Li H (1991) Pore pressures and permeabilities measured in marine sediments with a tethered probe. J Geophys Res 96(B4):5975–5984

Davis EE, Becker K, Pettigrew T, Carson B, MacDonald R (1992a) CORK: A hydrologic seal and downhole observatory for deep-ocean boreholes. In: Proc. ODP, Init. Repts., Ocean Drilling Program, Collage Station, TX, vol 139, pp 43–52

Davis EE, Becker K, Pettigrew T, Carson B, MacDonald R (1992b) CORK: A hydrologic seal and downhole observatory for deep-ocean boreholes. In: Proc. ODP, Init. Repts., Ocean Drilling Program, Collage Station, TX, vol 139, pp 43–52

Davis EE, Villinger H, MacDonald RD, Meldrum RD, Grigel J (1997) A robust rapid-response probe for measuring bottom-hole temperatures in deep-ocean boreholes. Marine Geophys Res 19:267–281

D'Hondt SL, Jørgensen BB, Miller DJ, Shipboard Scientific Party (2003) Init. repts. In: Proc. ODP, Available from World Wide Web:http://www-odp.tamu.edu/publications/201_IR/201ir.htm, vol 201 [Online]

Dutta NC (1987) Geopressure. No. 7 in Geophysics reprint series, Society of Exploration Geophysicists

Elsworth D, Lee DS (2005) Indentation of a free-falling lance penetrometer into a poroelastic seabed. International Journal for Numerical and Analytical Methods in Geomechanics 29(2):141–162, URL http://dx.doi.org/10.1002/nag.408

Fang WW, Langseth MG, Schultheiss PJ (1993) Analysis and application of in situ pore pressure measurements in marine sediments. J Geophys Res 98(B5):7921–7938

Fisher AT, Becker K (1993) A guide to ODP tools for downhole measurements. Ocean Drilling Program, Technical Note 10

Fisher AT, Zwart G, ODP Leg 156 Scientific Party (1996) Relation between permeability and effective stess along a plate-boundary fault, Barbados accretionary complex. Geology 24(4):307–310

Flemings P, Behrmann J, John C, the Expedition 308 Scientists (eds) (2006) Proc. IODP, vol 308, College Station TX (Integrated Ocean Drilling Program Management International, Inc.), DOI 10.2204/iodp.proc.308.2006

Flemings P, Long H, Dugan B, Germaine J, John C, Behrmann J, Sawyer D, Scientists IE (2008) Pore pressure penetrometers document high overpressure near the seafloor where multiple submarine landslides have occurred on the continental slope, offshore Louisiana, Gulf of Mexico. Earth and Planetary Science Letters In Press, Corrected Proof:–, URL http://www.sciencedirect.com/science/article/B6V61-4RC6RB1-4/1/511ef93c53dc8aac5c0017310f358dc9

Hyndman RD, Davis EE, Wright JA (1979) The measurement of marine geothermal heat flow by a multipenetration probe with digital acoustic telemetry and insitu thermal conductivity. Marine Geophys Res 4:181–205

Kappel E, Adams J (2001) Earth, oceans and life; IODP Initial Science Plan. International Working Group Support Office, URL http://www.iodp.org/isp/

Kaul N, Villinger H, Kruse M (2004) Satellite-linked autonomous pore pressure instrument - SAPPI. Sea Technology 45(8):54–58

Law BE, Ulmishek GF, Slavin VI (1998) Abnormal pressures in hydrocarbon enviornments. No. 70 in AAPG Memoir, The American Association of Petroleum Geologists

Lee DS, Elsworth D (2004) Indentation of a free-falling sharp penetrometer into a poroelastic seabead. J Eng Mech 130(2):170–179, DOI 10.1061/(ASCE)0733-9399(2004)130:2(170)

Long H, Flemings PB, Germaine JT (2007) Interpreting in situ pressure and hydraulic properties with borehole penetrometers in ocean drilling: Dvtpp and piezoprobe deployments at southern hydrate ridge, offshore oregon. J Geophys Res 112:B04,101, DOI 10.1029/2005JB004165

Moore GF, Taira A, Klaus A, Shipboard Scientific Party (2001) Init. repts. In: Proc. ODP, Available from World Wide Web:http://www-odp.tamu.edu/publications/190_IR/190ir.htm, vol 190 [Online]

Moore JC, Tobin H (1997) Estimated fluid pressures of the Barbados accretionary prism and adjacent sediments. In: Proc. ODP, Sci. Results, Ocean Drilling Program, Collage Station, TX, vol 156, pp 229–237

Moore JC, Shipley TH, Goldberg D, Ogawa Y, Filice F, Fisher A, Jurado MJ, Moore GF, Rabaute A, Yin H, Zwart G, Brückmann W, Henry P, Ashi J, Blum P, Meyer A, Housen B, Kastner M, Labaume P, Laier T, Leitch EC, Maltman AJ, Peacock S, Steiger TH, Tobin HJ, Underwood MB, Xu Y, Zheng Y (1995) Abnormal fluid pressures and fault-zone dilation in the Barbados accretionary prism: Evidence from logging while drilling. Geology 23(7):605–608

Morris JD, Villinger HW, Klaus AS (2003) Init. repts. In: Proc. ODP, Available from World Wide Web:http://www-odp.tamu.edu/publications/205_IR/205ir.htm, vol 205 [Online]

Paroscientific, Inc (2001) Submersible depth sensors - Series 8000. http://www.paroscientific.com

Raghavan R, Ozkan E (1994) A method for computing unsteady flows in porous media. No. 318 in Pitman Research Notes in Mathematics, Longman Scientific & Technical

Saffer DM (2007) Pore pressure within underthrust sediment in subduction zones. In: Dixon T, Moore C (eds) The seismogenic zone of subduction thrust faults, Columbia University Press, New York

Schultheiss PJ, McPhail SD (1986) Direct indication of pore-water advection from pore pressure measurements in Madeira Abyssal Plain sediments. Nature 320(3):348–350

Screaton EJ, Fisher AT, Carson B, Becker K (1997) Barbados Ridge hydrologic tests: Implications for fluid migration along an active decollement. Geology 25(3):239–242

Stegmann S, Kopf A (2007) Marine deep-water free-fall cpt measurements for landslide characterisationoff Crete, Greece (Eastern Mediterranean Sea) part 1: A new 4000m cone penetrometer. In: Lykousis V, Sakellariou D, Locat J (eds) Submarine Mass Movements and Their Consequences, Springer Netherlands, pp 171–177.

Stegmann S, Villinger H, Kopf A (2006) Design of a modular, marine free-fall cone penetrometer. Sea Technology pp 27 – 33

Strout JM, Tjelta TI (2005) In situ pore pressures: What is their significance and how can they be reliably measured? Marine and Petroleum Geology 22(1-2):275–285, URL http://www.sciencedirect.com/science/article/B6V9Y-4FFH21X-3/1/9bc97590a6f03a19f1f268e9e3f56f6b

Tréhu AM, Bohrmann G, Rack FR, Torres ME, Shipboard Scientific Party (2003) Init. repts. In: Proc. ODP, Available from World Wide Web:http://www-odp.tamu.edu/publications/204_IR/204ir.htm, vol 204 [Online]

Whittle AJ, Sutabutr T, Germaine JT, Varney A (2001) Prediction and interpretation of pore pressure dissipation for a tapered piezoprobe. Geotechnique 51(7):601–617

4 Interpretation of temperature and pressure measurements

The studies presented in this Chapter show how the combination of different types of temperature measurements with other geophysical and geological data sheds light on processes at convergent margins. The first manuscript (*Heesemann et al.*, submitted 2008a, pp. 109) presents a numerical finite element (FE) model which is used to estimate the temperature at the subduction thrust fault of the 1992 Nicaragua tsunami earthquake. In the remaining two publications, inputs and outputs of the subduction factory are detected using violin-bow heat-flux probe measurements. Firstly, *Contreras-Reyes et al.* (2007, pp. 124) interpret reduced seismic velocities as evidence that structures of the oceanic crust and the uppermost mantle are altered by fracturing and hydration before they enter the subduction zone. Using the heat-flux data it was possible to identify a location where cold seawater infiltrates the oceanic crust. Secondly, *Grevemeyer et al.* (2004, pp. 144) inferred active fluid venting through the mud dome Mound Culebra, located on the continental slope offshore Nicoya Peninsula, Costa Rica, from violin bow heat-flux probe measurements, and data from other geophysical surveys and gravity coring.

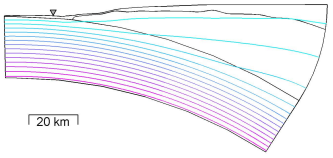

FE Model of subduction zone

Manuscript: Thermal constraints on the frictional conditions of the nucleation and rupture area of the 1992 Nicaragua tsunami earthquake

Heesemann, M., I. Grevemeyer, and H. Villinger (submitted 2008a), Thermal constraints on the frictional conditions of the nucleation and rupture area of the 1992 Nicaragua tsunami earthquake, *Geophysical Journal International*, submitted.

Contributions

In following manuscript, a finite element model is used to compute the temperature field at the rupture area of the 1992 Nicaragua tsunami earthquake. Model parameters (e.g. the convergence rate of the Cocos plate in respect to the overriding Caribbean plate) were, if possible, constrained by geophysical and geological observations. Subsequently, a genetic algorithm was used to find combinations of model parameters that meet all parameters constraints and generate model results that agree with heat-flux measurements which supply independent constraints for the model.
Martin Heesemann compiled the manuscript, designed and implemented the finite element model and the genetic algorithm, compiled the model constraints, processed the heat-flux data, and analyzed the results. Ingo Grevemeyer compiled the seismological facts about the 1992 Nicaragua earthquakes and supervised the research along with Heinrich Villinger.

Thermal constraints on the frictional conditions of the nucleation and rupture area of the 1992 Nicaragua tsunami earthquake

Martin Heesemann[1,⋆], Ingo Grevemeyer[2], Heinrich Villinger[1]
[1]*Department of Geosciences, University of Bremen, Bremen, Germany.*
[2]*IFM-GEOMAR, Leibniz-Institute of Marine Sciences, Kiel, Germany.*

14 October 2008

SUMMARY
The 1992 Nicaragua earthquake was a tsunami earthquake, which generated tsunamis disproportionately large for its surface wave magnitude $M_s = 7.2$. Seismological studies and tsunami simulation indicated that the event was a slow earthquake which occurred on the plate boundary between the subducting Cocos plate and the overriding Caribbean plate. We present a finite element model that enables us to estimate for the first time the temperature and inferred frictional conditions in the rupture area of a tsunami earthquake. Direct and indirect observations are used to constrain all model parameters, and surface heat flux measurements provide independent information to verify the model results. Furthermore, we used a genetic algorithm to perform a sensitivity analysis of all model parameters and to define the spatial range of thermally defined updip limit of the seismogenic zone. The earthquake nucleated in the seismogenic zone at temperatures of ∼150 °C and propagated up-dip toward the trench axis. The centroid or center of mass of moment release was located in a region characterized by temperatures of ∼50 °C. Thus, the rupture propagated through a region with velocity strengthening properties, where plate motion is normally accommodated by aseismic creep. Our observations support a model in which tsunami earthquakes nucleate in the seismogenic zone near its updip limit. However, in such an environment coupled asperities are perhaps too small to cause large earthquakes. Seamounts, however, are abundant on the incoming Cocos plate. Therefore, in addition to temperature-dependent metamorphic induration of sediments, increased normal stress by seamount subduction may contribute to accumulate stress sufficiently large to release enough energy near the up-dip limit of the seismogenic zone to promote dynamic slip along a normally aseismic décollement all way to the ocean.

Key words: Subduction zone processes, Heat flow, Numerical solutions, Seismicity and tectonics, Heat generation and transport.

1 INTRODUCTION

Any great shallow subduction zone earthquake is expected to be followed by a substantial tsunami caused by the large displacement of water near the seafloor. However, a subclass of events called tsunami earthquakes excites considerably larger tsunamis than expected from its seismic magnitude Kanamori (1972). For instance, although they were much smaller in seismic moment magnitude (M_w), the tsunamis generated by two historic tsunami earthquakes, the 1946 Aleutian earthquake ($M_w = 8.2$) and the 1896 Sanriku earthquake ($M_w = 8.0$), produced devastating tsunamis of similar magnitudes as the 1960 Chile ($M_w = 9.6$), the 1964 Alaska ($M_w = 9.2$), and the 2004 Sumatra ($M_w > 9$) earthquakes (Geist 2002; Geist et al. 2006).

Because of the discrepancy between seismic and tsunami magnitude, tsunami earthquakes are particularly dangerous. The 1896 Sanriku earthquake, for example, was felt only moderately along the Japanese coast, but very large tsunamis hit the coast ca. 30 minutes later and drowned more than 22,000 people. Due to the absence of strong ground motion, people did not evacuate to safe areas. Consequently, for disaster mitigation, it is particularly important to understand the processes governing tsunamigenic earthquakes.

To study tsunami earthquakes, the 1992 Nicaragua event is particularly well suited since it is the largest tsunami earthquake ($M_w = 7.7$, $M_t = 7.9$) ever recorded by global seismic broadband networks (Kanamori & Kikuchi 1993; Satake & Tanioka 1999). Digital data have been a treasure trove for detailed studies of seismic body waves, surface waves and tsunami simulation to calculate the nucleation and rupture history of the slow earthquake (Ide et al. 1993; Velasco et al. 1994; Satake 1994; Ihmle 1996a). Moreover, the convergent margin off Nicaragua and Costa Rica is well studied e.g. by numerous deep sea drilling sites, active and passive seismic surveys, surface heat flux measurements, and GPS installations.

⋆ Corresponding author: Martin Heesemann (heesema@uni-bremen.de)

Compared to other thrust earthquakes, tsunami earthquakes usually have a longer source time function, and a slower and smoother rupture. Seismic body waveform inversions of tsunami earthquakes indicate shallow dipping thrust fault mechanisms (dip angle ∼6-10°), occurring at shallow depth (<15-20 km) near the trench axis and seaward of most other thrust zone events (Pelayo & Wiens 1992). Overall, these observations suggest that the slow rupture results from seismic slip along a weak basal décollement cutting through shallow sedimentary rocks (Pelayo & Wiens 1992). Due to the low rigidity of these sedimentary rocks, shallow thrust faulting will cause larger seismic slip and hence increase tsunami amplitudes (Geist & Bilek 2001).

This interpretation contradicts the concept that subduction thrust earthquakes result from stick-slip frictional instability, as proposed by Scholz (1998). At shallow depth, unconsolidated sediments in the subduction thrust should cause stable sliding and hence prevent earthquake nucleation and rupture propagation. There is a transition from stable sliding to unstable stick-slip behavior at greater depths. This transition, defining the updip limit of the seismocenic zone, occurs when either the backstop of competent continental rock is reached (Byrne et al. 1988) or dehydration and metamorphic induration of the subducting sediments takes place at temperatures of 100-150 °C (Hyndman & Wang 1993; Moore et al. 2001). Thrust earthquakes are expected in the stick-slip condition environment below the updip limit.

Accordingly, tsunami earthquakes may nucleate below the seismogenic updip limit with enough energy to dynamically propagate up-dip and cause slip along the normally aseismic basal décollement (Scholz 1998; Seno 2002). Alternatively, they may nucleate at shallow non-sedimentary asperities where seamounts or abyssal hills cause contact zones with the overriding plate (Polet & Kanamori 2000; Bilek & Lay 2002).

We developed a thermal finite element (FE) model to yield the thermal state of the coupling zone and hence to constrain the thermally defined updip limit of the rupture area. Firstly, we used the reported results of seismic and GPS surveys to constrain the model geometry. Secondly, model parameters were derived from physical properties measured at several Ocean Drilling Program (ODP) drill sites, previously reported seafloor heat flux data, and the sediment distribution on the subducting oceanic crust. Finally, new heat flux data, measured on the continental slope off Nicaragua, provided independent constraints for a genetic algorithm (GA), which we used to find model parameters in agreement with our data and to estimate the uncertainties in the computed thermal state of the rupture zone.

2 THE 1992 NICARAGUA EARTHQUAKE

The September 2, 1992 Nicaragua earthquake, which originated at the coupling zone between the subduction Cocos Plate and the overriding Caribbean Plate (cf. Figure 1), generated tsunamis that caused extensive damage on the Pacific coast of Nicaragua despite its moderate seismic surface wave magnitude of $M_s = 7.2$. Field surveys for seismic intensity and tsunami run-up height showed that the seismic intensity was small (III of the Modified Mercalli scale), but the tsunami run-up was ∼10 m above mean sea level (Baptisa et al. 1993; Satake et al. 1993) and caused at least 170 causalities.

The epicenter of the 1992 Nicaragua event, computed by the National Earthquake Information Center (NEIC), using short-period teleseismic data, is located near the shelf break, approximately 65-70 km from the trench axis (red star Figures 1, 2, and 6). Seismic body waveform inversion indicates a thrust faulting mechanism with a dip of 14-15° and a depth of ∼21 km (Ide et al. 1993). This corresponds roughly to the depth and dip of the plate interface as derived from reflection and refraction seismic data (cf. Figure 2) (Walther et al. 2000; Ranero et al. 2000). Due to the long duration and slow rupture velocity of the earthquake, seismologists observed differences of 45-52 s between the centroid time and the NEIC origin time (Kanamori & Kikuchi 1993; Ide et al. 1993). Centroids represent the center of mass of moment release and are calculated from long-period surface waves. While short-period data indicates the nucleation area of the tsunami event, long-period data can be used to study the propagation of seismic slip. Ihmle (1996a) studied different wave bands and found that with decreasing frequencies centroids move toward the trench. The center of lowest frequency radiation is situated closest to the trench, about 40 km seaward of the NEIC epicenters, while intermediate frequencies centroids range between low frequency centroids and the epicenter (Figure 1B). Spectral inversion of long-period Rayleigh and Love waves (157-288 s) yield similar results, indicating a centroid location 54 km SW of the NEIC epicenter, at <10 km depth, with a fault zone dipping at ∼6° (blue star Figures 1, 2, and 6), and a predominant rupture azimuth of 140° (Velasco et al. 1994). The shallow depth and low dip angle correspond roughly to the geometry of the plate interface up-dip from the NEIC epicenters and supports rupture propagation toward the trench (Figure 2). Tsunami simulation supports the fact that rupture reached into the trench (Bilek & Lay 2002; Satake 1994).

Most aftershocks occur in a 40 km wide zone parallel to the trench (Figure 1), which stretches 100 km to the NW and 150 km to the SE of the epicenter (Ihmle 1996a). Only a few events occurred seaward of the epicenter near the trench axis and available Harvard centroid moment tensor (CMT) solutions indicate normal faulting mechanisms. Thus, earthquakes near the trench axis may represent intraplate events being related to bending of the subducting lithosphere rather than being related to earthquake processes in the subduction thrust. Nevertheless, large interplate earthquakes may affect the regional stress field and may therefore trigger intraplate earthquakes (Christensen & Ruff 1983). Harvard CMT solutions of aftershocks further landward indicate thrust faulting mechanisms. In contrast to the mainshock, the aftershock distribution suggests that most events ruptured down-dip. It is important to note that the location of the aftershocks correspond well with the seismic front (Byrne et al. 1988; Newman et al. 2002), which marks the up-dip limit of the seismogenic zone. Byrne et al. (1988) suggest that the shallow subduction thrust seaward of the seismic front is velocity strengthening. Therefore, the mainshock propagated into a regime expected to be characterized by stable sliding (Scholz 1998) and hence slip occurred along a normally aseismic and weak décollement.

3 THE NUMERICAL MODEL

To constrain the thermal updip limit of the seismogenic zone, we study the temperature of the décollement zone using a steady state FE model, which is based on the Comsol Multiphysics® toolbox, and Matlab®. The geometry of the FE model (Figure 2) is derived from time migrated and depth converted reflection seismic data, using velocities from focusing analysis (Ranero et al. 2000) and seismic refraction work (Walther et al. 2000). These data indicate two different main units building the continental margin: slope sediments and an underlying basement consisting of oceanic ig-

Figure 1. (*next page*): Artificially illuminated seafloor relief in the area of the 1992 Nicaragua tsunami event. The red star is the NEIC epicenter, indicating the area where the rupture started. Blue stars are centroids (Newman et al. 2002; Velasco et al. 1994). The aftershocks (white circles) relocated by Ihmle (1996a) occurred in a three-month period following the main event. The first part of model transect (NIC80) is marked by dashed gray line. At model temperatures >100 °C the line turns red and model temperatures >150 °C are marked by a solid red line. The 150 °C isotherm is extrapolated to both sides of the transect. A. The moment release within the slip area (boxed region) (Ihmle 1996b) was used for tsunami simulation (Geist & Bilek 2001). Harvard CMT solutions, which have been assigned to relocated events, are shown for the main shock and largest aftershocks. Yellow dots are earthquakes relocated by (Newman et al. 2002). B. The triangles are spatial centroids (Ihmle 1996a), illustrating the slow rupture process; with decreasing frequency spatial centroids moved further trenchward. Small red dots on the seismic profile (Walther et al. 2000) mark locations where heat flux measurements were obtained during the RV Meteor cruise M54-2. The arrow illustrates the velocity of the Cocos Plate with respect to the Caribbean Plate.

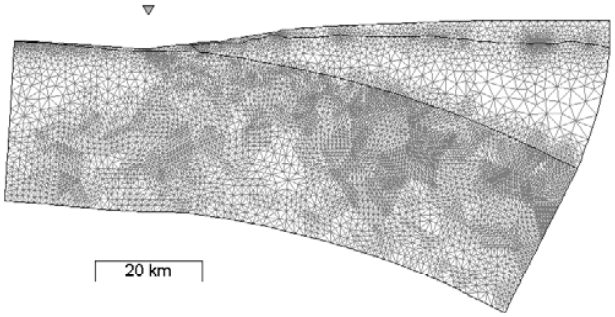

Figure 2. Complete geometry and mesh of the FEM model. The mesh, shown without vertical exaggeration, consists of 20289 triangular elements and has 40914 degrees of freedom. The triangle above the geometry marks the location of the deformation front.

neous rocks. Therefore, the model geometry is divided into three domains: a sedimentary layer (Seds), the continental basement (CnBs), and the subducting oceanic crust (OcCr).

The upper boundaries of the domains are approximated by cubic B-splines using a modified version of the "splinefit" script implemented by Nielsen (2005). B-splines offer a high level of flexibility during geometry assembly and avoid geometric singularities at the same time, by ensuring smooth boundaries (existence of continuous second derivative). Then, a method described by Casciola & Romani (2004) is used to transform the B-splines into an equivalent series of cubic Bézier curves that can directly be handled by Comsol Multiphysics®. See Figure 2 for an illustration of the complete meshed geometry with 40914 degrees of freedom, and 20289 triangular elements.

The 2D-model is based on the non-conservative steady state heat conduction and advection equation

$$\nabla \cdot (-k\,\nabla T) = Q - \rho c_p\,\vec{v}\cdot\nabla T \tag{1}$$

which assumes incompressible flow and ensures that no unphysical source term arises from a flow field where the incompressibility constraint is not absolutely fulfilled (Comsol 2005, pp. 162). Hence, the temperature distribution in the model domains depends not only on the geometry but also on the boundary conditions at the edges of the domains, the thermal conductivity (k), the volumetric heat capacity (ρc_p), the heat production (Q), and the velocity ($\vec{v}$) determining the advective heat transport.

3.1 Parameter constraints

Since all model parameters interact and influence the temperature distribution at the décollement, it is important to constrain them as good as possible by direct and indirect observations. Defining the velocity field, we assume that the Cocos Plate subducts beneath a stationary Caribbean Plate and computed a convergence rate of 82 mm/a, using the Plate Motion Calculator (UNAVCO 2006) and the corresponding rotation pole published by DeMets (2001). Accordingly, the OcCr is the only domain with advective heat transport and the magnitude of its velocity (78 mm/a) is given by plate velocity component that is parallel to the model transect (cf. Figure 1B). The direction of the modeled velocity field is parallel to the upper boundary of the oceanic crust.

The thermal properties and the boundary conditions of the OcCr domain are based on global models of oceanic crust cooling histories evaluated by Stein & Stein (1992). We chose the half space cooling model

$$T(t,\ z) = (T_i - T_{sf})\mathrm{erf}\left(\frac{z}{2\sqrt{\kappa\ t}}\right) \tag{2}$$

with

$$\kappa = k/(\rho c_p)$$

to prescribe the temperature field at the seaward and lower boundaries of the 24 Ma old (Barckhausen et al. 2001) subducting oceanic crust. Following values for the model parameters were reported by Stein & Stein (1992): $k = 3.138$ W/(m K), $c_p = 1.171$ kJ/(kg K), and $\rho = 3330$ kg/m^3. Furthermore, no heat production in the OcCr domain, and an initial crust temperature T_i of 1450 °C and a constant seafloor temperature T_{sf} of 0 °C are assumed.

We adopted these parameter values, constrained by global heat flux and bathymetry data (Stein & Stein 1992), except for the temperature of the upper oceanic crust. Harris & Wang (2002) found that it is important to modify this simple half space cooling model to account for advective cooling of the upper oceanic crust by circulating seawater. This is especially important in models that are designed to investigate the frontal part of the subduction zone including the updip limit of the seismogenic zone. Having a closer look at the oceanic crust – seawater interface, there are two facts that deviate from the assumption of a constant temperature of 0 °C. Firstly, we observed bottom water temperatures of 2 °C during our heat-flux measurements. Secondly, the oceanic crust is not in direct contact with the water column but insulated with a blanket of sediments and cooled by fluid advection beneath the cover at the same time. To account for the first observation, one can add 2 °C to all temperatures in the model. To include the second observation, we calculated the temperature difference between bottom water and oceanic crust - sediment interface (ΔT), assuming the heat transfer in the sediments to be purely conductive, by using Fourier's law of conduction:

$$q = k\,\Delta T/\Delta z \iff \Delta T = q\ I \tag{3}$$

Here, k is the thermal conductivity, Δz the thickness of the sediments, q the surface heat-flux, and I the thermal insulance, the quotient of Δz and k. The depth dependency of I (Fig. 3B) was computed based on the geometric mean thermal conductivities (Fig. 3A) of sediments covering the subducting oceanic crust segment. The thermal conductivities were measured on split cores

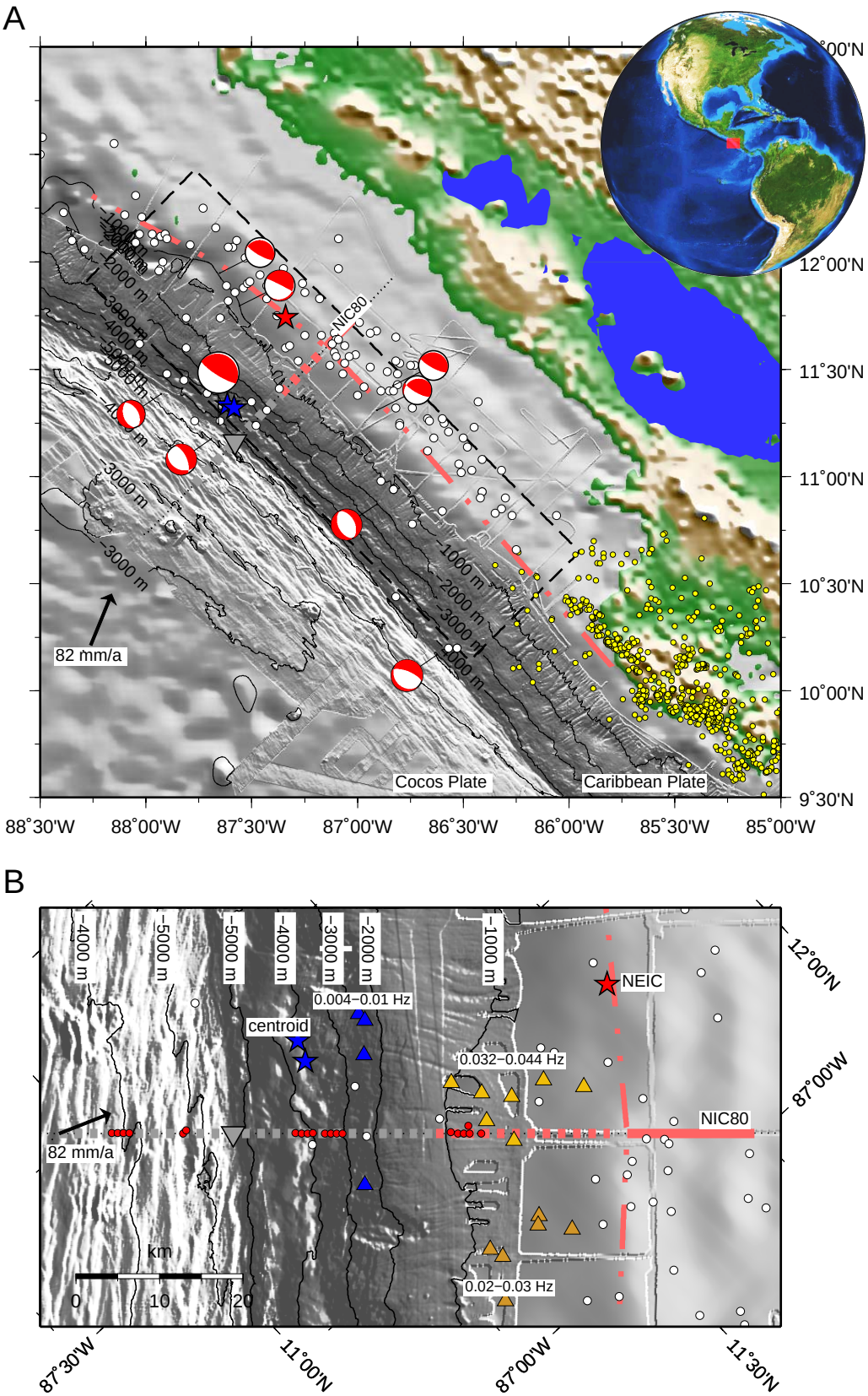

Figure 1. (*previous page*)

from ODP Sites 844, 845 (Mayer et al. 1992), and 1256 (Wilson et al. 2003), the locations of which are shown in Figure 4. Along with abundant heat-flux data from (Vaquier et al. 1967; Bookman et al. 1972; Sclater et al. 1970; Langseth et al. 1971) that is included in the global heat-flux compilation of Pollack et al. (1992) (Fig. 3C), and sediment thickness data (Fig. 3D) published by Divins (2005), the local thermal insulance was used to compute temperatures at the sediment – basement interface (Fig. 3D), assuming a constant bottom water temperature of 0 °C.

Estimated averages over time of the computed temperatures are used to prescribe the temperature of the upper OcCr boundary until it reaches the deformation front. Past the deformation front, a continuous boundary condition is applied, assuming the ceasing of advective circulation in the upper oceanic crust when it is subducted. Note that in the model surface heat flux values seaward of the deformation front are used as boundary conditions and cannot be used to verify the model by comparison to field measurements.

The thermal properties of the Seds and CnBs domains are derived from measurements at three ODP Sites (Fig. 5). Thermal conductivities were directly measured on cored material whereas the rate of radiogenic heat production (Q_r) is computed using downhole logging data and the empiric equation

$$Q_\mathrm{r}\,[\mu\mathrm{W/m^3}] = 10^{-5}\rho(9.51c_\mathrm{U} + 2.56c_\mathrm{Th} + 3.48c_\mathrm{K}).$$

Here, ρ is the rock density (kg/m^3), c_U (ppm), c_{Th} (ppm), and c_K (wt%) are radioactive-element contents (Buecker & Rybach 1996; Grevemeyer et al. 2003). Density data is provided by the Hostile Environment Lithodensity Tool (HLDT), and the contents of the radioactive-elements were measured using the Natural Gamma Ray Spectrometry Tool (NGT).

In the data, the Seds domain is represented by a ∼150 m thick section of slope sediments which is probed ∼1 km landwards of the Middle America Trench off Costa Rica at ODP Site 1040 (Kimura et al. 1997) (cf. inset Fig. 4). The CnBs domain, which presumably consists of oceanic igneous rocks, is represented by two ∼70 m and ∼390 m thick sections of oceanic basement penetrated at ODP Sites 1253 (Morris et al. 2003), and 1256 (Wilson et al. 2003), respectively. The oceanic rocks at Site 1253 are recovered from two different intervals: a 30 m thick upper igneous unit (gabbro sill), and a 40 m lower igneous, separated by a 30 m thick sedimentary unit.

3.2 Initial model

We used the parameter constraints, derived in the previous section and summarized in Figures 3 and 5, to define a set of parameters for an initial model and a constraining range for each model parameter both shown in Table 1. Surprisingly, all values of our initial model parameters are notably lower than used by other authors in similar models. As an example, the parameters used by Harris & Wang (2002) for a thermal model of the subduction zone off Nicoya Peninsula, Costa Rica, are listed in Table 1. Measured surface heat flux values on the subduction plate are exceptionally low (Langseth & Silver 1996), signaling low upper oceanic crust temperatures, and new measurements on our modeled transect are even below the regional average (see Fig. 3). Moreover, average sediment thermal conductivies below 1 W/(m K) are lower than usually found in ODP boreholes (cf. supplementary material), and finally the thermal conductivity and radiogenic heat production values of the igneous oceanic rocks that are believed to build the continental basement are much lower than found in usual continental basement. Therefore, parameter values for the CnBs domain often used by other authors are beyond of our constrained range. To verify the chosen parameters, we compared surface heat flux values computed with our initial parameter set (Fig. 6A), as well as with the parameters used by Harris & Wang (2002) (Fig. 6B), to new heat flux data from the continental slope.

During RV Meteor cruise M54-2 in summer 2002, we obtained 25 surface heat flux measurements on the continental slope off Nicaragua (Grevemeyer et al. 2005). 15 of these measurements are located on our modeled transect, the seismic multi-channel line NIC80, shot with a 6-km steamer in 2000 by the University of Texas at Austin. Two different heat flux probes of violin bow design (Hyndman et al. 1979) were used to acquire the data. The instruments have 11 and 22 thermistors, which are spaced in 0.27 m intervals and mounted inside an oil filled hydraulic tube that penetrates into a sedimented seafloor. Thus, the probes are able to obtain thermal gradients over a length of 3 and 6 m, respectively. Both probes are equipped with on-line data transmission for operation control and independent data storage inside the instrument for double data security. During every other probe penetration, in situ thermal conductivity measurements were made by applying a 20 s pulse of electric current along heater wires within the tubing. The recorded temperature decays caused by this calibrated heat pulse allow to estimate the thermal conductivities of the sediments surrounding temperature sensor (Hartmann & Villinger 2002).

In addition to measurements with the heat-flux probes, thermal gradients were measured by autonomous temperature loggers (Pfender & Villinger 2002) mounted on gravity corers. Thermal conductivities from the recovered core material have been measured using needle probes von Herzen & Maxwell (1959), which were inserted into undisturbed areas of split cores. After penetration into the sedimented seabed, the sensors record a pulse of frictional heating which decays while the tools remains in the seafloor for 7–10 min. Then, temperatures and thermal conductivity measurements are jointly inverted to obtain the surface heat flux. Individual heat flux values and the number of temperature measurements used to derive the thermal gradients are published in Grevemeyer et al. (2005).

In addition to the measured heat flux data, we calculated seafloor heat flux values from bottom simulating reflectors (BSR), which were imaged on the middle part of the slope off Nicaragua. Due to the uncertainties in the absolute magnitude of the BSR-derived heat flux values, we used the procedure described by Grevemeyer & Villinger (2001) to calibrate the data with heat flux probe measurements at the same location. Unfortunately, this calibration is ambiguous since our relevant heat flux probe measurements, located ∼40 km landward from the deformation front, can be categorized into two distinct groups. Consequently, we considered two calibrations with surface heat flux values which represent endmembers of the measured data: scenario one based on the lower heat flux values (6A), and scenario two based on higher values (6B).

Our initial model provides an excellent fit to the first scenario (Fig. 6A), while the model parameters used by Harris & Wang (2002) favor the second scenario (Fig. 6B). The good fit with the initial model and the fact, that the spatially spread out group of lower heat flux values is more likely to represent an undisturbed background, whereas the group of higher heat flux values appears to be a localized anomaly, support the first scenario. Nevertheless, we designed a set of numerical experiments based on a genetic algorithm (GA) to test each scenario and to determine the uncertainties in the modeled temperature distribution on the plate interface.

Figure 3. (*next page*): A. Mean (stars) and standard deviation (boxes) of thermal conductivities measured in sedimentary sections of ODP Sites 844, 845 (Mayer et al. 1992), and 1256 (Wilson et al. 2003). B. Mean thermal insulance of the sedimentary column at the ODP Sites. Errors are derived from standard deviation of thermal conductivities. The fit of dotted line is used for linear extrapolation of the thermal insulation to greater sediment thicknesses. C. Heat-flux measurements on the subducting Cocos Plate, reported by Pollack et al. (1992) (plain symbols) and Grevemeyer et al. (2005) (bold symbols), vs. the crustal age (Barckhausen et al. 2001). D. Thickness of sediment cover at the locations of the heat-flux measurements. If not otherwise available the sediment cover is interpolated using global data published by Divins (2005). E. Temperatures at the sediment-basement interface (filled symbols) are the product of the conductive surface heat flux (C.) and the thermal insulance of the sedimentary column (B.) with the thickness (D.) at the specific location. Stars and boxes show the binned mean values and standard deviations of the upper crust temperatures. The dashed line represents the temperatures that would results from a conductive cooling model (C.) and a linearly increasing sedimentary column (D.).

3.3 Genetic algorithm

The term genetic algorithm (GA) refers to a family of computational codes that are inspired by evolutionary processes. GAs are often used in function optimization, even though the range of possible uses is much broader (Whitley 1994). We chose a GA, because it allows us to find a whole range of optimized solutions while exploring the parameter space in a relatively short period of time. To solve a problem using a GA, a chromosome-like data structure has to be defined which is capable to represent all possible solutions. Then, evolutionary operators are applied to consecutive generations of chromosome sets in order to iteratively increase the overall fitness of the generations. We defined a chromosome as a vector of five floating point numbers containing the variable model parameters, namely the temperature of the upper oceanic crust seawards of the deformation front (T_{in}), the thermal conductivities and heat production rates of the Seds and the CnBs domains. The allowed range for each parameter (cf. GA range in Table 1) is intentionally chosen much wider than we expect from the parameter constraints provided above. This allows the GA to test solutions that deviate from our expectations.

The algorithm starts with a random initial generation consisting of 100 chromosomes which is subdivided into 5 populations of 20 chromosomes each (Fig. 7). Consecutively, the fitness of each chromosome is evaluated by the subprocess "Compute objectives". The returned objective value depends on the intention with which each of the experiments, described below, is designed. However, the misfit between measured heat flux data and the heat flux values computed using the FE model is always a basic component of the objective value. The fit is done using pieces of linear approximations (red dashed lines in Figure 6) of the measured surface heat-flux data to prevent weighting effects of unevenly distributed data and "locking" of spikes, present in the modeled data between measured data points. An example for "locking" being an issue are the heat flux probe measurements at $\sim$10 km from the deformation front shown in Figure 6A. The subprocess also keeps a record of evaluated chromosomes in order to avoid multiple evaluations of a FEM model with the same set of parameters, since the model runs, lasting $\sim$30 s each, are demanding most of the computational time.

Choosing parameters controlling the evolutionary operators provided by the Genetic Algorithm Toolbox for use with Matlab (Chipperfield et al. 1994) involves a trade off between fast convergence of the GA with a single possibly locally optimal solution, and a broader exploration of the parameter space. In our experiments, we favored a broader exploration, since we are interested in the whole range of parameter combinations that solve our problem within the given constraints rather than in a single theoretically best solution.

As shown in Figure 7, each iteration starts with a ranking of the individual chromosomes which is based on their objective value. Using this ranking, individuals within the different subpopulations of the current generation are selected and recombined to produce a pool of 80 children. Following, some of the generated children are randomly changed by the mutation operator to enhance the genetic diversity. The newly generated children are then rasterized, by rounding, to a discrete parameter grid so that negligible parameter variations are mapped onto the same chromosome. After several iterations, this procedure dramatically reduces the number of new FE models that have to be evaluated in each iteration, without loosing a significant amount of information.

Then, a number of children is selected which is reinserted into the parent generation by replacement. Conditionally, some individuals are exchanged between subpopulations by the migration operator in case the generation counter, which is increased with every iteration, reaches predefined levels. Finally, the next iteration step is initiated unless a stop criteria is fulfilled. The stop criteria used by us depend on the amount of computational time has passed, and on the generation diversity. A diversity below a certain threshold indicates that the GA converged against a single solution.

4 NUMERICAL EXPERIMENTS

In a first numerical experiment, we tried to discriminate the two scenarios where the BSR derived heat flux values are calibrated with the lower or the higher heat flux probe measurements. To do this, we applied the GA two consecutive times with different objective functions. The two objectives were to minimize the misfit between the modeled surface heat flux and the observed values in respect to the different scenarios. The parameter and result distributions of this and the following numerical experiment are jointly shown in Figure 8.

Models that represent the low heat flux scenario are represented by white and black bar segments. Black segments contain models that fit the scenario with a maximum average misfit of 2.5 mW/m^2 (gray area in the Fit panel), while white bar segments represent the models that additionally fall into the constrained range of all model parameters (highlighted areas in the parameter panels correspond to constraints listed in Table 1). One example for a model that is represented by a white bar segment (good model) is our initial model, which is marked by solid vertical lines in Figure 8. The solid lines are within the gray areas of all panels. Also the two models that result in smallest and biggest distance of the 150 °C isotherm from the deformation front (listed as deep and shallow in Table 1) while meeting all constraints at the same time are therefore represented by white bar segments.

Having a look at the black segments, it appears that the low heat flux scenario is satisfied by a wide range of models within the parameter constraints as well as going much beyond them. Actually, the model that provides the best fit to the low heat flux scenario (cf. Table 1) is represented by a black bar segment, since it is based on a very unlikely parameter combination, where the Seds thermal conductivity (1.8 W/(m K)) is higher than of the CnBs

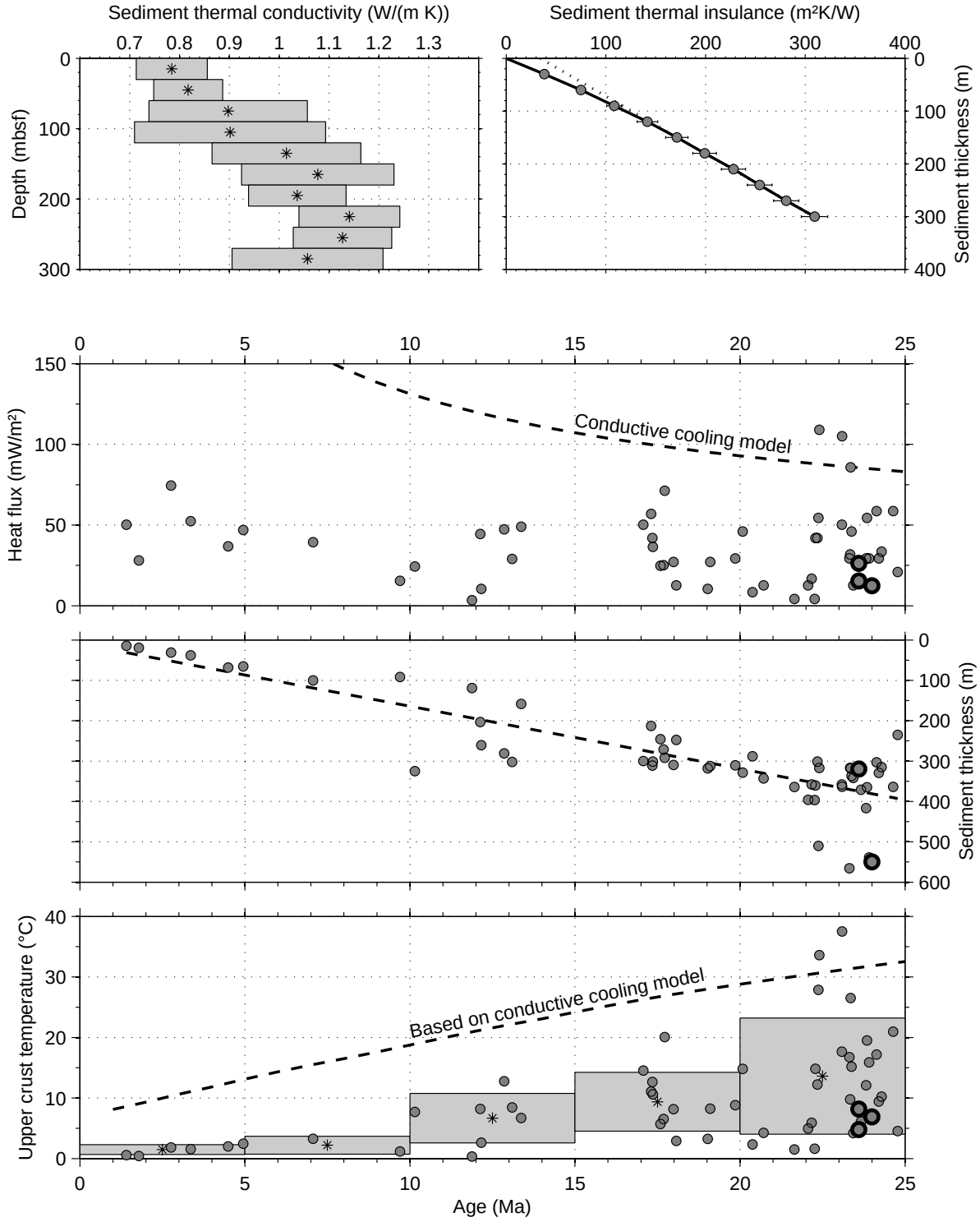

Figure 3. (*previous page*)

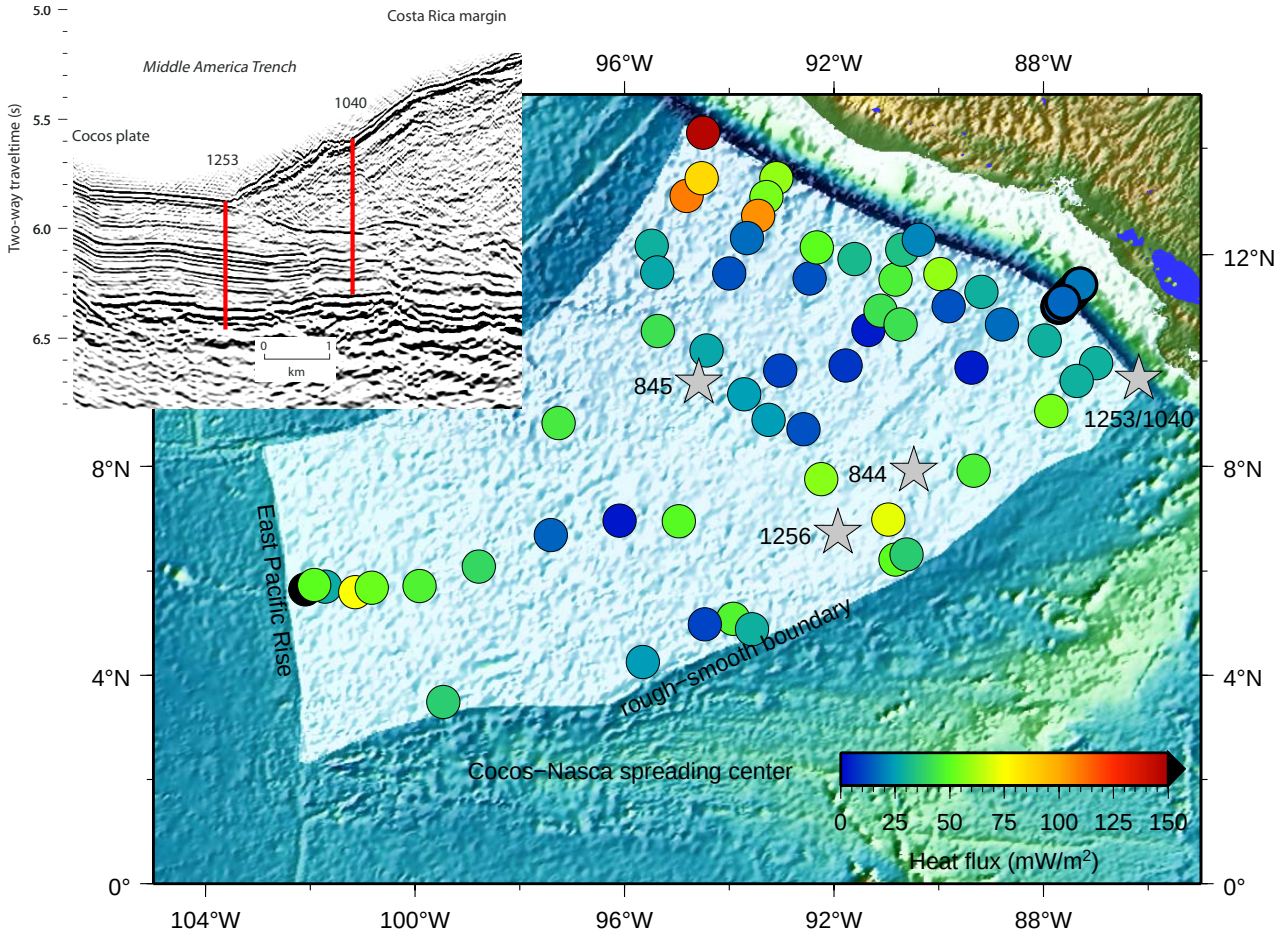

Figure 4. Locations of ODP Sites and seafloor heat flux measurements over elevation model (NGDC 2005). Inset shows detailed locations of ODP Sites 1253 and 1040 off Costa Rica. The oceanic crust segment that originates from the East Pacific Rise and subducts off Nicaragua is highlighted.

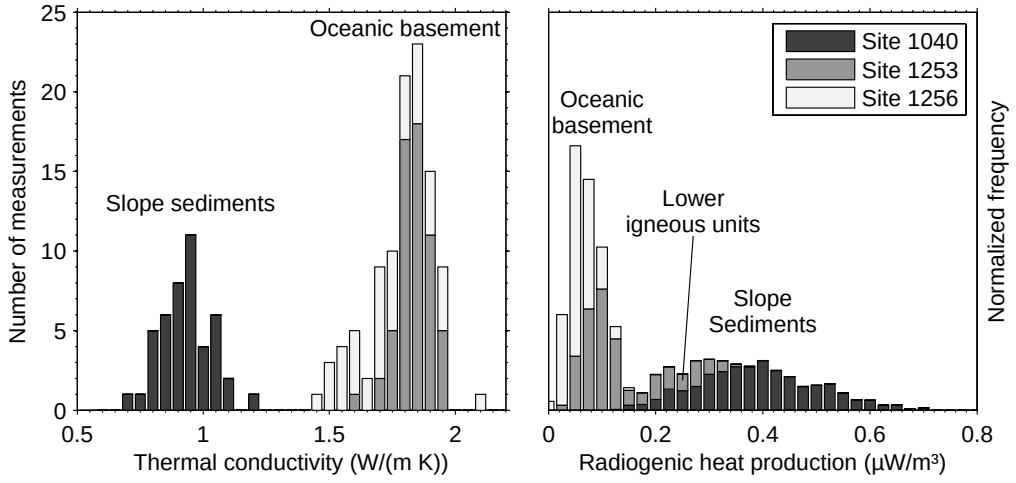

Figure 5. Thermal conductivies measured on core-samples (A) and radiogenic heat production derived from downhole logging data (B) at three ODP Sites (cf. Fig. 4).

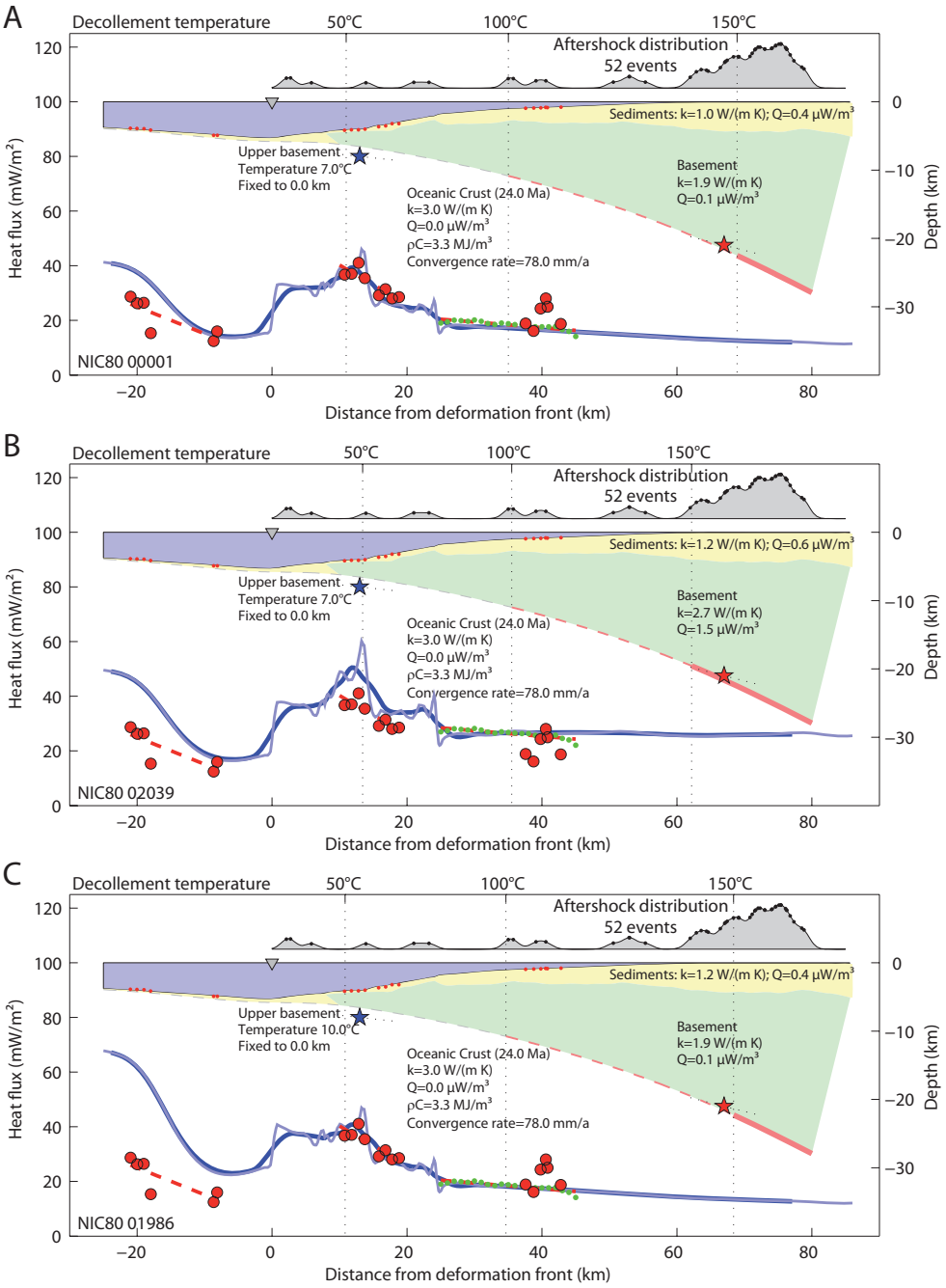

Figure 6. Results from model runs using different sets of parameters used for the three model domains. Smoothed model surface heat-flux values (dark blue line) are compared to measured values (red circles) and estimates from BSR depth (green dots). Locations of the heat flux measurements with respect to the model geometry are shown as red dots. A. Initial model based on parameters constrained by parameter observation. B. Model with parameters chosen by Harris & Wang (2002). C. Model found by GA which keeps all parameters in the constrained range and provides a good fit with surface heat-flux data at the same time

(1.6 W/(m K)). Moreover, it is evident that the low heat flux scenario is best satisfied by models with low CnBs thermal conductivities. Values exceeding 2.5 W/(m K), expected for regular continental basement, are not conform with the low heat flux scenario.

Models that meet the high heat flux scenario within a maximum mean misfit of 2.5 mW/m^2 are symbolized by dark gray bar segments, and models with a misfit exceeding 2.5 mW/m^2 in respect to either heat flux scenario (i.e. the model represented by the dashed lines (Harris & Wang 2002)) are shown as light gray bar segments. Having a look at the dark gray bar segments, it turns

Table 1. Parameters and results of selected models. Numbers in parentheses in the highlighted lines result from the other given ranges. All misfit values, except for the Harris & Wang (2002) model, are in respect to the scenario with low BSR derived heat-flux values.

Domain	Variable parameters					Results			Reference
	OcCr	CnBs		Seds					
	T_{in} (°C)	k (W/(m K))	Q (μW/m³)	k (W/(m K))	Q (μW/m³)	$x_{100°C}$ (km)	$x_{150°C}$ (km)	Misfit (mW/m²)	ID #
Constraints	0 – 20	1.8 – 2.2	0 – 0.4	0.8 – 1.2	0.2 – 0.6	(30.0 – 38.5)	(60.7 – 73.9)	0 – 2.5	
Initial model	7.0	1.90	0.1	1.00	0.4	35.0	68.9	2.1	1
Best Model	10.0	1.90	0.1	1.15	0.5	34.6	68.4	1.2	1986
Shallow model	18.0	1.80	0.3	0.90	0.5	30.0	60.7	1.6	534
Deep model	0.0	2.15	0.1	1.00	0.4	38.5	73.9	1.9	1173
GA range	0 – 40	0.6 – 3	0 – 2.5	0.6 – 3	0 – 2.5	(16.3 -45.6)	(39.3 – 79.7)	(0.9 – 21.5)	
Best fit	21.5	1.60	0.2	1.80	0.0	31.3	62.8	0.9	3795
Harris & Wang	7.0	2.70	1.5	1.20	0.6	35.5	62.2	7.9	2039

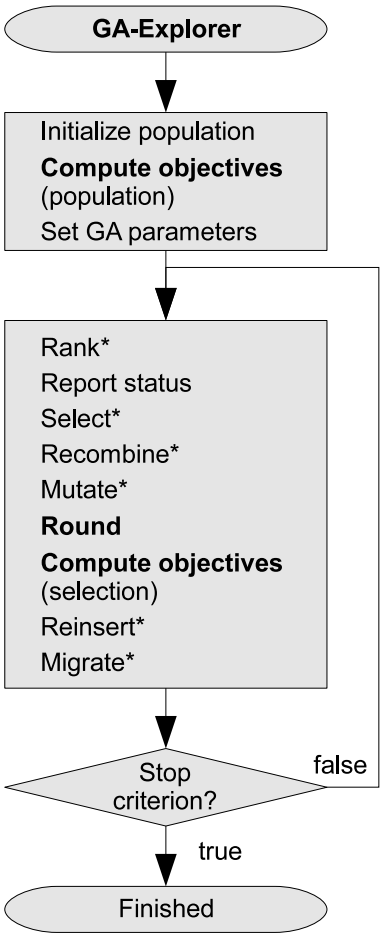

Figure 7. Genetic algorithm used to explore the parameter space of the finite element forward model. Standard evolutionary operators (e.g. Whitley 1994), which are tagged above (*), are based on functions from the genetic algorithm toolbox by Chipperfield et al. (1994), while we specifically developed the operators in bold font to reduce the number of forward model evaluations.

out that models satisfying the high heat flux scenario generally provide a slightly poorer fit to measured data than models that represent the low heat flux scenario (white and black segments). Moreover, the high heat flux scenario requires unreasonable Seds thermal conductivities which are greater than 2.5 W/(m K). Since there are no known sediments with thermal conductivities exceeding 2.5 W/(m K) (cf. supplementary materials), we reject this scenario.

Having rejected the high heat flux scenario and verified that models that comply with our parameter constraints are able to reproduce the measured surface heat flux values, we modified the objective function to study the uncertainty in the model results. To do this, we altered the objective function of the first scenario by adding a penalty for chromosomes containing model parameters that are beyond the range of the parameter constraints. Doing this, more good models, complying with the parameter constraints and fitting the measured heat flux data at same time (white bar segments), are generated during the iterations of the GA. These additional models provide a good estimate about how much the temperature field along the plate boundary can vary without violating any of the imposed parameter constraints. This is illustrated in the right column of Figure 8, where the white segments show the possible distances from the deformation front with the 50 °C, 100 °C, and 150 °C isotherms intersecting the plate boundary, respectively. Ranges of these distances are summarized in the constraints row of Table 1. Furthermore, parameters of the models satisfying all parameter constraints and providing the best fit, the shallowest isotherms, and the deepest isotherms are listed. The temperature in the subduction thrust increases from 50 °C ∼10 km landward of the trench axis to 150 °C at ∼20 km depth ∼65 km from the deformation front. As illustrated in Figure 1 and 6, the NEIC hypocenter coincides with the 150 °C isotherm within the given uncertainties.

To study how changes in different parameters effect the modeled results, we computed the Spearman rank correlation coefficients of the relations between the model parameters and the resulting distances of intersection between the 50 °C, 100 °C, and 150 °C isotherms with the plate boundary. The Spearman rank correlation is a nonparametric rank statistic proposed by Spearman in 1904 as a measure of the strength of the associations between two variables (Lehmann & D'Abrera 1975). It assesses how well an arbitrary monotonic function describes the relationship between two variables, without making any assumptions about the frequency distribution of the variables. It does not require the assumption that the relationship between the variables is linear, nor does it require the variables to be measured on interval scales.

The correlation coefficients were computed along with their significance using Matlab® functions implemented by Schloegl (2003). All correlation coefficients, tabulated in Table 2, are significant with a probability of at least 98%. In our model, the temperature of the upper oceanic crust has the strongest correlation with the temperature distribution on the plate boundary, followed by the thermal conductivity off the CnBs and Seds domains. While the correlation of the temperature distribution an the model param-

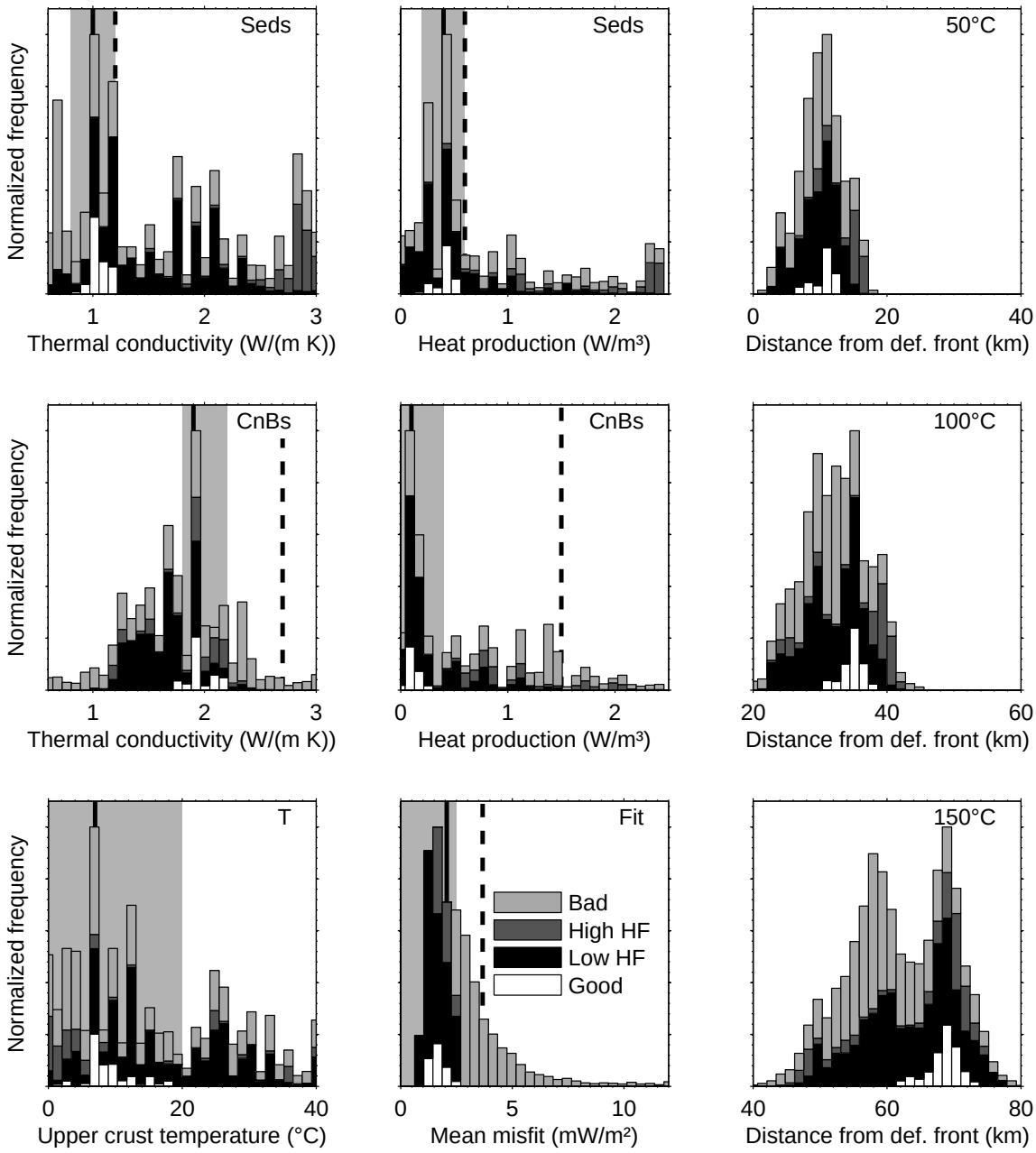

Figure 8. Parameter and result distributions including all 7014 solutions obtained during different numerical experiments. White segments represent good models, which satisfy all constraints highlighted (gray areas) in the six panels of the first two columns. Black and dark gray segments satisfy only the constraint highlighted in the Fit panel in respect to the low and the high heat flux scenario, respectively. Models that do not meet the Fit criteria are symbolized by light gray segments. The solid vertical line represents the parameters of our initial model, while the dashed lines show the parameters chosen by Harris & Wang (2002).

eters generally decreases with increasing distance from the deformation front, the correlation with the radiogenic heat production in the CnBs domain is increasingly pronounced.

5 DISCUSSION AND CONCLUSIONS

We presented a numerical model which is capable of predicting the temperature field at the seismogenic updip limit off Nicaragua, while integrating and satisfying all imposed constraints. We are, however, aware that the relatively simple model cannot fully represent the complex processes that are effect an active subduction zone. As is common practice and mentioned earlier, we used 0 °C as a constant value for the bottom water temperature. If the temperatures in the whole model domain were increased by 2 °C to account for the present bottom water temperatures, the 150 °C isotherm would be displaced by about 1 km down slap. Due to the lack of proper constraints, we also had to neglect many other processes

Table 2. Spearman correlation coefficients of correlation between model parameters and resulting distances of intersection between the 50 °C, 100 °C, and 150 °C isotherms with the plate boundary sorted by magnitude of correlation.

	T_{in}	kCnBS	kSeds	QCnBs	QSeds
$x_{50°C}$	-0.85	0.56	0.48	-0.11	-0.16
$x_{100°C}$	-0.85	0.64	0.40	-0.20	-0.18
$x_{150°C}$	-0.80	0.63	0.38	-0.37	-0.17

with possibly large impact on the thermal state. Firstly, the subduction of sediments was ignored, even thought it is known that erosion takes place in the working area (Ranero & von Huene 2000). Furthermore, we did not assign a specific thickness to the cooled layer of the upper oceanic crust as done by Harris & Wang (2002). These effects would lower the temperatures at the décollement, while other processes like frictional heating, which is supposed to be low (Harris & Wang 2002), would increase the temperature. However, adding any of these effects to the model without supplying good constraints would not enhance the performance of the model since all constraints are already satisfied by a whole range of simpler models.

On the other hand, the uncertainty of the model could be reduced by refining the current constraints. Our numerical experiments demonstrated that reliable surface heat flux measurements provide very useful independent constraints on the model, and the analysis of the correlation coefficients suggest that a refinements of the constraints on the initial thermal state of the subducting oceanic plate and the thermal conductivity of the continental basement have the greatest potential to decrease the uncertainties in the modeled results.

Pelayo & Wiens (1992) investigated several tsunami earthquakes world-wide, including tsunami events in the Kurile trench. It is striking that the 1992 Nicaragua event mimics major features of the October 20, 1963 and June 10, 1975 Kurile tsunami earthquakes. Most important, all three earthquakes were followed by aftershocks arcward and down-dip of the main shock. In contrast to this observation, most large interplate earthquakes show aftershocks located seaward of the epicenter, consistent with up-dip rupture propagation (Kelleher & Sykes 1973). To explain this behavior, (Pelayo & Wiens 1992) suggested that tsunami earthquakes generally nucleate within the typically aseismic region between the updip limit of the seismogenic zone and the trench axis, and that seaward propagation of aftershocks is inhibited by the velocity strengthening behavior of this zone. In contrast, our results suggest that tsunami earthquakes may nucleate in the uppermost region of the seismogenic zone at temperatures of $\sim$150 °C.

Faults, like the San Andreas fault, show an upper and lower cutoff of seismicity (Marone & Scholz 1988), indicating that earthquakes only nucleate over a limited depth range in a frictionally unstable region the seismogenic zone. In subduction zones, the upper transition is defined by the seismic front. No earthquake can nucleate seaward of the seismic front as a consequence of the frictional properties of sediment in the shallow fault zone. In this zone, the plate motion is accommodated by aseismic creep. If earthquakes propagate into this zone of stable sliding, a negative stress drop will occur, resulting in a rapid stop of rupture propagation (Scholz 1998). However, very large earthquakes, that rupture the entire seismogenic zone, can propagate dynamically through the upper stability transition zone and breach the surface (Scholz 1998, 2002). Thus, the main shock of a tsunami earthquake may release enough energy to propagate through this (velocity strengthening) region. In addition, up-dip propagation could be exacerbated by the presence of elevated fluid pressure that promotes rapid seismic slip at very low frictional resistance (Seno 2002). For Northeast Japan, (Tanioka et al. 1997) propose an other mechanism. Off Japan, the incoming oceanic lithosphere is highly faulted and exhibits a well-developed horst and graben structure. The same features are observed off Nicaragua (Figure 1). Though the crust is covered with sediment, horsts and seamounts may breach the sediment blanket and create contact with the hanging wall, which may promote rupture propagation. Consequently, rupture propagation is not governed by the frictional properties of the sediment, but by the frictional properties of the outcropping basement and the overriding plate. Nevertheless, only very few aftershocks are located in this region (Figure 1). This suggests that although the rupture could propagate through this area, there is no or little nucleation of events possible seaward of the seismic front. Therefore, using the classification of Scholz (1998, 2002), the region may be characterized by conditionally stable friction behavior.

The majority of large and great subduction zone earthquakes nucleate near the downdip limit of the seismogenic zone and propagate up-dip (Kelleher & Sykes 1973). Such patterns are particularly typical for interface events from the Kuriles, Kamchatka, Aleutians and Mexico (Tichelaar & Ruff 1993) and suggest that confining pressure and temperature have rigidified sediments at depth and caused large and strong contact zones between both plates (Moore et al. 2001). During rupture propagation, most subduction thrust earthquakes lose their energy and stop near the up-dip limit. Tsunami earthquakes, in contrast, tend to nucleate near the up-dip limit of the coupling zone, where coupling might still be laterally heterogeneous along the thrust contact. In such an environment locked asperities of consolidated and cemented sediment patches are perhaps too small to accumulate stresses required to cause a $M_s > 7$ earthquake. Other processes may therefore contribute to increase normal stress along the plate interface.

Seamount subduction or the subduction of other topographic highs and ridges profoundly affects the state of stress in the subduction thrust. A seamount forced into a subduction zone will increase the normal stress on the subduction interface and hence will enhance seismic coupling (Scholz & Small 1997). Seamounts are indeed abundant on the incoming Cocos plate offshore Nicaragua (Figure 1). We conclude that in addition to temperature-dependent induration of sediments, increased normal stress by seamount subduction may contribute to accumulate stress sufficient enough to support a $M_s > 7$ earthquake near the up-dip limit of the seismogenic zone. The resulting energy release may promote dynamic up-dip rupture propagation through the generally aseismic region seaward of the seismic front.

ACKNOWLEDGMENTS

We are grateful to scientists, master, and crew of RV Meteor cruise M54-2 for having provided support, information and discussion. Special thanks to Norbert Kaul and Bernd Heesemann for assistance during the heat flow deployments. This study was funded by the Deutsche Forschungsgemeinschaft through grant Vi 133/7-1 to University of Bremen and the SFB 574 Volatiles and fluids in subduction zones at Christan-Albrechts University, Kiel.

REFERENCES

Baptisa, A., Priest, G., & Murty, T., 1993. Field survey of the 1992 Nicaragua tsunami, *Mar. Geodesy*, **16**, 169–203.

Barckhausen, U., Ranero, C. R., von Huene, R., Cande, S. C., & Roeser, H. A., 2001. Revised tectonic boundaries in the Cocos Plate off Costa Rica: Implications for the segmentation of the convergent margin and for plate tectonic models, *J. Geophys. Res.*, **106**, 19207–19220.

Bilek, S. L. & Lay, T., 2002. Tsunami earthquakes possibly widespread manifestations of frictional conditional stability, *Geophys. Res. Lett.*, **29**, 18–1.

Bookman, C. A., Malone, I., & Langseth, M. G., 1972. Sea floor geothermal measurements from conrad cruise 13, Tech. Rept. 5-CU-5-72, Columbia University, In global heat-fux compilation by Pollack 1991.

Buecker, C. & Rybach, R., 1996. A simple method to determine heat production from gamma-ray logs, *Mar. Petrol. Geol.*, **13**, 373–375.

Byrne, D. E., Davis, D. M., & Sykes, L. R., 1988. Loci and maximum size of thrust earthquakes and the mechanics of the shallow region of subduction zones, *Tectonics*, **7**, 833–857.

Casciola, G. & Romani, L., 2004. A generalized conversion matrix between non-uniform b-spline and bezier representations with applications in CAGD, in *Multivariate Approximation: Theory and Applications*.

Chipperfield, A., Fleming, P. J., Pohlheim, H., & Fonseca, C. M., 1994. Genetic algorithm toolbox for use with matlab, Tech. Rep. 512, Department of Automatic Control and Systems Engineering, University of Sheffield, Version 1.2.

Christensen, D. H. & Ruff, L. J., 1983. Outer-rise earthquakes and seismic coupling, *Geophysical Research Letters*, **10**, 697–700.

Comsol, 2005. *Comsol Modeling Guide*, 3rd edn.

DeMets, C., 2001. A new estimate for present-day cocos-caribbean plate motion: Implications for slip along the central american volcanic arc, *Geophys. Res. Lett.*, **28**(21), 4043–4046.

Divins, D. L., 2005. NGDC total sediment thickness of the world's oceans & marginal seas, Tech. rep., NGDC.

Geist, E. L., 2002. Complex earthquake rupture and local tsunamis, *Journal of Geophysical Research (Solid Earth)*, **107**, 2–1.

Geist, E. L. & Bilek, S. L., 2001. Effect of depth-dependent shear modulus on tsunami generation along subduction zones, *Geophys. Res. Lett.*, **28**(7), 1315–1318.

Geist, E. L., Bilek, S. L., Arcas, D., & Titov, V. V., 2006. Differences in tsunami generation between the december 26, 2004 and march 28, 2005 sumatra earthquakes, *Earth Planets Space*, **58**(2), 185–193.

Grevemeyer, I. & Villinger, H., 2001. Gas hydrate stability and the assessment of heat flow through continental margins, *Geophysical Journal International*, **145**(3), 647–660.

Grevemeyer, I., Diaz-Naveas, J. L., Ranero, C. R., & Villinger, H. W., 2003. Heat flow over the descending nazca plate in central chile, 32[deg]s to 41[deg]s: observations from odp leg 202 and the occurrence of natural gas hydrates, *Earth and Planetary Science Letters*, **213**(3-4), 285–298.

Grevemeyer, I., Kaul, N., Diaz-Naveas, J. L., Villinger, H. W., Ranero, C. R., & Reichert, C., 2005. Heat flow and bending-related faulting at subduction trenches: Case studies offshore of nicaragua and central chile, *Earth and Planetary Science Letters*, **236**(1-2), 238–248.

Harris, R. N. & Wang, K., 2002. Thermal models of the Middle America Trench at the Nicoya Peninsula, Costa Rica, *Geophys. Res. Lett.*, **29**, 6–1.

Hartmann, A. & Villinger, H., 2002. Inversion of marine heat flow measurements by expansion of the temperature decay function, *Geophysical Journal International*, **148**(3), 628–636.

Hyndman, R. D. & Wang, K., 1993. Thermal constraints on the zone of major thrust earthquake failure - the cascadia subduction zone, *J. Geopyhs. Res.*, **98**, 2039–2060.

Hyndman, R. D., Davis, E. E., & Wright, J. A., 1979. The measurement of marine geothermal heat flow by a multipenetration probe with digital acoustic telemetry and insitu thermal conductivity, *Marine Geophysical Researches*, **V4**(2), 181–205.

Ide, S., Imamura, F., Yoshida, Y., & Abe, K., 1993. Source characteristics of the Nicaraguan tsunami earthquake of September 2, 1992, *Geophys. Res. Lett.*, **20**, 863–866.

Ihmle, P. F., 1996a. Frequency-dependent relocation of the 1992 nicaragua slow earthquake: an empirical green's function approach, *Geophysical Journal International*, **127**(1), 75–85.

Ihmle, P. F., 1996b. Monte Carlo slip inversion in the frequency domain: Application to the 1992 Nicaragua slow earthquake, *Geophys. Res. Lett.*, **23**, 913–916.

Kanamori, H., 1972. Mechanism of tsunami earthquakes, *Physics of the Earth and Planetary Interiors*, **6**, 346–359.

Kanamori, H. & Kikuchi, M., 1993. The 1992 nicaragua earthquake: a slow tsunami earthquake associated with subducted sediments, *Nature*, **361**(6414), 714–716.

Kelleher, J. L. & Sykes, J. O., 1973. Possible criteria for predicting earthquake locations and their applications to major plate boundaries of the pacific and caribbean, *J. Geophys. Res.*, **78**, 2547–22585.

Kimura, G., Silver, E., Blum, P., & Shipboard Scientific Party, 1997. Init. repts., in *Proc. ODP*, vol. 170, College Station, TX (Ocean Drilling Program).

Langseth, M. G. & Silver, E. A., 1996. The Nicoya convergent margin-a region of exceptionally low heat flow, *Geophys. Res. Lett.*, **23**(8), 891–894.

Langseth, M. G., Malone, I., & Berger, D., 1971. Sea floor geothermal measurements from vema cruise 24, Tech. Rept. 3-CU-3-71, Columbia University, In global heat-fux compilation by Pollack 1991.

Lehmann, E. L. & D'Abrera, H. J. M., 1975. *Nonparametrics : statistical methods based on ranks*.

Marone, C. & Scholz, C. H., 1988. The depth of seismic faulting and the upper transition from stable to unstable slip regimes, *Geophysical Research Letters*, **15**, 621–624.

Mayer, L., Pisias, N., Janecek, T., & Shipboard Scientific Party, 1992. Init. repts., in *Proc. ODP*, no. 138, College Station, TX (Ocean Drilling Program).

Moore, G. F., Taira, A., Klaus, A., & Shipboard Scientific Party, 2001. Init. repts., in *Proc. ODP*, vol. 190 [Online], Available from World Wide Web:http://www-odp.tamu.edu/publications/190_IR/190ir.htm.

Morris, J. D., Villinger, H. W., Klaus, A., & Shipboard Scientific Party, 2003. Init. repts., in *Proc. ODP*, vol. 205 [Online], Available from World Wide Web:http://www-odp.tamu.edu/publications/205_IR/205ir.htm.

Newman, A. V., Schwartz, S. Y., Gonzalez, V., DeShon, H. R., Protti, J. M., & Dorman, L. M., 2002. Along-strike variability in the seismogenic zone below nicoya peninsula, costa rica, *Geophys. Res. Lett.*, **29**, 38–1.

NGDC, 2005. Global digital elevation model (ETOPO2), National Geophysical Data Center.

Nielsen, H. B., 2005. *immoptibox: A Matlab toolbox for optimization and data fitting*, Informatics and Mathematical Modelling, Technical University of Denmark.

Pelayo, A. M. & Wiens, D. A., 1992. Tsunami earthquakes - Slow thrust-faulting events in the accretionary wedge, *Journal of Geophysical Research*, **97**(B11), 1532115337.

Pfender, M. & Villinger, H., 2002. Miniaturized data loggers for deep sea sediment temperature gradient measurements, *Mar. Geol.*, **186**, 557–570.

Polet, J. & Kanamori, H., 2000. Shallow subduction zone earthquakes and their tsunamigenic potential, *Geophysical Journal International*, **142**, 684–702.

Pollack, H. N., Hurter, S. J., & Johnston, J. R., 1992. Global heat flow data set, Tech. rep., World Data Center A for Solid Earth Geophysics, NOAA E/GCI, 325 Broadway, Boulder, CO 80303, USA.

Ranero, C. R. & von Huene, R., 2000. Subduction erosion along the Middle America convergent margin, *Nature*, **404**, 748–752.

Ranero, C. R., von Huene, R., Flueh, E., Duarte, M., Baca, D., & McIntosh, K., 2000. A cross section of the convergent Pacific margin of Nicaragua, *Tectonics*, **19**, 335–357.

Satake, K., 1994. Mechanics of the 1992 Nicaragua tsunami earthquake, *Geophys. Res. Lett.*, **21**, 2519–2522.

Satake, K. & Tanioka, Y., 1999. Sources of tsunami and tsunamigenic earthquakes in subduction zones, *Pure and Applied Geophysics*, **V154**(3), 467–483.

Satake, K., Abe, K., Abe, K., Bourgeois, J., Estrada, F., Iio, Y., Imamura, F., Katao, H., Noguera, E., & Tsuji, Y., 1993. Tsunami field survey of the 1992 nicaragua earthquake, *EOS Transactions*, **74**, 145–145.

Schloegl, A., 2003. *The NaN-toolbox: A statistic-toolbox for Octave and Matlab*, Version 1.52.

Scholz, C. H., 1998. Earthquakes and friction laws, *Nature*, **391**(6662), 37–42.

Scholz, C. H., 2002. *The mechanics of earthquakes and faulting*, Cambridge [u.a.]: Cambridge Univ. Press, 2002.

Scholz, C. H. & Small, C., 1997. The effect of seamount subduction on seismic coupling, *Geology*, **25**(6), 487–490.

Sclater, J. G., G., R. U., & Dixon, F. S., 1970. Heat flow in the southwestern pacific, *J. Geophys. Res.*, **75**, 333–348, In global heat-fux compilation by Pollack 1991.

Seno, T., 2002. Tsunami earthquakes as transient phenomena, *Geophys. Res. Lett.*, **29**(10), 1419.

Stein, C. A. & Stein, S., 1992. A model for the global variation in oceanic depth and heat flow with lithospheric age, *Nature*, **359**(6391), 123–129.

Tanioka, Y., Ruff, L., & Satake, K., 1997. What controls the lateral variation of large earthquake occurrence along the japan trench, *The Island Arc*, **6**, 261–266.

Tichelaar, B. W. & Ruff, L. J., 1993. Depth of seismic coupling along subduction zones, *Journal of Geophysical Research*, **98**, 2017–2037.

UNAVCO, 2006. Plate motion calculator.

Vaquier, V., Sclater, J. G., & Corry, C. E., 1967. Studies of the thermal state of the earth, the 21st paper - heat flow, eastern pacific, *Bull. Earthq. Res. Inst. Tokyo Univ.*, **45**, 375–393, In global heat-fux compilation by Pollack 1991.

Velasco, A. A., Ammon, C. J., Lay, T., & Zhang, J., 1994. Imaging a slow bilateral rupture with broadband seismic waves: The September 2, 1992 Nicaraguan tsunami earthquake, *Geophys. Res. Lett.*, **21**, 2629–2632.

von Herzen, R. & Maxwell, M. E., 1959. The measurement of thermal conductivity of deep sea sediments by a needle probe method, *J. Geophys. Res.*, **64**, 1557–1563.

Walther, C. H. E., Flueh, E. R., Ranero, C. R., von Huene, R., & Strauch, W., 2000. Crustal structure across the pacific margin of nicaragua:evidence for ophiolitic basement and a shallow mantle sliver, *Geophysical Journal International*, **141**, 759–777.

Whitley, D., 1994. A genetic algorithm tutorial, *Statistics and Computing*, **4**, 65–85.

Wilson, D., Teagle, D., Acton, G., & Shipboard Scientific Party, 2003. Init. repts., in *Proc. ODP*, no. 206, College Station, TX (Ocean Drilling Program).

Publication: Alteration of the subducting oceanic lithosphere at the southern central Chile trench-outer rise

Contreras-Reyes, E., I. Grevemeyer, E. R. Flueh, M. Scherwath, and M. Heesemann (2007), Alteration of the subducting oceanic lithosphere at the southern central Chile trench-outer rise, *Geochem. Geophys. Geosyst.*, *8*, Q07,003, doi:10.1029/2007GC001632.

Contributions

In the following publication, the reduced seismic velocities of subducting oceanic lithosphere seaward of the Chile trench provide evidence that structures of the oceanic crust and the uppermost mantle have been altered by fracturing and hydration. The reduced velocities start at the trench outer rise were bending causes extensional faulting. In Addition, to the seismic evidence for hydration, low heat-flux values measured in the vicinity of an outcropping basement high indicate inflow of cold sea water into the oceanic crust. Eduardo Contreras-Reyes compiled the publication and determined the seismic velocity structure using seismic tomography. Martin Scherwath contributed to the processing of the seismic data. Martin Heesemann processed the heat-flux data and provided the thermal model indicating influx of cold seawater into the oceanic crust. Ingo Grevemeyer and Ernst Flueh supervised the research.

Alteration of the subducting oceanic lithosphere at the southern central Chile trench–outer rise

Eduardo Contreras-Reyes, Ingo Grevemeyer, Ernst R. Flueh, and Martin Scherwath
Leibniz-Institute of Marine Sciences (IFM-GEOMAR), Wischhofstrasse 1-3, D-24148 Kiel, Germany (econtreras-reyes@ifm-geomar.de; igrevemeyer@ifm-geomar.de; eflueh@ifm-geomar.de; mscherwath@ifm-geomar.de)

Martin Heesemann
Department of Earth Sciences, University of Bremen, Postfach 330440, D-28334 Bremen, Germany (heesema@uni-bremen.de)

[1] Hydrothermal circulation and brittle faulting processes affecting the oceanic lithosphere are usually confined to the upper crust for oceanic lithosphere created at intermediate to fast spreading rates. Lower crust and mantle rocks are therefore relatively dry and undeformed. However, recent studies at subduction zones suggest that hydration of the oceanic plate is most vigorous at the trench–outer rise, where extensional bending-related faulting affects the hydrogeology of the oceanic crust and mantle. To understand the degree of hydration, we studied the seismic velocity structure of the incoming Nazca plate offshore of southern central Chile (~43°S); here the deep-sea trench is heavily filled with up to 2 km of sediments. Seismic refraction and wide-angle data, complemented by seismic reflection imaging of sediments, are used to derive a two-dimensional velocity model using joint refraction and reflection traveltime tomography. The seismic profile runs perpendicular to the spreading ridge and trench axes. The velocity model derived from the tomography inversion consists of a ~5.3-km-thick oceanic crust and shows P wave velocities typical for mature fast spreading crust in the seaward section of the profile, with uppermost mantle velocities as fast as ~8.3 km/s. Approaching the Chile trench, seismic velocities are significantly reduced, however, suggesting that the structures of both the oceanic crust and uppermost mantle have been altered, possibly due to a certain degree of fracturing and hydration. The decrease of the velocities roughly starts at the outer rise, ~120 km from the deformation front, and continues into the trench. Even though the trench is filled with sediment, basement outcrops in the outer rise frequently pierce the sedimentary blanket. Anomalously low heat flow values near outcropping basement highs indicate an efficient inflow of cold seawater into the oceanic crust. Hydration and crustal cracks activated by extensional bending-related faulting are suggested to govern the reduced velocities in the vicinity of the trench. Considering typical flow distances of 50 km, water might be redistributed over most of the trench–outer rise area. Where trapped in faults, seawater may migrate down to mantle depth, causing up to ~9% of serpentinization in at least the uppermost ~2 km of the mantle between the outer rise and the trench axis.

Components: 10,027 words, 9 figures.

Keywords: trench–outer rise; bending-related faulting; seismic tomography.

Index Terms: 8170 Tectonophysics: Subduction zone processes (1031, 3060, 3613, 8413); 8150 Tectonophysics: Plate boundary: general (3040); 7220 Seismology: Oceanic crust.

Received 15 March 2007; **Accepted** 4 May 2007; **Published** 7 July 2007.

Contreras-Reyes, E., I. Grevemeyer, E. R. Flueh, M. Scherwath, and M. Heesemann (2007), Alteration of the subducting oceanic lithosphere at the southern central Chile trench–outer rise, *Geochem. Geophys. Geosyst.*, *8*, Q07003, doi:10.1029/2007GC001632.

1. Introduction

[2] Oceanic lithosphere created at moderate to fast spreading mid-ocean ridges is characterized by a ridge-parallel fault pattern. Pervasive fracturing and hydrothermal activity, however, are largely confined to crustal levels [e.g., *Carbotte and Scheirer*, 2004; *Karson*, 1998]. As the crust ages, cracks and pore spaces inherently related to the formation of crust are clogged by precipitation of secondary hydrothermal alteration products in the extrusive lava pile [e.g., *Alt et al.*, 1986; *Wilkens et al.*, 1991; *Grevemeyer and Bartetzko*, 2004]. Global compilations of seismic refraction velocities for the uppermost oceanic crust [*Grevemeyer and Weigel*, 1996; *Carlson*, 1998] and dedicated seismic refraction experiments [e.g., *Grevemeyer and Weigel*, 1997; *Grevemeyer et al.*, 1999] have established an empirical relationship between lithospheric age and seismic velocity. The global trend suggests that uppermost P wave velocities of layer 2 increase rapidly close to the spreading axis and within ~8 Ma reach values of mature oceanic crust (>4.5 km/s) [*Carlson*, 1998; *Grevemeyer and Bartetzko*, 2004]. Within this context, we will refer to "normal" mature oceanic lithosphere typical of fast spreading structures if (1) hydration is confined to the permeable upper lava pile, (2) the ridge flank hydrothermal circulation system has largely ceased, and (3) the oceanic lithosphere is positioned away from anomalous regions such as fracture zones and hot spots regions [e.g., *White et al.*, 1992].

[3] Growing observational evidence in subduction zones suggest that this condition of "normal" and "unaltered" ocean lithosphere can be dramatically perturbed at the outer rise seaward of deep-sea trenches [e.g., *Peacock*, 2004; *Ranero et al.*, 2003]. The outer rise is formed when the ocean lithosphere approaches a subduction zone and bends into the trench, thus producing a prominent outer bulge seaward of the trench axis. Here, outer rise earthquakes are linked to bending-related normal faulting [*Chapple and Forsyth*, 1979] and possibly rupture the oceanic mantle [e.g., *Kanamori*, 1971; *Christensen and Ruff*, 1983], creating a pervasive tectonic fabric that may cut across the crust, penetrating deep into the uppermost mantle [e.g., *Peacock*, 2001; *Ranero et al.*, 2003]. Moreover, new crustal cracks and fissures are caused by bending-related faulting seaward of the trench axis, modifying the structure of the crust. Therefore bending-related faulting plays a crucial role for the alteration of oceanic lithosphere; it affects the porosity and permeability structure of the entire oceanic crust and consequently generates pathways for fluids down to mantle depth.

[4] One key factor controlling the local hydrogeological regime of the oceanic lithosphere is the thickness of the sedimentary blanket. Convergent margins such as Central America and north Chile are poorly sedimented, and seawater can easily enter the igneous oceanic crust where the permeable basement rocks are widely exposed (e.g., surface-cutting tectonic faults or outcropping basement highs). These subduction zones have been suggested to be characterized by a high degree of hydration at the outer rise [*Ranero et al.*, 2003; *Ranero and Sallares*, 2004; *Grevemeyer et al.*, 2005, 2007]. In contrast, in well sedimented margins (Cascadia and southern central Chile), a thick sedimentary cover is believed to hinder interaction between the ocean and the basement. Therefore the degree of hydration is expected to be lower than in poorly sedimented trenches, although mechanisms by which fluids may bypass thick sediments remain still under debate. In general, the hydrothermal activity in the oceanic crust is controlled by faulting and the presence of outcropping basement highs. Heat flow data suggest that hydrothermal circulation is more vigorous at trenches where bending-related normal faults breach the seafloor and thus facilitate fluid flow into the crust [*Grevemeyer et al.*, 2005]. Outcropping basement also play a crucial role, since it may act as transmissive pathway for fluids and heat in areas where the surrounding basement is blanketed by sediments, as it has been evidenced by anomalous low heat flow values near seamounts, indicating an efficient inflow of cold seawater into the oceanic crust [*Villinger et al.*, 2002; *Fisher et al.*, 2003a, 2003b]. Isolated basement outcrops penetrating through thick sediments might guide hydrothermal circulation between sites separated by large distances [*Fisher et al.*, 2003a]. Once cold seawater

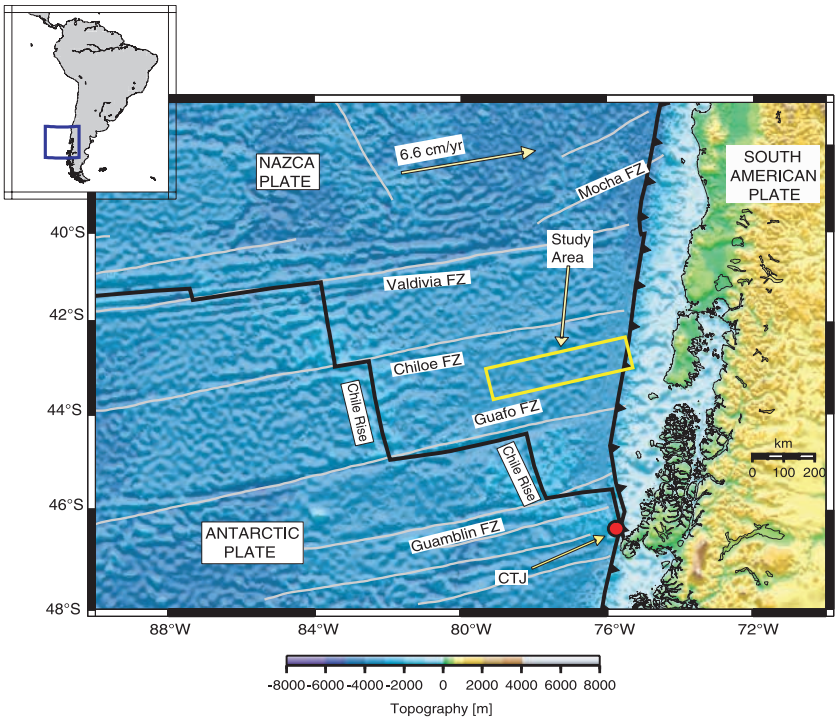

Figure 1. Geodynamic setting of Nazca, Antarctic, and South American plates. These plates join at the Chile Triple Junction (CTJ), where the Chile Rise is currently subducting at ~46.5°S. The oceanic Nazca plate is segmented by several fracture zones (FZs), resulting in a strong variability of the age of the subducting plate. The study area is located between two Fracture Zones, Chiloe FZ and Guafo FZ, and its plate age ranges from 18.5 to 10 Ma along the Chile trench.

is infiltrated and bounded in the upper oceanic crust, tectonic faulting may allow fluids trapped within crustal pores spaces to enter the lower crust and perhaps even the upper mantle [e.g., *Grevemeyer et al.*, 2005].

[5] To better understand the transition from "normal" and "dry" to deformed and hydrated subducting lithosphere and its degree of hydration in the trench–outer rise area, we studied the velocity structure of the incoming oceanic Nazca plate offshore of south central Chile. Seismic wide-angle reflection and refraction data are used to derive an accurate 2-D tomography velocity model of a ~250 km long seismic profile located oceanward from the Chile trench axis. We present new geophysical evidence documenting changes in the seismic structure of the incoming oceanic plate from the outer rise to just before its subduction in the deep-sea trench. A nonlinear Monte Carlo uncertainty analysis is performed to estimate a posteriori model variance of the tomography velocity model. In addition, heat flow data recorded at the outer rise are used to study the distribution of temperature along the sediment/crust boundary. The data were acquired during the R/V *Sonne* cruise SO181 as part of the TIPTEQ (from The Incoming Plate to Mega-thrust EarthQuake processes) project [*Flueh and Grevemeyer*, 2005].

2. Tectonic Setting

[6] Along the south central Chile trench the southern Nazca plate subducts at a relatively high convergence rate of ~6.6 cm/yr beneath the South American plate, with a convergence azimuth of ~78°E [*Angermann et al.*, 1999] (Figure 1). The southern Nazca plate has been formed at the Chile Rise (a fast mid-ocean spreading ridge). Fracture zones (FZs) cut the Chile Rise into several segments (Figure 1), resulting in abrupt changes of thermal states along the plate boundary. The spreading center segments bounded by these fracture zones are roughly parallel to the trench strike (Figure 1). At ~46.5°S the Chile Rise is currently subducting, defining the Chile Triple Junction (CTJ) of the subducting Nazca and Antarctic plates, and the continental South American plate. North of the CTJ occur a series of age jumps across several fracture zones, from 0 Myr up to 18.5 Myr at the Valdivia FZ (Figure 1). The south central Chile trench is filled by terrigenous sediments sourced from the Andes [*Thornburg and Kulm*,

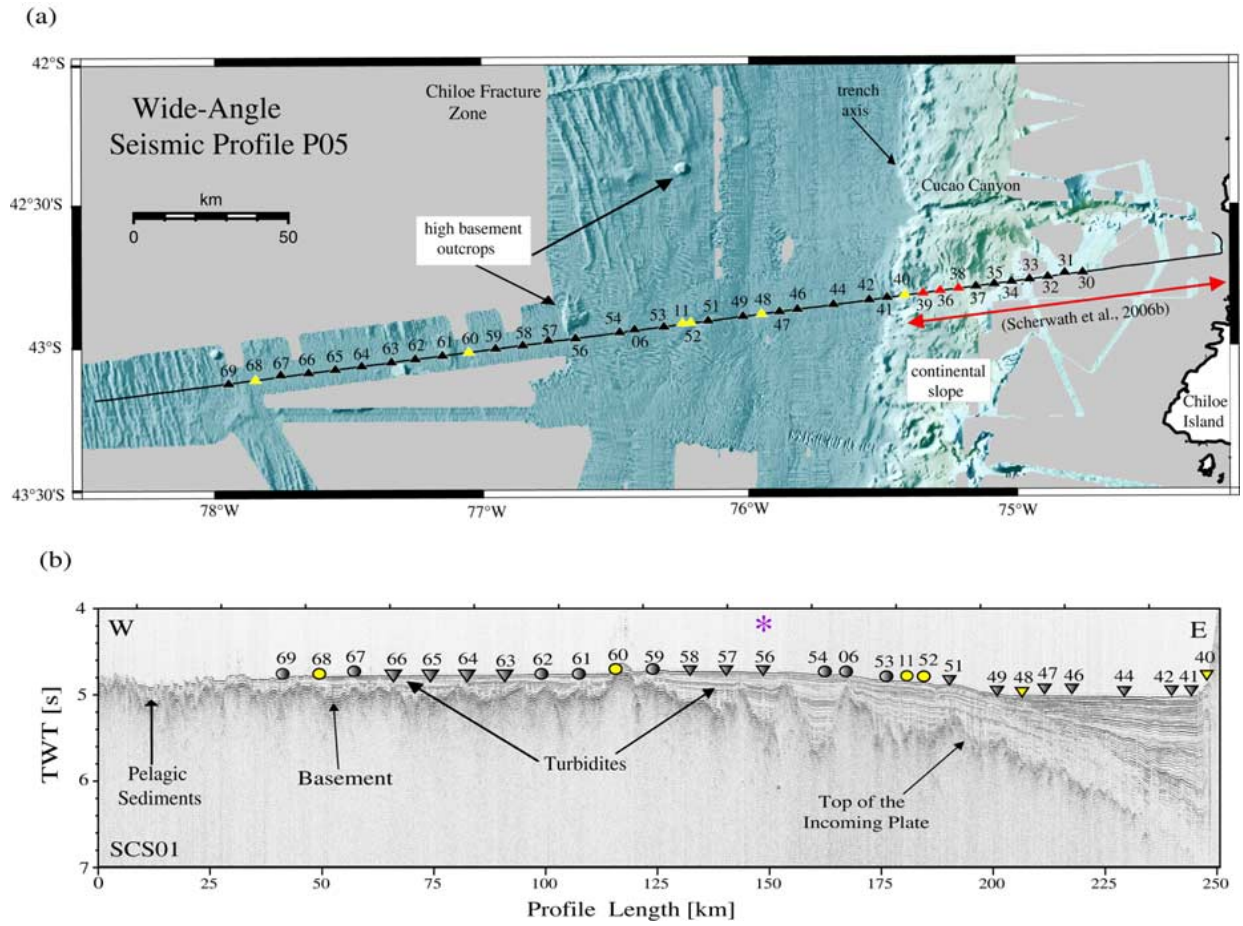

Figure 2. (a) High-resolution bathymetric image and wide-angle seismic profile P05. The seismic line begins ~280 km from the Chile Rise (see Figure 1), and it extends up to the deep-sea trench and part of the continental slope. Yellow triangles indicate the six stations of which data examples are shown in Figures 3 and 8. Red dots indicate the three stations positioned on the continental slope [*Scherwath et al.*, 2006b], which are included in our tomographic model. (b) High-resolution seismic line SCS01 coincident with wide-angle seismic profile P05. Locations of OBH are shown by solid circles, and locations of OBS are shown by solid triangles. Location of the high basement outcrop is denoted by asterisk. Some tensional normal faults are reflected by offsets in the trench–outer rise region.

1987]. Sediment within the trench are redistributed from south to the north [*Thornburg et al.*, 1990], which is explained by the slight northward dip of the trench floor [e.g., *Thornburg et al.*, 1990]. Trench fans (33–41°S) are built at the mouths of major submarine canyons and channels which act as point sources of sediment supply [*Thornburg and Kulm*, 1987]. South of 41°S, sheet turbidites extend across the entire width of the trench [*Thornburg and Kulm*, 1987].

[7] The westward terminus of the seismic wide-angle profile studied here is located approximately 280 km eastward of the Chile Rise on 9 Myr old crust [*Tebbens et al.*, 1997], the line orientation being parallel to the plate motion vector (Figure 1). The profile is located between Chiloe and Guafo FZs (Figure 1), where the plate age decrease from 18.5 to 10 Myr along the Chile trench, and the half-spreading rate ranges between 45 and 35 mm/yr [*Tebbens et al.*, 1997]. The trench basin is broad, owing to the large extension of turbidite deposits seaward [*Voelker et al.*, 2006]. Further to the west, the Nazca plate is covered by a few hundred meters of hemipilagic and pelagic sediments, whereas toward the trench, the sedimentary cover becomes thicker due to the turbiditic deposits filling the trench with a total thickness of ~2 km [*Scherwath et al.*, 2006a]. The continental slope is steep and is characterized by the presence of the submarine Cucao Canyon (Figure 2a), while the continental shelf is broad and probably trapped large volume of Pliocene sediments [*Reichert et al.*, 2002].

3. Seismic Data

[8] From December 2004 to February 2005, the TIPTEQ project investigated the subduction zone

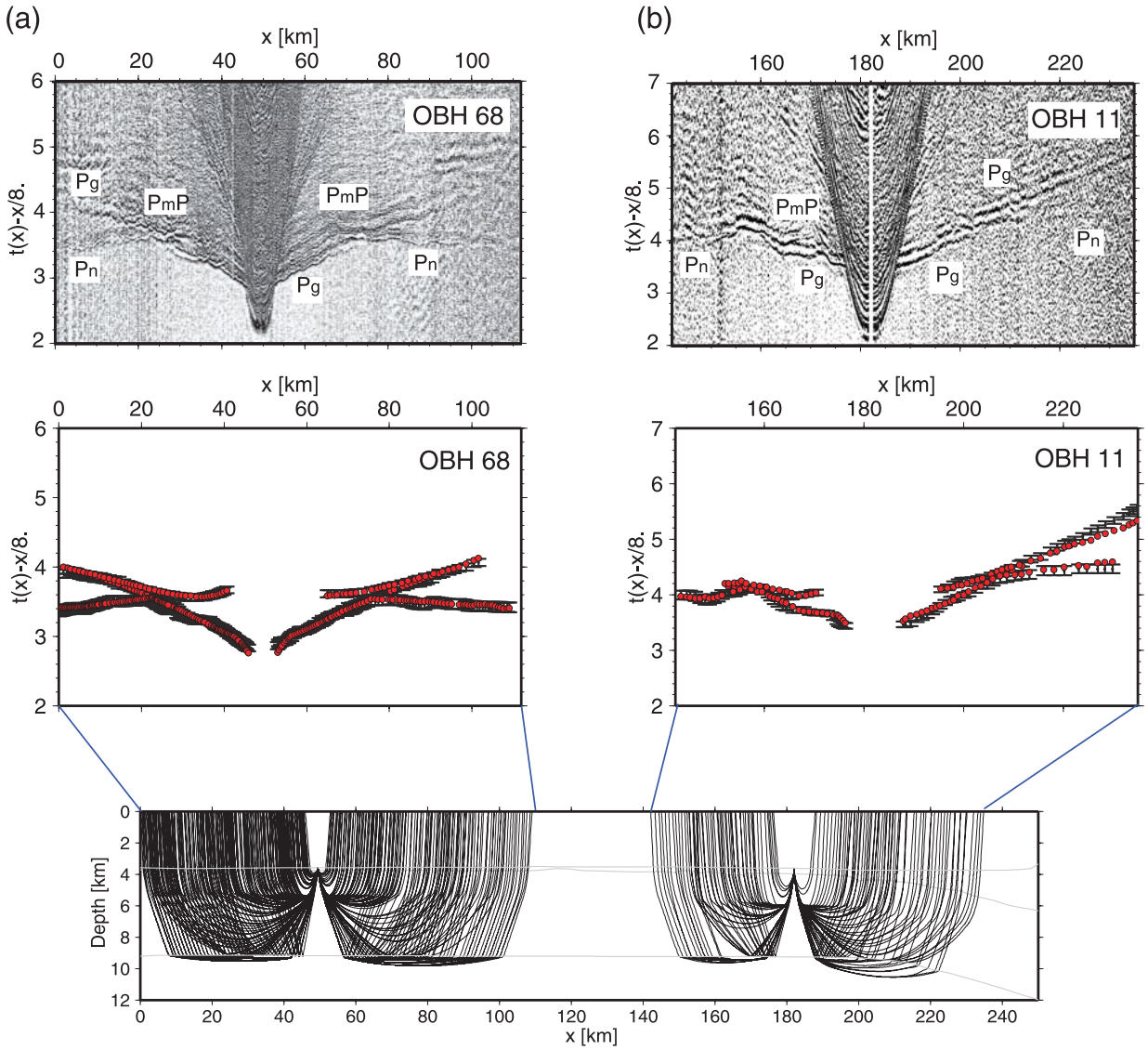

Figure 3. Examples of wide-angle seismic data with picked (solid circle with pick error) and predicted (red circles) traveltimes. Calculated traveltimes are based on the velocity model presented in Figure 7a, and corresponding raypaths are also plotted at the bottom. (a) OBH 68, (b) OBH 11, (c) OBH 60, (d) OBH 48, and (e) OBH 40.

offshore south-central Chile between 35° and 48°S aboard of the German R/V *Sonne*. During the cruise seismic wide-angle reflection and refraction data, high-resolution seismic reflection data, multibeam bathymetry, heat flow, and seismological data were acquired in this region [*Flueh and Grevemeyer*, 2005; *Scherwath et al.*, 2006a] to study the physical properties of the incoming Nazca plate and its impact on seismogenesis, offshore of the rupture area of the 1960 Chile megathrust earthquake. In this paper, we present seismic wide-angle data that were collected along the profile P05 located seaward of the trench axis on the oceanic Nazca plate, supplemented by high-resolution swath bathymetric images of the surrounding seafloor (Figure 2a). Shots were recorded with 38 OBS (Ocean Bottom Seismometers) [*Bialas and Flueh*, 1999] and OBH (Ocean Bottom Hydrophones) [*Flueh and Bialas*, 1996] spaced at a distance of ~5.5 km. Coincident seismic reflection data were also collected along this profile (Figure 2b). For the reflection investigation a 100-m-long 16-channel streamer and a Generator/Injector (GI) gun with a volume of 1.5 liters were used, providing high-resolution images of the sedimentary sequences blanketing the incoming plate. From the 38 seismic ocean bottom stations, 28 were deployed on the oceanic plate and the rest

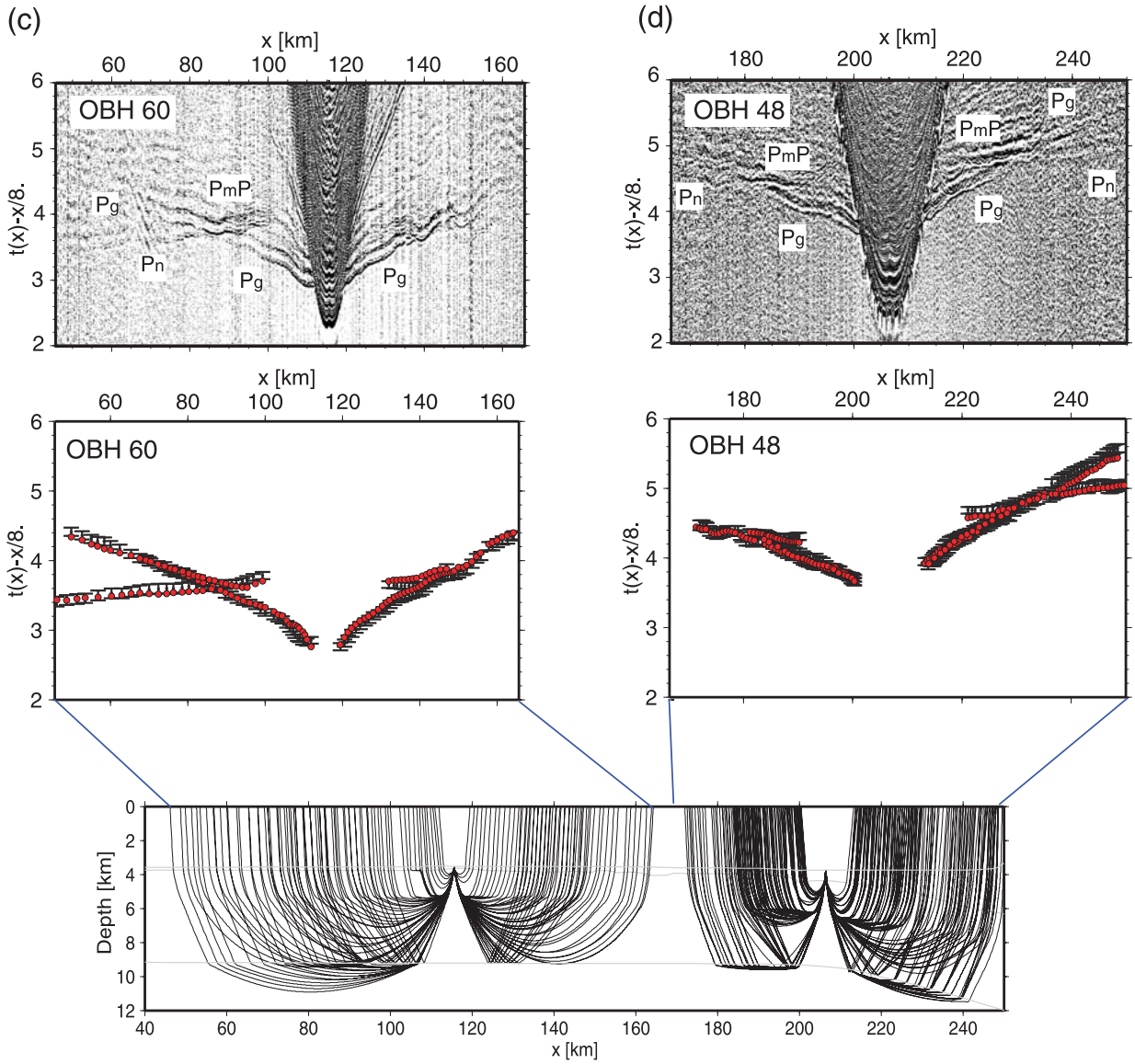

Figure 3. (continued)

along the continental slope. In order to study the seismic structure of the oceanic Nazca plate, we used the OBH/S deployed seaward of the trench. Three stations on the continental slope were also included in the inversion approach to constrain the velocity structure and Moho depth below the trench (see Figure 2a).

[9] The seismic source for the refraction work was a cluster of 8x8-liters G-guns, providing a total volume of 64 liters for each shot. This source was fired at a time interval of 60 s, which corresponds to an average shot spacing of ∼150 m. The record sections were interpreted after bandpass filtering and predictive deconvolution. The signal-to-noise ratio obtained for most of the stations is high (Figure 3). Crustal refractions (P_g), Moho reflections (P_mP) and upper mantle refractions (P_n) were recorded on almost all stations with excellent quality. Five examples of seismic record sections are shown in Figure 3, with their respective seismic phases identified. Apparent velocities, which are influenced by the trench-sediment, decrease toward the trench. Refractions through trench-sediment (P_s), and reflections from the top of the igneous crust (P_bP) start to appear at approximately profile-km 200 and hence 50 km from the trench axis. Figure 3e shows P_s and P_bP of good quality at OBH 40 at the trench. Those traveltimes complement the high-resolution seismic reflection data

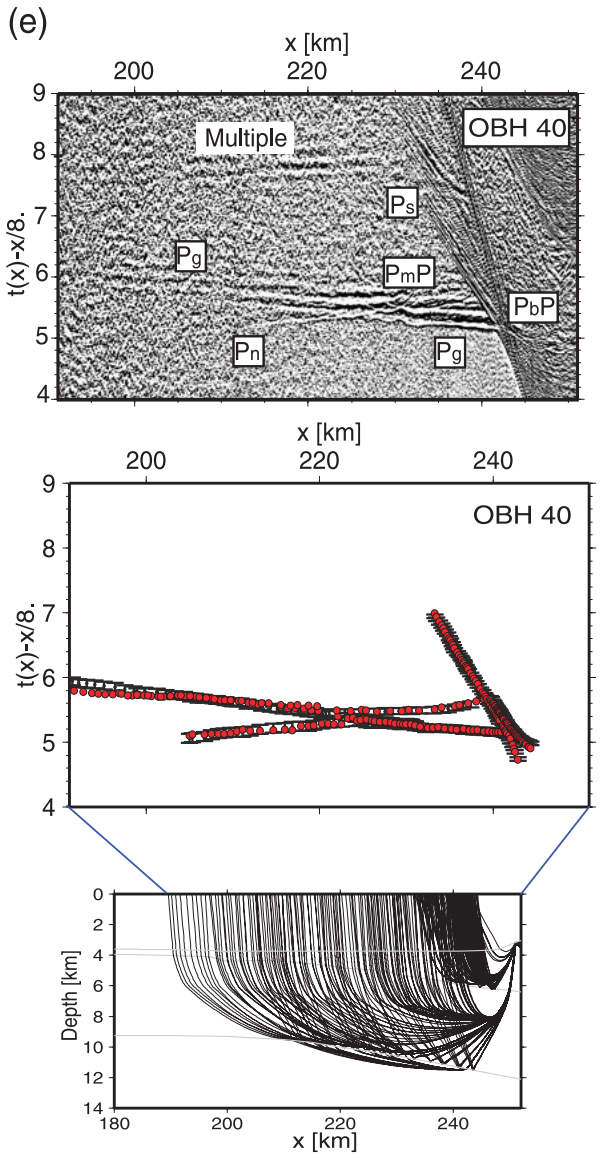

Figure 3. (continued)

(Figure 2b) and are used to constrain the sedimentary section in this part of the model.

[10] Picking of the seismic phases was done manually, and picking errors were assigned on the basis of the dominant period of the phase. A total of 5048 first arrivals (P_g and P_n), and 1721 Moho reflections (P_mP) were picked from 31 record sections. For the sedimentary section only stations located to the east of x = 200 km were utilized, because clear P_s and P_bP phases are confined to the trench basin. A total of 1456 P_s and 654 P_bP were picked from these stations. Typically, errors were assumed to be half a period of one arrival, to account for a possible systematic shift in the arrival identification, and were weighted according to the phase quality. Average picking uncertainties are ~50 ms at near offsets and ~70 ms at far offsets for refracted arrivals, and ~50 ms and ~70 ms for P_bP and P_mP phases, respectively.

4. Traveltime Tomography Scheme

[11] The velocity-depth model was derived using the joint refraction and reflection traveltime inversion method of *Korenaga et al.* [2000]. This method allows simultaneous refraction and reflection traveltimes inversion for a 2-D velocity field that is parameterized as a sheared mesh hanging beneath the seafloor and where node spacings can vary laterally and vertically. The floating reflector is represented as an array of linear segments whose nodal spacing is independent of that used in the velocity grid and it has just one degree of freedom (vertical direction). Traveltimes and raypaths are calculated by utilizing a hybrid ray-tracing scheme based on the graph method and local ray-bending refinement [*van Avendonk et al.*, 1998]. Smoothing constraints using predefined correlation lengths (average-smoothness window) and optimized damping constraints for the model parameters are employed to regularize an iterative linearized inversion [*Korenaga et al.*, 2000]. We use a hybrid approach of multistep tomography using four layers, (1) water, (2) sedimentary section, (3) oceanic crust, and (4) upper mantle. To derive the velocity depth model, the water depths were taken from the multibeam bathymetry, which remained fixed during the inversion. The vertical incidence reflection data, sediment refracted P_s and reflected P_bP phases were used to invert for the velocities and thickness of the sedimentary trench fill and hence the geometry of the top of the downgoing plate. Sedimentary velocities and basement depth were then held fixed in the following iterative inversions. The oceanic crust was inverted using P_g and P_mP phases in order to derive the velocity field and Moho depth, and similarly, the crustal velocities and Moho depth remained fixed for the next inversion. Finally, the upper mantle velocities were inverted using P_n phases. The applied hybrid scheme uses both first and second arrivals to constrain the velocity model, without the need to disregard for example secondary arrivals such as lower crustal P_g, phases which become secondary arrivals where P_n arrivals overtake P_g.

[12] Horizontal grid spacing of the model used for the velocity inversion is 0.5 km, whereas the vertical grid spacing is varied from 0.05 km at the top of the model to 0.5 km at the bottom.

Depth nodes defining the reflectors are spaced at 2 km. We used horizontal correlation lengths ranging from 2 km at the top to 10 km at the bottom of the model, and vertical correlation lengths varying from 0.4 km at the top to 2.5 km at the bottom. Depth and velocity nodes are equally weighted in the joint refraction and reflection traveltime inversion.

4.1. Sedimentary Section Tomography

[13] Seaward from the trench, the basement was derived by picking and converting the vertical incidence reflections from two-way-time (TWT) data to depth using a constant velocity of 1.7 km/s. Approaching the trench (up to profile distance km 200), a 2-km deep trench basin has been developed with incoming pelagic sediments and turbidites (Figure 2b). Here, refracted P_s phases and reflected P_bP phases (Figure 3e) were used to invert the velocity structure of the sediments in the trench and the top of the oceanic crust. The starting model for the sedimentary trench fill and lower continental slope is shown in Figure 4a and was set up using the semi forward modeling approach of *Zelt and Smith* [1992]. The starting model includes the known bathymetry; the velocity at the top of the sedimentary layer is set to 1.7 km/s. Below the seafloor the velocity varies depending on the depth using a constant vertical velocity gradient of 1 s^{-1}. The starting reflector is directly computed by converting the TWT data of the corresponding basement reflector to depth. For this reference model, the initial root-mean square (RMS) traveltime misfits for P_s and P_bP are 407 ms and 567 ms, respectively. As the crustal phases were omitted in this step, the input model still contains sedimentary velocity below the sediment-crust boundary (Figure 4a).

[14] Tests with several starting models converge to nearly the same final model. In order to study the accuracy of the final model, we employed the Monte Carlo method [e.g., *Korenaga et al.*, 2000]. The uncertainty of a nonlinear inversion can be expressed in terms of the posterior model covariance matrix [e.g., *Tarantola*, 1987], which can be approximated by the standard deviation of a large number of Monte Carlo realizations assuming that all the realizations have the same probability [e.g., *Tarantola*, 1987]. The uncertainty estimated by this method should be interpreted as the uncertainty for our model parameters (i.e., starting velocity model and smoothing constraints). The procedure to estimate velocity uncertainties consisted of randomly perturbing velocities of our reference model (Figure 4a). We generated 100 random initial velocity models by adding smooth perturbations randomly distributed (maximum velocity perturbations of ±0.1 km/s at the top and ±0.4 km/s at the bottom of the model, with wavelength perturbations of 5 km horizontally and 0.5 km vertically). The basement reflector depth was found by converting the TWT data of the reflector into depth using the velocity distribution of every initial model. In addition to the perturbed reference models we produced 100 so-called noisy arrival time sets constructed by adding random phase errors (±50 ms) and common receiver errors (±50 ms) to the original data set [*Korenaga et al.*, 2000]. Then we performed a tomographic inversion for each velocity model with one noisy data set, in order to estimate not only the dependence of the solution on the reference model but also the effect of phase arrival time picking errors. The mean deviation of all realizations of such an ensemble is considered to be a statistical measure of the model parameter uncertainties [e.g., *Tarantola*, 1987]. All of the Monte Carlo inversions converged in less then 10 iterations to $\chi^2 = 1$, where χ^2 is the normalized sum of the RMS misfits divided by the corresponding picking uncertainties; a value of 1 means that the model error is equal to the data uncertainty. Figure 4b shows the average model from the 100 final models. The RMS error was reduced to ~50 ms for refractions and ~55 ms for reflections. Figure 4c shows the derivative weight sum (DWS), which is a statistical parameter indicating the model resolution and ray density. The standard deviation of the calculated velocities for most of the model is below 0.1 km/s and for the reflector depth <0.1 km, except at the eastern edge of the model (Figure 4d) where the velocity uncertainty increases to values larger than 0.2 km/s and for the depth uncertainty to values of ~0.3 km due to the reduced data coverage.

4.2. Oceanic Crust Tomography

[15] For the determination of the crustal part of the velocity model we held the previously determined sedimentary section fixed by using spatial damping [*Korenaga et al.*, 2000]. We inverted the oceanic crust by including all crustal phases (first and later arrivals) to their maximum offset, and the depth of the floating reflector (Moho) was identified using the mantle phases P_mP simultaneously in the tomographic inversion [*Korenaga et al.*, 2000]. As with the inversion of sedimentary layer, we use the Monte Carlo scheme for determining the

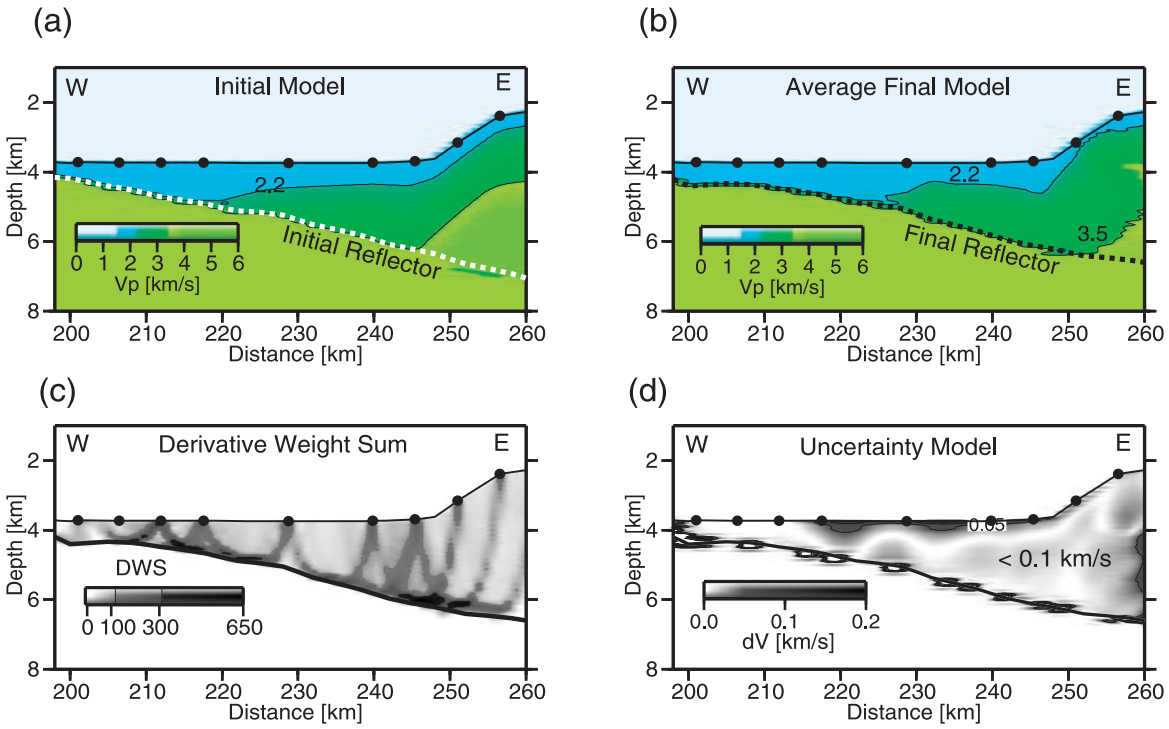

Figure 4. Result of sedimentary tomographic inversion using P_s and P_bP phases, and reflection data. (a) Initial velocity model used as a reference for the Monte Carlo analysis and for velocity inversion. (b) Final average model of the Monte Carlo ensembles. (c) Derivative Weight Sum (DWS) for rays traveling throughout model shown in Figure 4b. (d) Velocity depth uncertainty model after Monte Carlo type realizations.

crust velocities and thicknesses, and therefore a suite of starting models was required.

4.2.1. Reference Model

[16] The 2-D starting velocity models were obtained by hanging 1-D crustal velocity profiles beneath the basement (see Figure 5c). The reference 1-D velocity depth model was composed of oceanic upper crust (layer 2) and the lower crust (layer 3). Minimum values for top, mid, and bottom velocities were 3.0, 6.0, and 6.5 km/s, while corresponding maximum values were 5.0, 7.0, and 7.5 km/s, respectively. The upper crustal thickness could vary from 1 to 3 km, and the lower crustal thickness could vary from 3 to 5 km. The initial geometry of the Moho boundary was chosen as the sum of the obtained smoothed basement geometry in the previous sedimentary modeling and a given crustal thickness, which allowed variations between 4 and 8 km. Different tests showed that variation of the starting model within this model space did not affect significantly the solution. Figure 5a shows the final velocity model derived by averaging all Monte Carlo ensembles.

4.2.2. Model Uncertainty, Monte Carlo–Type Analysis

[17] Velocity and Moho-depth uncertainties of the model parameters in the oceanic plate were estimated by performing a Monte Carlo–type analysis [e.g., *Tarantola*, 1987], as we described above. Figure 5c shows the area covered for the 100 initial two-layer crustal velocity profiles and the 100 starting Moho reflectors underneath the basement.

[18] Initial RMS traveltime misfits were generally higher than 900 ms, and χ^2 was initially greater than 100. The stopping criterion for each inversion was $\chi^2 \sim 1.0$, which was reached typically after 5 iterations. Using the 100 realizations, the final average crustal velocity model and its standard deviation were computed (Figure 5d). The standard deviation of the velocities is lower than 0.1 km/s in the upper crust and the main part of the lower crust as well, increasing to values of 0.1–0.15 km/s in the deepest region of the lower crust. Velocity and Moho depth uncertainties are larger at the western edge of the model where the ray coverage is poor. Moho depth uncertainties in the middle of the model are as low as 0.15 km and reach 0.4 km at

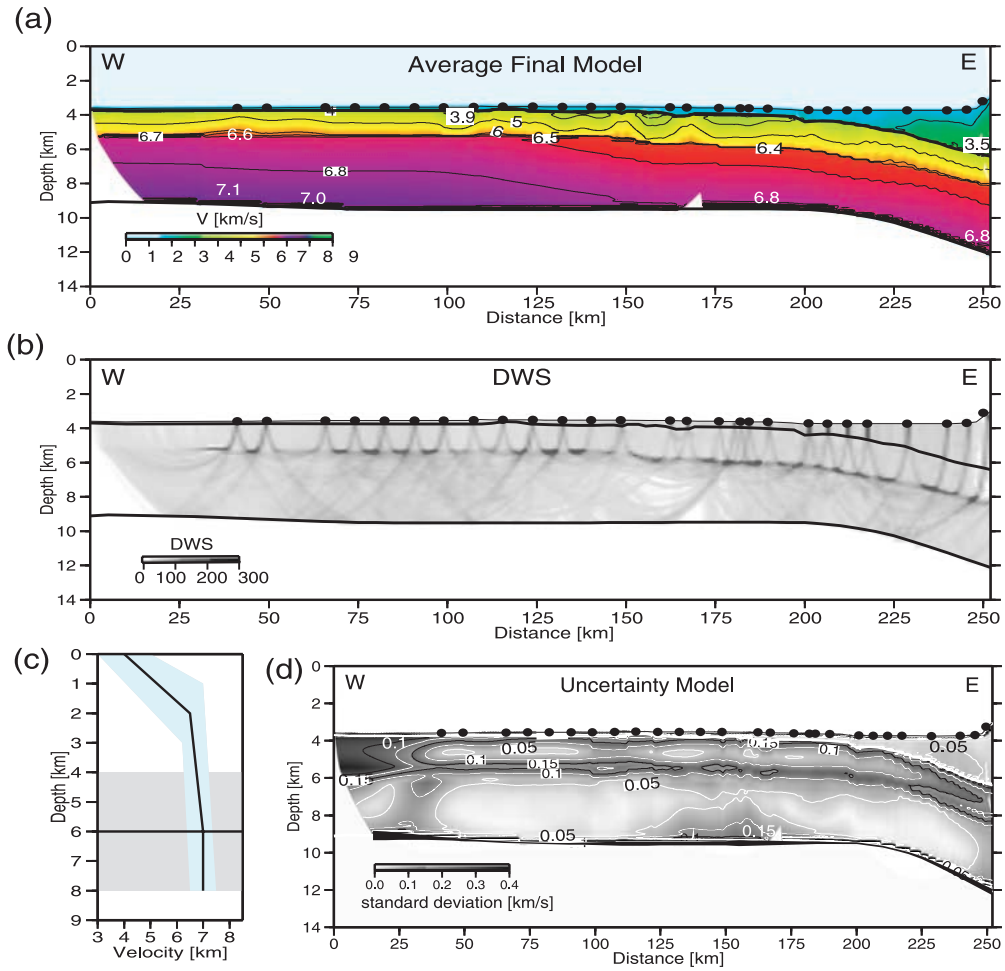

Figure 5. Result of crustal tomographic inversion using P_g and P_mP phases. (a) Final velocity model derived by averaging all Monte Carlo ensembles. (b) Derivative weight sum. (c) Range of parameters for Monte Carlo ensembles. A starting model consists of a 1-D crustal velocity profile; the Moho depth is the sum of the previously obtained smoothed basement and a given crustal thickness. Gray and light blue regions show possible variations in Moho depth and velocity randomization, respectively. (d) Corresponding standard deviation for velocity and depth nodes; contour interval is at 0.05 km/s.

the edges of the velocity model. At the trench, velocities and Moho depth are well constrained with the inclusion of stations on the continental slope [*Scherwath et al.*, 2006b]. The DWS for the model is shown in Figure 5b, which shows excellent ray coverage.

4.2.3. Resolution Test

[19] To check the resolvability of the obtained velocity model, in particular the anomalous low-velocity zones in the trench–outer rise region (Figure 5a), we have created a synthetic model consisting of four sinusoidal anomalies located in the oceanic crust (see Figure 6a), which are superimposed onto the final average velocity model. The maximum amplitude of each Gaussian anomaly is ±6% (Figure 6). Synthetic traveltime data with the same source-receiver geometry as in the real data set have been generated with the perturbed model, and they were inverted using an initial unperturbed model to see how well given perturbations are recovered. The recovery model is plotted in Figure 6b, which was gained after 3 iterations. The result shows that position, shape and amplitude of the velocity anomalies are reasonably well recovered within the uncertainty limits. Despite a certain deterioration in the shape of the anomalies, the result indicates that the geometry and instrument spacing yields a sufficiently high resolution for these structural anomalies, discerning between positive and negative variations along the oceanic crust. The tomographic inversion scheme used here is able to resolve structures with size and amplitude similar to the normal and low-velocity zone at this depth range. This shows that the crustal velocity reduction of the oceanic crust when approaching the trench

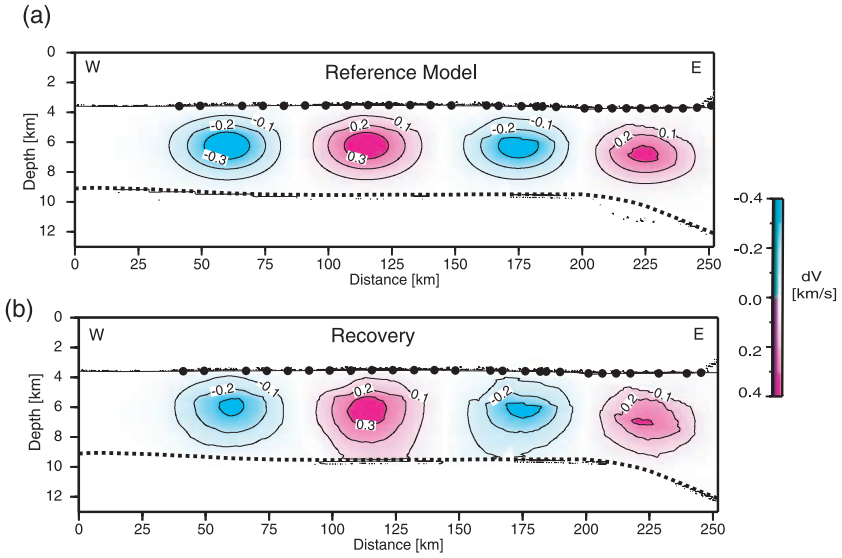

Figure 6. Results of resolution test. (a) Synthetic reference velocity model, consisting of three single sinusoidal anomalies superimposed onto the final velocity model of Figure 5a. (b) Recovery obtained after four iterations.

shown in Figure 5a is not an artifact of the seismic tomographic inversion procedure but a real feature.

4.3. Upper Mantle Tomography

[20] For the subsequent tomographic inversion of the mantle refraction P_n, a "layer-stripping" procedure was chosen, preserving the structural and velocity information above the Moho interface gained before. For the Monte Carlo inversion approach, we constructed several initial models by varying the uppermost mantle velocity between 7.5 to 8.5 km/s and the mantle velocity gradient between 0 and 0.04 s^{-1} respectively. The final average model and its uncertainties are plotted in Figure 7. The results exhibit a clear trend of velocity-reduction toward the trench, which is well correlated with the location of the outer rise but landward of the crustal velocity reduction. Uncertainties of the upper mantle velocity in the outer rise region range between 0.1–0.2 km/s and are well constrained in the seaward part (~0.1 km/s) where the plate geometry is relatively flat and the sediments are thin.

[21] To survey the robustness of our tomographic results, we conducted independent forward modeling seeking a minimum-structure model that satisfies the data. Model features common to the tomographic and forward-modeling output may be assessed without using subjective a priori information [e.g., *Zelt and Smith*, 1992]. We studied uppermost mantle velocity and different velocity gradients by keeping the structural and velocity information above the Moho interface gained for the crustal tomography (Figure 5a). Figure 8a shows the record section of OBH 68, which displays an example of the onset of the P_g, P_mP and P_n phases. "Normal" crustal velocities fit the crustal phases well, and the best-fitting uppermost mantle velocity is about 8.3 km/s. A comparison with a reduced upper mantle velocity of 8.0 km/s produces a large P_n traveltime misfit (Figure 8a), and so we conclude that the seismic data can only be explained with uppermost velocities as fast as 8.3 km/s. Toward the trench the situation changes; a "delay" of P_n arrivals is observed (Figure 8b). These delayed P_n arrivals are already apparent in most of the trenchward branches of seismic stations. A large amount of the total delay in P_n arrivals can be attributed to the thick sedimentary sequence, which covers the deflected downgoing plate (see Figure 4b). However, as our previous sedimentary tomography constrains the sediment structure, a remaining delay of 150 ms is still required to fit P_n arrivals within the uncertainty of the picked arrivals. A better P_n traveltime fit occurs with uppermost mantle velocities ranging between 7.7–8.0 km/s. We also plotted the predicted traveltimes for P_n with an uppermost mantle velocity of 8.2 km/s; the arrivals are predicted up to 150 ms earlier than observed (Figure 8b). In conclusion, the high-quality P_n phases clearly define a reduction of upper mantle velocities toward the trench.

5. Discussion

[22] The data presented in this paper show systematic changes of crustal and upper mantle seismic

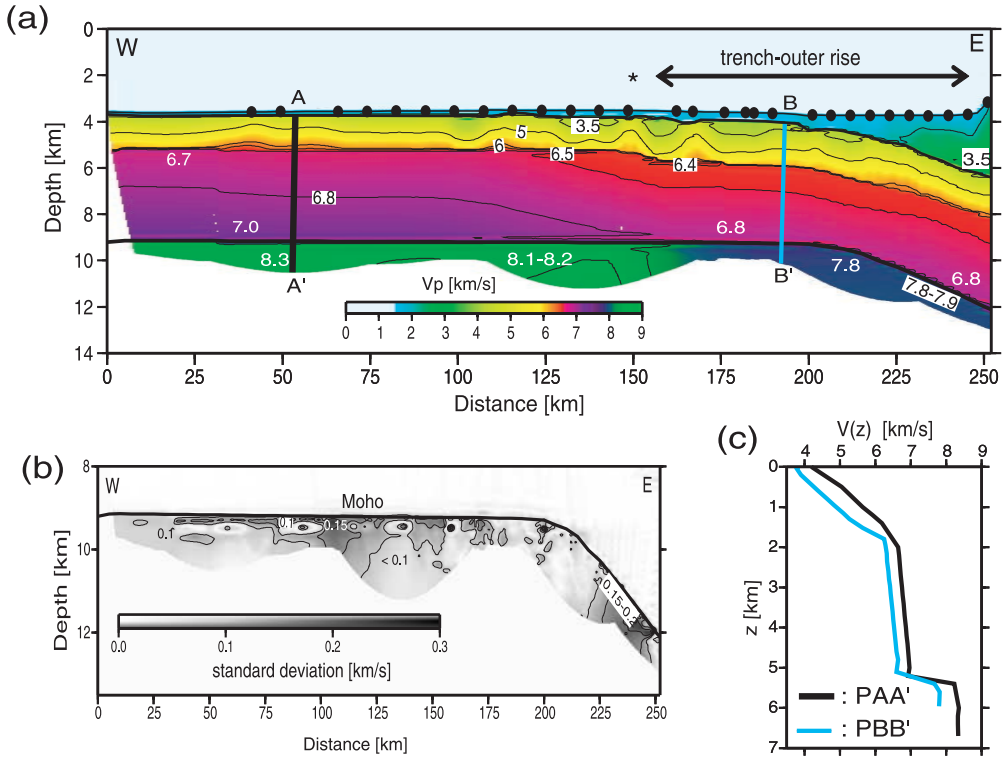

Figure 7. Result of mantle tomographic inversion using refracted P_n phases. (a) Final velocity model derived by averaging all Monte Carlo ensembles (see text for details). (b) Corresponding standard deviation for upper mantle velocity model; contours are drawn at 0.05 km/s interval. Velocity uncertainty is higher between x = 220–250 km below the thick sediments at the trench. (c) Comparison of velocity depth structure for extracted profile from our velocity model shown in Figure 7a. Black line shows velocity structure $V(z)$ away from the trench, and blue line shows $V(z)$ beneath the trench–outer rise.

structure in the form of velocity reduction in the oceanic Nazca plate while it approaches the Chile trench. In this section, we discuss the transition from "normal" to deformed and altered oceanic subducting lithosphere and its possible causes within the geodynamic framework.

5.1. Seismic Structure of the Oceanic Lithosphere

5.1.1. Sediments and Basement Topography

[23] Seaward from the trench (>200 km) the southern Nazca plate is covered by a thin sequence of pelagic and hemipelagic sediments (<150 m). Here, high-resolution multibeam bathymetric mapping shows the typical topographic pattern of the tectonic fabric formed at the spreading center, which is obscured toward the trench due to turbidites deposits (Figure 2b). From profile km x ~ 50 to 200, turbidites fill the half-graben structure and overlay pelagic sediments, forming a mix-sedimentary sequence of 200–400 m thickness. Further to the east (in the trench basin), the sedimentary-cover becomes thicker, resulting in a total thickness of ~2.000 m (Figure 4b). Trench sediments were mainly delivered during the Pleistocene glaciation with a rapid sedimentation rate [*Bangs and Cande*, 1997]. At the bottom of the trench basin, compressional velocities of 3.0–3.5 km/s were detected at 2 km-depth below seafloor. These velocities are because of compaction processes and the increase of sediment size from top to bottom (graded bedding), associated to sedimentary deposit events.

[24] The basement topography is in general rough, and it is characterized by the presence of outcrops of basement highs (Figure 2a). In the outer-rise (x ~ 150 km), and approximately 5 km to the north of the seismic profile a basement outcrop rises ~200 m above the surrounding seafloor (Figure 9a), while its associated basaltic edifice rises ~400 m above regional basement. Ten kilometers to the north of this basement outcrop, several abyssal hills generated at the spreading

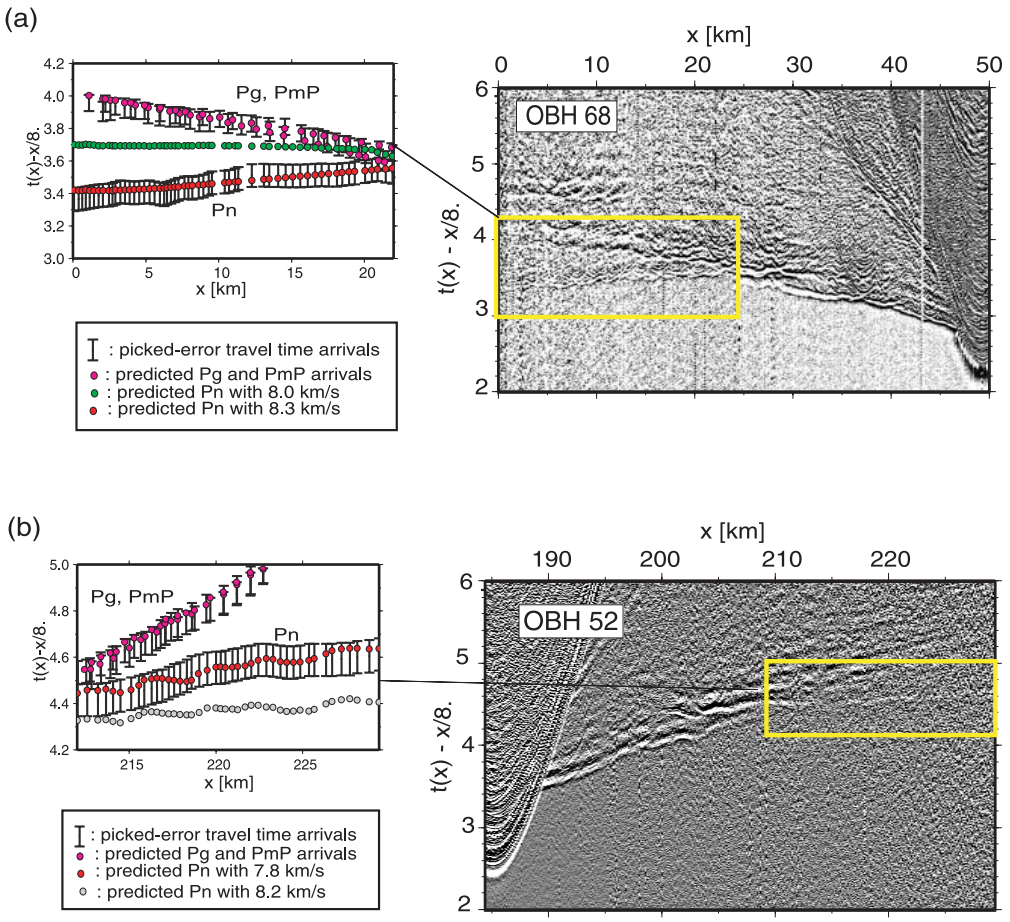

Figure 8. Detailed forward analysis of P_n traveltimes for (a) oceanward branch of OBH 68 and (b) trenchward branch of seismic record section of OBH 52. Predicted P_g and P_mP arrivals are based on the final crustal model shown in Figure 5a. (a) P_n oceanic phases can only be predicted with values as fast as 8.3 km/s (red dots); uppermost velocities values of 8.0 km/s produce a misfit >250 ms (green dots). (b) P_n arrivals are predicted up to 150 ms earlier than observed using an uppermost velocity of 8.2 km/s (gray dots); a better P_n traveltime fit occurs with uppermost mantle velocity of 7.8 km/s (red dots).

center with pervasive faulting and large offsets strike approximately parallel to the trench axis (Figure 2a). This area is characterized by pervasive normal faults exposing basement caused by plate bending. Southward and trenchward of the seismic profile, this fault pattern is not visible on the multibeam bathymetry owing to the thicker sedimentary cover. Under the trench fill, however, multichannel data reveal that as the plate approaches the trench, basement topography becomes rougher and the oceanic crust is probably pervasively fractured due to bending-related faulting (Figure 2b).

5.1.2. Oceanic Crust

[25] Two distinct zones of the oceanic crust can be identified in the final model: (1) the oceanward section, away from the trench, and (2) the trench–outer rise region just prior of the subduction of the oceanic plate. Figure 7c compares the velocity structure beneath the sediments for well resolved velocity-depth profiles of zones 1 and 2.

[26] In the oceanward section of the velocity model, the velocity structure below basement roughly follows the basement topography. Velocities in the ~1.7 km thick layer are between 4.0–4.2 km/s at the top and ~6.6 km/s at the bottom and correspond to oceanic layer 2; a typical sequence of extrusive basalts on top of a sheeted dike complex and high velocity gradient of about 1.4 s^{-1}. Both seismic velocity and gradient are similar to the seismic structure obtained off-axis in the upper crust of the southern East Pacific Rise [*Grevemeyer et al.*, 1998]. These values are in good agreement with mature oceanic crust sufficiently far way from the ridge crests so that strong hydrothermal circulation has largely ceased [*Grevemeyer et al.*, 1999]. Layer 2 overlies a ~3.6 km thick layer with velocities increasing from 6.6 km/s to ~7.0–7.1 km/s. This

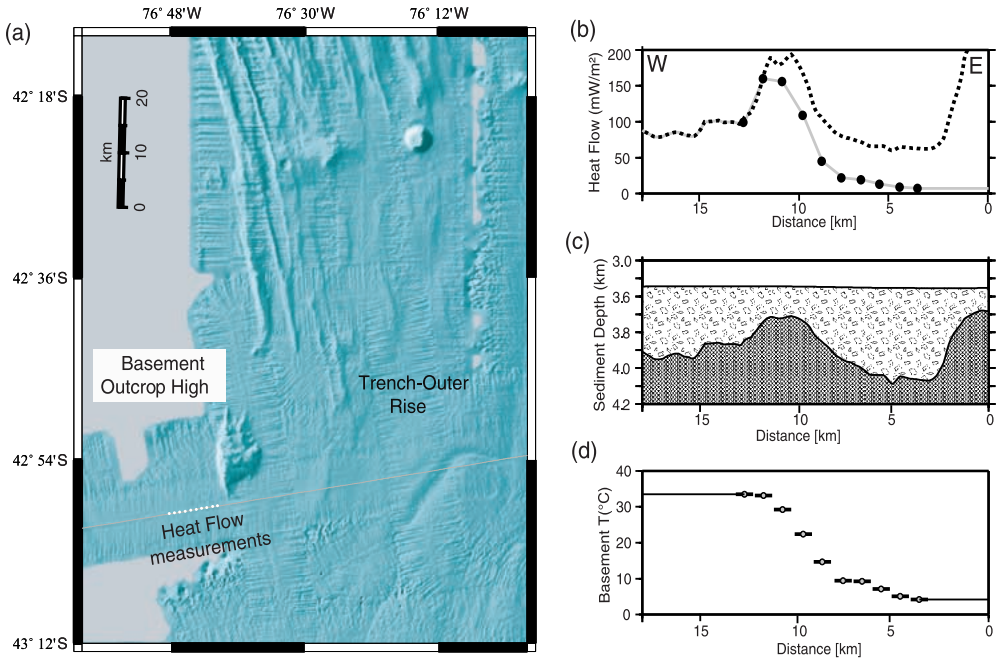

Figure 9. (a) Location of heat flow stations along seismic profile. (b) Heat flow measurements (black dots). Predicted heat flow values using a basement temperature of T_b = 40°C (dotted line). Predicted heat flow values incorporating hydrothermal cooling (gray line). (c) Basement topography obtained from seismic reflection data. (d) Temperature distribution at the basement used in our heat flow model with cooling. For Figures 9b, 9c, and 9d, distance is measured from the location of the basement outcrop high.

seismic structure is typical of oceanic layer 3 normally associated with gabbro and layered gabbro rocks (layer 3A and 3B) [e.g., *Vera et al.*, 1990]. The velocity range of 6.6–7.1 km/s is consistent with lower crust relative anhydrous in composition, which is typical for oceanic crust formed at fast spreading ridges [e.g., *Carbotte and Scheirer*, 2004; *Karson*, 1998]. The bulk porosity of the crust should be rather low due to the closure of cracks and fissures by hydrothermal mineralization [e.g., *Grevemeyer and Bartezko*, 2004].

[27] Approaching the trench, velocities for the igneous crust start to decrease 100 – 150 km from the deformation front (Figure 5a). The uppermost crustal velocities decrease to values lower than 3.7 km/s (Figure 7c), which are much lower than typical uppermost layer 2 velocities of mature oceanic crust (>4.5 km/s) [*Carlson*, 1998; *Grevemeyer and Bartetzko*, 2004]. Lowermost crustal velocities decrease to values lower than 6.9 km/s (Figure 5a), implying the likely presence of hydrous minerals, such as chlorite and amphibolites [e.g., *Hess*, 1962; *Christensen and Salisbury*, 1975]. The decrease of velocities is accompanied with an increase in roughness of the basement topography, and probably coincides with activation of new cracks and normal extensional faults induced by plate bending [e.g., *Ranero and Sallares*, 2004]. This process suggests a significant alteration of the porosity structure of the entire subducting oceanic crust.

[28] Moho reflections (P_mP) constrain the transition from "crustal" gabbros to "mantle" ultramafic rocks, which occurs at ~5.3 km depth below the top of the basement. Crustal thickness is therefore less than the average value of 6.48 ± 0.75 km reported by *White et al.* [1992] for Pacific crust younger than 30 Ma. *McClain and Atallah* [1986], however, estimated that Pacific crust averages 5.67 ± 0.88 km for crust of the same age, and *Walter et al.* [2000] and *Grevemeyer et al.* [2007] found in more recent studies that crust of the Cocos plate is 5.0–5.5 km thick.

5.1.3. Uppermost Oceanic Mantle

[29] Seaward from the trench, compressional velocity of 8.3 km/s was detected in the uppermost 2–2.5 km of the mantle (Figure 7a). Typical mature oceanic mantle velocities are faster than 8.1 km/s, which is usually associated to an anhydrous composition of mantle peridotite [e.g., *Peacock*, 1990]. Thus oceanic Nazca plate approaches the subduction zone with a mantle comparatively undeformed and dry (Figure 7a). Closer to the trench, however, a progressive velocity-reduction in the upper mantle

occurs. The velocity reduction is visible ~80 km from the deformation front (Figure 7a), and they decrease to minimum values of ~7.8 km/s, which is significantly lower than the velocity of mantle peridotite (>8.1 km/s). P_n phases image only the first ~2 km of the uppermost mantle in the outer rise area (Figure 7a). Thus the maximum depth of possible hydration in the mantle remains unconstrained.

[30] It has been documented that the uppermost mantle velocity reduction is even larger in poorly sedimented margins. In north Chile, for example, upper-mantle velocities in the trench–outer rise area reach values as low as 7.6 km/s [*Ranero and Sallares.*, 2004]. Offshore of Costa Rica, seismic velocities under the trench at the Moho are even lower (7.3–7.4 km/s), with velocities increasing to ~7.5–7.8 km/s at about 3–4 km below the Moho [*Grevemeyer et al.*, 2007]. Offshore of south central Chile, upper mantle velocity reduction is slightly lower and solely restricted to the trench–outer rise area (Figure 7a), where bending-related faulting is suggested to lead to hydration of the upper mantle [*Ranero et al.*, 2003]. Since water is required to alter mantle peridotite to serpentinite, pervasive fracturing of the entire crust is suggested for the lithosphere entering the Chilean subduction zone offshore Chiloe Island.

5.2. Water Pathways

[31] The efficiency of fluid percolation depends on the sedimentary thickness and faulting history. Faults constitute the possible water pathways but they can be blocked by insulating sediments. Therefore slab hydration prior to subduction is believed to be largest where outcropping basement relief facilitates the flow of seawater into the crust [*Grevemeyer et al.*, 2005]. The abyssal hill fabric inherently related to the formation process of the oceanic lithosphere at the mid-ocean ridge is well imaged just 5 km to the north of the seismic line (Figure 2a). Therefore reactivation of fractures by bending-related normal faulting in this region might be an important mechanism for plate hydration.

[32] High-resolution seismic data provides evidence for some extensional faults reflected by offsets in the trench–outer rise region (Figure 2b), suggesting the trenchward increase of fracturing intensity. This indicates that the bending-related faulting is active in the outer rise, and it fractures the oceanic crust beneath the sedimentary bed. High-resolution multibeam bathymetry shows, though, that surface-cutting faults are not visible on the seafloor along this profile (Figure 2a). As the insulating sediments are several hundreds of meters thick (Figure 2b) an efficient inflow of seawater is unlikely to explain the reduced velocities in the outer rise. However, the onset of velocity reduction in the oceanic crust is well correlated with the location of an outcropping basement high or seamount (Figures 7a and 9), suggesting a relationship between plate hydration and basement outcrop. Seamounts or basement highs provide the necessary pathways to move huge volumes of fluid through oceanic crust over large distances, even when the crust is insulated by thick sediments [*Fisher et al.*, 2003a, 2003b].

[33] In order to study the hydrothermal activity in the outer rise, we have directly measured heat flow values on the outer bulge offshore of Chiloe Island [*Flueh and Grevemeyer*, 2005]. Figure 9a shows the location of 10 heat flow stations immediately at the seaward flank of the basement outcrop (see also the bathymetry in Figure 2a). The heat flow values decrease from 100–150 to ~7 mW/m^2 over a distance of less than 10 km toward the trench (Figure 9b). We computed two predicted heat flow models using two different temperature distributions at the top of the igneous basement. In the first model basement temperature is isothermal. In the second model basement temperatures varies as a function of distance from the basement high and hence mimics cooling by inflow of cold seawater. Crucial parameters are the temperature at the basement T_{bas} and at the seafloor T_{sea}, and the thermal conductivity structure k between the basement and the seabed. We use a linear temperature gradient and the simple conductive heat transport relation

$$q = k\, dT/dz$$

where q is the heat flow, $dz = z_{bas} - z_{sea}$ is the thickness of the sediments, and $dT = T_{bas} - T_{sea}$. The sedimentary thickness comes directly from the high-resolution reflection data and is plotted in Figure 9c. The seafloor temperature is assumed $T_{sea} = 0°C$, and thermal conductivity k was measured in situ. Testing with different $T_{bas}(x)$ distributions, the extreme low values toward the trench can only be predicted by the cooling model (Figures 9b and 9d). This finding suggests a very efficient inflow of cold seawater into the oceanic crust through the basement outcrop feature located just 5 km north of the profile.

[34] The flanks of the high outcrop basement probably act as an important and primary entry of cold seawater into the igneous oceanic crust. This process accompanied by the opening of new cracks and activation of extensional faults due to bending-related faulting increases the permeability and hence facilitates a deeper fluid inflow, probably, reaching mantle depths, as supported by our tomographic results (Figure 7a). We see a number of other mounds and basement ridges imaged in the multibeam bathymetry to the north of the profile, which may act as recharge and discharge sites and therefore fuel a hydrothermal circulation in the outer rise. Cold seawater might be transported laterally between separated basement outcrops for distances of more than 50 km [*Fisher et al.*, 2003a], which implies that fluids may circulate through most of the studied trench–outer rise area. Here, bending-related faulting might increases the permeability of the oceanic crust, and consequently facilitates and reactivates hydrothermal circulation.

[35] Moreover, the incoming plate may laterally carry water already percolated in the oceanward part of the outer rise (70–40 km from the trench axis), where plate bending is strongest, igneous basement is more exposed, and due to a higher water/rock ratio hydration might be more vigorous. In this part of the outer rise, the sedimentary thickness is comparable with the outer rise in Middle America (200–400 m thick), which is highly hydrated [*Ranero et al.*, 2003]. Once cold seawater is stored in cracks and/or faults and faulting continues toward the deformation front, water trapped within the crust may migrate deeper where larger faults cut into the mantle.

5.3. Volatiles Stored in the Oceanic Subducting Lithosphere

[36] The amount of volatiles stored in the subducting oceanic lithosphere consists mainly of three components: volatiles stored (1) in subducting sediments, (2) in the oceanic crust, and (3) in the oceanic mantle. Recent studies, however, suggest that most of the bound water enters subduction zones within the oceanic crust and mantle [*Peacock*, 1990; *Ranero et al.*, 2003].

[37] The observed crustal velocity reduction beneath the trench–outer rise is caused in part by cracks and fissures induced by plate bending. The similar trend for upper and lower crustal velocities has been observed in the northern Chile trench, which was explained as consequence of fracturing rather than hydration [*Ranero and Sallares*, 2004]. The amount of chemically bound water in the crust is therefore not straightforward to estimate by the magnitude of velocity reduction. *Peacock* [1990] concludes from chemical analysis of drill cores of oceanic crust that a 2.5-km-thick basaltic layer contains in average 2 wt.% H_2O and ~0.1 wt.% CO_2, and a 3- to 5-km-thick oceanic gabbro layer contains roughly 1% H_2O and ~0.1 wt.% CO_2. *Hacker et al.* [2003] calculated a maximum water content of 1.3 wt% H_2O for partially hydrated lower oceanic crust based on a global compilation of physical properties of minerals. *Carlson* [2003] shows that, based on the modal mineralogy and seismic properties of oceanic diabase and gabbro samples, gabbros with velocities typical for the lower oceanic crust (6.7–7.0 km/s) already contain a mean water content near 0.5 wt%. This value could be much larger if lower oceanic crust has been altered by tectonic processes, as is probably the case in our study area.

[38] Quantifying the amount of serpentine in subducting oceanic mantle is also difficult because relatively modest amounts of serpentine can represent a major H_2O input into the subduction factory [*Peacock*, 2001]. Following *Carlson and Miller* [2003], an approximate formula to estimate water content in the partially-serpentinized peridotites is $w(\%) \approx -0.33\Delta V$, where w is the water content (in weight percentage) and ΔV is the percent difference between the observed velocity and the velocity in unaltered peridotite. The upper mantle P wave velocity in our study region ranges between 7.8 to 8.3 km/s, corresponding to serpentinite contents of roughly 0 to 9%; and the corresponding range of water contents of 0 to 3.0% (0 to 4 moles/m^3). These values are lower compared to estimates in Central America (>20% of serpentinization) [*Ranero et al.*, 2003], the erosional margin in northern Chile (~17% of serpentinization) [*Ranero and Sallares*, 2004], and offshore Costa Rica (10–25% of serpentinization) [*Grevemeyer et al.*, 2007]. Nevertheless, the total amount of hydration and thus the total volume of fluids entering the subduction zone in south central Chile should be larger than the 9% bound in the upper mantle because of the volatile stored in the entire oceanic crust plus subducting sediments. Moreover, this degree of hydration can be even larger if the oceanic plate continues to hydrate during subduction [*Ranero et al.*, 2003].

6. Conclusions

[39] Joint inversion of seismic refraction and wide-angle data offshore of south-central Chile yields

the P wave velocity structure of the subducting oceanic Nazca plate. This information and the tectonic features obtained from high-resolution seismic data, multibeam bathymetry and heat flow measurements suggest that the structure of the incoming plate changes systematically within ~120 km off the trench axis as the lithosphere approaches the deep-sea trench. This work leads to the following conclusions:

[40] 1. The 2-D velocity model derived from tomographic traveltime inversion consist of a ~5.3 km thick oceanic crust and shows a classical mature fast spreading P wave velocity structure in the seaward part outside of the influence of plate bending at the trench–outer rise. Seismic analysis of P_n arrivals reveals fast uppermost mantle velocities of ~8.3 km/s, >120 km seaward of the trench. The velocity structure found in this zone indicates that the oceanic lithosphere is relatively dry and undeformed.

[41] 2. Approaching the Chile trench, seismic velocities decrease, indicating an evolutionary process changing the structure of the lithosphere, likely to be related to an increase in fracture porosity and hydration of both the oceanic crust and the uppermost mantle. Reduced velocities are only located in the trench and outer-rise area. The decrease of velocities is accompanied by an increase of basement-relief roughness and also by the amount of stress induced by the plate bending.

[42] 3. In spite of the thick sedimentary blanket on the incoming plate, an efficient inflow of cold seawater into the oceanic crust through outcropping basement highs or seamounts is supported by anomalously low heat flow values, which are spatially well correlated with the onset of velocity reduction in the crust and upper mantle. Cold seawater might be laterally transported between high basement outcrops over large distances (>50 km) in the vicinity of the trench–outer rise area. This primary water pathway could extend to mantle depth through bending induced trench parallel normal faults, and thus cause a hydration of the upper mantle.

[43] 4. Assuming that the mantle velocity reduction is produced only by hydration, serpentinization of the uppermost mantle from the outer rise to the trench axis is ~9% in the uppermost 2 km of the mantle, where seismic data provide enough resolution. This degree of hydration in the uppermost mantle is about 10% less than observed in poorly sedimented margins.

[44] In summary, seismic data of high resolution reveal a clear alteration of the oceanic lithosphere at the outer rise just prior to its subduction, showing that the alteration occurs where strong plate bending is likely to modify the large scale porosity and permeability structure of oceanic lithosphere, and simultaneously nurtures the migration of cold seawater through crustal faults down to mantle depth, resulting in hydration of both oceanic crust and upper mantle. Infiltration of cold seawater, and consequently hydration of the subducting oceanic lithosphere may also occur at heavily sedimented trenches through high basements outcrops where igneous crust is exposed.

Acknowledgments

[45] We are grateful to Masters Kull and Mallon and their officers and crew of R/V *Sonne* and all scientists who assisted in data collection during cruise SO181. This is publication GEOTECH-276 of the R&D-Programme GEOTECHNOLOGIEN funded by the German Ministry of Education and Research (BMBF) and German Research Foundation (DFG), grants 03G0181A, 03G0594E, and 03G0594F. One of the authors (E.C.-R.) gratefully acknowledges a scholarship granted by the German Academic Exchange Service (DAAD).

References

Alt, J. C., J. Honnorez, C. Laverne, and R. Emmermann (1986), Hydrothermal alteration of a 1 km section through the upper oceanic crust, Deep Sea Drilling Project Hole 504B: Mineralogy, chemistry, and evolution of seawater-basalt interactions, *J. Geophys. Res.*, *91*, 10,309–10,335.

Angermann, D., J. Klotz, and C. Reigber (1999), Space-geodetic estimation of the Nazca–South America Euler vector, *Earth Planet. Sci. Lett.*, *171*(3), 329–334.

Bangs, N. L., and S. C. Cande (1997), Episodic development of a convergent margin inferred from structures and processes along the Southern Chile margin, *Tectonics*, *16*, 489–503.

Bialas, J., and E. R. Flueh (1999), Ocean bottom seismometers, *Sea Technol.*, *40*(4), 41–46.

Carbotte, S., and D. S. Scheirer (2004), Variability of ocean crustal structure created along the global mid-ocean ridge, in *Hydrogeology of Oceanic Lithosphere*, edited by E. E. Davis and H. Elderfield, pp. 128–150, Cambridge Univ. Press, New York.

Carlson, R. L. (1998), Seismic velocities in the uppermost oceanic crust: Age dependence and the fate of layer 2A, *J. Geophys. Res.*, *103*(B4), 7069–7078.

Carlson, R. L. (2003), Bound water content of the lower oceanic crust estimated from modal analyses and seismic velocities of oceanic diabase and gabbro, *Geophys. Res. Lett.*, *30*(22), 2142, doi:10.1029/2003GL018213.

Carlson, R. L., and D. J. Miller (2003), Mantle wedge water contents estimated from seismic velocities in partially serpentinized peridotites, *Geophys. Res. Lett.*, *30*(5), 1250, doi:10.1029/2002GL016600.

Chapple, W. M., and D. W. Forsyth (1979), Earthquakes and bending plates at trenches, *J. Geophys. Res.*, *84*, 6729–6749.

Christensen, D. H., and L. J. Ruff (1983), Outer-rise earthquakes and seismic coupling, *Geophys. Res. Lett.*, *10*, 697–700.

Christensen, N. I., and M. H. Salisbury (1975), Structure and constitution of the lower oceanic crust, *Rev. Geophys.*, *13*, 57–86.

Fisher, A. T., C. A. Stein, R. N. Harris, K. Wang, E. A. Silver, M. Pfender, M. Hutnak, A. Cherkaoui, R. Bodzin, and H. Villinger (2003a), Abrupt thermal transition reveals hydrothermal boundary and role of seamounts within the Cocos Plate, *Geophys. Res. Lett.*, *30*(11), 1550, doi:10.1029/2002GL016766.

Fisher, A. T., et al. (2003b), Hydrothermal recharge and discharge across 50 km guided by seamounts on a young ridge flank, *Nature*, *421*, 618–621.

Flueh, E. R., and J. Bialas (1996), A digital, high data capacity ocean bottom recorder for seismic investigations, *Int. Underwater Syst. Design*, *18*(3), 18–20.

Flueh, E. R., , and I. Grevemeyer (Eds.) 2005. TIPTEQ SONNE Cruise SO-181, from the Incoming Plate to mega Thrust EarthQuakes, *Geomar Rep. 102*, Geomar, Kiel, Germany.

Grevemeyer, I., and A. Bartetzko (2004), Hydrothermal ageing of oceanic crust: Inferences from seismic refraction and bore hole studies, in *Hydrogeology of Oceanic Lithosphere*, edited by E. E. Davis and H. Elderfield, pp. 128–150, Cambridge Univ. Press, New York.

Grevemeyer, I., and W. Weigel (1996), Seismic velocities of the uppermost igneous crust versus age, *Geophys. J. Int.*, *124*, 631–635.

Grevemeyer, I., and W. Weigel (1997), Increase of seismic velocities in upper oceanic crust: The "superfast" spreading East Pacific Rise at 14°14′S, *Geophys. Res. Lett.*, *24*(3), 217–220.

Grevemeyer, I., W. Weigel, and C. Jennrich (1998), Structure and ageing of oceanic crust at 14°S on the East Pacific Rise, *Geophys. J. Int.*, *135*, 573–584.

Grevemeyer, I., N. Kaul, H. Villinger, and W. Weigel (1999), Hydrothermal activity and the evolution of the seismic properties of upper oceanic crust, *J. Geophys. Res.*, *104*(B3), 5069–5080.

Grevemeyer, I., N. Kaul, J. L. Diaz-Naveas, H. Villinger, C. R. Ranero, and C. Reichert (2005), Heat flow and bending-related faulting at subduction trenches: Case studies offshore of Nicaragua and Central Chile, *Earth Planet. Sci. Lett.*, *236*, 238–248.

Grevemeyer, I., C. R. Ranero, E. R. Flueh, D. Klaeschen, and J. Bialas (2007), Passive and active seismological study of bending-related faulting and mantle serpentinization at the Middle America trench, *Earth Planet. Sci. Lett*, doi:10.1016/j.epsl.2007.04.013.

Hacker, B. R., G. A. Abers, and S. M. Peacock (2003), Subduction factory: 1. Theoretical mineralogy, densities, seismic wave speeds, and H_2O contents, *J. Geophys. Res.*, *108*(B1), 2029, doi:10.1029/2001JB001127.

Hess, H. H. (1962), History of ocean basins, in *Petrological Studies: A Volume in Honor of A. F. Buddington*, edited by A. E. Engel, H. L. James, and B. F. Leonard, pp. 599–620, Geol. Soc. of Am., Boulder, Colo.

Kanamori, H. (1971), Seismological evidence for lithospheric normal faulting: The Sanriku earthquake of 1933, *Phys. Earth Planet. Inter.*, *4*, 289–300.

Karson, J. A. (1998), Internal structure of oceanic lithosphere: A perspective from tectonic windows, in *Faulting and Magmatism at Mid-Ocean Ridges*, *Geophys. Monogr. Ser.*, vol. 106, edited by W. R. Buck et al., pp. 177–218, AGU, Washington, D. C.

Korenaga, J., W. S. Holbrook, G. M. Kent, P. B. Kelemen, R. S. Detrick, H. C. Larsen, J. R. Hopper, and T. Dahl-Jensen (2000), Crustal structure of the southeast Greenland margin from joint refraction and reflection seismic tomography, *J. Geophys. Res.*, *105*, 21,591–21,614.

McClain, J. S., and C. A. Atallah (1986), Thickening of oceanic crust with age, *Geology*, *14*, 574–805.

Peacock, S. (1990), Fluid processes in subduction zones, *Science*, *248*, 329–337.

Peacock, S. (2001), Are the lower planes of double seismic zones caused by serpentine dyhydration in subducting oceanic mantle?, *Geology*, *29*, 299–302.

Peacock, S. M. (2004), Insight into the hydrogeology and alteration of oceanic lithosphere based on subduction zones and arc volcanism, in *Hydrogeology of Oceanic Lithosphere*, edited by E. E. Davis and H. Elderfield. pp. 659–676, Cambridge Univ. Press, New York.

Ranero, C. R., and V. Sallares (2004), Geophysical evidence for alteration of the crust and mantle of the Nazca Plate during bending at the north Chile trench, *Geology*, *32*, 549–552.

Ranero, C. R., J. Phipps Morgan, K. McIntosh, and C. Reichert (2003), Bending, faulting, and mantle serpentinization at the Middle America trench, *Nature*, *425*, 367–373.

Reichert, C., B. Schreckenberger. and SPOC Team (2002), Fahrtbericht SONNE-Fahrt SO-161 Leg 2&3 SPOC, Subduktionsprozesse vor chile-BMBF-Forschungsvorhaben 03G0161A- Valparaiso 16.10.2001–Valparaiso 29.11.2001, Bundesanst. für Geowissenschaften und Rohstoffe, Hannover, Germany.

Scherwath, M., E. R. Flueh, I. Grevemeyer, F. Tilmann, E. Contreras-Reyes, and R. W. Weinrebe (2006a), Investigating subduction zone processes in Chile, *Eos Trans. AGU*, *87*(27), 265–272.

Scherwath, M., E. Contreras-Reyes, I. Grevemeyer, E. R. Flueh, W. Weinrebe, and the TIPTEQ Working Group (2006b), Structural images of the southern Chile subduction zone system offshore, paper presented at Third EGU General Assembly, European Geosciences Union, Vienna2 -7 April .

Tarantola, A. (1987), *Inverse Problem Theory: Methods for Data Fitting and Model Parameter Estimation*, 613 pp., Elsevier, New York.

Tebbens, S. F., S. C. Cande, L. Kovacs, J. C. Parra, J. L. LaBrecque, and H. Vergara (1997), The Chile ridge: A tectonic framework, *J. Geophys. Res.*, *102*(B6), 12,035–12,060.

Thornburg, T. M., and D. M. Kulm (1987), Sedimentation in the Chile Trench: Depositional morphologies, lithofacies, and stratigraphy, *Geol. Soc. Am. Bull.*, *98*, 33–52.

Thornburg, T. M., D. M. Kulm, and D. M. Hussong (1990), Submarine-fan development in the southern Chile trench: A dynamic interplay of tectonics and sedimentation, *Geol. Soc. Am. Bull.*, *102*, 1658–1680.

van Avendonk, H. J. A., A. J. Harding, and J. A. Orcutt (1998), A two-dimensional tomographic study of the Clipperton transform fault, *J. Geophys. Res.*, *103*, 17,885–17,899.

Vera, E. E., J. C. Mutter, P. Buhl, J. A. Orcutt, A. J. Harding, M. E. Kappus, R. S. Detrick, and T. M. Brocher (1990), The structure of 0- to 0.2-m.y.-old oceanic crust at 9°N on the East Pacific Rise from expanded spread profiles, *J. Geophys. Res.*, *95*(B10), 15,529–15,556.

Villinger, H., I. Grevemeyer, N. Kaul, J. Hauschild, and M. Pfender (2002), Hydrothermal heat flux through aged oceanic crust: Where does the heat escape?, *Earth Planet. Sci. Lett.*, *202*, 159–170.

Voelker, D., M. Wiedicke, S. Ladage, C. Gaedicke, C. Reichert, K. Rauch, W. Kramer, and C. Heubeck (2006), Latitudinal variation in sedimentary processes in the Peru-Chile Trench off Central Chile, in *The Andes—Active Subduction Orogeny*, *Frontiers in Earth Sciences*, edited by O. Oncken et al., pp. 193–216, Springer, Berlin.

Walter, C., E. R. Flueh, C. R. Ranero, R. von Heune, and W. Strauch (2000), Crustal structure across the Pacific margin of Nicaragua: Evidence for ophiolitic basement and a shallow mantle sliver, *Geophys. J. Int.*, *141*, 759–777.

White, R. S., and D. McKenzie (1992), Oceanic crustal thickness from seismic measurements and rare earth element inversions, *J. Geophys. Res.*, *97*, 19,683–19,715.

Wilkens, R. H., G. J. Fryer, and J. Karsten (1991), Evolution of porosity and seismic structure of upper oceanic crust: Importance of aspect ratios, *J. Geophys. Res.*, *96*(B11), 17,981–17,995.

Zelt, C. A., and R. B. Smith (1992), Seismic traveltime inversion for 2-D crustal velocity structure, *Geophys. J. Int.*, *108*, 16–34.

Publication: Fluid flow through active mud dome Mound Culebra offshore Nicoya Peninsula, Costa Rica—evidence from heat flow surveying

Grevemeyer, I., A. J. Kopf, N. Fekete, N. Kaul, H. W. Villinger, M. Heesemann, K. Wallmann, V. Spiess, H. H. Gennerich, M. Muller, and W. Weinrebe (2004), Fluid flow through active mud dome Mound Culebra offshore Nicoya Peninsula, Costa Rica: evidence from heat flow surveying, *Mar. Geol.*, *207*(1-4), 145–157, doi:10.1016/j.margeo.2004.04.002.

Contributions

In the following publication, heat flux measurements are combined with other geophysical data and information from gravity coring to study the fluid flow through the active mud volcano, Mound Culebra, off the Nicoya Peninsula, Costa Rica. Ingo Grevemeyer and Achim Kopf compiled the publication that contains information collected and processed by various scientists mainly during the research cruises SO163 and M54. Martin Heesemann processed the geothermal data, i.e. the heat-flux and thermal conductivity data measured in-situ using violin bow design probes and the thermal conductivity data measured on gravity cores using needle probes.

Fluid flow through active mud dome Mound Culebra offshore Nicoya Peninsula, Costa Rica: evidence from heat flow surveying

Ingo Grevemeyer[a,b,c,*], Achim J. Kopf[b], Noemi Fekete[c], Norbert Kaul[b], Heinrich W. Villinger[b], Martin Heesemann[b], Klaus Wallmann[a,c], Volkhard Spieß[b], Hans-Hermann Gennerich[b], Meino Müller[b], Wilhelm Weinrebe[a,c]

[a] *IFM-GEOMAR, Leibniz Institut für Meereswissenschaften, Wischhofstraße 1-3, 24148 Kiel, Germany*
[b] *Fachbereich Geowissenschaften, Universität Bremen, Klagenfurter Straße, 28359 Bremen, Germany*
[c] *SFB 574, Christian-Albrechts Universität zu Kiel, Wischhofstraße 1-3, 24148 Kiel, Germany*

Received 19 March 2003; received in revised form 22 March 2004; accepted 7 April 2004

Abstract

Mud extrusion is frequently observed as a dewatering phenomenon in compressional tectonic settings such as subduction zones. Along the Middle American Trench, several of these features have been recently discovered. This paper presents a heat flow study of actively venting Mound Culebra, offshore Nicoya Peninsula, and is complemented by data from geophysical surveys and coring. The mud diapir is characterised by methane emission and authigenic carbonate formation at its crest, and is composed of overconsolidated scaly clays and clast-bearing muds. Compared with the conductive background heat flow, the flux through the mud dome is elevated by 10–20 mW/m^2, possibly related to advection of heat by fluids rising from greater depth. Decreased chlorinity in the pore waters from gravity cores may support a deep-seated fluid origin. Geothermal measurements across the mound and temperature measurements made with outriggers on gravity corers were corrected for the effects of thermal refraction, forced by the topography of the mound. Corrected values roughly correlate with the topography, suggesting advection of heat by fluids rising through the mound, thereby generating the prominent methane anomaly over the dome and nurturing vent biota. However, elevated values occur also to the southeast of the mound. We believe that the overconsolidated clays and carbonates on the crest form an almost impermeable lid. Fluids rising from depth underneath the dome are therefore partially channelled towards the flanks of the mound.

Keywords: heat flow; dewatering; fluid flow; mud diapir; subduction zone; Costa Rica

1. Introduction

Mud volcanism is a global phenomenon that has been studied for almost 200 years (e.g., Goad, 1816; Abich, 1857). Mud domes are most abundant along convergent margins (Higgins and Saunders, 1974; Kopf, 2002) and are related to the extrusion of fluid-rich, fine-grained sediments. The upward migration of mud through a lithologic succession is mainly driven by buoyancy, but processes like gas and fluid flow, petroleum formation and seismic activity may act as additional triggers (Kopf, 2002). In subduction zones, porous fluid-rich sediments accumulate in

* Corresponding author. IFM-GEOMAR, FB4 - Dynamik des Ozeanbodens, Christian Albrechts Universität, Wishhofstr. 1-3, Kiel D-24148, Germany. Tel.: +49-431-600-2337; fax: +49-431-600-2922.
E-mail address: igrevemeyer@geomar.de (I. Grevemeyer).

deep-sea trenches at high rates and then undergo deformation during which liquids and volatiles are expelled due to increasing compactional stress and temperature. Studies of geophysical data and samples of mud volcanoes have considerably improved the understanding of the mechanics, driving forces and evolution of these features through the most recent Earth history (e.g., Brown, 1990). In addition, deep ocean drilling and submersible studies shed crucial light on eruptivity, emission of volatiles and potential hazard originating from violent mud extrusion (e.g., Kopf, 2002). Although quantification of fluid and mud discharge of mud volcanoes is not easy due to the short-lived nature of individual discharge events and relative inaccessibility on the seafloor, first-order estimates regarding flux rates have recently been attempted for various features and regions (e.g., Henry et al., 1996; Kopf and Behrmann, 2000). When put into a broader context, such estimates indicate that mud extrusion contributes significantly to fluid backflux from the lithosphere to the hydrosphere. Along wide parts of large accretionary prisms (like the Barbados or Mediterranean Ridges), hundreds of mud volcanoes can cause fluid expulsion at rates exceeding those at the frontal part of the prism (see discussion in Kopf et al., 2001). Such fluids are believed to play a crucial role in heat transfer. However, temporal and spatial variability in the heat and fluid fluxes during the life cycle of mud domes complicates an assessment, primarily because heat flow data from active mud volcanoes are scarce.

In the vicinity of Nicoya Peninsula, Costa Rica, published heat flow surveying suggests that the downgoing lithosphere is colder than what has to be expected due to its age and sediment cover. It has been argued that a vigorous hydrogeological circulation system is mining heat (Langseth and Silver, 1996; Silver et al., 2000). Fluid flow is suspected to occur laterally, either by flow towards the trench or vertically through the margin wedge. Potential sites for vertical flow are dome-like features on the slope, which have been initially interpreted as mud volcanoes (Shipley et al., 1990; Zuleger et al., 1996; Bohrmann et al., 2002; Mörz et al., in press).

In this article, we present results from a transect of heat flow measurements across the prominent Mound Culebra mud dome offshore Nicoya Peninsula to reveal its local pattern of heat and fluid flux. In addition, a heat flow transect across the middle continental slope was obtained to yield the overall thermal state of the downgoing plate and margin wedge. This information is essential to determine the regional conductive heat flow through the margin, and hence a background reference for the Mound Culebra transect. Results will be compared with those from other mud volcano settings, and will be discussed in the context of geophysical data, structural observations and physical properties (density, porosity, thermal conductivity) of muds cored during leg 2 of cruise M54 with *RV Meteor* in summer 2002.

2. Geological background

West of Costa Rica and Nicaragua, late Oligocene to early Miocene oceanic crust of the Cocos Plate undergoes rapid (9.1 cm/year, DeMets et al., 1994) subduction along the Middle America Trench (Fig. 1). Recent drilling confirmed the fore-arc wedge to be of igneous origin, reflecting a non-accretionary scenario having followed subduction erosion (Kimura et al., 1997; Vannucchi et al., 2001). A ~ 400-m-thick sedimentary succession is underthrusting the igneous forearc wedge, which itself is covered by deformed slope sediments. Only a tiny thrust wedge is observed in the toe area of the overriding plate (von Huene et al., 2000; Kimura et al., 1997). Dewatering mechanisms in the frontal thrust wedge, the deformed slope sediments, the faulted igneous margin wedge, and the underthrust sediments play a crucial role in the understanding of the tectonic development of the margin (Hinz et al., 1996). Moreover, gas hydrate processes (and namely their dissociation), as suggested from the presence of BSRs (Bottom Simulating Reflectors) on seismic profiles (Pecher et al., 1998) and drillcore recovery (Kimura et al., 1997), may play a considerable role in fluid budget calculations along and across the active continental margin of Middle America.

The upper forearc off Costa Rica and Nicaragua has been investigated during numerous geophysical surveys, some of which observed mud volcanism (Shipley et al., 1990; Stoffa et al., 1991; Bohrmann et al., 2002). Recent results from deep sea drilling indicate that the frontal wedge of the overriding plate is of non-accretionary origin (Kimura et al., 1997), so that the mud volcanoes on the sediment apron

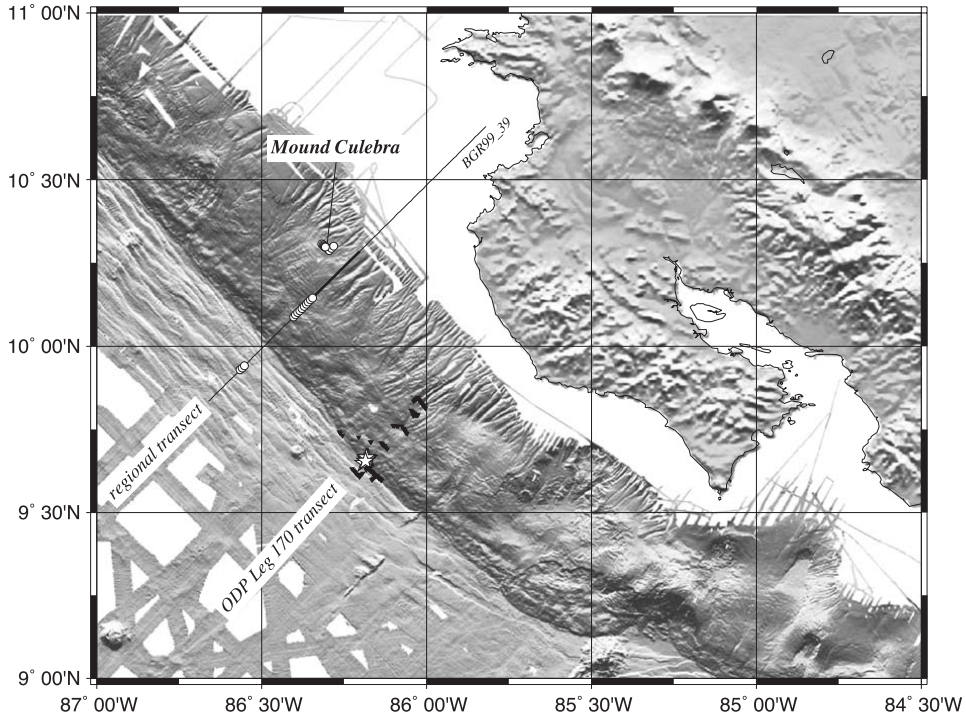

Fig. 1. Study area on the continental slope offshore Nicoya Peninsula, Costa Rica. Grey shaded areas are artificially illuminated bathymetry. Circles are the new heat flow measurements used in our study, surveying the continental slope and the mud diapir Mound Culebra. Inverted triangles are heat flow data from Langseth and Silver (1996); asterisks are ODP drill sites (Kimura et al., 1997).

overlying the igneous forearc wedge are either shallow dewatering products, or relate to deep-seated faults. The mud domes are numerous offshore Costa Rica and Nicaragua (H. Sahling, personal communication), generally cone-shaped, and do not exceed 1 km in diameter (Bohrmann et al., 2002; Mörz et al., in press).

Fluid venting has been documented on the Costa Rica forearc wedge, although not directly at the toe of the small accretionary structure (McAdoo et al., 1996). Instead, fluid venting was most abundant where normal faults and mud domes are observed at the seafloor some tens of kilometers behind the deformation front (Bohrmann et al., 2002; Hensen et al., 2003). These vents were typically accompanied by cold vent fauna (Kahn et al., 1996; Bohrmann et al., 2002). In addition, active seepage at landslides and headwall scarps related to seamount subduction releases fluids and gas into the ocean (Bohrmann et al., 2002). Enigmatic low heat flow of 8–14 mW/m^2 was detected offshore Nicoya Peninsula along the drilling transect of Ocean Drilling Program (ODP) Leg 170 and Leg 205, which is by a factor of 6 lower than what would be expected from sediment-covered crust of this age (Langseth and Silver, 1996; Silver et al., 2000). Unusual effective hydrothermal cooling is envisaged as explanation for the low-temperature crust, most likely via advection of heat by fluid flow through abundant faults, the latter perhaps originating from bending of the downgoing slab.

The chemistry of the fluids obtained from *Alvin* push cores reveal significant differences between vent-related sediments and slope apron samples (Zuleger et al., 1996). Sediment pore waters squeezed from cold vent areas and mud volcanoes indicate possible admixing of fluid from greater depth. Vice versa, interstitial waters of deposits from the sedimentary cover of the margin wedge show variations in sulfate and alkalinity, which are typical of material rich in organic matter, as it has been shown from deep drilling in the area (Hesse et al., 1985). Interstitial water compositions from ODP Leg 170 core material suggest mixing of deep fluids, gas

hydrate water and pore water (Kimura et al., 1997; Kopf et al., 2000).

3. Geology and structure of Mound Culebra

Detailed bathymetric charts of Mound Culebra have been obtained by RV *Sonne* using a Simrad EM120 swath mapping echosounder (Weinrebe and Flueh, 2002). The mound has an oval shape (~ 1500 m SW–NE-oriented long axis, ~ 700 m NW–SE-oriented short axis) and is topographically about 115 m higher than the surrounding seafloor (Fig. 2a). Its crest is situated at 86°18.3′W/ 10°17.8′N at a water depth of 1508 m and may juxtapose a normal fault through the forearc (Mörz et al., in press). Backscatter intensities are highest on the crestal plateau and the NE-flank (Fig. 2b). Ocean bottom video surveying suggests that high backscatter regions are characterised by authigenic carbonate precipitation, while the steep flanks are covered with soft sediments. A prominent methane anomaly over the mound, authigenic carbonate formation at its crest and typical cold seep fauna indicate that the feature is actively venting (Mau et al., 2003; Mörz et al., in press).

High-resolution multichannel seismic data were acquired during leg 1 of RV *Meteor* cruise M54 by the University of Bremen using a 600-m-long streamer and an airgun array with a total volume of 4.1 l. Fig. 3 displays a time-migrated seismic section, which is roughly orientated along the heat flow profile. The seafloor reflection is sharp and of high amplitude except on the steep flanks of the mound. The first 0.3 s TWT below the seafloor are characterised by distinct, subparallel reflectors that are often discontinuous. Reflectors show abrupt amplitude variations, and appear folded or tilted. Beneath the northwestern flank, the shallow strata are bent upwards and amplitudes decrease sharply towards the centre of the mound. Underneath the highly reflective package is a unit of low reflectivity and low continuity, with only few small high-amplitude patches. At approximately 0.6 s TWT below the seafloor, a sharp, reversed-polarity bottom simulating reflector is imaged, shoaling towards the mound, bending beneath its flanks. The BSR seems to be absent under the centre of the dome, although structural complexity, free gas or pronounced velocity anomalies may deteriorate the seismic image. It also displays local amplitude variations, as for example sudden decreases in amplitude near CDPs 2200, 2360 or southwest of 2400. Furthermore, fine scale seafloor topography, e.g., near CDP 2370, is not perfectly matched by the morphology of the BSR, indicating a smooth subseafloor temperature field.

4. Methods

4.1. Geothermal measurements

Geothermal measurements were made with a violin bow design "Lister probe" (Hyndman et al., 1979; Lister, 1979). This probe obtains the geothermal gradient from 11 thermistors mounted in a lance that penetrates 3 m into a sedimented seabed. After penetration, the frictional heating decays while the probe remains in the seafloor for 7 min. Equilibrium temperatures are calculated by extrapolating the decay of the frictional heating pulse (Hartmann and Villinger, 2002). At every other station, in situ conductivity measurements were made by applying a 20-s pulse of electric current along heater wires within the lance. The thermal decay of this calibrated heat pulse allows to estimate the conductivity at the location of in situ temperature measurements. Data from the individual thermistors were monitored in real time using a coaxial cable connecting the probe with the ship. In addition to measurements with the Lister probe, thermal gradients were measured by outriggers (Pfender and Villinger, 2002) mounted on some of the gravity corers. Thermal conductivities from the cores have been measured using needle probes (von Herzen and Maxwell, 1959), which were inserted into undisturbed areas of split cores recovered from the seafloor. All individual temperature and conductivity measurements were inverted to obtain surface heat flow. The complete processing sequence to obtain surface heat flow is described elsewhere (Hartmann and Villinger, 2002).

We investigated the measured gradients to search for direct evidence for heat advection and hence fluid

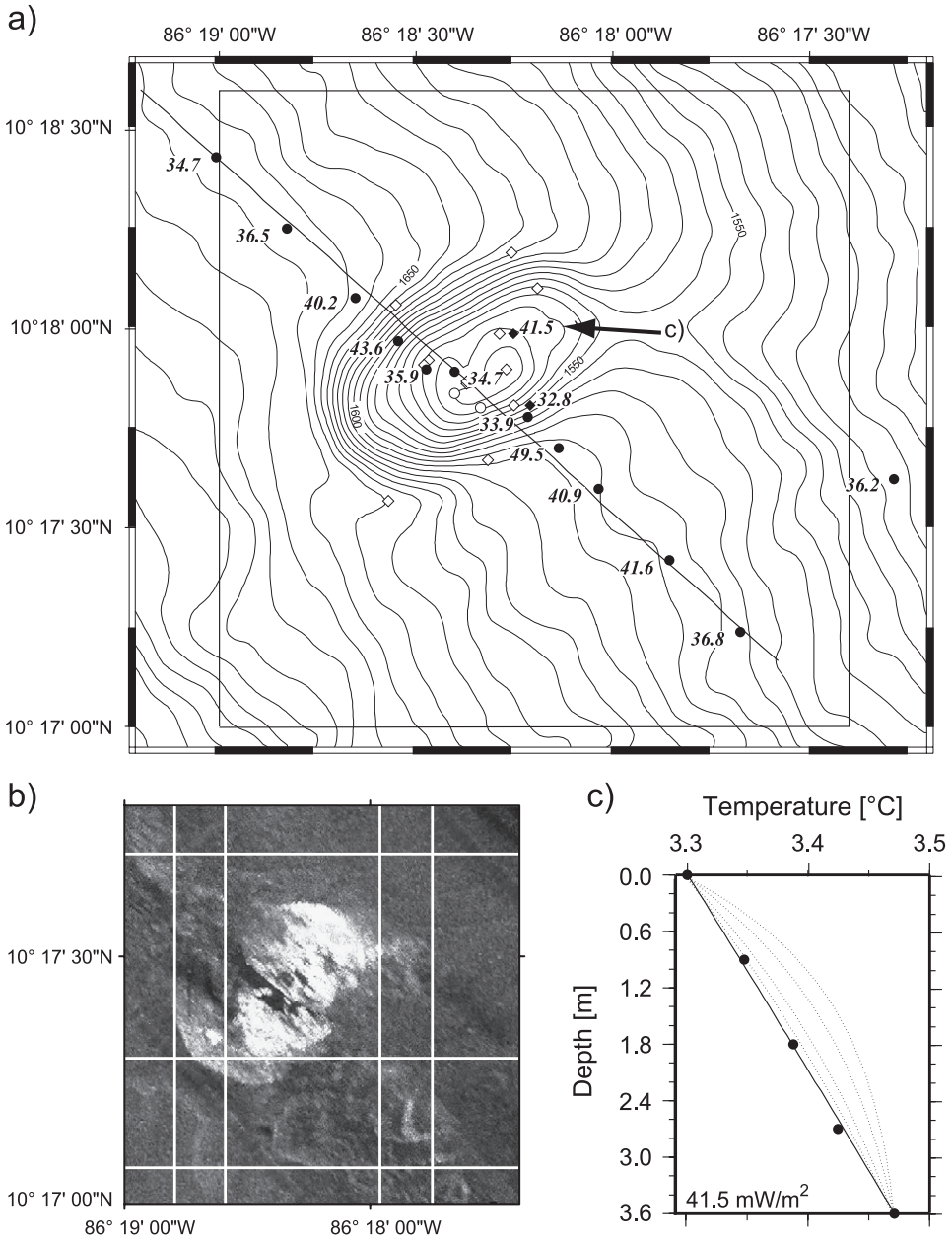

Fig. 2. (a) Detailed bathymetric map of Mound Culebra, showing geothermal stations (dots: heat probe measurements; diamonds: cores with outriggers) and heat flow values (in mW/m^2). Solid symbols indicate successful heat flow determinations. Outline shows the area covered with *TOBI* side-scan sonar. (b) *TOBI* backscatter image of Mound Culebra. White areas have high backscatter; black areas are shadows. Rough and hence light areas correlate with elevated carbonate outcrops seen in deep-tow video tracks. (c) Example of a measured thermal gradient [see (a) for location]. The linear trend clearly indicates that fluid flow rates are less than 1 cm/year. Doted curves are advective models with flow rates of 5, 10, 20 and 40 cm/year, respectively (Bredehoeft and Papadopulos, 1965).

flow. Fluid migration at rates of a few centimetres per year will generate nonlinear temperature–depth profiles (Bredehoeft and Papadopulos, 1965). However, even at the site of the deepest penetration on the crest of Mound Culebra, the temperature–depth trend is linear over the measured 3.6 m; thus, it does not

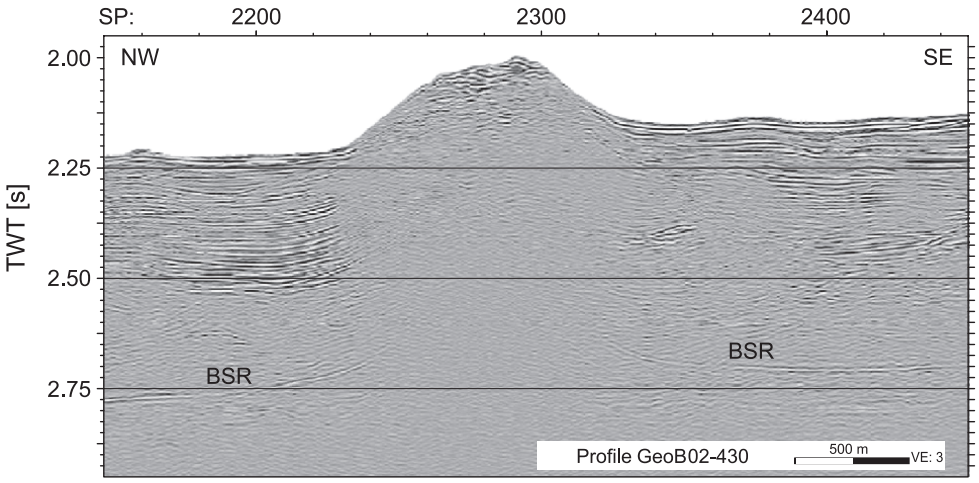

Fig. 3. Time-migrated high-resolution multichannel seismic profile (GeoB02-430) across Mound Culebra. The profile is orientated roughly along the heat flow transect. The most prominent features is a bottom simulation reflector (BSR). Note the lack of seismic reflections beneath the mound. The termination of reflectors and BSR under the mound may indicate fluid up flow.

provide any evidence for advective heat transfer (Fig. 2c). It is important to note that advection rates of less than ~ 1 cm/year cannot be discriminated from pure conductive heat transfer by thermal measurements. Nevertheless, elevated heat flow patches may still indicate locations of fluid outflow.

Measured heat flow values are supplemented by heat flow derived from the occurrence of natural gas hydrates; thus, bottom simulating reflectors. The temperature at BSR depth is expected to be controlled by a system of seawater and methane (Dickens and Quinby-Hunt, 1994; Grevemeyer and Villinger, 2001). Thermal gradients from heat probe measurements are generally higher than BSR-derived gradients, indicating that the thermal conductivity increases with depth. To calibrate BSR-derived heat flow values (e.g., Grevemeyer and Villinger, 2001), we used constraints from the measured gradients and thermal conductivities. For the surface heat flow, a one-to-one relationship between BSR-derived and measured data was archieved by using a thermal conductivity that is 0.1 W/mK higher than the reference values measured in the first 3 m of the seafloor, i.e., ~ 0.95 W/mK. BSR-derived heat flow was used to yield the regional heat flow along the seismic reflection line BGR99_39 (Ranero et al., 2003) shot across the continental slope adjacent to Mound Culebra (Fig. 1) and along line GeoB02-430 across the mud dome.

4.2. Complementary geophysical investigations and coring

To gain a better understanding of the extrusive nature of the mud mound, gravity and push coring were carried out. These cores were then examined for structural features and sampled for physical properties measurement (porosity, wet bulk density and grain density on discrete samples) and pore water analyses, e.g., Cl^-.

5. Results and discussion

5.1. Background heat flow and heat loss

On the middle continental slope in the vicinity of Mound Culebra, a regional transect was surveyed to yield the regional conductive heat flow through the margin wedge. The regional heat flow trend is defined by both measured and BSR-derived heat flow. To yield the thermal state of the incoming plate, a reference station was place seaward of the trench axis (Fig. 1). Values are scattered about the expected lithospheric heat flow (Fig. 4), indicating an average heat loss of the incoming plate, which roughly correlates with the expected heat flow anomaly of a 24-Myr-old plate. This observation indicates significantly different heat flow pattern than that obtained to the

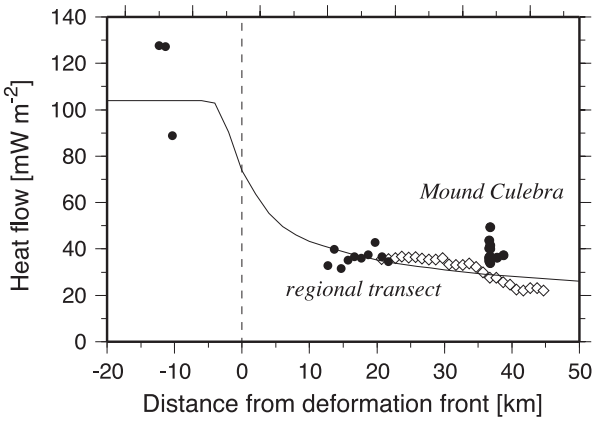

Fig. 4. Regional heat flow transect across the continental slope. Solid circles are measured heat flow values and open diamonds are BSR-derived data. Solid line represents the background conductive heat flow over the margin wedge and the downgoing lithosphere. Note the elevated heat flow over Mound Culebra.

south offshore Central Nicoya Peninsula, where—with respect to the age of the oceanic lithosphere—heat flow on the incoming oceanic plate is reported to be too low. This heat flow is interpreted to indicate vigourous mining of heat by hydrothermal flow of cold seawater through the permeable lava pile of the incoming Cocos plate (Silver et al., 2000). In consequence, the thermal state of the downgoing plate and hence of the margin wedge off Nicoya is affected (Harris and Wang, 2002). However, in accordance with our measurements, recent surveys on the incoming plate indicate profound changes of the thermal state parallel to the trench axis (Fisher et al., 2003), with higher heat flow to the northwest of Nicoya Peninsula. With respect to the thermal state of the incoming plate in the vicinity of Mound Culebra, a simple conductive cooling model with age-dependent basal heat flow seems to be appropriate.

To relate the surface heat flow through the margin wedge to the thermal properties of the downgoing lithosphere, heat flow was modelled using a two-dimensional analytical approximation to conduction through the upper plate and advection of heat into the subduction zone by the slab (Molnar and England, 1990). In general, frictional heating in the subduction zone thrust fault could be an important source of heat (e.g., Peacock, 1996). However, shear tests on clays sampled in the trench indicate that the coefficient of friction along the shallow decollement is low ($\mu \sim 0.2-0.25$; Kopf and Brown, unpublished data) and has been neglected. Thus, surface heat flow q is given by $q = q_0/S$, where q_0 is the flow related to the cooling lithosphere, and $S = \mathrm{sqrt}(z_f \upsilon \sin\delta/\kappa)$ is a denominator that accounts for advection of the descending lithosphere, where z_f is the depth to the plate interface, $\upsilon = 9.1$ cm/yr is the convergence rate, $\delta = 13°$ is the dip angle of the subducting plate and $\kappa = 1.1 \times 10^{-6}$ m^2/s is the thermal diffusivity of forearc crust. The dip angle of the downgoing plate is derived from seismic refraction studies (Ye et al., 1996; Walter et al., 2000), the convergence rate is from the NUVEL-1A model (DeMets et al., 1994) and the age of the incoming lithosphere (Barckhausen et al., 2001) is in agreement with the measured basal heat flow $q_0 = 104$ mW/m^2 (Fig. 4).

The conductive model derived from these parameters approximates the measured and BSR-derived heat flow trend across the slope (Fig. 4). Both the modelled heat flow and BSR-derived data indicate a regional surface heat flow of 25–30 mW/m^2 for Mound Culebra. Over the dome and adjacent to the feature, observations indicate values about 10–20 mW/m^2 (i.e., 30–80%) higher than the regional heat flow, and hence indicate additional sources of heat, possibly related to fluid flow through the margin wedge.

Unfortunately, only a few other mud domes and volcanoes have been investigated to yield their heat loss. In terms of thermal significance, the most spectacular mounds are located seaward of the deformation front of the Barbados accretionary prism (Henry et al., 1996; Sumner and Westbrook, 2001). Heat flow values on some of the features are well above 1000 mW/m^2. Similarly high values have been found on the Håkon Mosby mud volcano (Eldholm et al., 1999) in the Norwegian–Greenland Sea. However, these features may not be representative for the majority of mud domes at convergent margins. For example, in the vicinity of mud volcanoes investigated on the Mediterranean Ridge, heat flow roughly mimics the regional heat flow pattern, though values tend to increase towards the mounds (Camerlenghi et al., 1995).

Geochemical data from pore fluids sampled in Costa Rican mud domes suggest that the thermal regime in the vicinity of Mound Culebra may reflect fluids escaping out of the subduction zone along normal faults. The heat and fluid supply is therefore most

likely related to diagenetic and metamorphic reactions in the subduction zone (Hensen et al., 2003); thus, it may indicate fluid return flow out of the deep subduction zone (Moore and Vrolijk, 1992; Kopf et al., 2001). Evidence for deep fluids is perhaps found by decreased chlorinity in the pore waters from the gravity cores recovered from the lower flanks of Mound Culebra. Chlorinity decreases from seawater background concentration of 550 to ~ 510 mmol/l within 8 m. Reduced chlorinity may indicate the dissociation of gas hydrate. However, chlorinity may also indicate water release either from clay mineral dehydration (Colten-Bradley, 1987) or tectonic dewatering (Fitts and Brown, 1999). For mud domes offshore Central Costa Rica, Hensen et al. (2003) show that chloride anomalies are due to fluids rising from greater depth. Further evidence for fluids rising from greater depth has been found on other mounds off Nicoya Peninsula by Zuleger et al. (1996).

The significance of Mound Culebra and the other mud domes on the total advective heat transfer through the Costa Rican margin is difficult to assess. Although Mound Culebra is venting fluids and transferring heat advectively into the ocean, the magnitude of its heat flow anomaly suggests that the total energy loss over the whole feature is only moderate at present time, especially if we compare it to mud volcanoes seaward of the deep sea trench off Barbados (Henry et al., 1996) and off Norway (Eldholm et al., 1999). The fact that most of the mud domes offshore Nicoya Peninsula show little (and possibly episodic) activity is supported by observations made from dives with *Alvin* (Zuleger et al., 1996).

5.2. Hydrogeological implications

Heat flow data have been obtained along a northwest–southeast striking line across Mound Culebra and by outriggers during coring elsewhere on the dome. Away from the mound and on its flanks, all measurements were successful. On the crest, however, the probe or the gravity corers were not always able to penetrate the seafloor, possibly related to massive carbonates outcropping at the seafloor (Fig. 2b). However, the data show a systematic trend along the survey line and increase from local background values of ~ 34 mW/m^2 at approximately 2 km distance from the mound to ~ 40–50 mW/m^2 at the foot and steep slope (Figs. 2a and 5b). This trend is consistent with the upward curvature of the BSR as it approaches the mound (Fig. 3). In total, four successful penetrations were made on the crest. Surprisingly, heat flow on the mound and uppermost slope drops back to approximately local background flux. The only exception is a single site where outriggers made successful measurements. Heat flow is with 41.5 mW/m^2 well above the local background flux, suggesting that the anomaly may be caused by both conductive and advective effects.

However, topographic features on the seafloor may cause significant deviation of the conductive background flux by refraction of heat (Lachenbruch, 1968). We therefore calculate the impact of topography on the heat flow across Mound Culebra using a simple numerical model. Constraints from the numerical approach are in excellent agreement with an assessment based on analytical solutions provided by Lachenbruch (1968). The topography of the mound has indeed a profound effect on heat flow pattern, as it focuses and defocuses heat flow, with an elevated flux near the foot of the mound and decreased flux on the mound itself (Fig. 5). After correcting the heat flow for the effects of topography, heat flow over Mound Culebra roughly approximates the topographic relief with background values of 34 mW/m^2 to the northwest and elevated values of up to 58 mW/m^2 on the top. Values higher than the background flux may indicate advective transfer of heat through the mound. Fluid advection is supported by the formation of authigenic carbonate crusts (Fig. 2b), carbonate chimneys (Fig. 6; Mörz et al., in press), and methane venting on top of Mound Culebra (Mau et al., 2003) and methane plumes over other mounds offshore Costa Rica (Bohrmann et al., 2002). Additionally, recovered core material and deep-tow video tracks across Mound Culebra (Mörz et al., in press) show vent fauna and therefore support advective gas and fluid flow through Costa Rican mud domes.

It is interesting to note that BSR-derived heat flow to the northwest of the mound matches exactly with the measured surface heat flow, while measured heat flow to the southeast is elevated by 5–8 mW/m^2 with respect to the BSR-derived data (Fig. 5). On the accretionary prism of Vancouver Island, Davis et al. (1990) relate the discrepancy between higher values of measured heat flow and lower values of BSR-

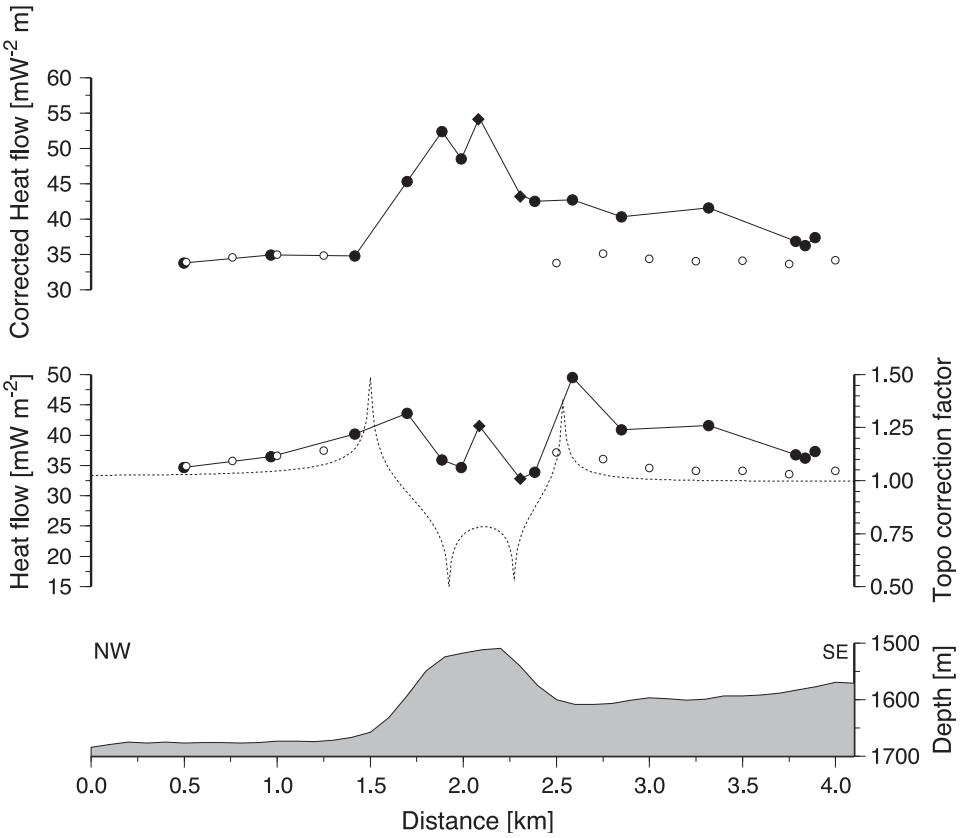

Fig. 5. Heat flow along the transect shown in Fig. 2a. (bottom) Topographic relief; (middle) observed heat flow over the mound (solid dots: measured heat flow; circles: BSR-derived heat flow) and the computed focusing and defocusing produced by the topography (broken line). The correction term of heat flow is expressed as heat flow fraction; thus, values normalised to the basal heat flow. (top) Corrected heat flow.

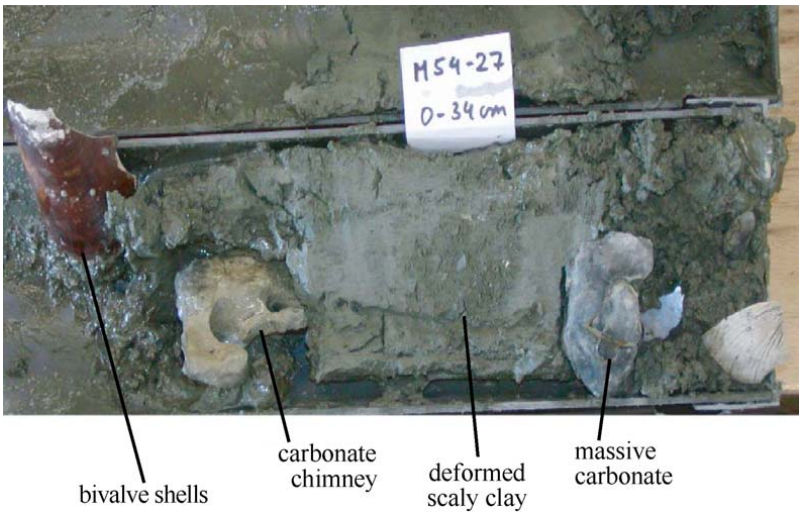

Fig. 6. Lithology of core M54-27, taken on the top of Mound Culebra.

derived heat flow to the advection of heat by fluid flow between the BSR and the seafloor. We therefore suggest that the region to the southeast of Mound Culebra, which is offset from the crestal plateau by ~ 1 km, may reflect seepage of fluids at the base of the mud dome.

Models of mud mounds generally suggest that warm fluids migrate upwards within an ascending mud diapir, causing venting on its top. However, because elevated values are not confined to the mound alone, fluid flow might be diverted. A series of gravity and push cores allow us to characterise the nature and origin of the mound. The cores at the foot of Mound Culebra recovered undisturbed silty clays, which have been interpreted as background sedimentation in the area. Thermal conductivity of the silty clays is low ($k = 0.73 - 0.8$ W/mK), indicating a relatively high porosity (e.g., Grevemeyer and Villinger, 2001). At the flank, the recovered material was intensely deformed, showing scaly fabrics, hydrofractures due to pore fluid overpressure (Behrmann, 1991), and striations on polished surfaces. Thermal conductivity increases ($k = 0.77 - 0.85$ W/mK), indicating a reduction of the porosity. Given the shallow depths of the cores, lower porosity and induration suggest that the material is slightly overconsolidated. The same is true for sediment obtained from the crestal cores. Here, muds are highly deformed and have collected mudstone clasts and carbonate fragments during ascent (Fig. 6). Brecciation and hydrofracturation allow soupy silts to migrate along ~ 1-cm-wide conduits to accommodate for the elevated pore pressures. Authigenic carbonate crusts of considerable thickness (in places exceeding 20 cm so that coring was impossible) cover the mound and indicate that methane gas or methane-rich fluids are emitted in the central area (Mörz et al., in press). Thermal conductivity increases further on the crest (maximum of $k = 1.17$ W/mK measured on the most intensely deformed scaly clays). Porosity of core material is between 50% and 60%. Therefore, physical properties show a systematic change across the mound, from watery muds away from the mound to overconsolidated muds on the flanks and competent clasts and authigenic carbonate on the crest (see also Mörz et al., in press). We therefore suggest that the overconsolidated clays and carbonates may form an almost impermeable lid that may affect the transfer of rising volatiles. As a consequence, fluid migration from depth may be diverted in some areas. While some volatiles (and namely the methane gas) ascend and emit at discrete crestal vent sites (see high heat flow value on the crest; Fig. 2a), a significant portion of the fluid is channelled along the base of the mud mound, where it may seep at slow rates out of the seafloor at the foot of the dome.

Based on our observations, a conceptual model for the evolution of Mound Culebra is summarised schematically in Fig. 7. During an initial phase, a

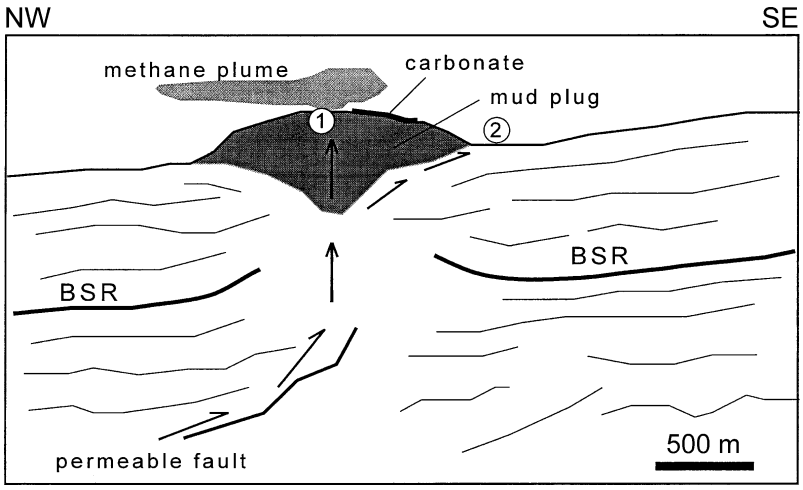

Fig. 7. Schematic cross section through Mound Culebra showing fluids rising along fractures and other high-permeability pathways through the mound (1), forming vent sites on top of Mound Culebra. In some areas, however, fluid migration from depth may be diverted (2) as a result of low permeability of indurated scaly clays (see text for discussion).

mud diapir started to ascend in the upper portion of the forearc. The mud now forming Mound Culebra has been most likely mobilised in the lowermost part of the sedimentary apron (i.e., ~ 1000-m depth) because the underlying forearc wedge consists of nonsedimentary, igneous material (Hinz et al., 1996; Kimura et al., 1997). The fluids, triggering ascent of the mud, may have originated at greater depth, possibly as deep as the plate boundary thrust (Moore and Vrolijk, 1992). These fluids may have migrated upwards along permeable faults cutting through the margin wedge (Hensen et al., 2003) before they helped create a density inversion in the slope apron sediment. Methane from depth may have further lowered the density of the mud (e.g., Hedberg, 1974). The liquefied mud then started to rise slowly as a diapir (rather than vigorously as a diatreme; see Brown, 1990), as indicated by the intensely deformed and dewatered scaly clays recovered by coring. Similar material has been found in diapiric mélanges elsewhere and has been interpreted as the product of maximised strains where the mud diapir is in contact with the surrounding host rock (Kopf, 2002). After having pierced the seafloor, fluid supply may have been shut off (at least temporarily), as suggested by the absence of mud debris flows at the crest and flanks. With time, the deformed scaly clays may have consolidated even further, so that the feature now acts as a plug to ascending fluids. As a consequence, fluid pressure transients rose to cause hydrofracture, this way creating pathways and small conduits for liquefied muds and gas to reach the crest. Such episodically active fluid flow is suggested from both heat flow data and evidence in the cores. The bulk portion of the dome, however, consists of muds of low porosity (~ 50%) and permeability. In addition to flow through the subvertical conduits in the cores, we propose that a considerable amount of fluid escapes beneath the plug and is conducted along the foot of the dome (Fig. 7). Here, slightly decreased chlorinity in the pore waters may support a deep origin of the fluid, perhaps related to clay mineral dehydration (Colten-Bradley, 1987; Hensen et al., 2003). Further research on both the muds and the fluids is required to assess the exact depths of their mobilisation and to date the rise and piercement of the mud mass.

Acknowledgements

We are grateful to scientists, masters and crews of research cruises *SO163* and *M54* for having provided support, information and discussion. Thanks also to Bernd Heesemann and Julia Schneider for assistance during the heat flow deployments. Marion Pfender assisted in calculating topographic corrections. Reviews of B. della Vedova, A. Camerlenghi, and G. Westbrook are appreciated. This study was funded by the Deutsche Forschungsgemeinschaft through grant Vi 133/7-1 to University of Bremen and the SFB 574 "Volatiles and fluids in subduction zones" at Christian-Albrechts University, Kiel. SFB 574 contribution no. 45.

References

Abich, O.W.H., 1857. Über Schlammvulkane und ihre Bedeutung für die Geologie. Ber. Ver. Deutsch. Nat. 33, 101.

Barckhausen, U., Ranero, C.R., von Huene, R., Cande, S.C., Roeser, H.A., 2001. Revised tectonic boundaries in the Cocos Plate off Costa Rica: implications for the segmentation of the convergent margin and for plate tectonic models. J. Geophys. Res. 106, 19207–19220.

Behrmann, J.H., 1991. Conditions for hydrofracture and the fluid permeability of accretionary wedges. Earth Planet. Sci. Lett. 107, 550–558.

Bohrmann, G., Heeschen, K., Jung, C., Weinrebe, W., Baranov, B., Cailleau, B., Heath, R., Hühnerbach, V., Hort, M., Masson, D., Trummer, I., 2002. Widespread fluid expulsion along the seafloor of the Costa Rica convergent margin. Terra Nova 14, 69–79.

Bredehoeft, J.D., Papadopulos, J.D., 1965. Rates of vertical ground water movement estimated from the Earth's thermal profile. Water Resour. Res. 1, 325–328.

Brown, K.M., 1990. The nature and hydrogeologic significance of mud diapirs and diatremes for accretionary systems. J. Geophys. Res. 95, 8969–8982.

Camerlenghi, A., Cita, M.B., della Vedova, B., Fusi, N., Mirabile, L., Pellis, G., 1995. Geophysical evidence of mud diapirism on the Mediterranean Ridge accretionary complex. Mar. Geophys. Res. 17, 115–141.

Colten-Bradley, V.A., 1987. Role of pressure in smectite dehydration—effects on geopressure and smectite-to-illite transformation. AAPG Bull. 71, 1414–1427.

Davis, E.E., Hyndman, R.D., Villinger, H., 1990. Rates of fluid expulsion across the northern Cascadia accretionary prism: constraints from new heat flow and multichannel seismic reflection data. J. Geophys. Res. 95, 8869–8889.

DeMets, C., Gordon, R.G., Argus, D.F., Stein, S., 1994. Effect of recent revisions to the geomagnetic reversal time scale on estimates of current plate motions. Geophys. Res. Lett. 21, 2191–2194.

Dickens, G.R., Quinby-Hunt, M.S., 1994. Methane hydrate stability in seawater. Geophys. Res. Lett. 21, 2115–2118.

Eldholm, O., Sundvor, E., Vogt, P.R., Hjelstuen, B.O., Crane, K., Nilsen, A.K., Gladczenko, T.P., 1999. SW Barents sea continental margin heat flow and Hakon Mosby mud volcano. Geo-Mar. Lett. 19, 29–37.

Fisher, A.T., Stein, C.A., Harris, R.N., Wang, K, Silver, E.A., Pfender, M., Hutnak, M., Cherkaoui, A., Bodzin, R., Villinger, H., 2003. Abrupt thermal transition reveals hydrothermal boundary and role of seamounts within the Cocos Plate. Geophy. Res. Lett. 30 (DOI:10.1029/2002GL016766).

Fitts, T.G., Brown, K.M., 1999. Stress induced smectite dehydration ramifications for patterns of freshening fluid expulsion in the N. Barbados accretionary wedge. Earth Planet. Sci. Lett. 172, 179–197.

Goad, S.T., 1816. Miscellaneous observations on the volcanic eruptions at the islands of Java and Sumbawa, with a particular account of the mud volcano at Grobogan. J. Sci. Arts 1, 245–258.

Grevemeyer, I., Villinger, H., 2001. Gas hydrate stability and the assessment of heat flow through continental margins. Geophys. J. Int. 145, 647–660.

Harris, R.N., Wang, K., 2002. Thermal models of the Middle America Trench at the Nicoya Peninsula, Costa Rica. Geophys. Res. Lett. 29, 2010 (doi 10.1029/2002GL015406).

Hartmann, A., Villinger, H., 2002. Inversion of marine heat flow measurements by expansion of the temperature decay function. Geophys. J. Int. 148, 628–636.

Hedberg, H., 1974. Relation of methane generation to undercompacted shales, shale diapirs and mud volcanoes. AAPG Bull. 58, 661–673.

Henry, P., LePichon, X., Lallemant, S., Lance, S., Martin, J.B., Foucher, J.P., Fiala-Médioni, A., Rostek, F., Guilhaumou, N., Pranal, V., Castrec, M., 1996. Fluid flow in and around a mud volcano field seaward of the Barbados accretionary wedge: results from Manon cruise. J. Geophys. Res. 101, 20297–20323.

Hensen, C., Wallmann, K., Schmidt, M., Ranero, C.R., Sahling, H., Suess, E., 2003. Fluid expulsion related to mud volcanism at Costa Rica continental margin—a window to the subducting slab. Geology 32, 201–204.

Hesse, R., Lebel, J., Gieskes, J.M., 1985. Interstitial water chemistry of gas-hydrate-bearing sections on the middle America trench slope. Proc. DSDP, vol. 84. U.S. Govt. Printing Office, Washington, DC, pp. 727–737.

Higgins, G.E., Saunders, J.B., 1974. Mud volcanoes–their nature and origin. Verh. Natforsch. Ges. Basel 84, 101–152.

Hinz, K., von Huene, R., Ranero, C., 1996. Tectonic structure of the convergent Pacific margin offshore Costa Rica from multichannel seismic reflection data. Tectonics 15, 54–66.

Hyndman, R.D., Davis, E.E., Wright, J.A., 1979. The measurement of marine geothermal heat flow by a multi-penetration probe with digital acoustic telemetry and in situ thermal conductivity. Mar. Geophys. Res. 4, 181–205.

Kahn, L.M., Silver, E.A., Orange, D., Kochevar, R., McAdoo, B., 1996. Surficial evidence of fluid expulsion from the Costa Rica accretionary prism. Geophys. Res. Lett. 23, 887–890.

Kimura, G., Silver, E.E., Blum, P., Shipboard Scientific Party Leg 170, 1997. Proc. ODP, Init. Repts., vol. 170. Ocean Drilling Program, College Station, TX. 458 pp.

Kopf, A.J., 2002. Significance of mud volcanism. Rev. Geophys. 40 (2), 1005 (doi: 10.1029/2000RG000093).

Kopf, A., Behrmann, J.H., 2000. Extrusion dynamics of mud volcanoes on the Mediterranean Ridge accretionary complex. In: Vendeville, B., Mart, Y., Vigneresse, J.-L. (Eds.), From the arctic to the Mediterranean: salt, shale, and igneous diapirs in and around Europe. J. Geol. Soc. Lond., Spec. Publ., vol. 174, pp. 169–204.

Kopf, A., Deyhle, A., Zuleger, E., 2000. Evidence for deep fluid circulation and gas hydrate dissociation using boron and boron isotopes in forearc sediments from Costa Rica (ODP Leg 170). Mar. Geol. 167, 1–28.

Kopf, A., Klaeschen, D., Mascle, J., 2001. Extreme efficiency of mud volcanism in dewatering accretionary prisms. Earth Planet. Sci. Lett. 189, 295–313.

Lachenbruch, A.H., 1968. Rapid estimation of the topographic disturbance to superficial thermal gradients. Rev. Geophys. 6, 365–400.

Langseth, M.G., Silver, E.A., 1996. The Nicoya convergent margin—a region of exceptionally low heat flow. Geophys. Res. Lett. 23, 891–894.

Lister, C.R.B., 1979. The pulse probe method of conductivity measurements. Geophys. J. R. Astron. Soc. 57, 451–461.

Mau, S., Rehder, G., Sahling, H., Hensen, C., Linke, P., 2003. The emission of methane from mud diapirs offshore Nicaragua and Costa Rica (abstract). EGS-AGU-EUG Joint Assembly 2003, Geophysical Research Abstracts, p. 5.

McAdoo, B.G., Orange, D.L., Silver, E.A., McIntosh, K., Abbott, L., Galewsky, J., Kahn, L., Protti, M., 1996. Seafloor structural observations, Costa Rica accretionary prism. Geophys. Res. Lett. 23, 883–886.

Molnar, P., England, P.C., 1990. Temperatures, heat flux, and frictional stress near major thrust faults. J. Geophys. Res. 95, 4833–4856.

Moore, J.C., Vrolijk, P., 1992. Fluids in accretionary prisms. Rev. Geophys. 30/2, 113–135.

Mörz, T., et al., 2003. Styles and productivity of mud diapirism along the Middle America margin—Part 2: Mound Culebra and Mounds 11 and 12. NATO Science Series. Kluwer Academic Publishing. In press.

Peacock, S.M., 1996. Thermal and petrologic structure of subduction zones. In: Bebout, G.E., Scholl, D.W., Kirby, S.H., Platt, J.P. (Eds.), Subduction: Top to Bottom. AGU Geophysical Monograph 96, 119–133.

Pecher, I.A., Ranero, C.R., von Huene, R., Minshull, T.A., Singh, S.C., 1998. The nature and distribution of bottom simulating reflectors at the Costa Rican convergent margin. Geophys. J. Int. 133, 219–229.

Pfender, M., Villinger, H., 2002. Miniaturized data logger for deep sea sediment temperature measurements. Mar. Geol. 186, 557–570.

Ranero, C.R., Phipps Morgan, J., McIntosh, K., Reichert, C., 2003. Bending-related faulting and mantle serpentinization at the Middle America trench. Nature 425, 367–373.

Silver, E., Kastner, M., Fisher, A., Morris, J., McIntosh, K., Saffer, D., 2000. Fluid flow path in the Middle America trench and Costa Rica margin. Geology 28, 679–682.

Shipley, T.H., Stoffa, P.L., Dean, D.F., 1990. Underthrust sediments, fluid migration paths and mud volcanoes associated with the accretionary wedge off Costa Rica, middle America trench. J. Geophys. Res. 95, 8743–8752.

Stoffa, P.L., Shipley, T.H., Kessinger, W., Dean, D.F., Elde, R., Silver, E.A., Reed, D., Aguilar, A., 1991. Three-dimensional seismic imaging of the Costa Rica accretionary prism: field program and migration examples. J. Geophys. Res. 96, 21693–21712.

Sumner, R.H., Westbrook, G.K., 2001. Mud diapirism in front of the Barbados accretionary wedge: the influence of fracture zones and North America–South America plate motion. Mar. Pet. Geol. 18, 591–613.

Vannucchi, P., Scholl, D.W., Meschede, M., McDougall-Reid, K., 2001. Tectonic erosion and consequent collapse of the pacific margin of Costa Rica: combined implications from ODP leg 170, seismic offshore data, and regional geology of the Nicoya Peninsula. Tectonics 20, 649–668.

von Herzen, R., Maxwell, M.E., 1959. The measurement of thermal conductivity of deep sea sediments by a needle probe method. J. Geophys. Res. 64, 1557–1563.

von Huene, R., Ranero, C.R., Weinrebe, W., Hinz, K., 2000. Quaternary convergent margin tectonics of Costa Rica, segmentation of the Cocos Plate, and central American volcanism. Tectonics 19, 314–334.

Walter, C.H.E., Flueh, E.R., Ranero, C.R., von Heune, R., Strauch, W., 2000. Crustal structure across the pacific margin of Nicaragua: evidence for ophiolitic basement and a shallow mantle sliver. Geophys. J. Int. 141, 759–777.

Weinrebe, W., Flueh, E.R. (Eds.), 2002. Cruise Report SO163, Subduction I. GEOMAR Reports 106, 534 pp.

Ye, S., Bialas, J., Flueh, E.R., Stavenhagen, A., von Huene, R., Leandro, G., Hinz, K., 1996. Crustal structure of the Middle American Trench off Costa Rica from wide-angle seismic data. Tectonics 15, 1006–1021.

Zuleger, E., Gieskes, J.M., You, C.-F., 1996. Interstitial water chemistry of sediments of the Costa Rica accretionary complex off the Nicoya Peninsula. Geophys. Res. Lett. 23, 899–902.

5 Conclusions and Outlook

Direct measurements of subseafloor temperatures and pressures provide important information that help us to improve our understanding of processes at convergent margins and in many other fields of marine research and exploration. Consequently, this thesis was directed towards two main objectives. The first objective was to increase the quantity, quality, and accessibility of future subseafloor formation temperature and pore pressure data for the scientific community. This was done by evaluating and improving data acquisition and processing tools and methods (Chapter 2 and 3). The second objective was to study convergent margin processes by developing thermal models that allow the joint interpretation of subseafloor temperature data along with other geophysical data and geologic evidences, as shown in Chapter 4.

5.1 Acquisition and processing of temperature and pressure data

The great success of many different probes developed to measure subseafloor temperatures and pressures—e.g. MTLs (*Heesemann et al.*, 2005, pp. 40), APCT-3 (*Heesemann et al.*, 2007, pp. 20), and DVTPP (*Heesemann et al.*, submitted 2008b, pp. 96)—underlines the potential of current technology. Moreover, exiting algorithms and software packages, e.g. TP-Fit (*Heesemann et al.*, in prep. 2008a, pp. 61), are capable to estimate undisturbed formation temperatures and pressures from transient tool responses. In the same way the APCT-3 and TP-Fit are major improvements compared to previous downhole temperature tools and data analysis software, it will always be possible to improve existing tools and algorithms.

Many potential improvements are not limited by the technology that is currently available; they depend primarily on the allocation of time and money for further developments. Regarding the temperature and pressure probes presented in Chapter 2 and 3, a new delivery system for the DVTPP that does not disturb the measurement when the probe is decoupled from the drill-string is the most important improvement that will have to be addressed in the future.

Besides simply increasing resolution, reliability, and handling of the tools, more sensors that monitor the insertion of the probe should be considered. These sensors could provide additional information about the nature of the disturbances that are created during the insertion. Taking advantage of this information in future versions of TP-Fit could lead to better estimates of undisturbed formation values. Other anticipated improvements of TP-Fit include making it not only a standard tool to process temperature data from ODP/IODP temperature tools, but also for DVTPP pressure data and temperature data from heat-flux probes.

Regarding seafloor measurements of pressure and temperature, reliable probe penetration is one of the most important problems that have to be solved in the future. For example, measurements on continental slopes are often challenging with current instruments as violin-bow heat-flux probes. Especially at the shallower parts of continental margins, where the first meters of the sediments are disturbed by seasonal bottom water temperature changes, temperature gradients over long depth intervals are required in order to obtain undisturbed data. In contrast to this requirement, however, sandy slope sediments often impede the probes' penetration. To overcome these problems, alternative probe insertion methods have to be developed. One new approach is the hard ground heat-flux probe developed by *Delisle and Zeibig* (2007). The design of the hard ground heat-flux probe overcomes the necessity of a strength-member, which is used in the violin-bow design to protect the sensor rod from bending but causes most of the resistance during insertion. Instead of the strength member, an innovative guiding system protects the sensor rod during insertion. A different approach would be to attach temperature sensors to active coring devices—e.g. the seafloor drilling rig (MeBo) (*Freudenthal and Wefer*, 2007) or a vibrocoring system.

5.2 Interpretation of temperature and pressure data

The studies presented in Chapter 4 give examples how numerical and conceptual models—constrained by subseafloor temperature data and other geophysical and geological observations—shed light on processes at convergent margins that are otherwise inaccessible using the technologies and resources that are available, today. Besides that models are always simplifications of reality, uncertainties in the model results are often a problem. In respect to the thermal FE model of subduction zones presented in this thesis (*Heesemann et al.*, submitted 2008a, pp. 109), these uncertainties are mainly due to the uncertainties of model parameters constraints. Moreover, the number of constraints is small compared to the degrees of freedom of the model. There are two ways to reduce the model uncertainties in the future.

Firstly, more model constraints could be measured with a higher accuracy. This can be done by employing new technologies to measure temperature gradients on the continental slope, discussed above, or by scientific drilling, as proposed by the SEIZE initiative. Besides probing temperatures and pressures at greater depth, boreholes can also provide constraints on model parameters as the thermal properties (i.e. thermal conductivity, heat capacity and radiogenic heat production) of the drilled formations.

The second way to minimize model uncertainties is to extend the model in a way that already existing measurements can be incorporated as additional constraints. However, extensions have to be made with care, since more complex models have a higher number of degrees of freedom. Therefore, these extensions can lead to increased model uncertainties, even though the number of constraints is increased. A promising extension of the model would be to define the thermal properties, e.g. thermal conductivity, as functions of seismic velocity. This approach would make better use of the information content of the seismic data which is relatively easy to obtain and is required to constrain the model geometry, anyway. This would, however, require research on the empirical relation between thermal conductivity of continental basement and its seismic velocity. Adding frictional heat production at the plate interface to the model is an extension that would be desirable, since frictional heating could have major influences on the temperature distribution at the subduction thrust-fault (e.g. *Molnar and England*, 1990). Numerically, it is possible to include frictional heating in the model—in fact it is already implemented in the model presented in this thesis. The dilemma is, however, that the presented model—of the thermal state of subduction zone off Nicaragua—already satisfies all of the existing constraints within their uncertainties, even without considering frictional heating. Since there are currently hardly any constraints on the magnitude of the basal friction, the addition of frictional heating would only increase the model uncertainties.

To increase the number of constraints, the thermal model could be coupled with other types of numerical models. For example, a numeric model of fluid flow in porous media could be coupled with the thermal model, since it is known that hydrothermal circulation plays an important role in subduction zone processes (e.g. *Peacock*, 1990; *Kummer and Spinelli*, 2008). I considered to include this type of coupling when I started to develop the thermal model. Yet, as with including frictional heating, it turned out that there are hardly any parameter constraints for the fluid flow part of the model; permeabilities of the different model domains are not well constrained and the fluid flow through the margin wedge, having a diffusive and focused component, is difficult to measure and consequently largely unconstrained. Especially for the sedimentary margin wedge, visco-elastic models (e.g. *Wang and Hu*, 2006; *Wang et al.*, 2006) may provide constraints for model parameters related to frictional heating, fluid flow, and transient processes throughout earthquake cycles, in the future. Using these visco-elastic models, geodetical measurements—for instance bathymetry data and time-series of seafloor deformation (e.g. *Fabian and Villinger*, 2007, 2008)—can be related to basal friction at the detachment fault and to pore pressures and stresses in the margin wedge.

Bibliography

Becker, K., and E. E. Davis (2000), Plugging the seafloor with corks, *OCEANUS*, *42*(1), 14–16.

Becker, K., and E. E. Davis (2004), In situ determinations of the permeability of the igneous oceanic crust, in *Hydrogeology of the Oceanic Lithosphere*, pp. 189–224, Cambridge University Press.

Bekins, B. A., and E. J. Screaton (2007), Pore pressure and fluid flow in the northern Barbados accretionary complex, in *The seismogenic zone of subduction thrust faults*, edited by T. Dixon and C. Moore, Columbia University Press, New York.

Brace, W. F., and J. Byerlee (1966), Stick-slip as a mechanism for earthquakes, *Science*, *153*(3739), 990–992.

Contreras-Reyes, E., I. Grevemeyer, E. R. Flueh, M. Scherwath, and M. Heesemann (2007), Alteration of the subducting oceanic lithosphere at the southern central Chile trench-outer rise, *Geochem. Geophys. Geosyst.*, *8*, Q07,003, doi: 10.1029/2007GC001632.

Davis, E. E., and H. Villinger (2006), Transient formation fluid pressures and temperatures in the Costa Rica forearc prism and subducting oceanic basement: CORK monitoring at ODP sites 1253 and 1255, *EPSL*, *245*, 232 – 244, doi: 10.1016/j.epsl.2006.02.042.

Davis, E. E., G. Horel, R. D. MacDonald, H. Villinger, R. H. Bennett, and H. Li (1991), Pore pressures and permeabilities measured in marine sediments with a tethered probe, *J. Geophys. Res.*, *96*(B4), 5975–5984.

Davis, E. E., K. Becker, T. Pettigrew, B. Carson, and R. MacDonald (1992), CORK: A hydrologic seal and downhole observatory for deep-ocean boreholes, in *Proc. ODP, Init. Repts.*, vol. 139, pp. 43–52, Ocean Drilling Program, Collage Station, TX.

Davis, E. E., H. Villinger, R. D. MacDonald, R. D. Meldrum, and J. Grigel (1997), A robust rapid-response probe for measuring bottom-hole temperatures in deep-ocean boreholes, *Marine Geophys. Res.*, *19*, 267–281, doi: 10.1023/A:1004292930361.

Delisle, G., and M. Zeibig (2007), Marine heat flow measurements in hard ground offshore Sumatra, *Eos Trans. AGU*, *88*(4), 38–39.

Dixon, T., and C. Moore (2007), The seismogenic zone of subduction thrust faults, in *The seismogenic zone of subduction thrust faults*, edited by T. Dixon and C. Moore, Columbia University Press, New York.

Fabian, M., and H. Villinger (2007), The Bremen ocean bottom tiltmeter (OBT)—a technical article on a new instrument to monitor deep sea floor deformation and seismicity level, *Marine Geophysical Researches*, *28*(1), 13–26.

Fabian, M., and H. Villinger (2008), Long-term tilt and acceleration data from the Logatchev Hydrothermal Vent Field, Mid-Atlantic Ridge, measured by the Bremen Ocean Bottom Tiltmeter, *Geochem. Geophys. Geosyst.*, doi: 10.1029/2007GC001917.

Fisher, A. T., E. E. Davis, M. Hutnak, V. Spiess, L. Zuhlsdorff, A. Cherkaoui, L. Christiansen, K. Edwards, R. Macdonald, H. Villinger, M. J. Mottl, C. G. Wheat, and K. Becker (2003a), Hydrothermal recharge and discharge across 50 km guided by seamounts on a young ridge flank, *Nature*, *421*(6923), 618–621.

Fisher, A. T., C. A. Stein, R. N. Harris, K. Wang, E. A. Silver, M. Pfender, M. Hutnak, A. Cherkaoui, R. Bodzin, and H. Villinger (2003b), Abrupt thermal transition reveals hydrothermal boundary and role of seamounts within the Cocos Plate, *Geophys. Res. Lett.*, *30*(11), 1550.

Flemings, P., H. Long, B. Dugan, J. Germaine, C. John, J. Behrmann, D. Sawyer, and I. E. . Scientists (2008), Pore pressure penetrometers document high overpressure near the seafloor where multiple submarine landslides have occurred on the continental slope, offshore Louisiana, Gulf of

Mexico, *Earth and Planetary Science Letters*, *In Press, Corrected Proof*, –.

Freudenthal, T., and G. Wefer (2007), Scientific drilling with the sea floor drill rig MeBo, *Scientific Drilling*, *2007*(5), 63–66, doi:10.2204/iodp.sd.5.11.2007.

Graber, K., E. Pollard, B. Jonasson, and E. Schulte (2002), Overview of ocean drilling program engineering tools and hardware, *Tech. rep.*, ODP, http://www-odp.tamu.edu/publications/tnotes/tn31.

Grevemeyer, I., A. J. Kopf, N. Fekete, N. Kaul, H. W. Villinger, M. Heesemann, K. Wallmann, V. Spiess, H. H. Gennerich, M. Muller, and W. Weinrebe (2004), Fluid flow through active mud dome Mound Culebra offshore Nicoya Peninsula, Costa Rica: evidence from heat flow surveying, *Mar. Geol.*, *207*(1-4), 145–157, doi:10.1016/j.margeo.2004.04.002.

Hartmann, A., and H. Villinger (2002), Inversion of marine heat flow measurements by expansion of the temperature decay function, *Geophysical Journal International*, *148*(3), 628–636.

Heesemann, M. (2002), Modeling and analysis of transient pressure measurements in ODP boreholes for undisturbed formation pressure estimation, Diploma thesis, University of Bremen, Bremen, Germany.

Heesemann, M. (2008), TP-Fit Version 1.0, a free software package to estimate undisturbed formation temperatures from downhole tool measurements, http://tp-fit.sourceforge.net/.

Heesemann, M., H. Villinger, H. W. Jannasch, M. Kastner, and the Expedition 301T Scientists (2005), Long-term temperature measurements in Holes 1253A and 1255A off Costa Rica, ODP Leg 205, in *Proc. ODP, Sci. Results*, vol. 205, edited by J. Morris, H. Villinger, and A. Klaus.

Heesemann, M., H. Villinger, A. T. Fisher, A. M. Tréhu, and S. Witte (2007), Testing and deployment of the new APCT-3 tool to determine insitu temperatures while piston coring, in *Expedition Reports*, *Proceedings of the Integrated Ocean Drilling Program*, vol. 311, doi:10.2204/iodp.proc.311.108.2006.

Heesemann, M., A. T. Fisher, and H. Villinger (in prep. 2008a), Estimation of in-situ formation temperatures from transient tool response in unconsolidated sediments during piston coring, *Geochem. Geophys. Geosyst.*, in prep.

Heesemann, M., I. Grevemeyer, and H. Villinger (submitted 2008a), Thermal constraints on the frictional conditions of the nucleation and rupture area of the 1992 Nicaragua tsunami earthquake, *Geophysical Journal International*, submitted.

Heesemann, M., H. Villinger, and E. E. Davis (submitted 2008b), Estimating in-situ formation pressures from penetration transients of a borehole probe, *Marine Geophys. Res.*

Horai, K., and R. P. Von Herzen (1985), Measurement of heat flow on Leg 86 of the Deep Sea Drilling Project, *Initial reports of the Deep Sea Drilling Project covering Leg 86 of the cruises of the Drilling Vessel Glomar Challenger, Honolulu, Hawaii, to Yokohama, Japan, May-June 1982*, *86*, 759–777, geoRef ID: 1986-018136.

Hutnak, M., A. T. Fisher, C. A. Stein, R. Harris, K. Wang, E. Silver, G. Spinelli, M. Pfender, H. Villinger, R. MacKnight, P. Costa Pisani, H. DeShon, and C. Diamente (2007), The thermal state of 18-24 ma upper lithosphere subducting below the Nicoya Peninsula, northern Costa Rica margin, in *The seismogenic zone of subduction thrust faults*, edited by T. Dixon and C. Moore, Columbia University Press, New York.

Hyndman, R. D., E. E. Davis, and J. A. Wright (1979), The measurement of marine geothermal heat flow by a multipenetration probe with digital acoustic telemetry and insitu thermal conductivity, *Marine Geophysical Researches*, *4*(2), 181–205.

Kaul, N., H. Villinger, and M. Kruse (2004), Satellite-linked autonomous pore pressure instrument - SAPPI, *Sea Technology*, *45*(8), 54–58.

Kummer, T., and G. A. Spinelli (2008), Hydrothermal circulation in subducting crust reduces subduction zone temperatures, *Geology*, *36*(1), 91–94.

Long, H., P. B. Flemings, and J. T. Germaine (2007), Interpreting in situ pressure and hydraulic properties with borehole penetrometers in ocean drilling: DVTPP and Piezoprobe deployments at southern

Hydrate Ridge, offshore Oregon, *J. Geophys. Res.*, *112*, B04,101, doi:10.1029/2005JB004165.

MARGINS Office (Ed.) (2003), *NSF MARGINS Programm – Science Plans 2004*, NSF, Lamont-Doherty Earth Observatory.

Molnar, P., and P. England (1990), Temperatures, heat flux, and frictional stress near major thrust faults, *J. Geophys. Res.*, *95*, 4833–4856.

Moore, G. F., A. Taira, A. Klaus, and Shipboard Scientific Party (2001), Init. repts., in *Proc. ODP*, vol. 190 [Online], Available from World Wide Web:http://www-odp.tamu.edu/publications/190_IR/190ir.htm.

Moore, J. C., and H. Tobin (1997), Estimated fluid pressures of the Barbados accretionary prism and adjacent sediments, in *Proc. ODP, Sci. Results*, vol. 156, pp. 229–237, Ocean Drilling Program, Collage Station, TX.

Moore, J. C., T. H. Shipley, D. Goldberg, Y. Ogawa, F. Filice, A. Fisher, M.-J. Jurado, G. F. Moore, A. Rabaute, H. Yin, G. Zwart, W. Brückmann, P. Henry, J. Ashi, P. Blum, A. Meyer, B. Housen, M. Kastner, P. Labaume, T. Laier, E. C. Leitch, A. J. Maltman, S. Peacock, T. H. Steiger, H. J. Tobin, M. B. Underwood, Y. Xu, and Y. Zheng (1995), Abnormal fluid pressures and fault-zone dilation in the Barbados accretionary prism: Evidence from logging while drilling, *Geology*, *23*(7), 605–608.

Morris, J. D., H. W. Villinger, A. Klaus, and Shipboard Scientific Party (2003), Init. repts., in *Proc. ODP*, vol. 205 [Online], Available from World Wide Web:http://www-odp.tamu.edu/publications/205_IR/205ir.htm.

Nagihara, S., and C. R. B. Lister (1993), Accuracy of marine heat-flow instrumentation: Numerical studies on the effects of probe construction and the data reduction scheme, *Geophysical Journal International*, *112*(2), 161–177.

Peacock, S. A. (1990), Fluid processes in subduction zones, *Science*, *248*(4953), 329–337.

Pfender, M., and H. Villinger (2002), Miniaturized data loggers for deep sea sediment temperature gradient measurements, *Mar. Geol.*, *186*, 557–570.

Revelle, R., and A. E. Maxwell (1952), Heat flow through the floor of the eastern north pacific ocean, *Nature*, *170*(4318), 199–200.

Saffer, D. M. (2007), Pore pressure within underthrust sediment in subduction zones, in *The seismogenic zone of subduction thrust faults*, edited by T. Dixon and C. Moore, Columbia University Press, New York.

Schultheiss, P. J., and S. D. McPhail (1986), Direct indication of pore-water advection from pore pressure measurements in Madeira Abyssal Plain sediments, *Nature*, *320*(3), 348–350.

Stegmann, S., and A. Kopf (2007), Marine deep-water free-fall CPT measurements for landslide characterisation off Crete, Greece (Eastern Mediterranean Sea) part 1: A new 4000m cone penetrometer, in *Submarine Mass Movements and Their Consequences*, edited by V. Lykousis, D. Sakellariou, and J. Locat, pp. 171–177, Springer Netherlands.

Stegmann, S., H. Villinger, and A. Kopf (2006), Design of a modular, marine free-fall cone penetrometer, *Sea Technology*, pp. 27 – 33.

Stein, C. A., and S. Stein (1992), A model for the global variation in oceanic depth and heat flow with lithospheric age, *Nature*, *359*(6391), 123–129.

Uyeda, S., and K. Horai (1982), Heat flow measurements on Deep Sea Drilling Project Leg 60, in *DSDP Initial Reports*, vol. LX, doi: 10.2973/dsdp.proc.60.146.1982.

von Herzen, R. P., and A. E. Maxwell (1964), Measurement of heat flow at the preliminary Mohole Site off Mexico, *J. Geophys. Res.*, *69*, 741–748.

Wang, K., and Y. Hu (2006), Accretionary prisms in subduction earthquake cycles: The theory of dynamic Coulomb wedge, *J. Geophys. Res.*, *111*, B06,410, doi:doi:10.1029/2005JB004094.

Wang, K., T. Mulder, G. C. Rogers, and R. D. Hyndman (1995), Case for very low coupling stress on the Cascadia subduction fault, *J. Geophys. Res.*, *100*, 12,907–12,918, doi:10.1029/95JB00516.

Wang, K., J. He, and Y. Hu (2006), A note on pore fluid pressure ratios in the coulomb wedge

theory, *Geophys. Res. Lett.*, *33*, L19,310, doi: 10.1029/2006GL027233.

Whittle, A. J., T. Sutabutr, J. T. Germaine, and A. Varney (2001), Prediction and interpretation of pore pressure dissipation for a tapered piezoprobe, *Geotechnique*, *51*(7), 601–617, doi: 10.1680/geot.51.7.601.51388.

Yamano, M., S. Honda, and S. Uyeda (1984), Nankai trough: A hot trench?, *Marine Geophysical Researches*, *6*(2), 187–203.

Danksagung

Viele Menschen haben mit ihren Anregungen und ihrem Interesse zum Inhalt dieser Arbeit beigetragen oder sie durch ihre Unterstützung erst möglich gemacht.

Besonders bedanken möchte ich mich bei…
Many thanks to…

… Herrn Prof. Dr. Heinrich Villinger sowohl für die Ermunterungen und die Geduld, die er mir in den vielen Jahren entgegen gebracht hat, als auch für die Betreuung dieser Arbeit.

… Prof. Dr. Achim Kopf dafür, dass er trotz des ganzen Hin und Her bereitwillig die Gutachterrolle übernommen hat und, dass er immer Zeit für die Erörterung von mehr und auch weniger wichtigen Fragen des Lebens aufgebracht hat.

… PD. Dr. Ingo Grevemeyer sowohl für die vielen fruchtbaren Diskussionen und Ideen, als auch für die Geduld die er mir entgegen gebracht hat.

… Prof. Dr. Andrew T. Fisher who not only shared his thoughts and ideas, but also his house and family life with me.

… Dr. Earl E. Davis for many fruitful discussions, a considerable amount of advice, and enlightening conversations.

… Dr. Peter Blum and Paul Foster for their interest in TP-Fit and for the opportunity to work with them in College Station.

… allen Mitgliedern der Arbeitsgruppe Meerestechnik und Sensorik für die gute Atmosphäre und die Hilfsbereitschaft in allen Lebenslagen.

… Inis, Anne, Oliver, Thomas, Mathias und Hie-Sun für die Unterstützung bei meiner Arbeit, für die schönen Zeiten in Bremen und dafür, dass sie immer da waren.

… meiner Großmutter, die mich so manches Mal ohne zu murren vermisst hat, während ich mich mal wieder in der Weltgeschichte herumgetrieben habe.

… meinen Eltern für ihr großes Verständnis, ihre Geduld und die viele Unterstützung.

… Angela, die mir immer mit viel Geduld und Ausdauer zur Seite gestanden hat.

LEBENSLAUF

PERSÖNLICHE ANGABEN

Martin Heesemann
Würzburger Str. 86
28215 Bremen
heesema@uni-bremen.de

Geboren am 19. Oktober 1973 in Bremerhaven.

SCHULAUSBILDUNG

08.1991 – 06.1994	Besuch der Oberstufe an der Waldschule Schwanewede.
08.1990 – 07.1991	AFS Gastschüler an der Lamar High School, Houston, Texas.

ZIVILDIENST

07.1994 – 10.1995	Häusliche Krankenpflege bei der Sozialstation Hagen.

STUDIUM

10.1995 – 05.2002	Studium der Geophysik mit dem Schwerpunkt marine Geophysik an der Universität Bremen. • Diplomarbeit: „Modeling and analysis of transient pressure measurements in ODP boreholes for undisturbed formation pressure estimation“ wurde mit dem RCOM-Forschungspreis 2003 ausgezeichnet. • Diplom am 21. Mai 2002 mit der Gesamtnote „sehr gut“ (1,1).

WISSENSCHAFTLICHER WERDEGANG

seit 09.2007	Freiberufliche Arbeit • Planung und Implementierung einer Software mit grafischer Oberfläche zur Analyse von Bohrlochtemperaturdaten für das Integrated Ocean Drilling Program, Texas A&M University.
09.2002 – 07.2007	Wissenschaftlicher Mitarbeiter an der Universität Bremen. „from The Incoming Plate to mega Thrust EarthQuakes“ (TIPTEQ) • Vorbereitung, Durchführung und Auswertung von Messungen zur Bestimmung von Wärmestrom und Wärmeleitfähigkeit auf der FS Meteor-expedition „M54/2“.

	• Erstellung von finite Elemente Modellen zur Berechnung der Temperaturverteilung in der Subduktionszone „Costa Rica Hydrogeology“ • Bergung und Installation von Temperatursonden für Langzeitbeobachtungen in ODP Löchern 1253 & 1255 vor der Küste Costa Ricas. • Auswertung der Temperaturdaten. „Temperature Probes of ODP“ (TEMPO) • Numerische Modellierung der thermischen Ansprechverhalten von hochauflösenden Temperatursonden. „Middle America Margin Subsurface Temperature"(MAMAST) • Vorbereitung, Durchführung und Auswertung von Messungen zur Bestimmung von Wärmestrom und Wärmeleitfähigkeit auf der FS Meteorexpedition „M54/2“. • Erstellung von finite Elemente Modellen zur Berechnung der Temperaturverteilung in der Subduktionszone
03.1999 – 08.2002	Studentische Hilfskraft an der Universität Bremen. • Entwicklung, Programmierung und Nutzung einer Sonde für das ROV „Cherokee“ zur gezielten Messung von Temperaturprofilen in den obersten 50 cm des Meeresbodens während der FS Poseidon Expedition „PO291“. • Entwicklung von Software zur Berechnung von Wärmeleitfähigkeiten aus Nadelsondenmessungen. • Bestimmung der Wärmeleitfähigkeit und des elektrischen Widerstandes mariner Sedimente. • Wärmestromdichtemessungen während der FS Sonne Expedition „SO145".
04.2002 – 07.2002	Studentische Hilfskraft am Alfred-Wegener-Institut für Polar- und Meeresforschung. • Bestimmung von Wärmestrom und Wärmeleitfähigkeit aus Daten, die auf der FS Polarsternexpedition „PS59“ gewonnen wurden.
04.2000 – 06.2000	Berufspraktikum bei der SONTEC GmbH. • Magnetische Sondierungen. • Magnetische Untersuchungen von archäologischen Ausgrabungsstätten in den Vereinigten Arabischen Emiraten.
09.1998 – 02.1999	Studentische Hilfskraft am Max-Planck-Institut für marine Mikrobiologie • Numerische Simulation von Fluidflüssen in porösen Medien.

SONSTIGES

Sprachkenntnisse	Deutsch, Englisch, Spanisch
EDV	Unix/Linux, MS-Windows, Shell Programmierung, Matlab, C/C++, Python, Pascal, LaTeX, GMT, MS-Office